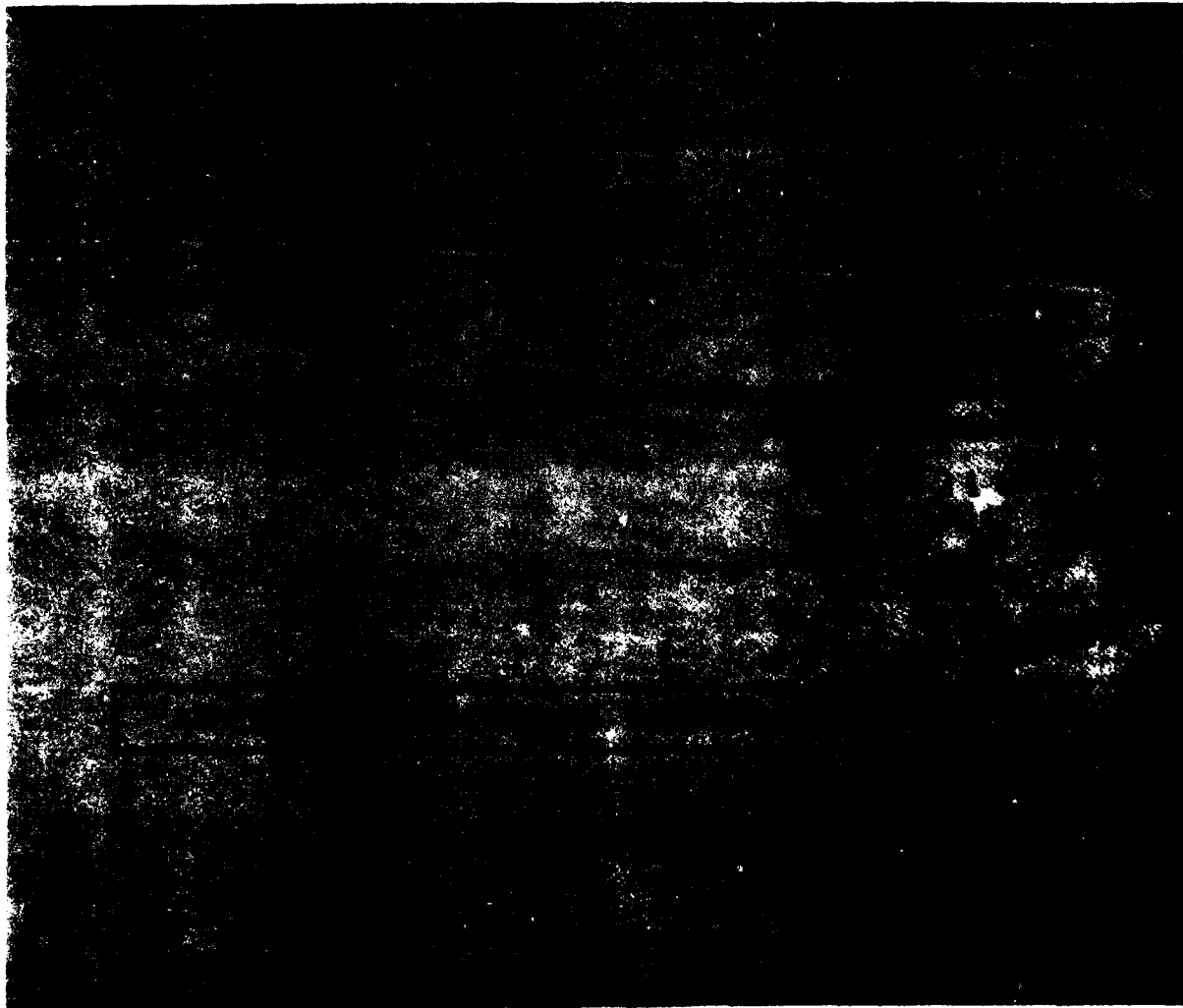


MICROCOPY RESOLUTION TEST CHART  
NATIONAL BUREAU OF STANDARDS-1963-A

**CSL** *COORDINATED SCIENCE LABORATORY*

AD-A161 279

**THEORETICAL STUDIES OF HIGH ENERGY TRANSPORT OF ELECTRONS AND HOLES IN GALLIUM ARSENIDE, INDIUM PHOSPHIDE, INDIUM ARSENIDE, AND GALLIUM ANTIMONIDE**



DTIC FILE COPY

**UNIVERSITY OF ILLINOIS AT URBANA-CHAMPAIGN**

**11 18-85 025**

AD-A161279

REPORT DOCUMENTATION PAGE

1a. REPORT SECURITY CLASSIFICATION Unclassified		1b. RESTRICTIVE MARKINGS None	
2a. SECURITY CLASSIFICATION AUTHORITY N/A		3. DISTRIBUTION/AVAILABILITY OF REPORT Approved for public release, distribution unlimited	
2b. DECLASSIFICATION/DOWNGRADING SCHEDULE N/A			
4. PERFORMING ORGANIZATION REPORT NUMBER(S) R-1011 UILU-ENG 84-2205		5. MONITORING ORGANIZATION REPORT NUMBER(S) N/A	
6a. NAME OF PERFORMING ORGANIZATION Coordinated Science Laboratory, Univ. of Illinois	6b. OFFICE SYMBOL (If applicable) N/A	7a. NAME OF MONITORING ORGANIZATION Office of Naval Research	
6c. ADDRESS (City, State and ZIP Code) 1101 W. Springfield Avenue Urbana, Illinois 61801		7b. ADDRESS (City, State and ZIP Code) 800 N. Quincy St. Arlington, VA 22217	
8a. NAME OF FUNDING/SPONSORING ORGANIZATION Office of Naval Research	8b. OFFICE SYMBOL (If applicable) N/A	9. PROCUREMENT INSTRUMENT IDENTIFICATION NUMBER N/A	
8c. ADDRESS (City, State and ZIP Code) 800 N. Quincy St. Arlington, VA 22217		10. SOURCE OF FUNDING NOS.	
		PROGRAM ELEMENT NO. N/A	PROJECT NO. N/A
		TASK NO. N/A	WORK UNIT NO. N/A
11. TITLE (Include Security Classification) Theoretical Studies of High Energy Transport of Electrons and . . .			
12. PERSONAL AUTHOR(S) Brennan, Kevin Francis			
13a. TYPE OF REPORT Thesis	13b. TIME COVERED FROM N/A TO	14. DATE OF REPORT (Yr., Mo., Day) June 1984	15. PAGE COUNT 181
16. SUPPLEMENTARY NOTATION N/A			
17. COSATI CODES		18. SUBJECT TERMS (Continue on reverse if necessary and identify by block number)	
FIELD	GROUP	SUB. GR.	
		compound semiconductors, Monte Carlo transport, impact ionization	
19. ABSTRACT (Continue on reverse, if necessary and identify by block number)			
<p>In this thesis, the high field behavior of both electrons and holes is studied using a Monte Carlo calculation including a complete band structure. The Monte Carlo method is particularly useful since it can be applied to both steady state and transient problems.</p> <p>The calculated steady state high field properties include the drift velocity and the impact ionization rate. It is determined theoretically that either GaAs or InP the electron and hole steady state drift velocities are roughly the same. The calculated carrier drift velocities in InP are larger than in GaAs.</p> <p>The impact ionization rate of both electrons and holes is calculated including quantum effects. It is found that the electron impact ionization rate is larger in GaAs than in InP because of the higher ionization threshold energy and greater density of states in InP. The electron ionization rate is greater than the hole ionization rate in GaAs because the electrons can drift to energies at or above the threshold energy, which is the same for both carriers, easier than the holes can. In InP, the hole ionization rate is larger than the</p>			
20. DISTRIBUTION/AVAILABILITY OF ABSTRACT UNCLASSIFIED/UNLIMITED <input checked="" type="checkbox"/> SAME AS RPT. <input type="checkbox"/> DTIC USERS <input type="checkbox"/>		21. ABSTRACT SECURITY CLASSIFICATION Unclassified	
22a. NAME OF RESPONSIBLE INDIVIDUAL		22b. TELEPHONE NUMBER (Include Area Code)	22c. OFFICE SYMBOL None

electron ionization rate because the hole threshold energy is smaller than the electron ionization threshold energy.

Among the transient transport problems examined is velocity overshoot of both electrons and holes in GaAs, InP and InAs. It is determined that there exists a narrow range of parameters such as the applied electric field, the initial condition (launching energy and momentum), the boundary condition at the collecting contact, and the semiconductor dimensions that result in significant velocity overshoot. The calculations show that the overshoot is greater in InP than in GaAs. This is because the valley separation energies are larger in InP so the electrons are more easily confined to the low effective mass gamma valley.

Extended velocity overshoot is attainable through use of staircase heterostructures. The excess kinetic energy gained by the electrons from an overlaid applied electric field is lost by making the electrons 'climb' a series of potential steps. In this way the electrons are confined to the gamma valley where they can achieve high drift velocities.

THEORETICAL STUDIES OF HIGH ENERGY TRANSPORT OF  
ELECTRONS AND HOLES IN GALLIUM ARSENIDE, INDIUM PHOSPHIDE,  
INDIUM ARSENIDE, AND GALLIUM ANTIMONIDE

BY

KEVIN FRANCIS BRENNAN

B.S., Massachusetts Institute of Technology, 1978  
M. S., University of Illinois, 1980

THESIS

Submitted in partial fulfillment of the requirements  
for the degree of Doctor of Philosophy in Electrical Engineering  
in the Graduate College of the  
University of Illinois at Urbana-Champaign, 1984

Urbana, Illinois

Accession For	
NTIS GRA&I	<input checked="" type="checkbox"/>
DTIC TAB	<input type="checkbox"/>
Unannounced	<input type="checkbox"/>
Justification	
By _____	
Distribution/ _____	
Availability Codes	
Dist	Avail and/or Special
A-1	

THEORETICAL STUDIES OF HIGH ENERGY TRANSPORT OF  
ELECTRONS AND HOLES IN GALLIUM ARSENIDE, INDIUM PHOSPHIDE,  
INDIUM ARSENIDE, AND GALLIUM ANTIMONIDE

Kevin Francis Brennan, Ph.D.  
Department of Electrical Engineering  
University of Illinois at Urbana-Champaign, 1984

In this thesis, the high field behavior of both electrons and holes is studied using a Monte Carlo calculation including a complete band structure. The Monte Carlo method is particularly useful since it can be applied to both steady state and transient problems.

The calculated steady state high field properties include the drift velocity and the impact ionization rate. It is determined theoretically that in either GaAs or InP the electron and hole steady state drift velocities are roughly the same. The calculated carrier drift velocities in InP are larger than in GaAs.

The impact ionization rate of both electrons and holes is calculated including quantum effects. It is found that the electron impact ionization rate is larger in GaAs than in InP because of the higher ionization threshold energy and greater density of states in InP. The electron ionization rate is greater than the hole ionization rate in GaAs because the electrons can drift to energies at or above the threshold energy, which is the same for both carriers, easier than the holes can. In InP, the hole ionization rate is larger than the electron ionization rate because the hole threshold energy is smaller than the electron ionization threshold energy.

Among the transient transport problems examined is velocity overshoot of both electrons and holes in GaAs, InP and InAs. It is determined that there exists a narrow range of parameters such as the applied electric field, the initial condition (launching energy and momentum), the boundary condition at the collecting contact, and the semiconductor dimensions that result in significant velocity overshoot. The calculations show that the overshoot is greater in InP than in GaAs. This is because the valley separation energies are larger in InP so the electrons are more easily confined to the low effective mass gamma valley.

Extended velocity overshoot is attainable through use of staircase heterostructures. The excess kinetic energy gained by the electrons from an overlaid applied electric field is lost by making the electrons 'climb' a series of potential steps. In this way the electrons are confined to the gamma valley where they can achieve high drift velocities.

### ACKNOWLEDGEMENTS

The author would like to express his sincere appreciation to his thesis advisor, Professor Karl Hess, for his guidance, encouragement, and continuing support throughout the course of this work.

The author would like to especially thank Professor J. P. Leburton for many helpful discussions, and his interest and support in many aspects of this work.

The author would also like to thank Professors N. Holonyak Jr., G. Stillman, and B. Wheeler for their interest and helpfulness.

Special thanks go to Professor Y. C. Chang for his help in calculating the valence band structure using the K \* P method.

The author would also like to acknowledge the support and helpfulness of Dr. J. Y. Tang in the early stages of this work.

For their cooperation, good humor, and friendship the author is grateful to K. Kahen, D. Widiger, P. Martin, T. Wang, Dr. M. Keever, Dr. J. Oberstar, and the rest of the group.

Thanks go to E. Kesler for typing the equations and the Tables in the Appendices.

The excellent technical assistance of R. F. McFarlane and J. T. Gladdin is gratefully acknowledged.

The author would like to deeply thank his parents for their tremendous support and encouragement throughout the course of his education. The author

is also grateful to his parents-in-law for their support.

Finally, the author wishes to dedicate this work to his loving wife, Denise. Without her love, total support, and patience this work would not have been possible.

TABLE OF CONTENTS

CHAPTER	PAGE
1. INTRODUCTION . . . . .	1
2. SUMMARY OF SEMICLASSICAL AND QUANTUM TRANSPORT THEORY . . . . .	4
2.1 Introduction . . . . .	4
2.2 Limitations of Semiclassical Transport Theory . . . . .	5
2.3 Quantum Transport Theory . . . . .	8
3. STEADY STATE HIGH FIELD TRANSPORT IN GaAs, InP, AND InAs . . . . .	13
3.1 Introduction . . . . .	13
3.2 Band Structure . . . . .	14
3.3 Steady State Drift Velocity Theory . . . . .	17
3.4 Phonon Scattering Rate . . . . .	28
3.5 Electron Impact Ionization . . . . .	33
4. STEADY STATE HIGH FIELD TRANSPORT OF HOLES IN GaAs AND InP . . . . .	42
4.1 Introduction . . . . .	42
4.2 Band Structure . . . . .	43
4.3 Phonon Scattering Rate . . . . .	44
4.4 Steady State Drift Velocity Theory . . . . .	59
4.5 Impact Ionization . . . . .	62
4.6 Conclusions . . . . .	72
5. STEADY STATE HOLE TRANSPORT IN GaSb AND $Al_x Ga_{1-x} Sb$ . . . . .	73
5.1 Introduction . . . . .	73
5.2 Review of Experimental Results . . . . .	73
5.3 Band Structure and Phonon Scattering Rate . . . . .	78
5.4 Computational Method . . . . .	86

CHAPTER	PAGE
5.5 Results of the Impact Ionization Calculation . . . . .	88
5.6 Conclusions . . . . .	95
6. TRANSIENT ELECTRONIC TRANSPORT THEORY . . . . .	96
6.1 Introduction . . . . .	96
6.2 Basic Computational Method . . . . .	97
6.3 Transport in GaAs, InP, and InAs . . . . .	99
6.4 Effect of Collecting Contact . . . . .	114
6.5 Electronic Transport in Staircase Heterostructures . . . . .	123
7. TRANSIENT HOLE TRANSPORT THEORY . . . . .	129
APPENDIX 1 DETAILS OF THE TRANSIENT CALCULATION . . . . .	137
APPENDIX 2 PARAMETERS USED IN THE CALCULATIONS . . . . .	142
APPENDIX 3 SUMMARY OF THE SCATTERING MECHANISMS IN THE VALENCE BAND . . . . .	149
A3.1 Nonpolar Optical Scattering . . . . .	150
A3.2 Acoustic Phonon Scattering . . . . .	152
A3.3 Polar Optical Scattering . . . . .	157
A3.4 Treatment of the Split-Off Band . . . . .	160
REFERENCES . . . . .	163
VITA . . . . .	173

## 1. INTRODUCTION

High field transport is of prime importance in many device applications, particularly in avalanche photodiodes, and Gunn devices [1]. High field effects become of increasing importance to FET's [2] and other devices [3,4] as their physical dimensions shrink in size. Phenomena such as impact ionization and velocity overshoot can occur which greatly affect device performance. It is the purpose of this thesis to examine high field transport and the related phenomena of impact ionization and velocity overshoot in device structures and bulk material. Of particular interest is transport in the compound semiconductors, GaAs, InP, InAs and GaSb and related heterostructures.

Carrier multiplication through impact ionization is essential in the operation of avalanche photodiodes. Maximum device performance is achieved if the electron,  $\alpha$ , and hole,  $\beta$ , ionization coefficients differ greatly [5,6]. The excess noise in avalanche photodiodes is greatly reduced when the carrier with the largest ionization coefficient is injected into the high field region [7]. Consequently, it is essential to identify materials or device structures [8-10] which have very different electron and hole ionization coefficients.

Recent experimental measurements [11-13] have indicated that the ratio of  $\alpha$  and  $\beta$  is greater than one in GaAs but less than one in InP. It has not been demonstrated theoretically why the ratio of  $\alpha$  and  $\beta$  is reversed in GaAs and InP. We present detailed calculations of both the electron and hole impact ionization rates in GaAs and InP and offer an explanation for the

reversal of  $\alpha/\beta$ .

As originally proposed by Ruch [14], velocity overshoot of electrons in GaAs may lead to a significant increase in carrier velocity over the steady state value. The recent work of Tang and Hess [15] and Brennan et al. [16] has shown that there exists a limited set of conditions, the collision free window, under which velocity overshoot can be appreciable for electrons in GaAs and InP. However, the distances over which velocity overshoot persists have been found to be small [15,16].

The extent to which velocity overshoot occurs depends upon the energy relaxation time which can be related to the valley separation energy. Very strong energy relaxation greatly limits the effects of velocity overshoot. In most III-V semiconductors at low fields the energy relaxation is dominated by polar optical scattering [17]. As the electron energy increases to the threshold for intervalley transfer, the energy relaxation rate increases drastically due to the presence of very strong deformation potential scattering. Therefore, it is desirable for high speed transport to avoid transfer to the satellite valleys where the energy relaxation is strong and the effective mass of the electron is large.

Due to the greater valley separation energy in InP, velocity overshoot persists over a longer distance and for a wider range of applied electric fields and launching energies than in GaAs [16]. In InAs the valley separation is even greater such that velocity overshoot is much greater than in GaAs and InP [18]. However the small energy band gap in InAs gives rise to a very large impact ionization rate. The impact ionization rate competes with intervalley scattering such that the electrons impact ionize rather than scatter to the satellite valleys. In this way the electrons are

constrained within the central valley where they can achieve very high drift velocities. However, this is undesirable in device applications because of the high carrier multiplication.

Extended velocity overshoot can be achieved another way through use of staircase heterostructures [19,20]. We have found that very high drift velocities can be attained by confining the electrons to the gamma valley by losing excess kinetic energy gained from an overlaid accelerating field. The mechanism for the energy loss is a series of ascending steps. In this way transfer to the subsidiary minima is avoided similar to the action of impact ionization in InAs. However, in the case of staircase heterostructures there is no carrier multiplication.

All of the calculations reported herein are made using the Monte Carlo method with the unique inclusion of a realistic band structure calculated using either the pseudopotential or K \* P methods. The Monte Carlo program is based on the semiclassical Boltzmann equation with some quantum mechanical modifications; the phonon scattering rate is calculated using a field theoretic approach. In Chapter 2 we discuss more fully the theoretical basis of the Monte Carlo program in both steady state and transient calculations. Chapters 3 and 4 discuss electron and hole impact ionization and the behavior of  $\alpha$  and  $\beta$ . The special case of hole impact ionization in GaSb and  $\text{Al}_{1-x}\text{Ga}_x\text{Sb}$  and the nature of the 'resonance' are discussed within Chapter 5. Transient electronic transport in GaAs, InP, InAs, and heterostructures is discussed in Chapter 6. Chapter 7 describes transient hole transport in GaAs and its relation to electronic transport.

## 2. SUMMARY OF SEMICLASSICAL AND QUANTUM TRANSPORT THEORY

### 2.1 Introduction

The principal problem in hot electron transport theory is to describe how the electron or hole distribution function is modified by an applied electric field. The Boltzmann equation, which describes charge transport, is very difficult to solve except in very few cases which are usually not applicable to real systems. Furthermore, since most transport quantities of interest are derived from averages over many physical processes the formulation of reliable microscopic models for the physical system under investigation is difficult. In order to get a result by directly solving the Boltzmann equation one must make drastic approximations which usually are invalid [21].

To overcome the difficulties in analytically solving the Boltzmann transport equation, numerical methods have been developed. Chief amongst these is the Monte Carlo method which was first used in semiconductor transport theory by Kurosawa [22] in 1966. The Monte Carlo method, as applied to charge transport in semiconductors, consists of a simulation of the trajectory of one or more electrons in a crystal subject to applied electric fields and phonon or carrier scattering mechanisms. The carrier free flight time and the phonon scattering agents are selected stochastically in accordance with some given probabilities describing the microscopic process. Consequently, any Monte Carlo method relies on the generation of a random number sequence with a given probability distribution.

In this thesis, we are primarily concerned with modeling carrier transport under two conditions, either steady state or transient transport. In the case of steady state transport, it is desired to model the carriers' response to an applied field in a homogeneous, bulk material with infinite boundary conditions. In general, it is sufficient to model the motion of one carrier only; from ergodicity it is assumed that a sufficiently long path of one trial carrier will effectively reproduce the response of an ensemble of carriers. In transient transport the carriers are subjected to spatial or temporal inhomogeneities. The initial and boundary conditions are of particular importance. It is necessary then to simulate a large number of electrons and trace their dynamic histories in order to obtain the desired information on the process of interest.

The semiclassical Monte Carlo method for both steady state and transient transport is discussed thoroughly elsewhere [21,23-27]. We will refrain from further discussion here of the mechanics of the Monte Carlo method. The details of the transient velocity analysis are summarized in Appendix 1. We will discuss the limitations of semiclassical transport in Section 2.2, and the basis of quantum transport theory in Section 2.3.

## 2.2 Limitations of Semiclassical Transport Theory

The basis of semiclassical transport theory is the Boltzmann equation, which is of the form

$$\frac{\partial f}{\partial t} + \left. \frac{\partial f}{\partial t} \right|_{\text{diff}} + \left. \frac{\partial f}{\partial t} \right|_{\text{drift}} + \left. \frac{\partial f}{\partial t} \right|_{\text{scatt}} = 0, \quad (2.1)$$

where

$$\left. \frac{\partial f}{\partial t} \right|_{\text{diff}} = -\vec{v}_k \cdot \frac{\partial f}{\partial \vec{r}}, \quad (2.2)$$

$$\left. \frac{\partial f}{\partial t} \right|_{\text{drift}} = - \frac{e}{\hbar} \vec{F} \cdot \frac{\partial f}{\partial \vec{k}} \quad (2.3)$$

and

$$\left. \frac{\partial f}{\partial t} \right|_{\text{scatt}} = \sum_{\vec{k}'} \left[ f(\vec{k}') (1 - f(\vec{k})) S(\vec{k}', \vec{k}) - f(\vec{k}) (1 - f(\vec{k}')) S(\vec{k}, \vec{k}') \right] \quad (2.4)$$

In the case of nondegenerate semiconductors and elastic collisions,  $S(\vec{k}', \vec{k}) = S(\vec{k}, \vec{k}')$ , Equation 2.4 becomes

$$\left. \frac{\partial f}{\partial t} \right|_{\text{scatt}} = \sum_{\vec{k}'} \left[ f(\vec{k}') - f(\vec{k}) \right] S(\vec{k}, \vec{k}') \quad (2.5)$$

The Boltzmann equation can be applied to a large variety of transport problems with much success. However it contains several implicit assumptions which may not always be valid. The most basic limitation within the Boltzmann equation is the assumption that the distribution function,  $f$ , can always be defined in phase space,  $\phi(\mathbf{x}, \mathbf{p})$ . In light of the Uncertainty Principle, one cannot strictly define a phase space distribution function. Consequently, it makes no sense to discuss an equation for  $f(\mathbf{k}, \mathbf{x}, t)$ . It appears then that the Boltzmann equation is not a legitimate means of describing quantum transport processes if both the real space position and the momentum are needed simultaneously.

Other implicit assumptions made in the Boltzmann transport equation are [28-30],

(1) The electronic states are stationary and free-electron-like with a well defined momentum,  $\mathbf{k}$ .

(2) The duration of the collision,  $\tau_c$ , is much smaller than the mean free time,  $\tau$ , between collisions,  $\tau \gg \tau_c$ . Only the asymptotic initial and final states of each collision are considered.

time,  $\tau$ , between collisions,  $\tau \gg \tau_c$ . Only the asymptotic initial and final states of each collision are considered.

(3) The effects of impurities and phonons can be considered as perturbations causing weak scattering amongst the Bloch states.

The above features, which are assumed in the Boltzmann formalism, are the basis for its failure in certain applications. When the mean time between collisions,  $\tau$ , is of the order of the collision duration,  $\tau_c$ , the elementary treatment of collisions in the Boltzmann equation must be reconsidered. Two new effects become important, multiple scattering and the intra-collisional field effect. If  $\tau \sim \tau_c$ , the electron may be under the influence of more than one scattering center at the same time [29] and multiple scatterings may occur. Under strong driving forces, energy and momentum can be transferred to the carrier during the collision as well as between collisions. The intra-collisional field effect then alters the energy gained or lost by the carrier during the collision. A strong scattering rate voids the assumption that the electronic states are long lived and free-electron-like. In this situation the effects of the phonons and impurities can no longer be considered as perturbations. Other effects such as size quantization, which occurs in very small systems, and many body effects also place limitations upon the validity of the Boltzmann equation.

It is not surprising, therefore, that alternative approaches have been taken in transport theory. Unfortunately, alternative formalisms to the Boltzmann equation lack its relative conceptual and mathematical simplicity. In the next section we will discuss transport theories which overcome the limitations of the Boltzmann equation.

### 2.3 Quantum Transport Theory

The basis of quantum transport, as in classical transport, is the use of an ensemble description. The essential difference between classical and quantum statistical mechanics is the means by which the ensemble averaging is performed. In classical mechanics, macroscopically observable entities are identified with ensemble averages. In quantum mechanics a macroscopic observable is determined by taking quantum mechanical matrix elements and ensemble averages together. The formalism developed to accomplish this is that of the density matrix [31,32].

In statistical mechanics we consider systems that interact with the external world. The wave function for the entire system,  $\phi(x,q)$ , depends on both the coordinates of the system under consideration,  $x$ , and the coordinates of the external world,  $q$ . We can establish the density matrix by supposing that the state vector of the system,  $\phi(x,q,t)$  can be expanded using a complete orthonormal set of vectors,  $u_n(x)$  as

$$\phi(x,q,t) = \sum_n C_n(q,t) u_n(x) . \quad (2.6)$$

The density matrix is defined by

$$\rho(\vec{x},\vec{x}') = \int dq \phi^*(x,q) \phi(x,q) . \quad (2.7)$$

After substituting Equation 2.6 into Equation 2.7 the elements of the density matrix are found to be

$$\rho_{nm} = \overline{C_m^* C_n} . \quad (2.8)$$

where the bar denotes an ensemble average, average over  $q$ .

The density matrix can be used to calculate the ensemble average of the expectation value of an observable,  $A$ , as

$$\overline{\langle A \rangle} = \overline{\langle \phi, A \phi \rangle} = \sum_{m,n} \overline{C_m^* C_n} A_{mn} = \sum_{m,n} \rho_{mn} A_{mn} = \text{Tr}(\rho A) \quad (2.9)$$

The time dependence of the density matrix is given as [33]

$$i\hbar \frac{\partial \rho}{\partial t} = [H, \rho] \quad (2.10)$$

which is analogous to the Liouville equation. It has been shown that transport in a quantum system can be correctly described using the density matrix and Equation 2.10 [34].

The use of the density matrix in practical problems is limited by its great complexity. Kohn and Luttinger [34,35] have used the density matrix formalism to solve a simple system, noninteracting free electrons scattered by impurity centers in the presence of a uniform electric field. By assuming that the interaction between the electrons and the impurity centers is weak, the density matrix for the system can be calculated using a perturbation expansion. To the lowest order in the perturbation, the diagonal elements of the density matrix satisfy the usual Boltzmann equation [34]. In higher orders the quantum effects become apparent and the Boltzmann equation is no longer valid [33,34]. New effects begin to appear that are not usually apparent in classical transport theory. The principal effect is that energy is not conserved due to the Uncertainty Principle [33].

In principle, one can calculate all transport properties using the density matrix approach and the mechanics presented by Kohn and Luttinger [34,35]. Once the density matrix is known to the desired order of accuracy, macroscopic observables of the system can be calculated through the use of

Equation 2.9. Unfortunately, the higher order equations for the density matrix are very complicated and unwieldy if not impossible to use. It is necessary then to develop alternative approaches to the quantum transport problem.

One of the first attempts to simplify the density matrix approach was made by Wigner [36]. He developed a particular distribution function, now known as the Wigner distribution function. Because of its special properties, the Wigner function can be used to calculate observables in a manner analogous to that of classical theory, by directly integrating the product of the observable and the Wigner function over all phase space. Since no quantum mechanical phase space distribution can exist, the Wigner function cannot be interpreted as a probability function. Its use is a matter of convenience rather than principle.

The Wigner function is defined for a single coordinate and momentum as [33]

$$P_{\omega}(x, p) = \frac{1}{2\pi\hbar} \int_{-\infty}^{+\infty} dy \xi(x + y/2) \xi(x - y/2) e^{ipy/\hbar}, \quad (2.11)$$

where  $\xi(x)$  is the time dependent state of the system in the coordinate representation. The main utility of the Wigner function stems from its unusual properties,

$$\int_{-\infty}^{+\infty} P_{\omega}(x, p) dp = \xi^*(x) \xi(x), \quad (2.12)$$

and

$$\int_{-\infty}^{+\infty} P_{\omega}(x, p) dx = \rho^*(p) \rho(p), \quad (2.13)$$

where

$$\phi(p) = \frac{1}{\sqrt{2\pi\hbar}} \int_{-\infty}^{+\infty} e^{-ipx/\hbar} \xi(x) dx \quad (2.14)$$

The importance of the Wigner function is that for any classical quantity,  $Q(p, x)$ , its quantum mechanical ensemble average can be computed by

$$\langle Q \rangle = \iint dx dp Q(p, x) P_{\omega}(x, p) \quad (2.15)$$

This suggests that it is possible to translate the results of classical transport theory into quantum transport by simply replacing the classical distribution function by the Wigner function. From the time evolution of  $P_{\omega}(x, p)$ , one recovers the classical collisionless Boltzmann equation in the limit as  $\hbar$  approaches zero [33].

The difficulties inherent in the Wigner function approach, aside from its construction for a complicated system, arise because it is neither positive definite, it has no probability interpretation, nor unique. The Wigner function cannot be viewed as the quantum analog of the classical distribution function. It is only a "trick" which may simplify quantum mechanical ensemble averaging.

From the above discussion, it is apparent that the use of formal quantum transport theory is immensely difficult and impractical to use in real problems. The work of Scott and Moore [37] has shown that for problems of the kind discussed below the basic physics of quantum transport theory can be incorporated into a Boltzmann-like transport equation for quasiparticles. The complicated physics of an interacting system is replaced by a quasiparticle system, one with single particle characteristics. The

quasiparticles, electrons dressed by a phonon cloud [38], become the carriers of interest.

The quasiparticle approach is well suited to the Monte Carlo method since it involves single particle transport. The use of quasiparticles alters the physical picture two ways. An energy level shift arises from the real part of the self-energy (due to the interaction of the electron with the phonons), and the lifetime of the state is finite. Therefore, the sharp, unperturbed momentum states in the classical picture are replaced by broadened, finite lifetime states in the quasiparticle picture. The effect of the self-energy can be incorporated into the electron-phonon scattering rate [24,39]. In Chapter 3 we will discuss the details of the self-energy calculation and how the scattering rate is calculated using it.

### 3. STEADY STATE HIGH FIELD TRANSPORT IN GaAs, InP, AND InAs

#### 3.1 Introduction

As the need for faster electronic devices grows, materials such as the III-V compound semiconductors will play an ever increasing role in new device technology [40-43]. The unique physical properties of materials such as GaAs, InP, and InAs make them especially attractive in different device applications. At low energies the electrons in these materials reside entirely within the central valley where they can achieve very high drift velocities [44-46]. As the applied electric field increases, the electrons are heated sufficiently such that intervalley transfer can occur. When the electrons are scattered from the central valley to the subsidiary minima, their effective mass changes significantly resulting in a substantial decrease in carrier velocity [23,46,47]. Consequently, it is desirable to choose materials with large intervalley separation energies in order to limit intervalley transfer and to achieve high speed. Of the three materials, GaAs, InP, and InAs, the satellite valley separation energy is greatest in InAs and smallest in GaAs. Based on this criterion, InAs would appear to be the most favorable material for high speed device applications, but its strong impact ionization rate makes it undesirable.

Reduced carrier transit time through a device structure can also be achieved by scaling down the device dimensions. However, the applied voltage cannot be scaled down along with the physical dimensions. Very high fields may then arise throughout the structure. Phenomena such as impact ionization can become important which may have an adverse effect upon device

performance [48]. In materials such as GaAs and InP, where the energy band gap is relatively large, the electrons must be heated to high energies in order for impact ionization to occur. Narrow band gap semiconductors, such as InAs, have a low impact ionization threshold leading to a high ionization rate at low electron energies. Each type of material provides different advantages in various applications [1].

This chapter is devoted to the study of the steady state high field electronic transport properties of GaAs, InP, and InAs. In Section 3.2 we discuss the conduction band structure of GaAs and InP. The steady state electron drift velocity is discussed in Section 3.3. The various scattering mechanisms and the field theoretic approach to the scattering rate are discussed in Section 3.4. Finally, the experimental and theoretical results are presented and discussed in Section 3.5.

### 3.2 Band Structure

The conduction band structure is calculated using the empirical pseudopotential method of Cohen and Bergstresser [49]. The band structures of GaAs and InP are presented in Figures 3.1 and 3.2 respectively. As seen from these figures, the energy band gap of GaAs at 300 K is 1.42 eV, slightly larger than the band gap of InP, 1.35 eV. The band gap of InAs is much smaller, .36 eV at 300 K. The different energy band gap values greatly influence the impact ionization rates in each material as we shall see.

Because of energy conservation, an electron must have an energy at least as large as the band gap in order to impact ionize. Therefore in large band gap semiconductors, the carriers must be high up in the band before they can impact ionize. In the past, most theoretical studies [50-55] of

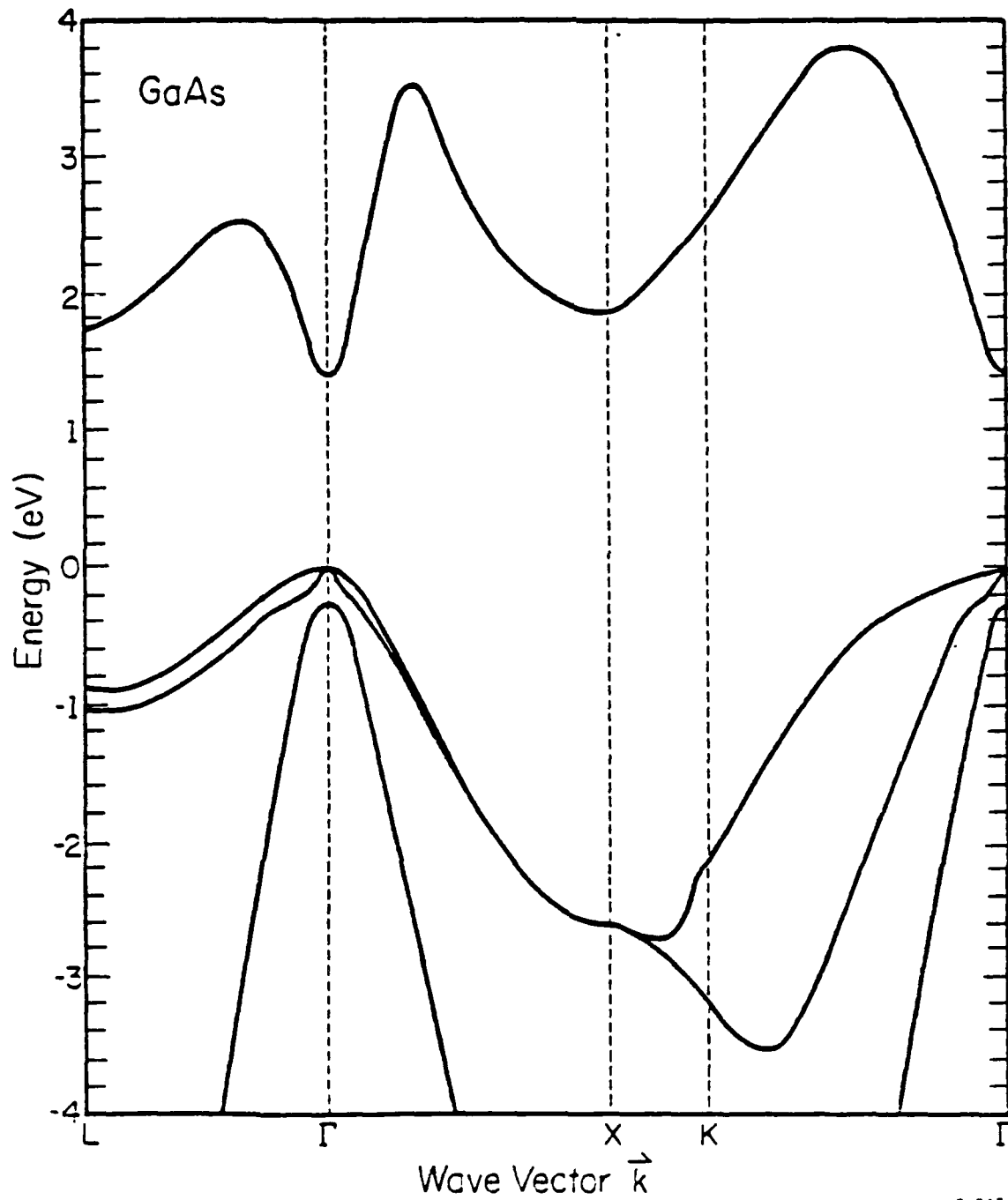


Fig. 3.1:  $E(k)$  relation for GaAs. The first conduction band is sketched based upon the results of a pseudopotential calculation while the valence bands are calculated using the  $K \cdot P$  method.

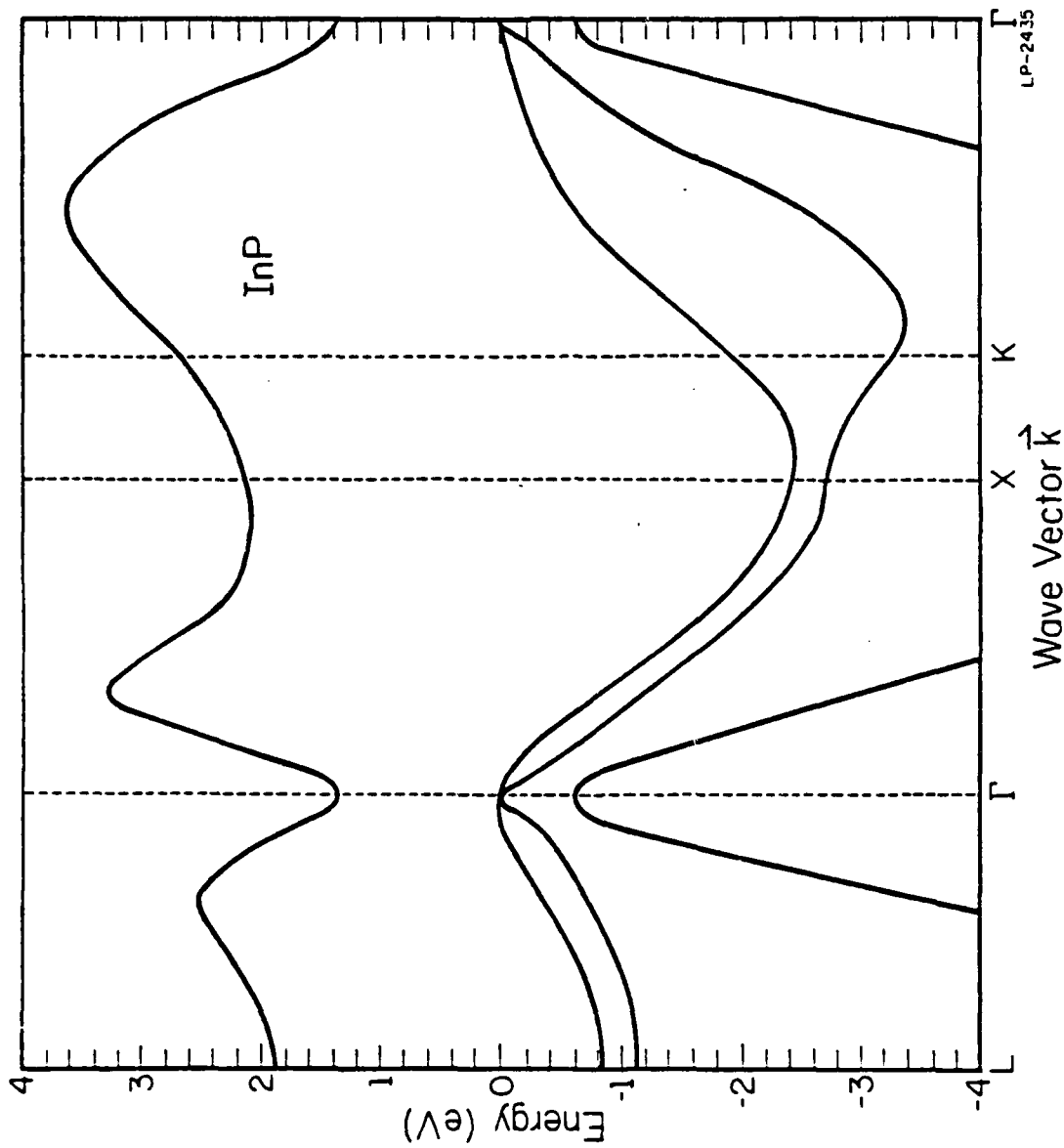


Fig. 3.2:  $E(k)$  relation for InP. The first conduction band is sketched based upon the results of a pseudopotential calculation while the valence bands are calculated using the  $K \cdot P$  method.

impact ionization have been based upon phenomenological fits which contain several adjustable parameters whose physical significance is not well understood. The most widely used of these theories is that given by Baraff [52], but the parameters employed in Baraff's theory are difficult if not impossible to calculate from first principles. The recent work of Shichijo and Hess [56] has provided a complete theory of impact ionization which can calculate the impact ionization parameters from first principles. The success of their theory is due to the abandonment of the effective mass approximation, which totally breaks down at high energies, in favor of a realistic band structure calculated using the pseudopotential method.

Figure 3.3 shows a cross section of the Brillouin zone. The isoenergy lines corresponding to this cross section for the first conduction band in InP are depicted in Figure 3.4. Notice that the bands are strongly warped and nonparabolic at high energy. Figure 3.5 shows another cross section of the Brillouin zone. Figure 3.6 illustrates the isoenergy lines corresponding to this cross section for the first conduction band in InP. Again we see that the bands are strongly warped at high energy. Therefore it is essential in high energy transport theory that a realistic band structure be used.

### 3.3 Steady State Drift Velocity Theory

The electron-phonon scattering rate depends upon parameters such as the intervalley phonon energies and coupling constants which are exceedingly difficult to measure directly. Their values are often ascertained by fitting the results of Monte Carlo calculations to more easily measured quantities [23,57] such as the electron drift velocity. From a comparison of the calculated and the experimental electron drift velocities, over a large range of applied electric fields, the overall electron-phonon scattering

impact ionization have been based upon phenomenological fits which contain several adjustable parameters whose physical significance is not well understood. The most widely used of these theories is that given by Baraff [52], but the parameters employed in Baraff's theory are difficult if not impossible to calculate from first principles. The recent work of Shichijo and Hess [56] has provided a complete theory of impact ionization which can calculate the impact ionization parameters from first principles. The success of their theory is due to the abandonment of the effective mass approximation, which totally breaks down at high energies, in favor of a realistic band structure calculated using the pseudopotential method.

Figure 3.3 shows a cross section of the Brillouin zone. The isoenergy lines corresponding to this cross section for the first conduction band in InP are depicted in Figure 3.4. Notice that the bands are strongly warped and nonparabolic at high energy. Figure 3.5 shows another cross section of the Brillouin zone. Figure 3.6 illustrates the isoenergy lines corresponding to this cross section for the first conduction band in InP. Again we see that the bands are strongly warped at high energy. Therefore it is essential in high energy transport theory that a realistic band structure be used.

### 3.3 Steady State Drift Velocity Theory

The electron-phonon scattering rate depends upon parameters such as the intervalley phonon energies and coupling constants which are exceedingly difficult to measure directly. Their values are often ascertained by fitting the results of Monte Carlo calculations to more easily measured quantities [23,57] such as the electron drift velocity. From a comparison of the calculated and the experimental electron drift velocities, over a large range of applied electric fields, the overall electron-phonon scattering

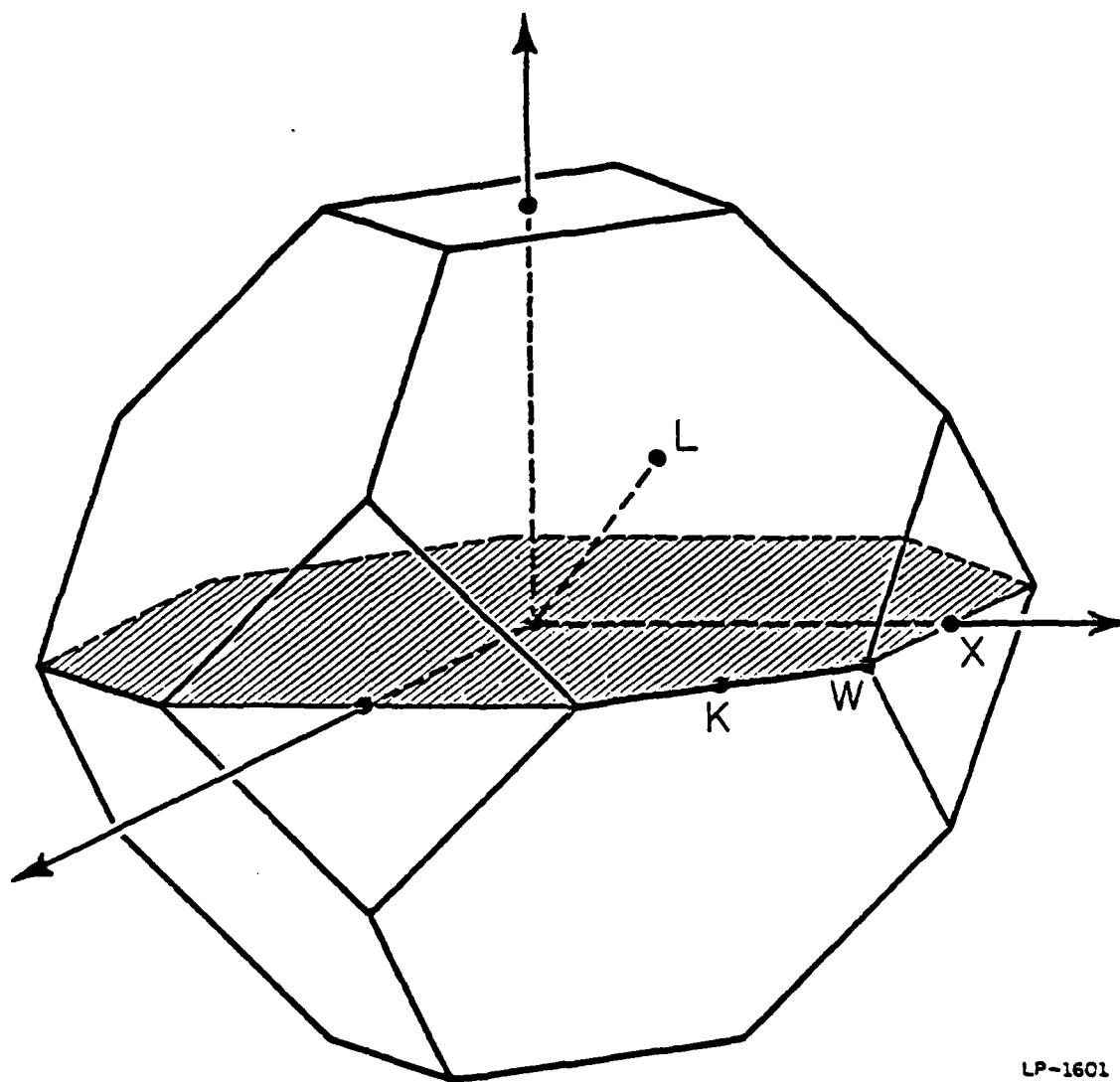


Fig. 3.3: Cross section of the Brillouin zone.

InP  
(Isoenergy Surface)  
Conduction Band

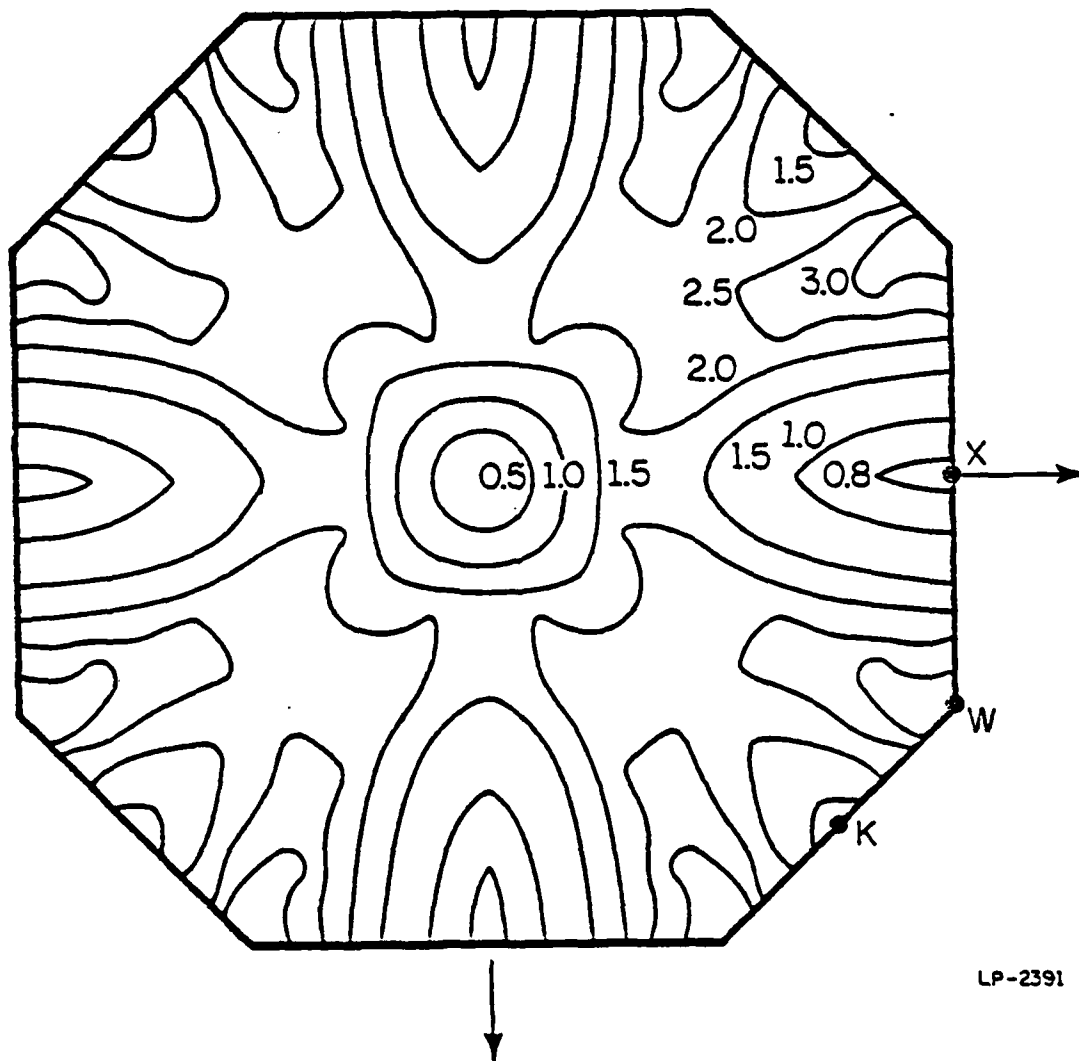
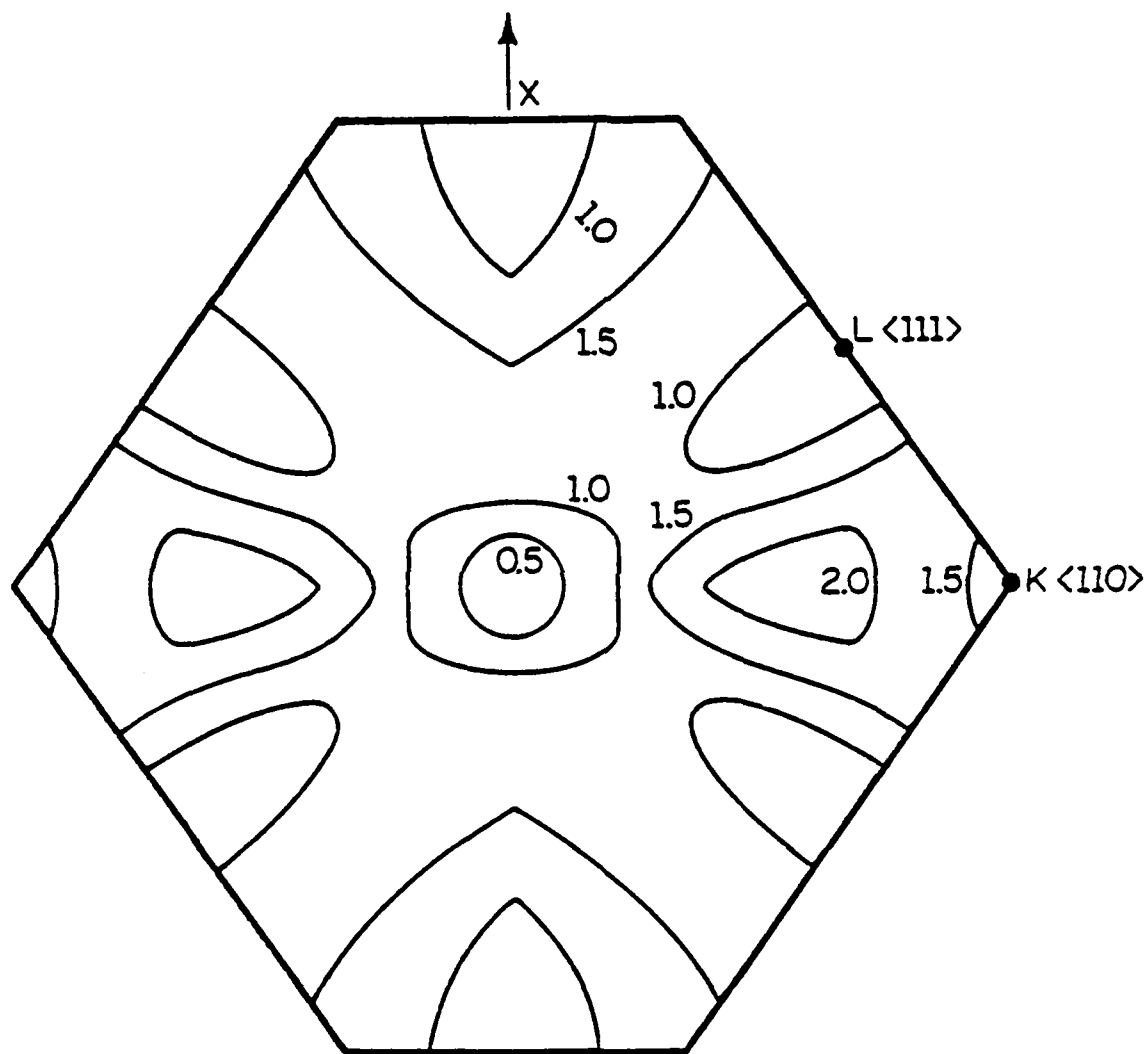


Fig. 3.4: Isoenergy lines of the first conduction band in InP in the cross section shown in Figure 3.3. The numbers represent the energies measured from the gamma minimum in eV.



InP  
First Conduction Band



LP-2392

Fig. 3.6: Isoenergy lines of the first conduction band in InP in the cross section shown in Figure 3.5. The numbers represent the energies measured from the gamma minimum in eV.

rate can be determined. Previous Monte Carlo calculations [23,57] have determined a set of coupling constants and phonon energies for electron-phonon scattering in GaAs. These results are in excellent agreement with experimental measurements of the low field drift velocity [58].

We have used the results of Littlejohn et al. [57] for the intervalley phonon energies and coupling constants for InP but have found that for GaAs we obtain a better fit to the experimental drift velocity measurements [58,59], Figure 3.7, if we use slightly lower values for the intervalley phonon energies. The parameters used in our computations for GaAs are collected in Appendix 2, Table A2.1. The parameters used in the Monte Carlo program for transport in InP are collected in Appendix 2, Table A2.2. As can be seen from Figure 3.8 the Monte Carlo calculation of the steady state drift velocity agrees well with the experimental data [60] for InP. The electron-phonon scattering rates for GaAs and InP derived from the drift velocity data are presented in Figures 3.9 and 3.10 respectively.

The material parameters used for InAs are listed in Appendix 2, Table A2.3. Due to the lack of extensive drift velocity data in InAs we have used the same intervalley phonon energies as for InP. Because of the similar deformation potentials between all three compounds [61,62], the intervalley coupling constants are taken to be the same. Since the satellite valleys are separated from the central valley by extremely large energies, the effect of intervalley scattering in InAs on the drift velocity is only important at very high applied fields. Figure 3.11 shows the steady state drift velocity in InAs as a function of field in the presence of impact ionization. Notice that the peak drift velocity is very high,  $8.0 \times 10^7$  cm/sec, at a field of 75 kV/cm. If impact ionization does not occur (which can be achieved

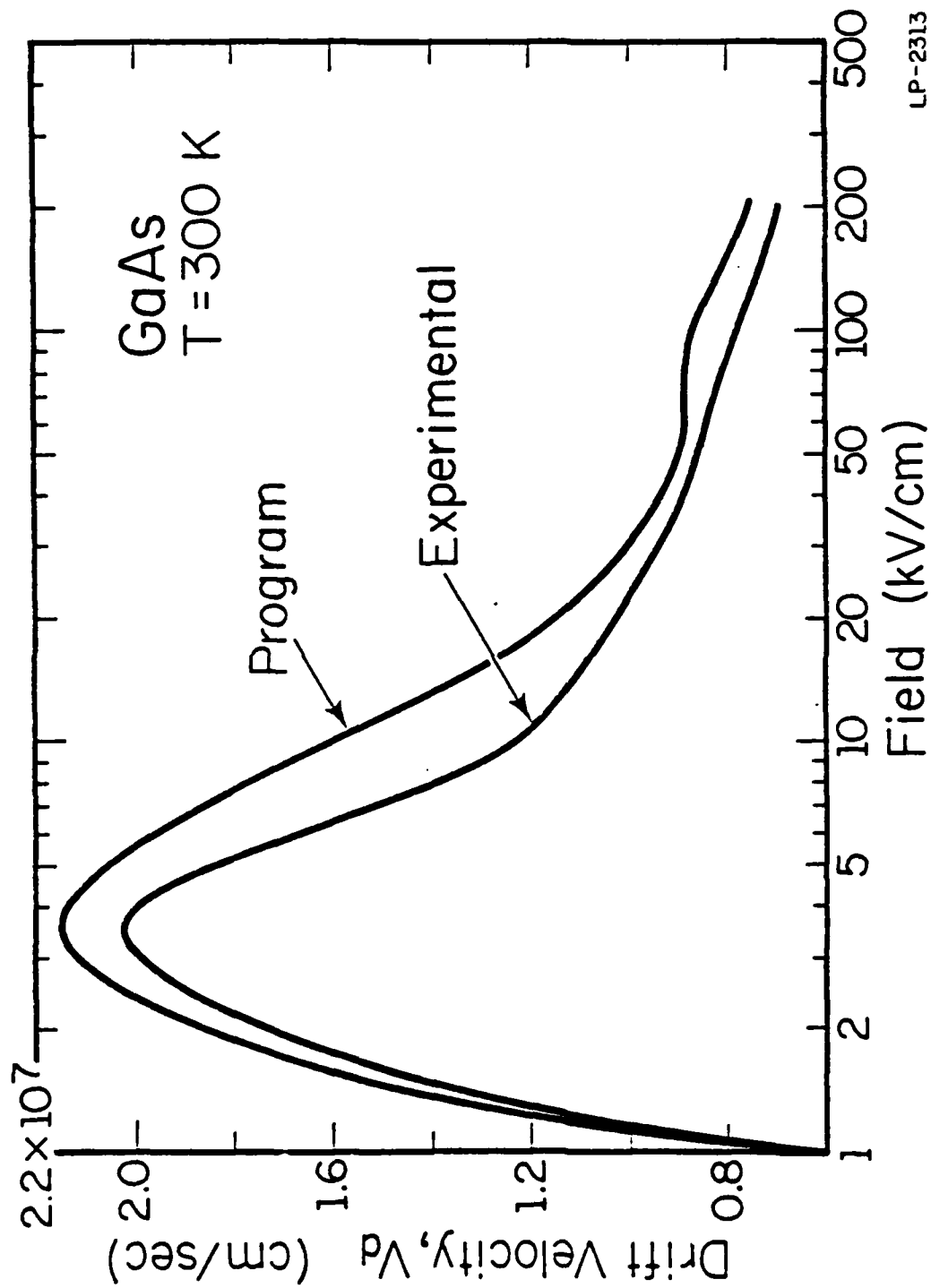


Fig. 3.7: Calculated steady state electron drift velocity in GaAs at room temperature compared with the experimental data of Windhorn et al. [59].

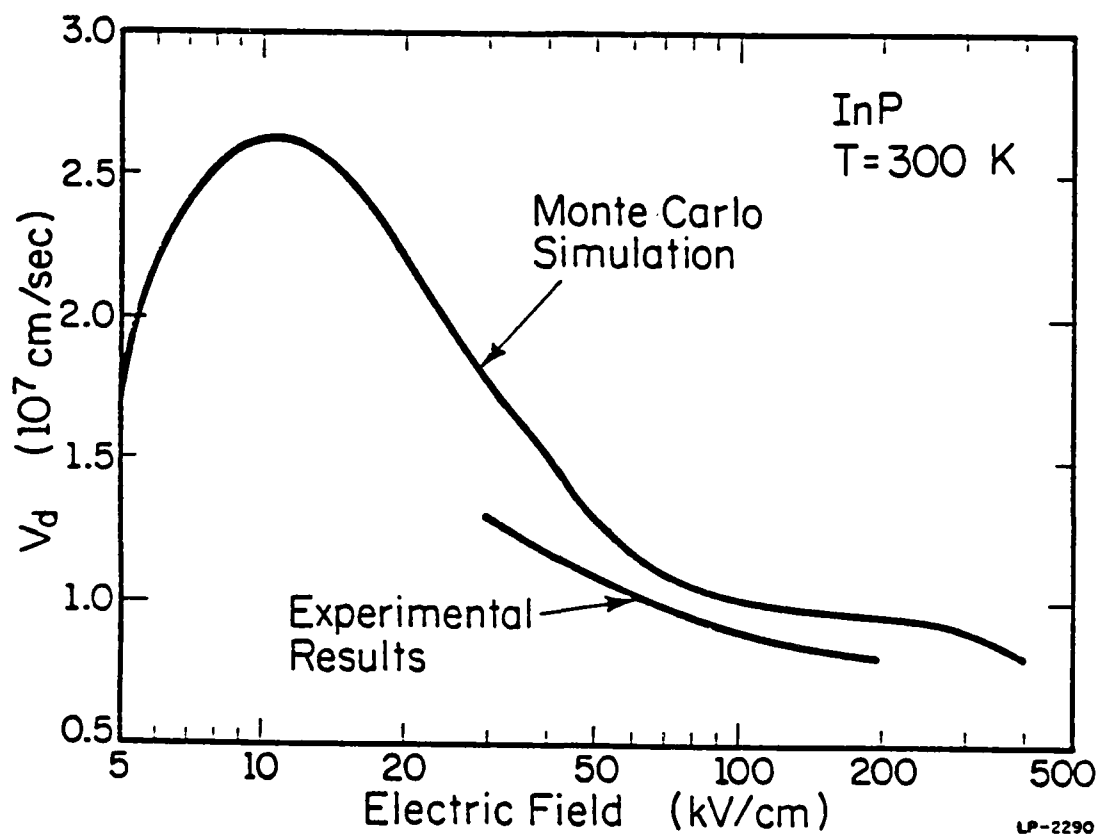
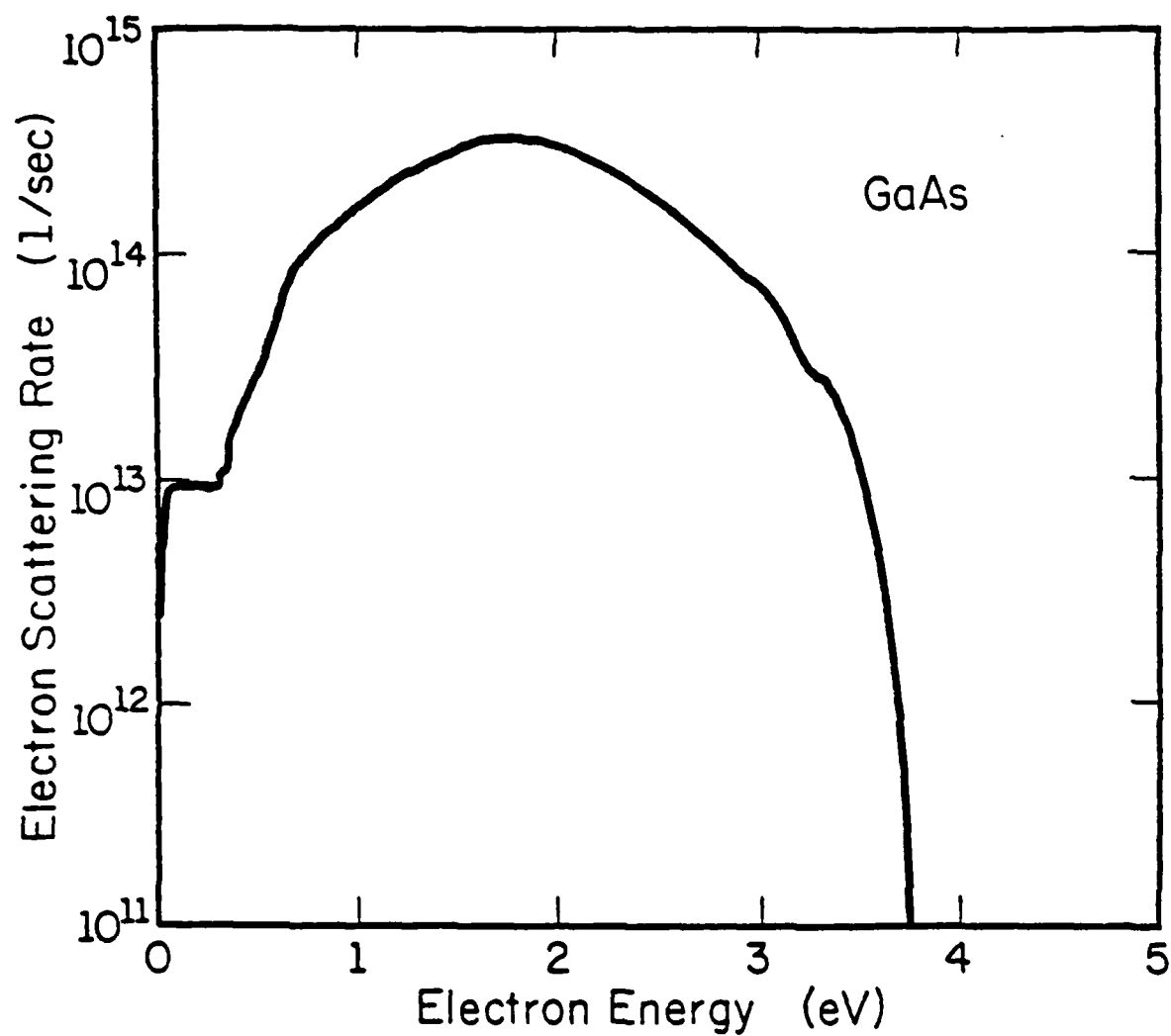
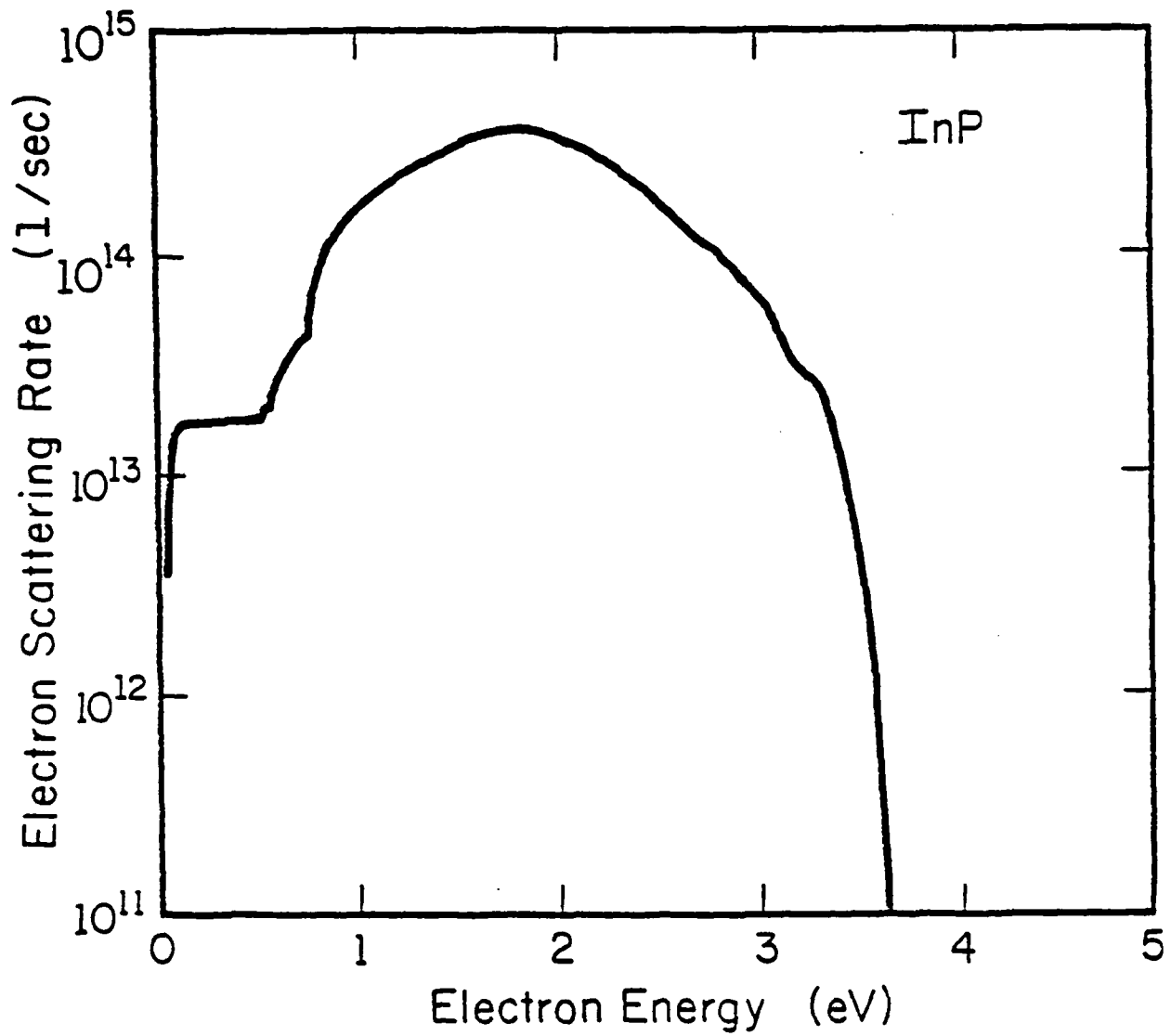


Fig. 3.8: Calculated steady state electron drift velocity in InP at room temperature compared with the experimental data of Windhorn et al. [60].



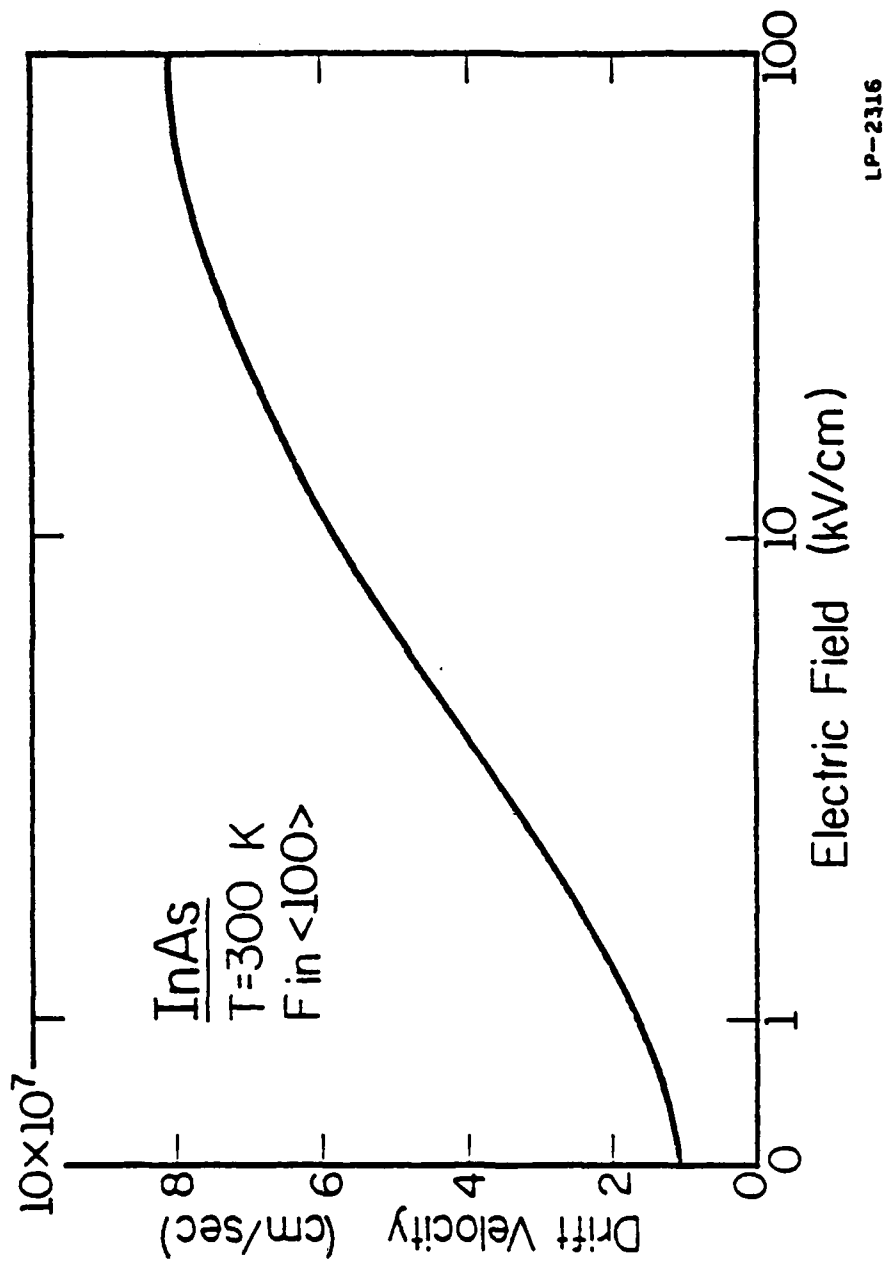
LP-2414

Fig. 3.9: The electron-phonon scattering rate in GaAs as a function of electron energy. The rate is calculated using a field theoretic scheme and does not include the effects of impact ionization.



LP-2415

Fig. 3.10: The electron-phonon scattering rate in InP as a function of electron energy. The rate is calculated using a field theoretic scheme and does not include the effects of impact ionization.



LP-2316

Fig. 3.11: Calculated steady state electron drift velocity in InAs at room temperature. The effects of impact ionization are included in the calculation.

experimentally by using very short current pulses), then the peak drift velocity in InAs is much lower and occurs at a much lower field as can be seen from Figure 3.12. In the absence of impact ionization the electron energy shows the usual 'runaway' effect; more energy is gained from the field than is lost to the phonons and the threshold for intervalley transfer is easily reached. The impact ionization acts to limit the electrons to low energy so they stay within the central valley. The valley separation energies are so large that few electrons survive impact ionization while within the central valley. After impact ionizing, the electron loses most of its energy and starts again near the gamma point. Again the electron drifts in the field and reaches the threshold for impact ionization well before it reaches the threshold for intervalley transfer. Unless the field is extremely high such that the electron can reach the intervalley threshold without collisions or by suffering only polar optical scatterings, it will impact ionize and will restart near gamma. In this way, the electrons are restricted to the central valley where their drift velocities can become very large.

#### 3.4 Phonon Scattering Rate

At high applied electric fields many of the approximations used previously [23,57] in the calculation of the scattering rate are no longer valid. As mentioned above, the effective mass approximation breaks down away from the band edge. Therefore, scattering rates determined using the effective mass approximation are unreliable at high electron energies. The semi-classical approximation also breaks down at high energy [63] due to the increased electron-phonon scattering rate. Scattering processes in the semi-classical approximation, as mentioned in Chapter 2, are treated as

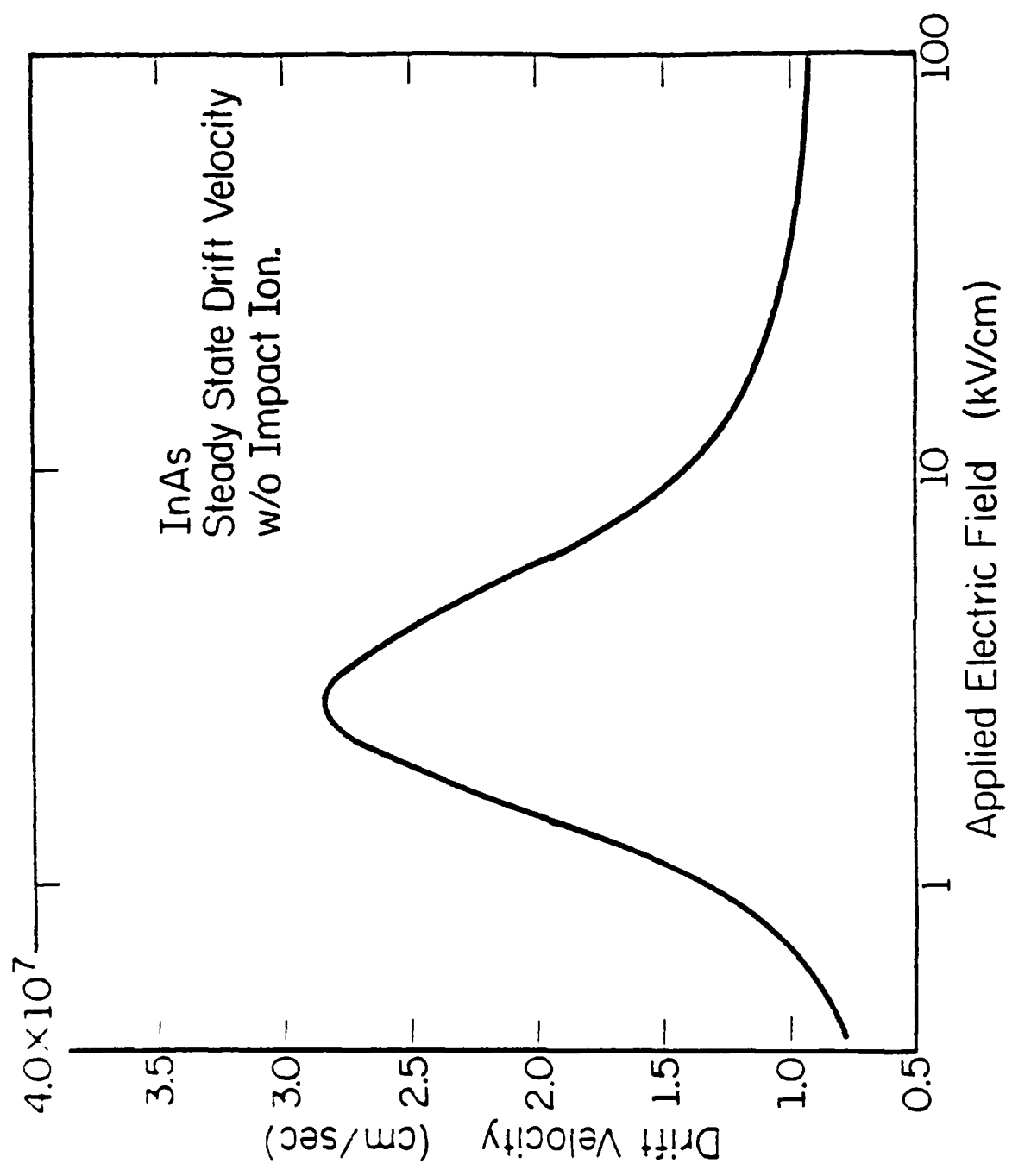


Fig. 3.12: Calculated steady state electron drift velocity in InAs at room temperature. The effects of impact ionization are not included in the calculation.

transitions between sharp, stationary, unperturbed momentum states. However, at high energy the classical picture of a free electron is no longer valid and one must replace it with the quasiparticle formulation.

In the quasiparticle picture, an additional energy, the self-energy,  $\Sigma(\mathbf{k})$ , must be added to the particle. Figure 3.13 shows diagrammatically the self-energy of the quasiparticle. The self-energy,  $\Sigma(\mathbf{k})$ , can be calculated neglecting the vertex correction as follows [64,65]

$$\Sigma(\vec{k}, E) = i \int \frac{d^3q d\omega}{(2\pi)^4} V^2(\vec{q}) D(\vec{q}, \hbar\omega) G(\vec{k}-\vec{q}, E-\hbar\omega), \quad (3.1)$$

where  $G$  is the electron Green function,  $D$  is the phonon Green function, and  $V(\mathbf{q})$  is the electron-phonon coupling. The electron Green function can be expressed as [65]

$$G(\vec{k}, E) = \frac{1}{E - E(\mathbf{k}) - \Sigma(\mathbf{k}, E) + i\delta} \quad (3.2)$$

while the phonon Green function has the form [65],

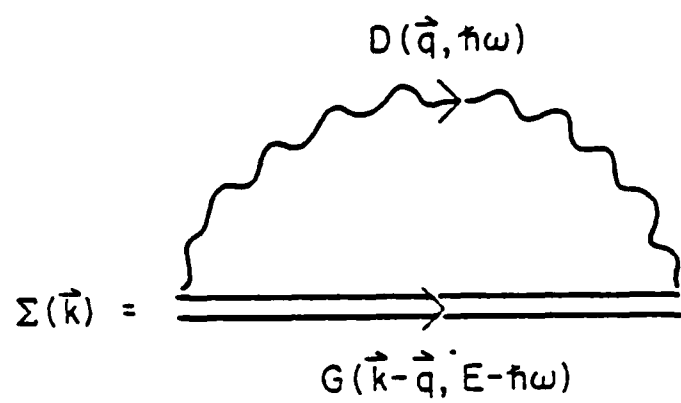
$$D(\vec{q}, \hbar\omega) = \frac{2}{\hbar} \left[ \frac{1}{\hbar\omega - \hbar\omega_{\vec{q}} + i\delta} - \frac{1}{\hbar\omega + \hbar\omega_{\vec{q}} - i\delta} \right], \quad (3.3)$$

where  $\delta$  is a positive infinitesimal quantity. After substituting the expressions for  $G(\mathbf{k}, E)$  and  $D(\mathbf{q}, \hbar\omega)$  into Equation 3.1 and evaluating the integral over  $\omega$  by use of contour integration, the expression for  $\Sigma(\mathbf{k}, E)$  becomes [24]

$$\Sigma(\vec{k}, E) = \int \frac{d^3q}{(2\pi)^3} \frac{G^2(\vec{k}+\vec{q})}{E - \hbar\omega_{\vec{q}} - E(\vec{q}') - \Sigma(\vec{q}', E - \hbar\omega_{\vec{q}}) + i\delta} \quad (3.4)$$

Using the approximation of a constant deformation potential,  $g^2(\mathbf{k}+\mathbf{q})$  becomes  $g^2$  and Equation 3.4 can be re-expressed as an integral over energy as

$$\Sigma(E) = g^2 \int \frac{dE' \rho(E')}{E - \hbar\omega - E' - \Sigma(E - \hbar\omega) + i\delta} \quad (3.5)$$



LP-2221

Fig. 3.13: Diagrammatic representation of the electron-phonon interaction.

where we have taken  $\omega$  to be independent of  $q$  and  $\rho(E)$  is the electron density of states. If we consider the weak coupling limit ( $g \ll 1$ ) then the term  $\Sigma(E - \hbar\omega)$  can be neglected in the denominator of Equation 3.5. Applying the Principal Value Theorem to the above integral yields

$$\Sigma(E) = \rho \int \frac{dE' g^2 \rho(E')}{E - \hbar\omega - E'} - i \pi g^2 \rho(E - \hbar\omega). \quad (3.6)$$

From Equation 3.6 the imaginary part of  $\Sigma(E)$  is clearly

$$\Gamma(E) = \pi g^2 \rho(E - \hbar\omega) \quad (3.7)$$

while the real part is

$$\Delta(E) = \rho \int \frac{dE' g^2 \rho(E')}{E - \hbar\omega - E'}. \quad (3.8)$$

Physically, the real part,  $\Delta(E)$ , corresponds to a level shift of the energy eigenstates while the imaginary part,  $\Gamma(E)$ , gives rise to a finite lifetime of the state [24]. Since the state has only a finite lifetime, via the Uncertainty Principle, the energy of the level is broadened.

It is easy to show [24] that the lifetime of the state can be expressed as

$$\tau_k = \frac{\hbar}{2 \Gamma(k)}. \quad (3.9)$$

To first order,  $1/\tau_k$  corresponds to the total scattering rate of the particle in the state  $k$  [24]. Neglecting the vertex correction [64],  $\Sigma(E(k))$  is simply  $\langle k | T | k \rangle$  where  $T$  is the transition matrix [62]. For elastic scattering the scattering probability is conserved and the optical theorem gives [66]

$$\sigma_{TOT} = \frac{-2}{\hbar v_k} \text{Im} \langle \vec{k} | T | \vec{k} \rangle. \quad (3.10)$$

The total scattering rate is then

$$1/\tau(E) = \sigma_{TOT} v_k = \frac{2 \Gamma(E(\vec{k}))}{\hbar} \quad (3.11)$$

Substituting for  $\text{Im}(\Sigma(E))$  one obtains in the limit of weak coupling

$$1/\tau(E) = \frac{2\pi}{\hbar} g^2 \rho(E - \hbar\omega) \quad , \quad (3.12)$$

where  $\rho(E - \hbar\omega)$  is the density of states and  $g$  is the coupling constant. For stronger coupling, the integral equation, Equation 3.5, must be solved. This has been accomplished by Tang [24] and Chang [39]. In the Monte Carlo calculations the total scattering rate at high energies is replaced by the above relation. The self-energy effectively reduces the overall scattering rate.

### 3.5 Electron Impact Ionization

The impact ionization data for both GaAs and InP have been calculated using this modified scattering rate. The results are presented in Figures 3.14 and 3.15 respectively. For GaAs, the calculated values match the experimental results of Bulman et al. [11] over a wide range of applied fields. Calculations are made for two applied field directions  $\langle 100 \rangle$  and  $\langle 111 \rangle$ . At high electric fields no appreciable anisotropy exists in agreement with our previous findings. At low electric fields, the calculation is extremely time-consuming because only few ionization events occur. Therefore there exists a large statistical uncertainty in the value of the calculated impact ionization rate. Nevertheless the results for the  $\langle 100 \rangle$  crystallographic direction are in good agreement with the experiments. In the limit of very low field, an anisotropy seems to develop and the results for  $\alpha$  in the  $\langle 111 \rangle$  direction are somewhat lower than the  $\langle 100 \rangle$

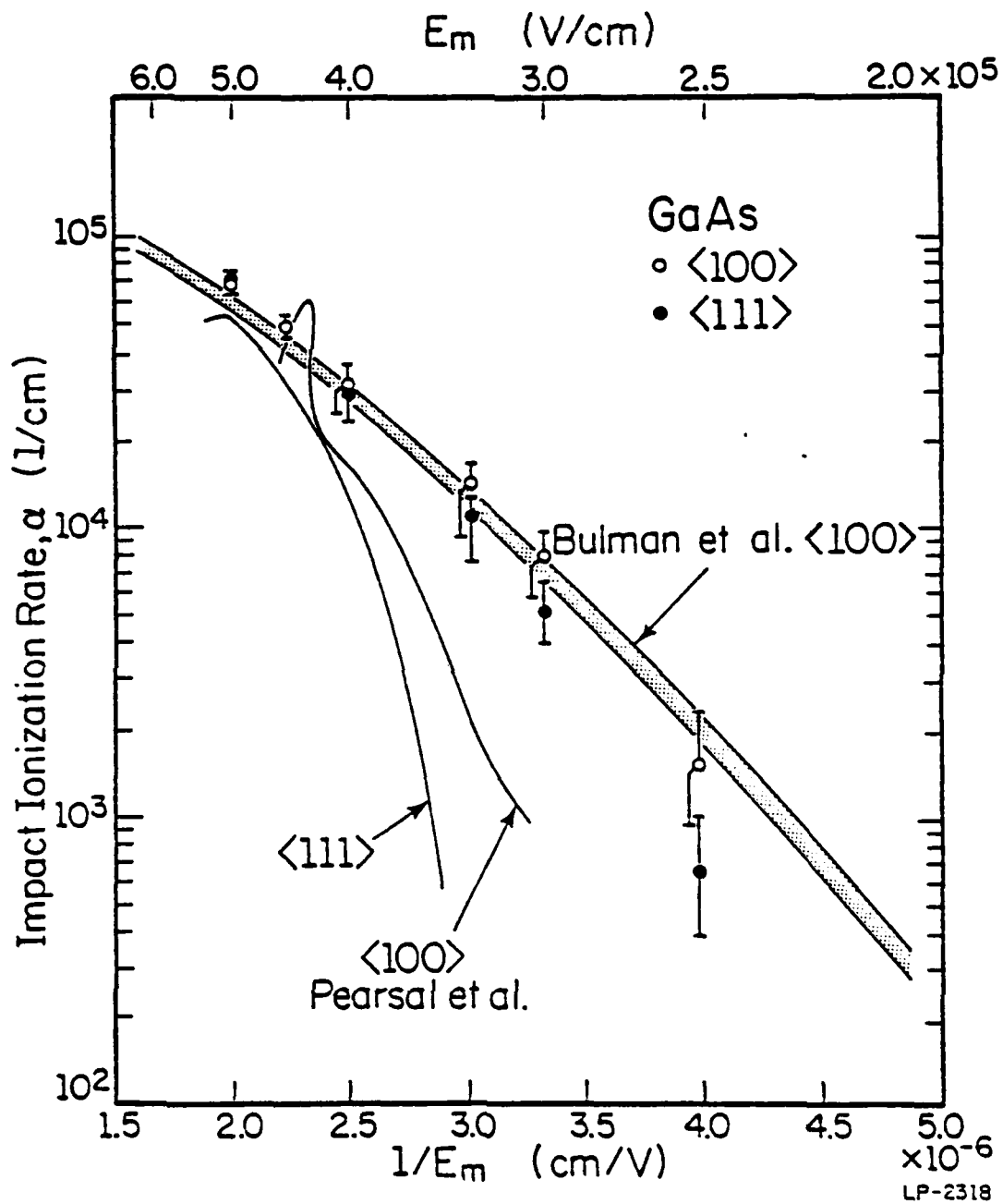


Fig. 3.14: Electron impact ionization rate in GaAs as a function of inverse electric field. The error bars are based on convergence error estimates from the calculation. The experimental data are from Bulman et al. [11] and from Pearsall et al. [69].

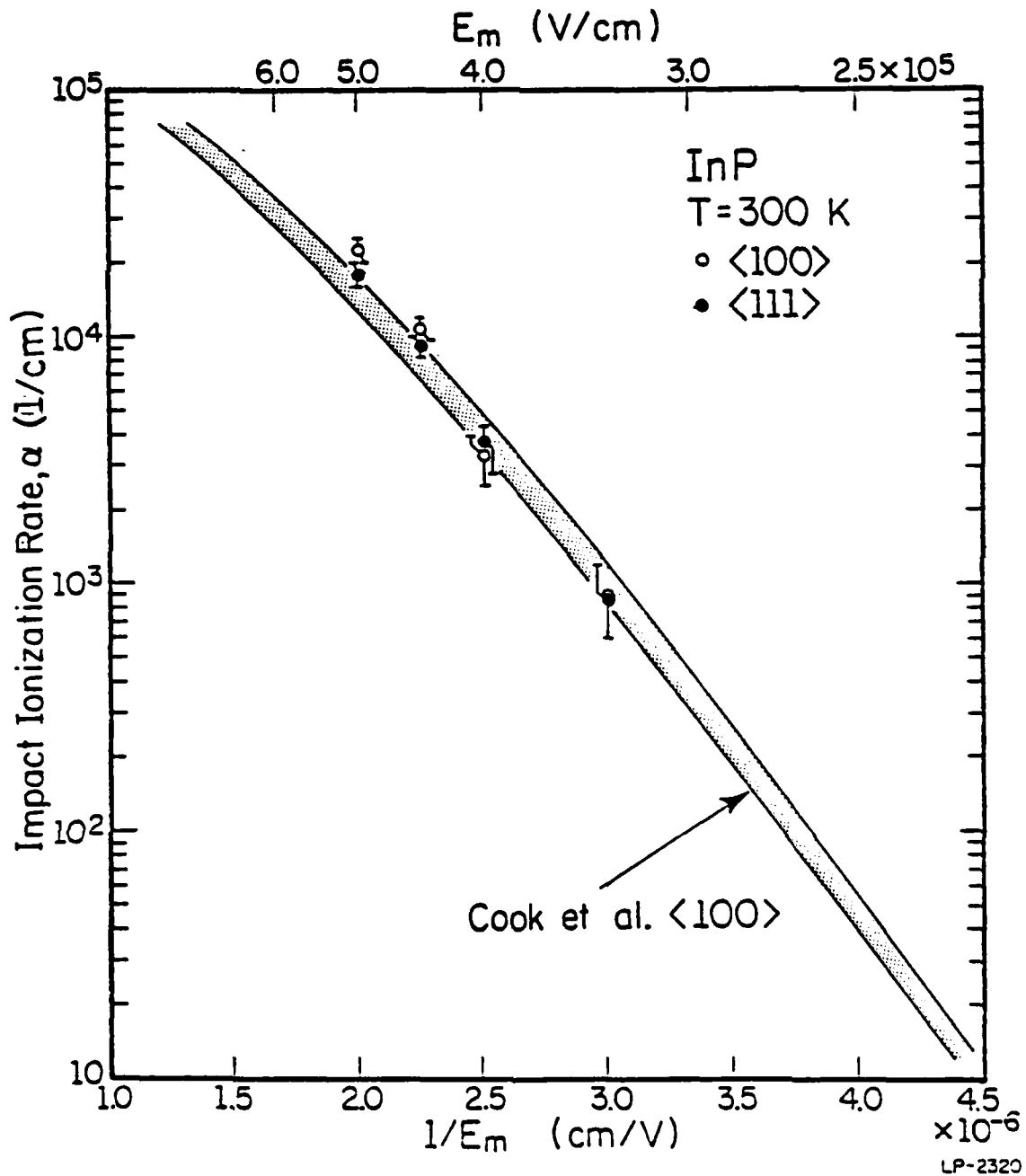


Fig. 3.15: Electron impact ionization rate in InP as a function of inverse electric field. The error bars are based on convergence error estimates from the calculation. The experimental data are from Cook et al. [12].

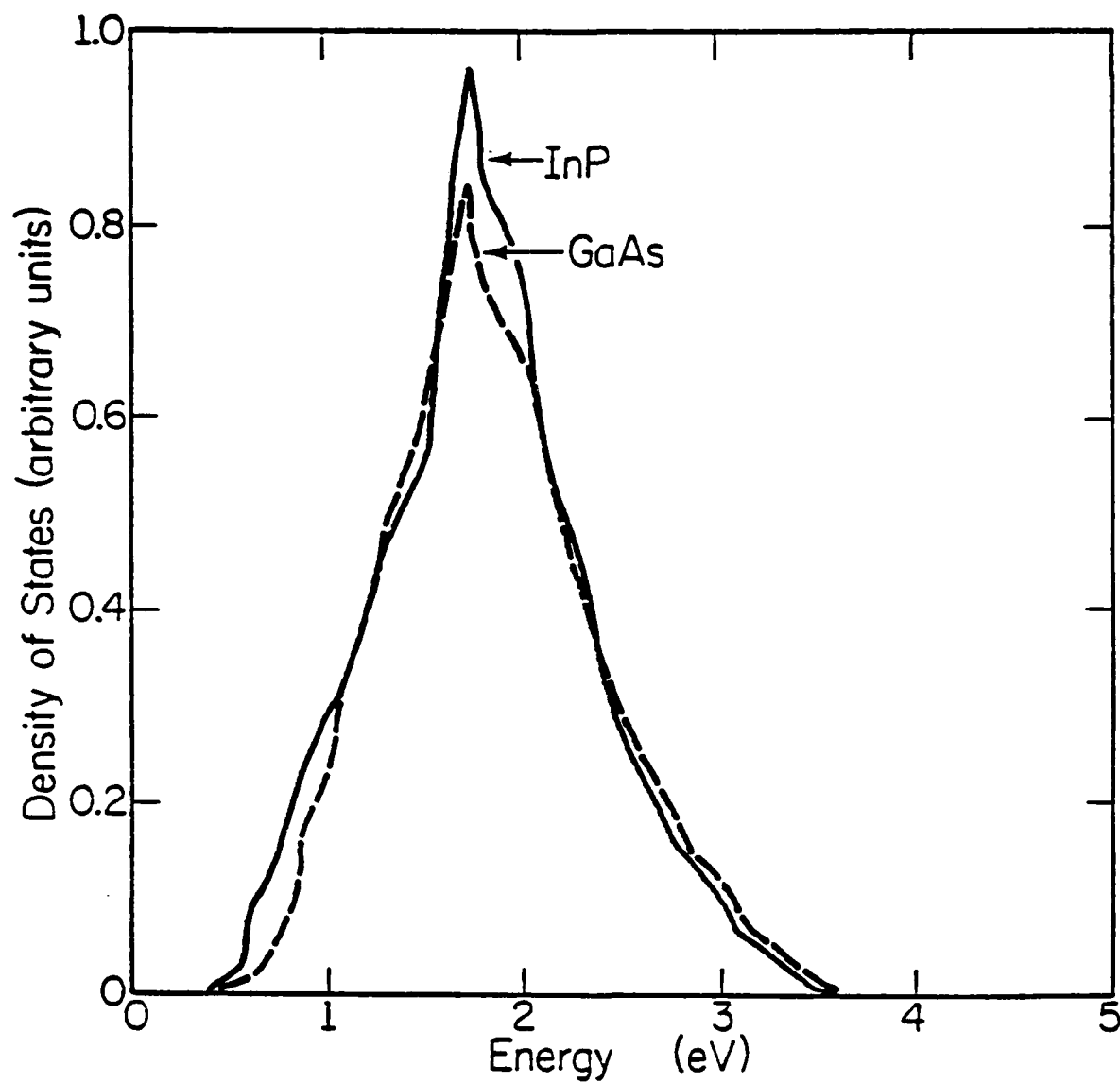
result. However, only six ionization events have been simulated at an expense of a day CPU time on a VAX 750 super-mini-computer. There has been some controversy concerning the anisotropy of  $\alpha$  in the past [67,68]. Notice that the calculated anisotropy is at much lower fields than observed by Pearsall et al. [69] and also much smaller in magnitude. We therefore have to conclude that the measured anisotropy is caused by effects not included in our simulation (e.g., transient phenomena or impurity correlations etc.). The small anisotropy seen from the Monte Carlo calculation seems connected with the fact that at low enough fields the electron distribution is centered closer to  $k=0$  than at high fields. Since the distribution is cooler, those electrons which reach the ionization threshold do so only after gaining much energy from the field. This requires that the electrons not be scattered much from the field direction, similar to Shockley's lucky electron theory [51]. A small anisotropy at low fields would be expected then because the ionization threshold may be different in different directions [70]. Also, due to the anisotropy of the band structure, an electron will gain different amounts of energy along different field directions per drift. The lucky electrons play an insignificant role at high fields [56] because the distribution is now much hotter which results in the electrons being distributed throughout the Brillouin zone. Since the vast majority of ionizing electrons start from anywhere in the Brillouin zone, the directional dependence of the rate vanishes. It is possible that the proper inclusion of the final state broadening may smear out the observed anisotropy at low fields.

The impact ionization rate is much lower in InP than in GaAs as can be seen from a comparison of Figures 3.14 and 3.15. In our calculation of the

impact ionization rate in InP we use the same intervalley coupling constants as were used in GaAs. This is appropriate since the band structures of the two materials are very similar [49] and it is believed that the deformation potentials are also [61,62]. The threshold for impact ionization is roughly 20% higher in InP than in GaAs. As can be seen from Figure 3.16, the density of states rises more abruptly and reaches a higher peak in InP than in GaAs. The scattering rate is roughly proportional to the density of states resulting in a higher scattering rate within InP than in GaAs. Also since the density of states is much greater in InP below the impact ionization threshold energy it is more difficult for an electron to drift to states at and above threshold. Hence fewer electrons will reach high enough energies for impact ionization to occur. The large difference in the impact ionization rate between these two materials therefore is mainly due to the density of states at high energy and to the higher threshold in InP.

It should be noted that the anisotropy in the impact ionization rate does not appear in InP. This is because the scattering rate is higher so the electrons are distributed throughout the Brillouin zone removing any directional dependence to the ionization rate. As in the case of GaAs, an anisotropy may appear for lower fields, but due to the lower ionization rates, the Monte Carlo simulation is too time consuming.

Due to its narrow band gap, impact ionization in InAs occurs at much lower fields than in either GaAs or InP. The threshold,  $E_{th}$ , for impact ionization in InAs can be readily calculated using the Anderson and Crowell criteria [71] since the parabolic approximation to the energy band is acceptable at low energy.  $E_{th}$  is found to be .383 eV at 300 K. Since the satellite valley separation energies are greater than 1 eV most of the

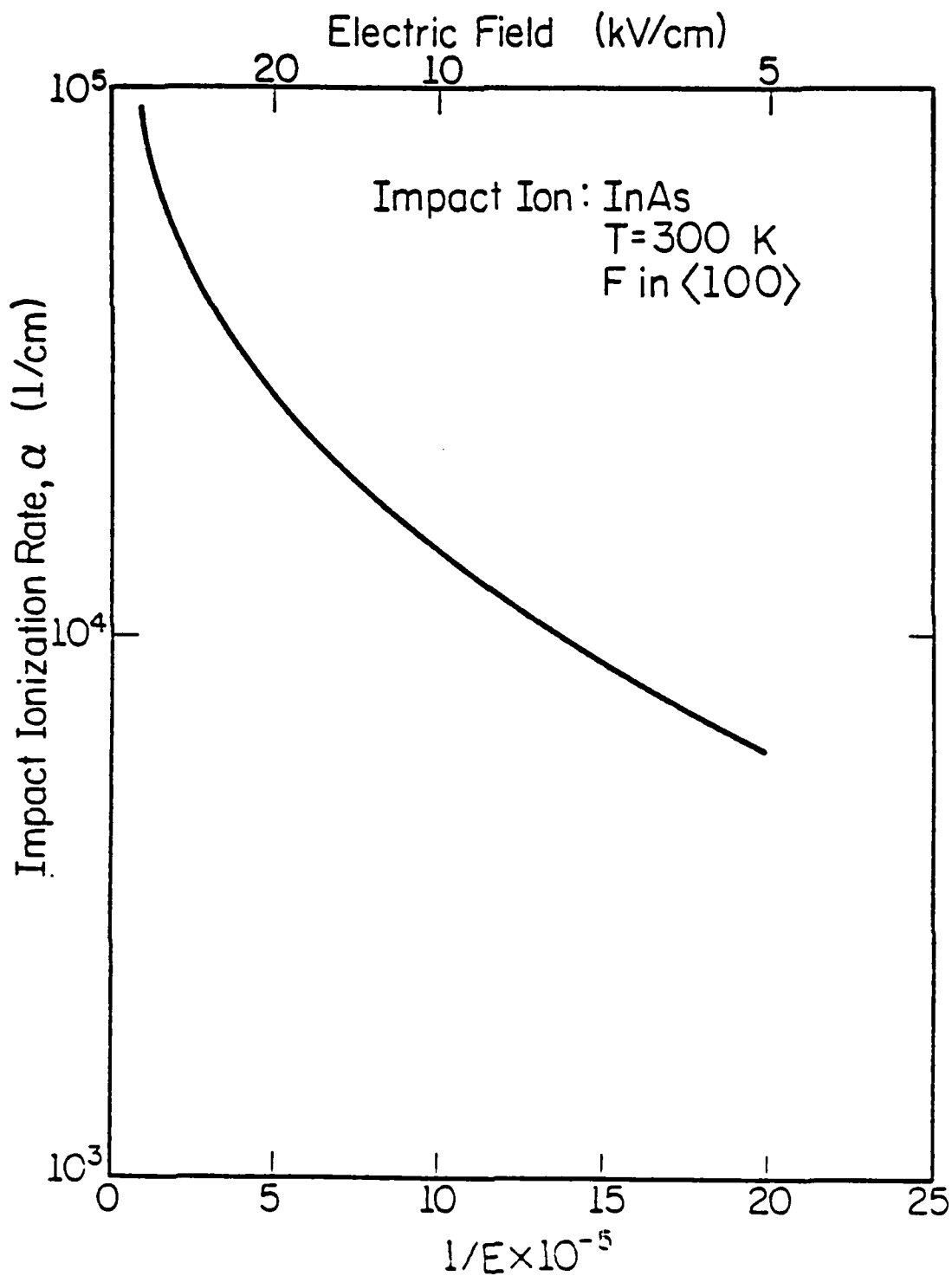


LP-2319

Fig. 3.16: Density of states of the first conduction band in GaAs and InP as a function of energy.

ionizations involve electrons within the central valley. In pure InAs the only important scattering mechanism in the central valley is produced by polar optical phonons [17]. Polar optical scattering is much weaker than intervalley scattering [17]. Therefore in the range in which impact ionization occurs in InAs the self-energy effect is negligible. The impact ionization results for InAs are presented in Figures 3.17 and 3.18. The impact ionization rate is determined at both 300 K and 77 K. The rate deviates strongly from the exponential  $1/E$  law as the temperature varies from 77 to 300 K. Notice that the impact ionization rate at both temperatures is extremely high at rather low electric fields.

It is interesting to note that the impact ionization rate is higher in InAs at 300 K than at 77 K as can be seen from a comparison of Figures 3.17 and 3.18. The band gap energy decreases with increasing temperature. In narrow band gap semiconductors, such as InAs, the change in the band gap energy is more than 10% as the temperature increases from 77 to 300 K. Consequently, the impact ionization threshold energy is smaller at 300 K than at 77 K by roughly the same percentage (since the threshold energy is sensitive to the band gap energy). The strength of the impact ionization mechanism is greater at 300 than at 77 K. In most semiconductors, such as GaAs and InP, the decrease in the impact ionization threshold energy is offset by the increased electron-phonon scattering rate at higher temperature. However in InAs, the electrons are confined to the gamma valley and only interact with polar optical phonons. The increase in the polar optical phonon scattering rate is insufficient and the impact ionization rate is higher at higher temperature.



LP-2315

Fig. 3.17: Electron impact ionization rate in InAs as a function of inverse electric field. Since many events occur, the convergence of the program is excellent and the resulting error is small. The calculation is made at a temperature of 300 K.

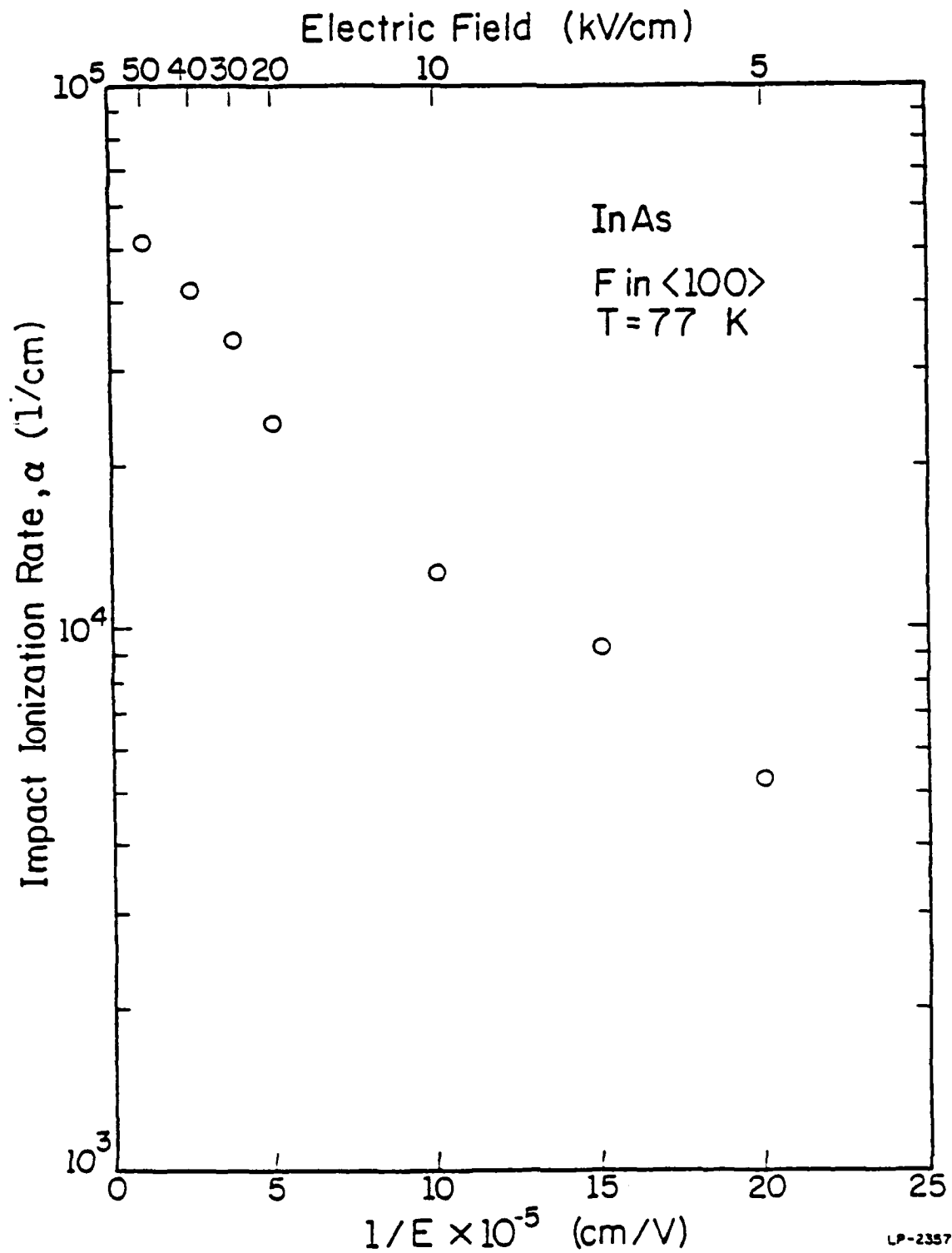


Fig. 3.18: Electron impact ionization rate in InAs as a function of inverse electric field. Since many events occur, the convergence of the program is excellent and the resulting error is small. The calculation is made at a temperature of 77 K.

#### 4. STEADY STATE HIGH FIELD TRANSPORT OF HOLES IN GaAs AND InP

##### 4.1 Introduction

Past experimental measurements of the impact ionization rate in compound semiconductors have all indicated that there is no significant anisotropy in the hole impact ionization rate [69]. Consequently, it is believed that if there is an anisotropy in the ratio of the electron and hole ionization rates it is due to the electron ionization rate and not the hole ionization rate. Current experimental measurements, though they do not show an anisotropy in the ratio of electron,  $\alpha$ , and hole,  $\beta$ , ionization coefficients, reveal that the ratio of  $\alpha/\beta$  is greater than one in GaAs at room temperature while  $\alpha/\beta$  is less than one in InP at 300 K [11-13].

It has not been demonstrated from first principles why the ratio of electron,  $\alpha$ , over hole,  $\beta$ , ionization coefficients is reversed between GaAs and InP. The recent work of Ridley [72,73] suggests that the ratio of  $\alpha$  over  $\beta$  can be entirely determined by the ratio of ionization threshold energies. However his results show that the ratio of  $\alpha$  over  $\beta$  is less than one for both GaAs and InP over a wide range of applied fields, in direct contradiction to recent experimental results [11-13]. In this chapter, calculations of the hole impact ionization rate and steady state drift velocity in GaAs and InP are presented using the Monte Carlo method with the unique inclusion of a realistic band structure based on a K \* P calculation [74]. We demonstrate how the reversal of the ratio of the electron and hole ionization coefficients in GaAs and InP can be understood based upon the data presented both here and in Chapter 3. Along with the results described

in Chapter 3, this work represents a first step towards a complete theory of electron and hole impact ionization in semiconductors.

#### 4.2. Band Structure

The valence band structure is calculated using the  $K * P$  method of Kane [74]. The effect of the spin-orbit interaction is included in Kane's calculation which produces the split-off band. It is essential to include the effects of the split-off band in hole transport calculations because of its influence upon the other bands, particularly the light hole band. The split-off band repels the other bands in such a way that they do not cross. If the split-off band is not included in the calculation, the light hole band appears to be parabolic and isotropic [49]. As can be seen from Figures 3.1 and 3.2, it is clear that when the split-off band is included the light hole band is strongly warped and follows the heavy hole band quite closely at high energy. This is a very different result from models that neglect the spin-orbit interaction. Consequently, the effective mass approximation is an unreliable description of the light and heavy hole bands.

Aside from its effect upon the other valence bands, the split-off band is of direct importance in hole transport. Due to the small density of states of the split-off band, holes within it can be accelerated to high energies by an applied electric field. At the gamma point the split-off band is non-degenerate with the heavy and light hole bands. The energy difference between the bands is known as the split-off energy. When the split-off energy is large, much greater than  $kT$ , the split-off band is virtually unoccupied at zero applied electric field. The holes must be scattered over to the split-off band from either the heavy or light hole bands by either deformation potential or polar optical scattering. Of course, by energy

conservation, a hole must drift to an energy at or above the split-off energy before it can be scattered to the split-off band. As we shall see, the magnitude of the split-off energy can greatly affect the importance of the split-off band in impact ionization.

To further illustrate the nature of the valence bands, particularly the heavy and light hole bands at high energy, cross sectional cuts through the Brillouin zone are presented in Figures 4.1 and 4.2 for GaAs in the cross section of Figure 3.3. As can be readily seen from these figures, the heavy and light hole bands deviate strongly from parabolic behavior and show a very complicated structure away from the gamma point. Even at very small energy,  $< 20$  meV, the bands are greatly distorted [75]. Nonparabolic behavior of the bands is equally as strong in InP. Comparable drawings of the isoenergy lines in the Brillouin zone cut of Figure 3.3 in InP show a strong resemblance to those for GaAs as can be seen from Figures 4.3 and 4.4. The forms of the heavy and light hole bands in GaAs in the cross sectional cut of Figure 3.5 are displayed in Figures 4.5 and 4.6. The isoenergy lines in the same cross sectional cut in the Brillouin zone is illustrated in InP in Figures 4.7 and 4.8. Figures 4.1-4.8 clearly illustrate that any successful theory of high energy transport must take into account the full nature of the band structure.

### 4.3 Phonon Scattering Rate

In the valence band the predominant scattering mechanisms are polar optical and deformation potential scattering when the effects of impurities can be ignored [76,77]. For simplicity, we neglect impurity scattering in our calculations. The total scattering rate includes both intraband and interband scattering and is based on the total density of states of all

GaAs  
Heavy Hole Band

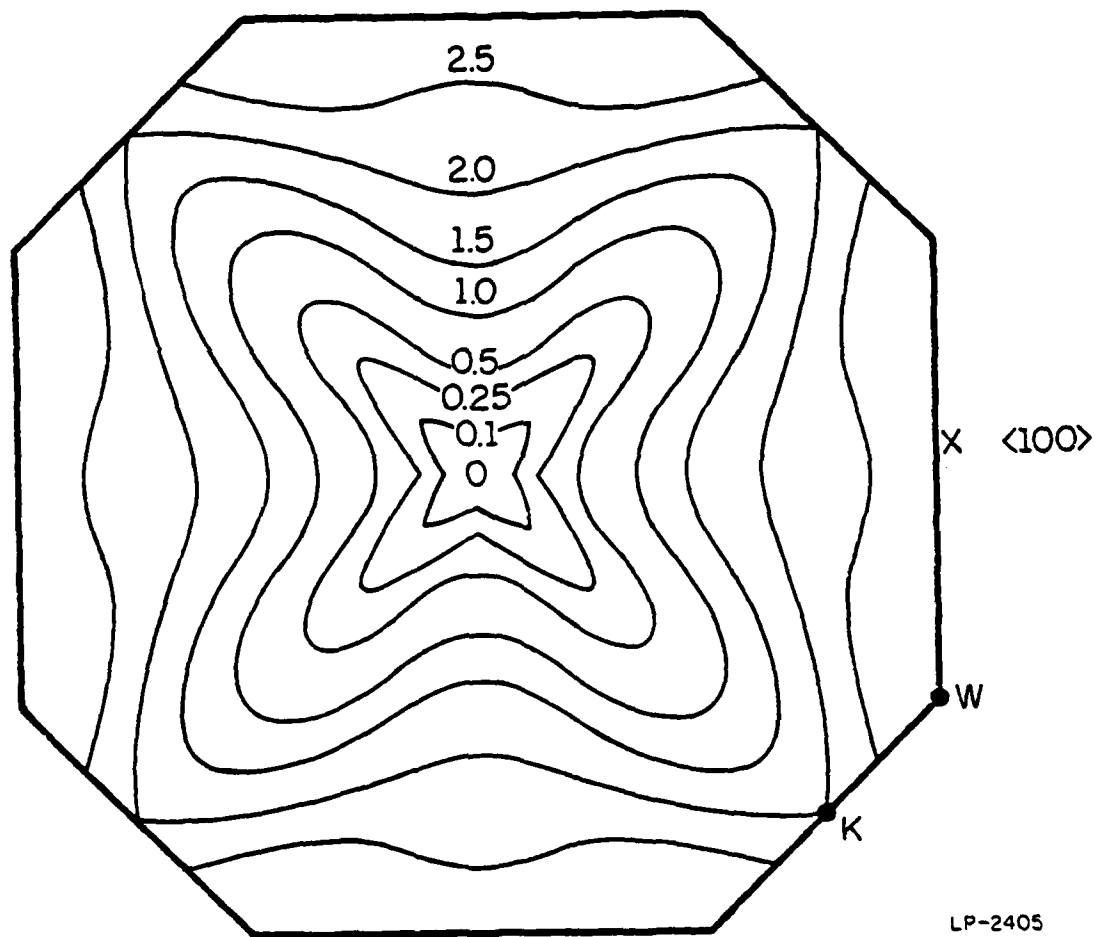
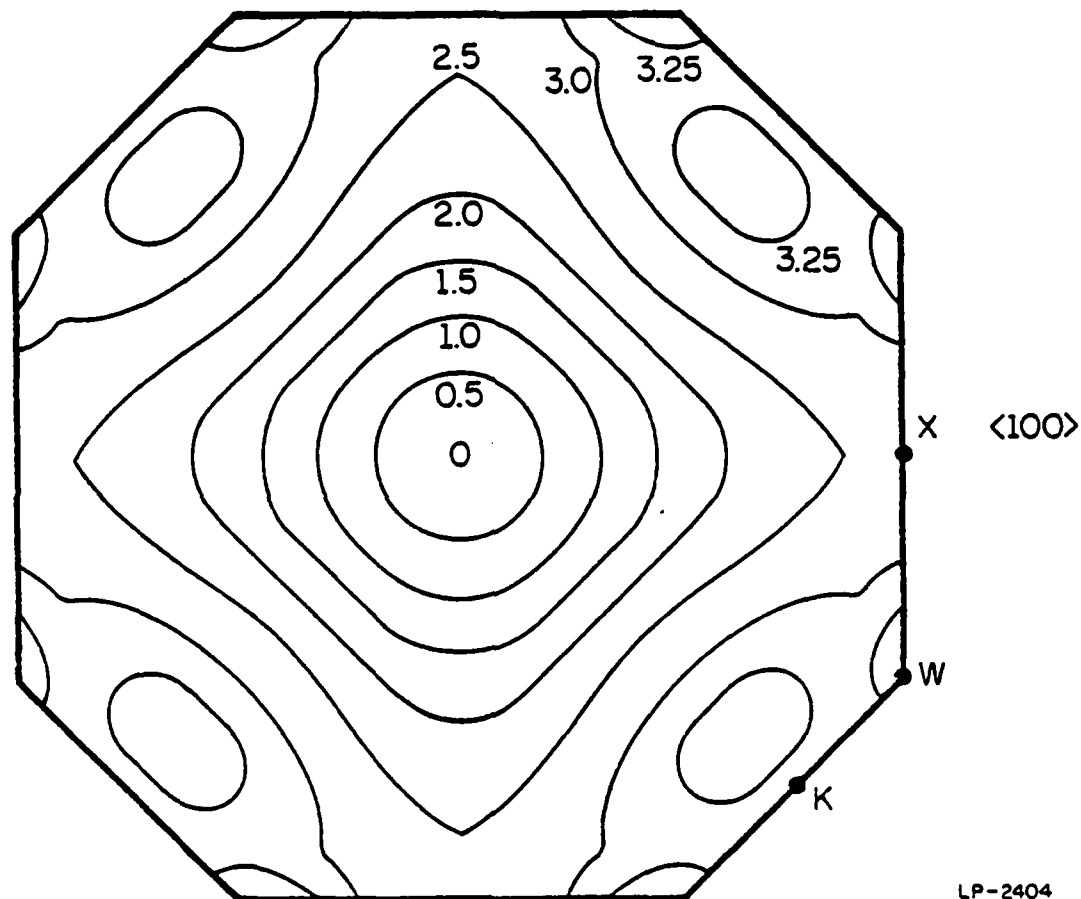


Fig. 4.1: Isoenergy lines of the heavy hole band of GaAs in the cross section of Figure 3.3. The numbers represent the energies measured from the gamma minimum in eV.

GaAs  
Light Hole Band



LP-2404

Fig. 4.2: Isoenergy lines of the light hole band of GaAs in the cross section of Figure 3.3. The numbers represent the energies measured from the gamma minimum in eV.

InP  
Heavy Hole Band

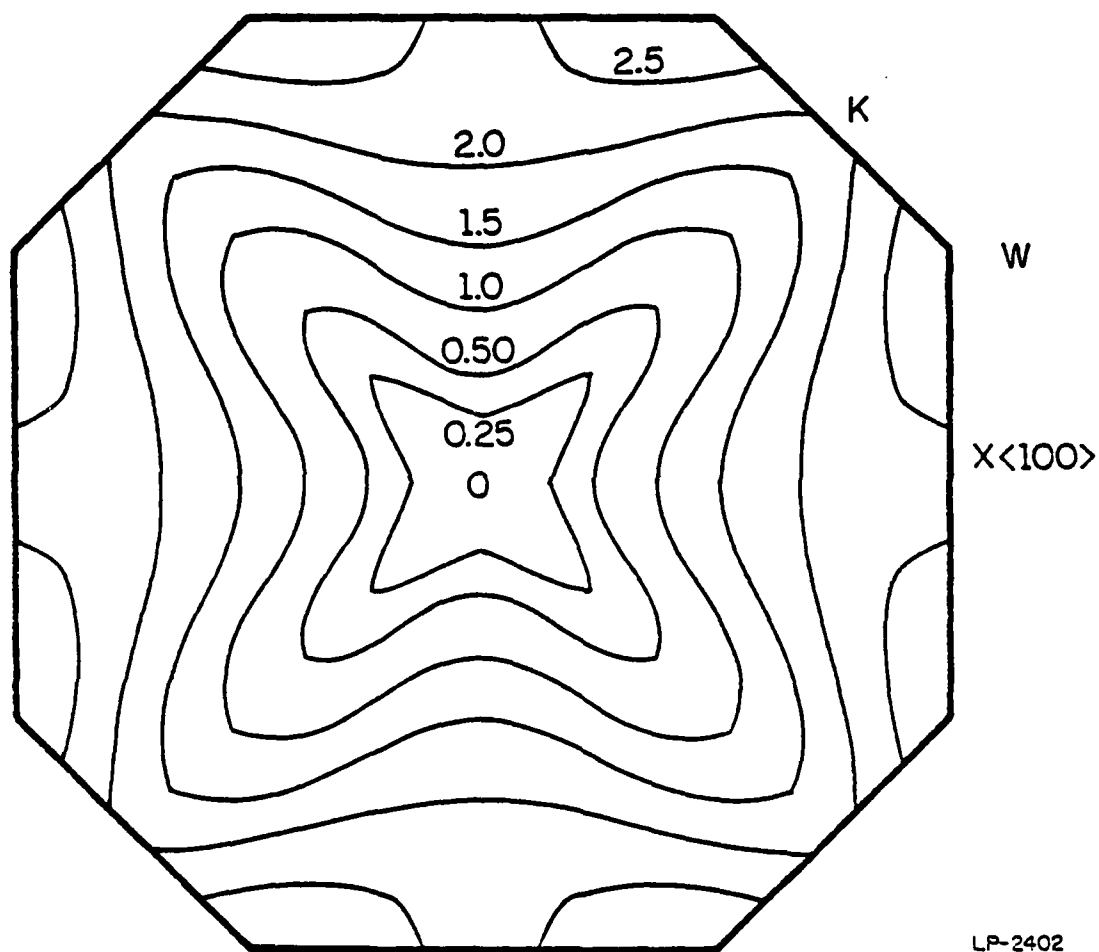
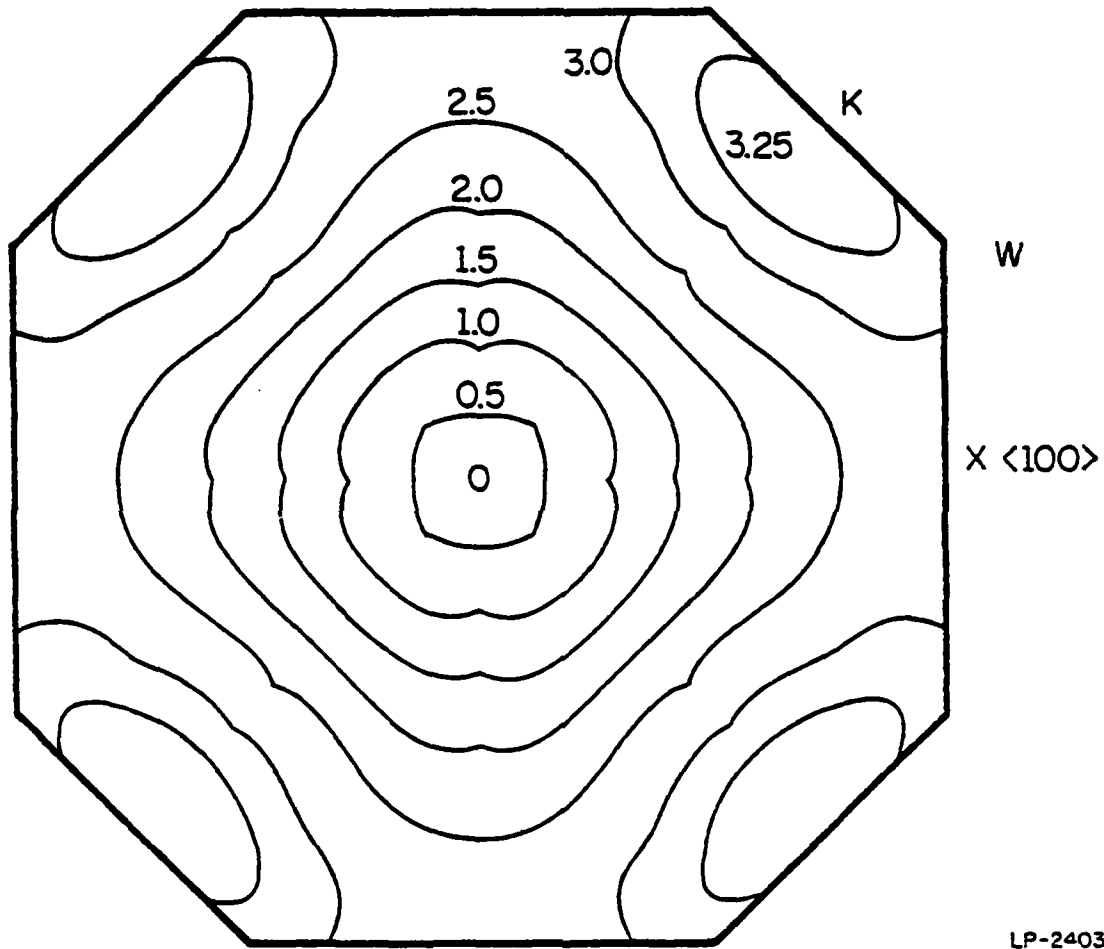


Fig. 4.3: Isoenergy lines of the heavy hole band of InP in the cross section of Figure 3.3. The numbers represent the energies measured from the gamma minimum in eV.

InP  
Light Hole Band



LP-2403

Fig. 4.4: Isoenergy lines of the light hole band of InP in the cross section of Figure 3.3. The numbers represent the energies measured from the gamma minimum in eV.

GaAs  
Heavy Hole Band

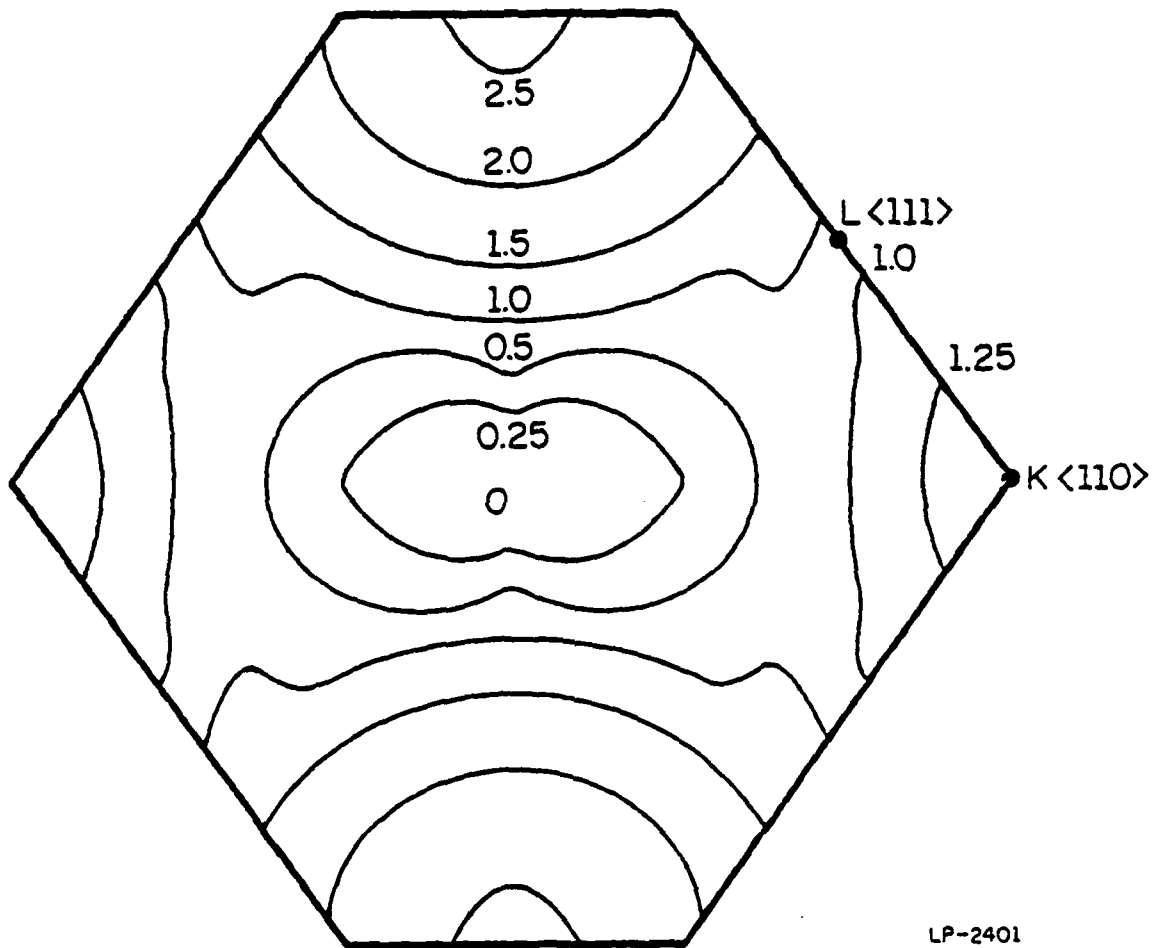


Fig. 4.5: Isoenergy lines of the heavy hole band in GaAs in the cross section of Figure 3.5. The numbers represent the energies measured from the gamma minimum in eV.

GaAs  
Light Hole Band

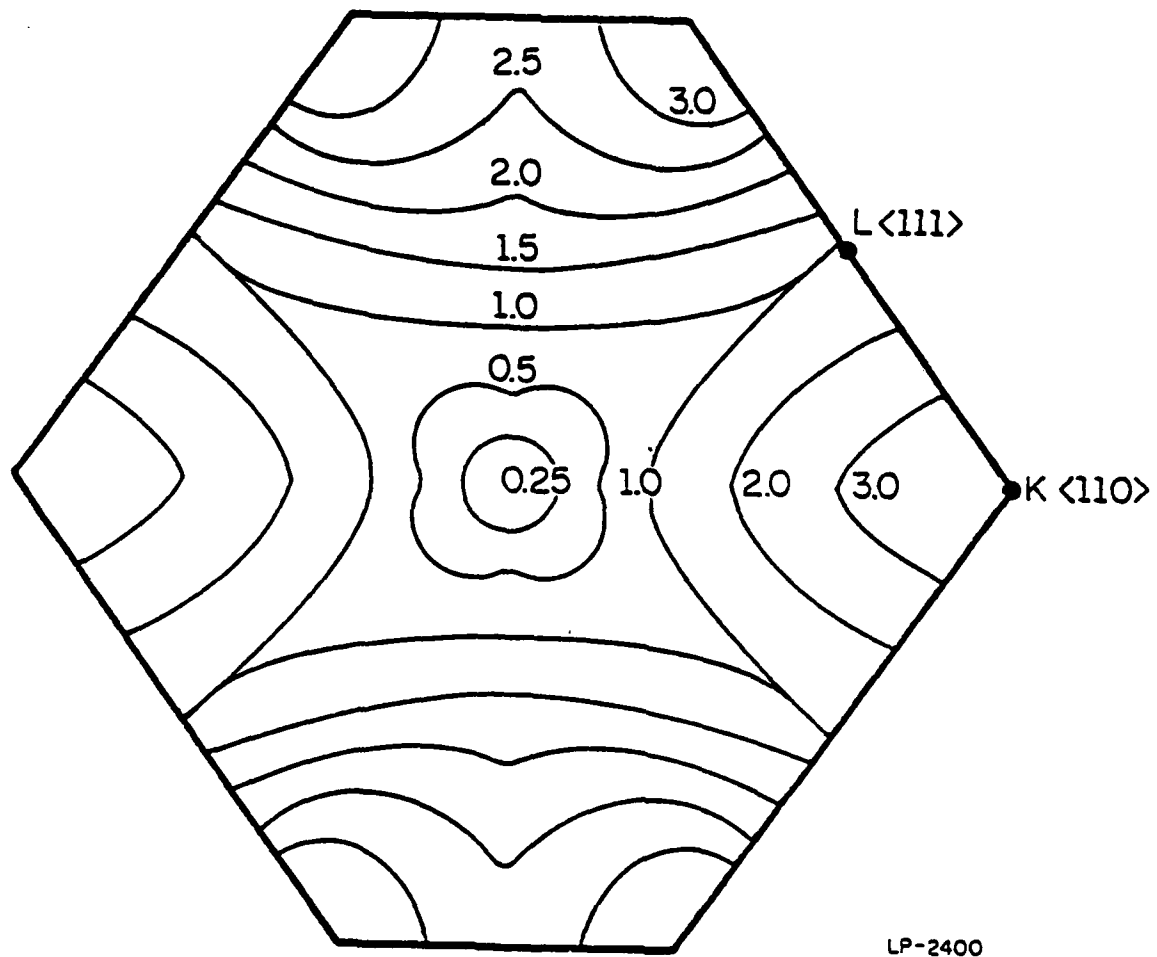


Fig. 4.6: Isoenergy lines of the light hole band in GaAs in the cross section of Figure 3.5. The numbers represent the energies measured from the gamma minimum in eV.

InP  
Heavy Hole Band

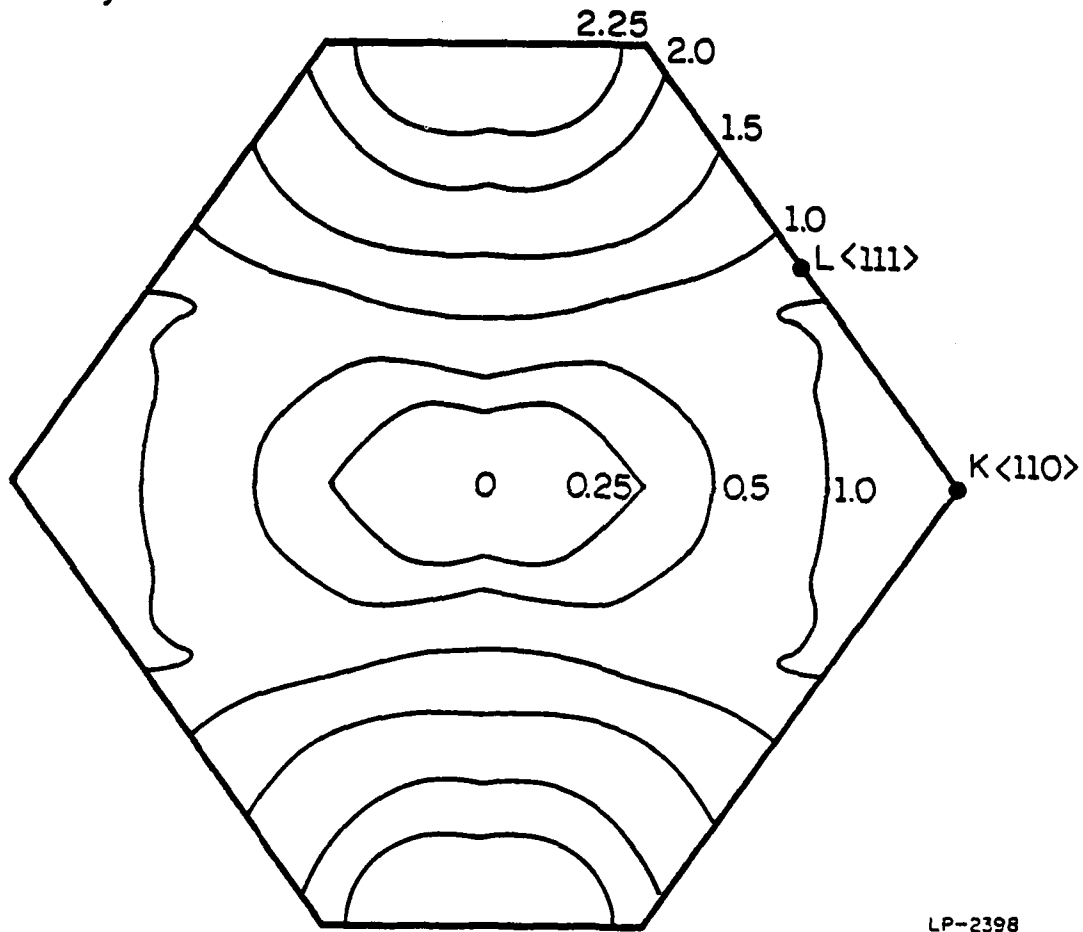
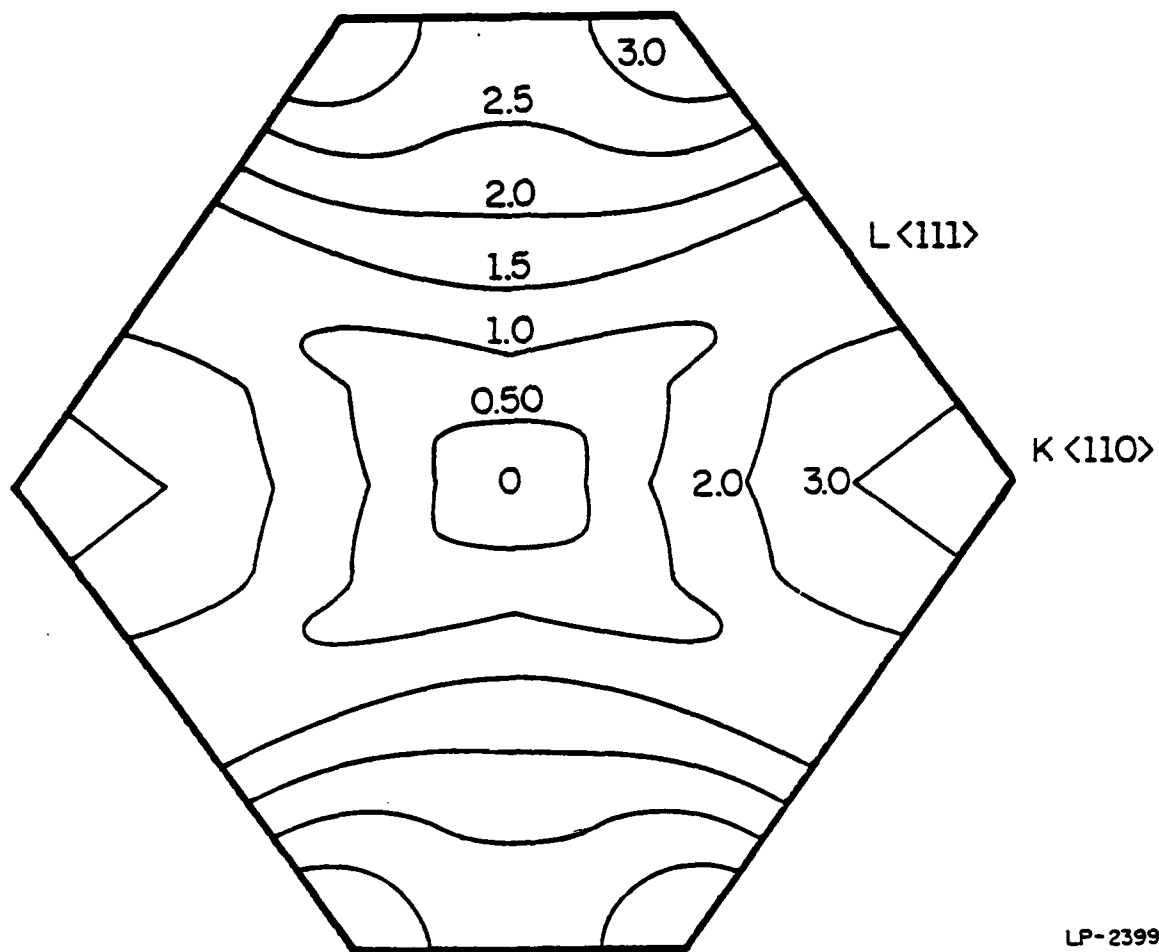


Fig. 4.7: Isoenergy lines of the heavy hole band in InP in the cross section of Figure 3.5. The numbers represent the energies measured from the gamma minimum in eV.

InP  
Light Hole Band



LP-2399

Fig. 4.8: Isoenergy lines of the light hole band in InP in the cross section of Figure 3.6. The numbers represent the energies measured from the gamma minimum in eV.

three valence bands using the field theoretic approach discussed in Chapter 3. The individual phonon scattering mechanisms are calculated using the approach of Costato and Reggiani [76,77]. The principal scattering agents are acoustic, nonpolar, and polar optical phonons.

The acoustic phonon scattering rate is calculated using the method of Canali et al. [78]. In their calculation, instead of the usual equipartition approximation, the Bose-Einstein distribution function is expanded in a power series and integrated with the transition rate to obtain the total scattering rate. At high energy, the energy lost or gained in an acoustic scattering event is not negligible which makes the equipartition approximation questionable [24]. The acoustic phonon coupling constant,  $E_1^2$ , is given by [76]

$$E_1^2 = 1/3 + 2/3 \left( \frac{s_t}{s_l} \right)^2, \quad a^2 + \frac{C_l}{C_t} (b^2 + 1/2 d^2), \quad (4.1)$$

where  $s_l$  is the longitudinal sound velocity and  $s_t$  is the transverse sound velocity. The values of  $C_l$  and  $C_t$  are given as

$$\begin{aligned} C_l &= 1/5 (3 C_{11} + 2 C_{12} + 4 C_{44}), \\ C_t &= 1/5 (C_{11} - C_{12} + 3 C_{44}), \end{aligned} \quad (4.2)$$

where  $C_{11}$ ,  $C_{12}$ , and  $C_{44}$  are the crystal elastic constants. All of the parameters used in the calculations are collected in Tables A2.4 and A2.5 of Appendix 2 for GaAs and InP respectively.

The transition probabilities due to nonpolar optical scattering can be written in a form analogous to that for acoustic phonon scattering [79] containing the optical deformation potential constant,  $d_0$ . However,  $d_0$  cannot be directly determined from piezoresistance data [76]. It is useful

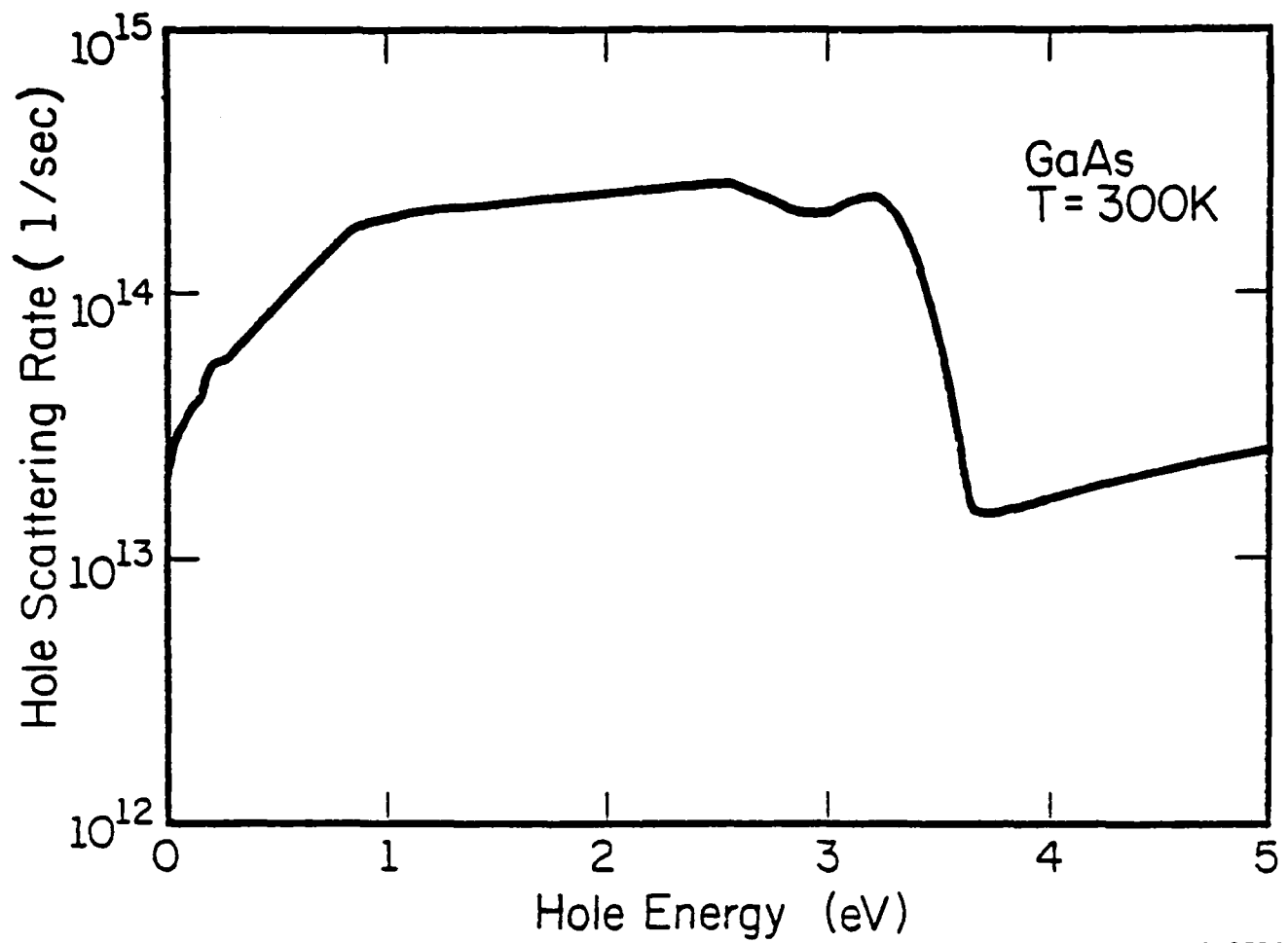
then to formulate the nonpolar optical scattering rate in terms of a more easily determined quantity. The optical phonon coupling constant,  $(DK)^2$ , can be determined from the acoustic deformation potential constant as [80]

$$(DK)^2 = 4 \left( \frac{\omega_0}{S_2} \right)^2 E_1^2, \quad (4.3)$$

where  $\omega_0$  is the optical phonon frequency.

The results of Costato and Reggiani [77] show that the overlap corrections due to the mixing of Bloch states introduce significant corrections to the overall hole-optical phonon scattering rate. We have included these effects into our calculation. The parameters used in the calculation of the polar optical scattering rate are also collected in Tables A2.4 and A2.5 of Appendix 2. The details of the scattering rate calculations for all three mechanisms are presented in Appendix 3.

The total hole-phonon scattering rates are calculated for both GaAs and InP and are presented in Figures 4.9 and 4.10. The rates depicted in these figures include only the hole-phonon processes and do not include impact ionization. The overall scattering rate including the effects of impact ionization is presented in Figure 4.11 for GaAs and in Figure 4.12 for InP. Impact ionization is treated as a separate scattering mechanism in accordance with the Keldysh theory [53]. There exist two adjustable parameters,  $E_{th}$  and  $p$ , in the Keldysh theory.  $E_{th}$  is the impact ionization threshold energy while  $p$  is a numerical multiplicative factor which varies for each material. These parameters are chosen to fit the calculated impact ionization rate to the experimental results. The work of Tang [24] has demonstrated that previous theories for impact ionization using Keldysh's formalism with  $p \gg 1$  are incorrect since the high energy tail of the energy



LP-2396

Fig. 4.9: The hole-phonon scattering rate in GaAs as a function of hole energy. The rate is calculated using a field theoretic scheme and the impact ionization rate is omitted.



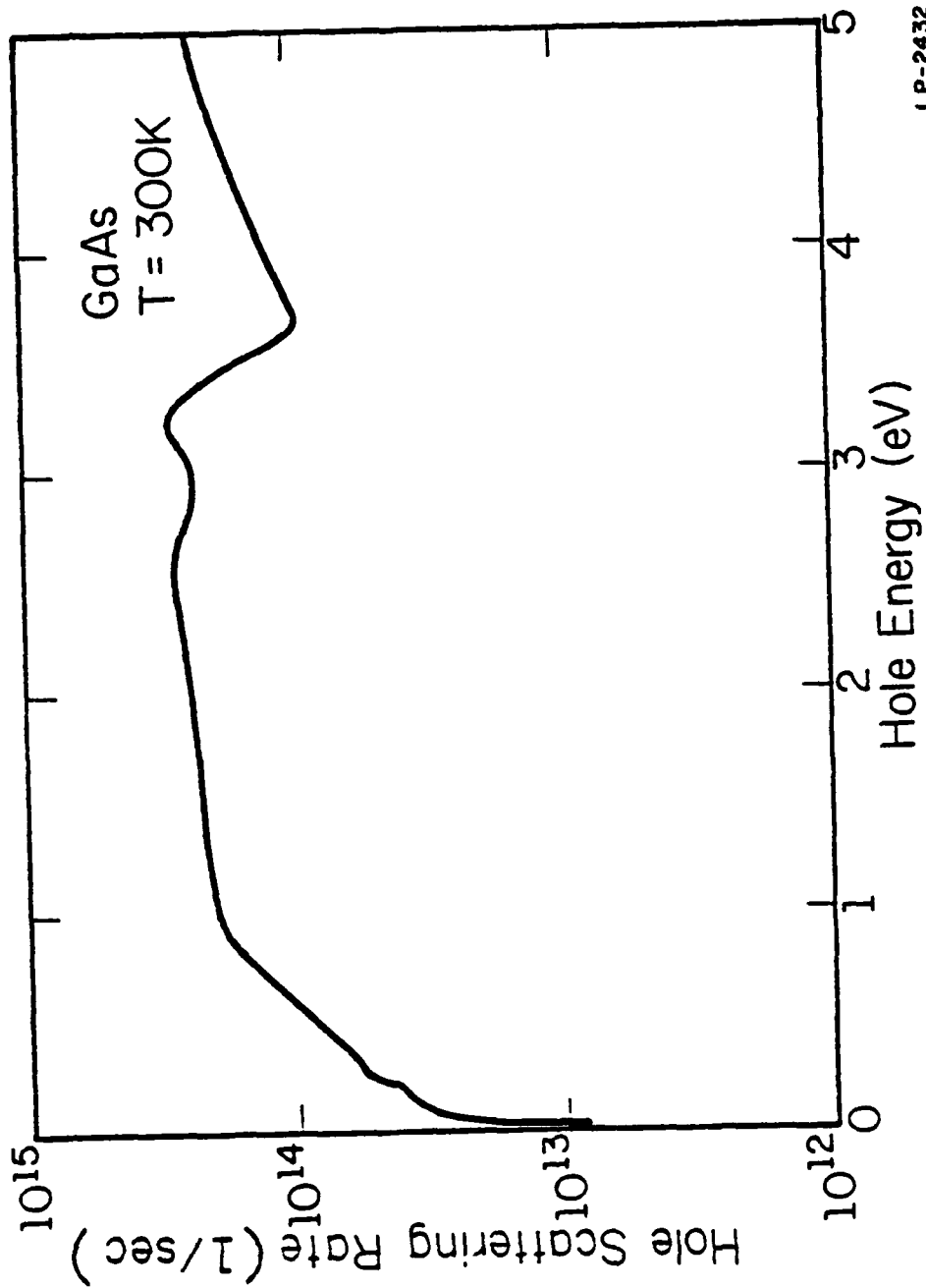


Fig. 4.11: The hole-phonon scattering rate in GaAs as a function of hole energy. The rate is calculated using a field theoretic scheme and the impact ionization rate is included in the calculation.

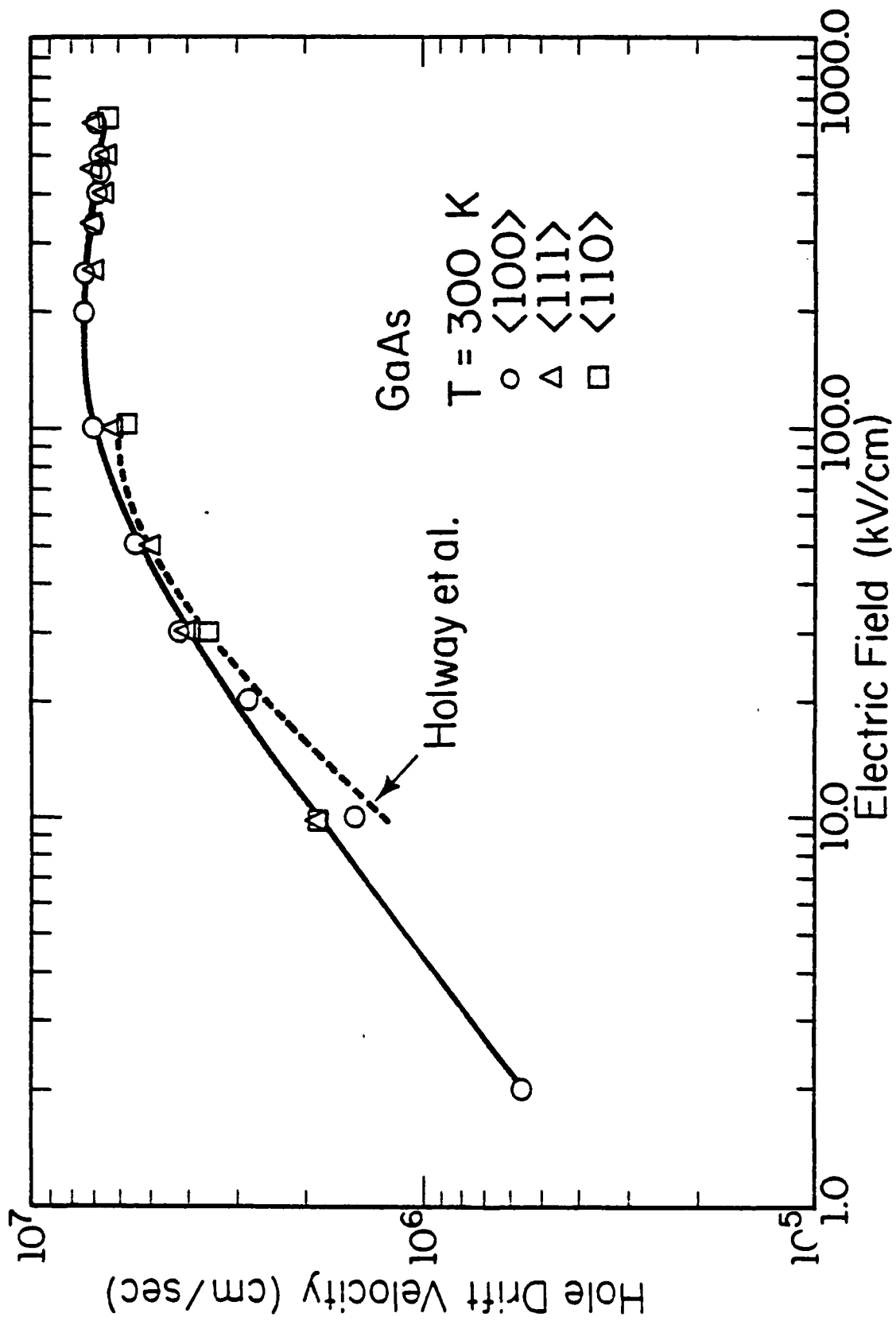


distribution function is overly suppressed. By restricting  $p$  to low values,  $\sim 10.0$  or less, the range of acceptable values for the impact ionization threshold is greatly limited particularly if only one band is considered in the calculation. Recent work in silicon [81] has shown that there exist more than one set of parameters for the Keldysh formula if multiple bands are considered. This is because it cannot be determined a priori which band if either plays the dominant role in impact ionization. It is desirable to remove the parameterizations of the Keldysh theory but this can only be done by reformulating the impact ionization probability using an inverse Anger calculation. Future work will attempt to address this problem.

#### 4.4 Steady State Drift Velocity Theory

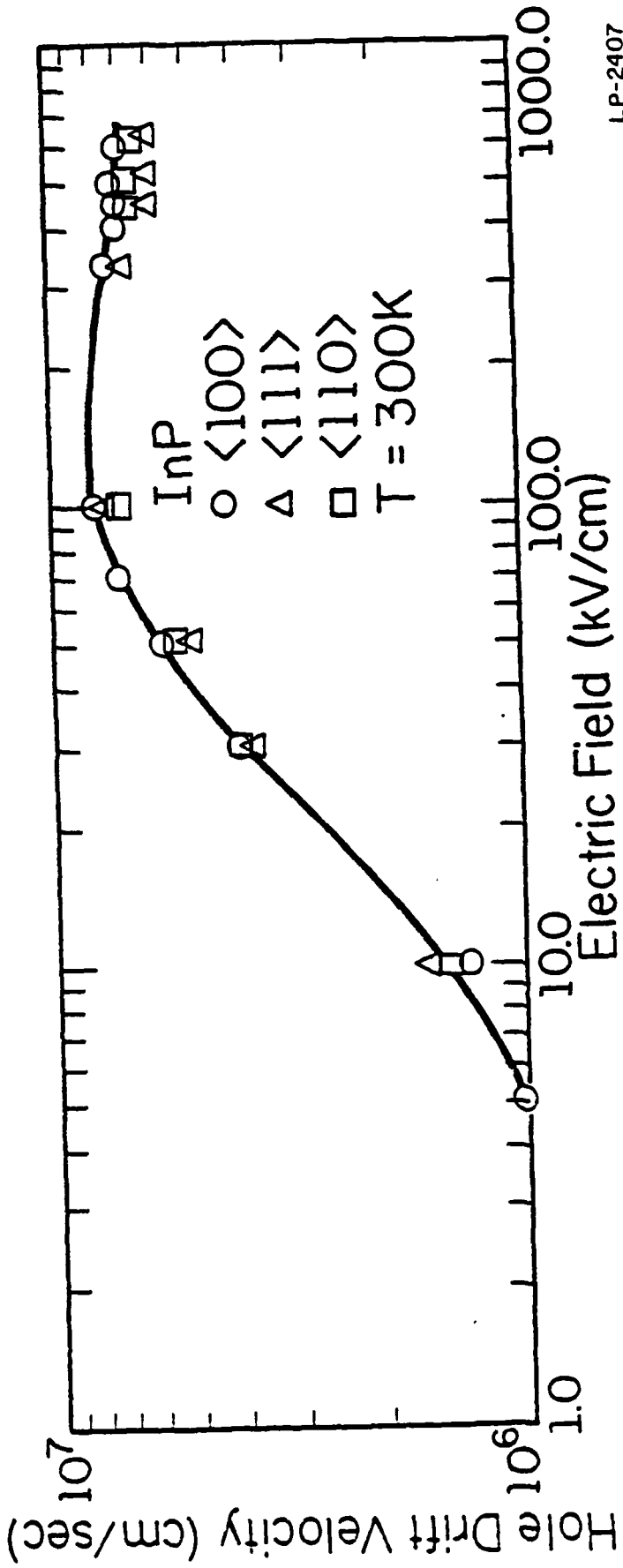
Little experimental data exist on the hole drift velocity in compound semiconductors and to the author's knowledge none are available for holes in InP. Figure 4.13 shows both experimental [82] and calculated drift velocity data for holes in GaAs. The experimental measurements are made for applied electric fields along only the  $\langle 100 \rangle$  direction while the Monte Carlo calculations are made for fields oriented along the  $\langle 100 \rangle$ ,  $\langle 110 \rangle$ , and  $\langle 111 \rangle$  directions. As seen from Figure 4.13, there is no significant anisotropy in the hole drift velocity through a large range of applied electric fields. The calculated results for the hole drift velocity in GaAs fit the experimental data extremely well.

The hole drift velocity is somewhat higher in InP, as seen in Figure 4.14, than in GaAs despite a greater scattering rate present in InP. The difference is only of the order of 10% which is roughly the error in the calculation. Therefore it is difficult to determine if the drift velocity difference is due to the different band structures or is a statistical



LP-2406

Fig. 4.13: Calculated steady state hole drift velocity in GaAs at room temperature as compared to the experimental data of Holway et al. [82].



LP-2407

Fig. 4.14: Calculated steady state hole drift velocity in InP at room temperature. Experimental data are not currently available.

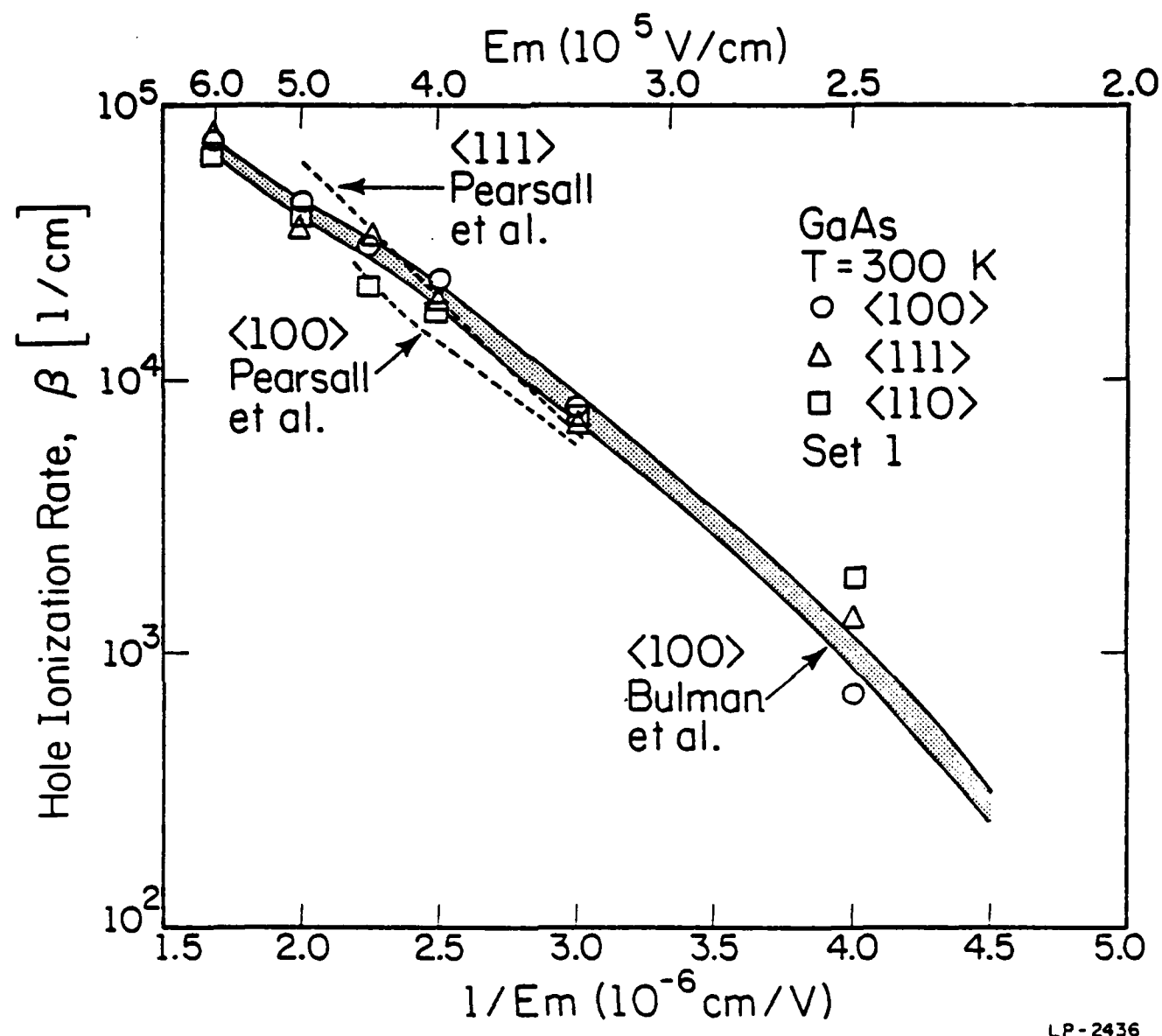
error. However, a similar situation occurs in the conduction bands of GaAs and InP. The work of Windhorn et al. [59,60] demonstrates that the electron drift velocity is higher in InP than in GaAs at high applied fields. Analysis of the saturation velocity of electrons in GaAs shows that it is approximately the same,  $7.0 \times 10^6$  cm/sec [58], as that for holes,  $6.5 \times 10^6$  cm/sec. The saturation velocity for electrons,  $7.5 \times 10^6$  cm/sec, is roughly the same as that for holes in InP,  $7.0 \times 10^6$  cm/sec, though both are larger than their counterparts in GaAs. It is most interesting that the saturation velocity of both electrons and holes in each material is essentially the same. Further experimental work is necessary to decide if the hole drift velocity is greater in InP than in GaAs as is the case for the electrons.

#### 4.5 Impact Ionization

As mentioned previously, a hole must attain an energy at least as great as the energy band gap in order to impact ionize. Since both momentum and energy must be conserved during an impact ionization event, often the threshold energy for impact ionization is significantly greater than the band gap [71]. In GaAs and InP all three valence bands, the heavy hole, light hole, and split-off bands extend to energies far beyond the band gap at which impact ionization can occur. Due to the strongly anisotropic behavior of the bands at high energy, a rigorous calculation of the threshold energy in all directions is unfeasible. It is common then to assume an isotropic threshold energy. The assumption of an isotropic threshold energy is valid since the band structure is slightly smeared out at high energy by phenomena such as collision broadening, the Stark ladder and intra-collisional field effects. An isotropic threshold energy is also consistent with the random  $k$  approximation of Kane [83]. If the isotropic

threshold energy is high enough, threshold cannot be reached in certain directions [40]. Therefore, the assumption of an isotropic ionization threshold energy does not preclude an anisotropic impact ionization rate.

We have found that the Monte Carlo impact ionization rate calculations can be fit to the experimental results in a variety of ways. As mentioned previously, there are two adjustable parameters,  $p$  and  $E_{th}$ , in the Monte Carlo calculations. In the first set of parameters we assume that the impact ionization behaves the same in all three bands; both  $p$  and  $E_{th}$  are identical in each of the bands. For the case of GaAs, the experimental results are fit extremely well through a wide range of applied fields, as seen in Figure 4.15, by using a universal threshold of 1.70 eV and a universal  $p$  factor of 0.25. Calculations are made for applied fields along the  $\langle 100 \rangle$ ,  $\langle 110 \rangle$ , and  $\langle 111 \rangle$  directions. The results show that there is no anisotropy in the impact ionization rate at high applied fields in GaAs. As the field decreases, there is more of a spread in the data. This may be due to statistical uncertainty since far fewer ionization events occur at low applied fields. A slight anisotropy in the impact ionization rate at low applied fields is expected however because the 'lucky' holes should contribute more to the impact ionization rate. At low applied fields the hole distribution is centered closer to  $k=0$  than at high fields. Since the distribution is cooler, those holes which reach the ionization threshold do so only after gaining much energy from the field. Maximum energy will be gained from the field provided that the holes are not scattered much from the field direction. A small anisotropy in the ionization rate is possible then because a hole, due to the anisotropy of the band structure, will gain different amounts of energy along different field directions per drift.



LP-2436

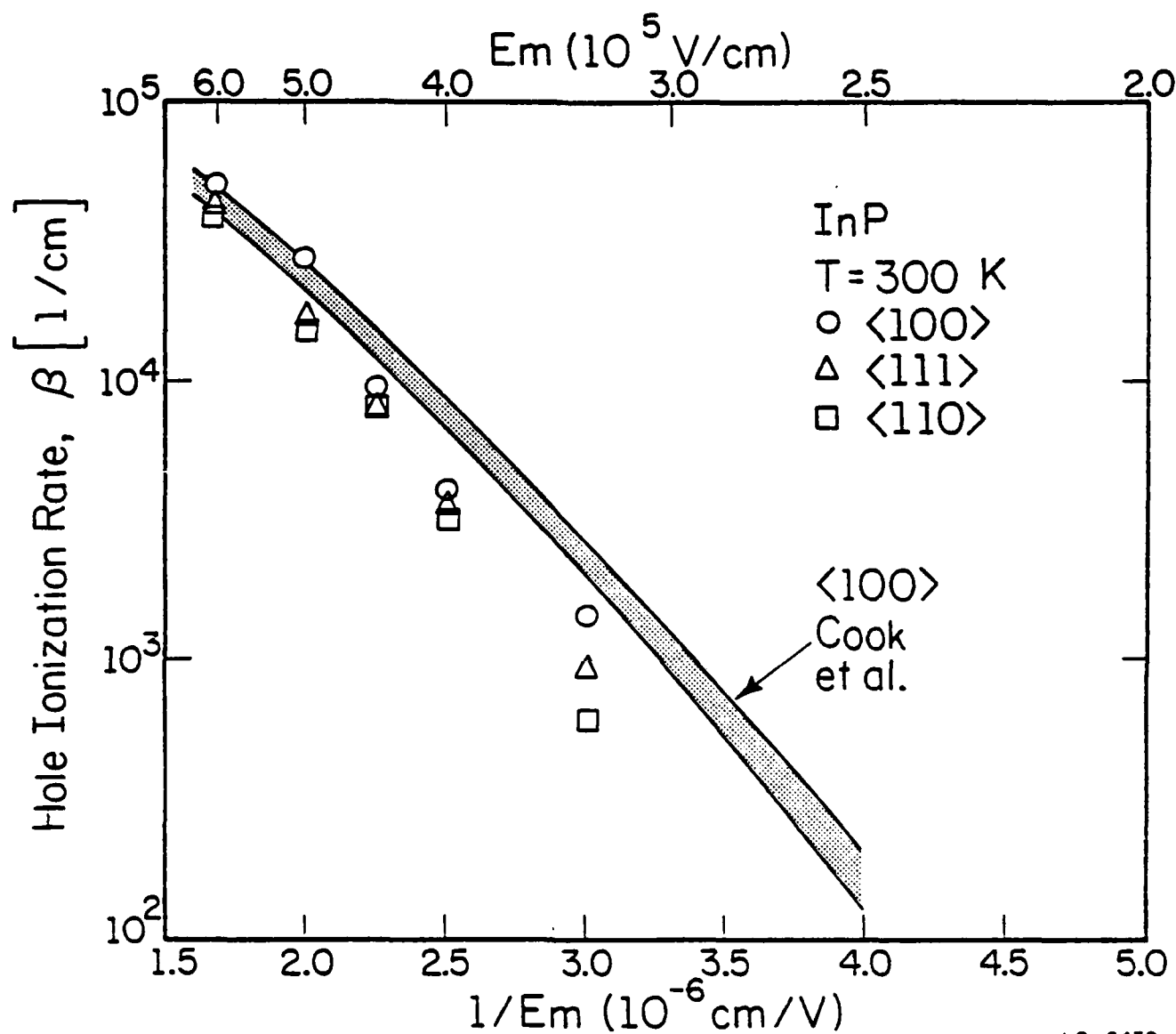
Fig. 4.15: Calculated hole impact ionization rate in GaAs as a function of inverse field in three crystallographic directions. The shaded region indicates the range of available experimental data [11]. All of the calculations are made with Set 1 parameters as discussed in the text.

Consequently, a hole can reach the ionization threshold energy faster for fields applied along certain directions. At high fields the distribution is much hotter and the holes are scattered randomly throughout the Brillouin zone by the deformation potential scattering. Therefore the majority of ionizing holes start from anywhere within the Brillouin zone and the directional dependence of the rate vanishes.

The hole impact ionization rate is much lower in InP than in GaAs as seen from a comparison of Figures 4.15 and 4.16. The Monte Carlo calculations presented in Figure 4.16 are made using a universal impact ionization threshold of 1.55 eV and a universal  $p$  factor of 20.0. Since the impact ionization rate is low in InP, far fewer ionization events occur than in GaAs. There is a much greater statistical uncertainty in the impact ionization calculations in InP than in GaAs. This may explain the greater deviation between the experimental InP data and the calculated data at low fields.

For the cases discussed above, where the ionization threshold and  $p$  factor are the same for each band, the majority of ionizing holes originate within the heavy hole band. Through the applied fields of interest here, the relative percentage of impact ionizing holes remains roughly constant in GaAs. While the heavy holes contribute the most to the ionization rate, the split-off holes contribute the least. This is true in both GaAs and InP but the split-off holes in GaAs are more important to the overall impact ionization rate since the split-off energy is less in GaAs than in InP.

The hole impact ionization rate is much lower in InP than in GaAs even though the calculated threshold energy in InP is lower. The  $p$  factor used in the InP calculation is larger as well. Therefore the relative strength of



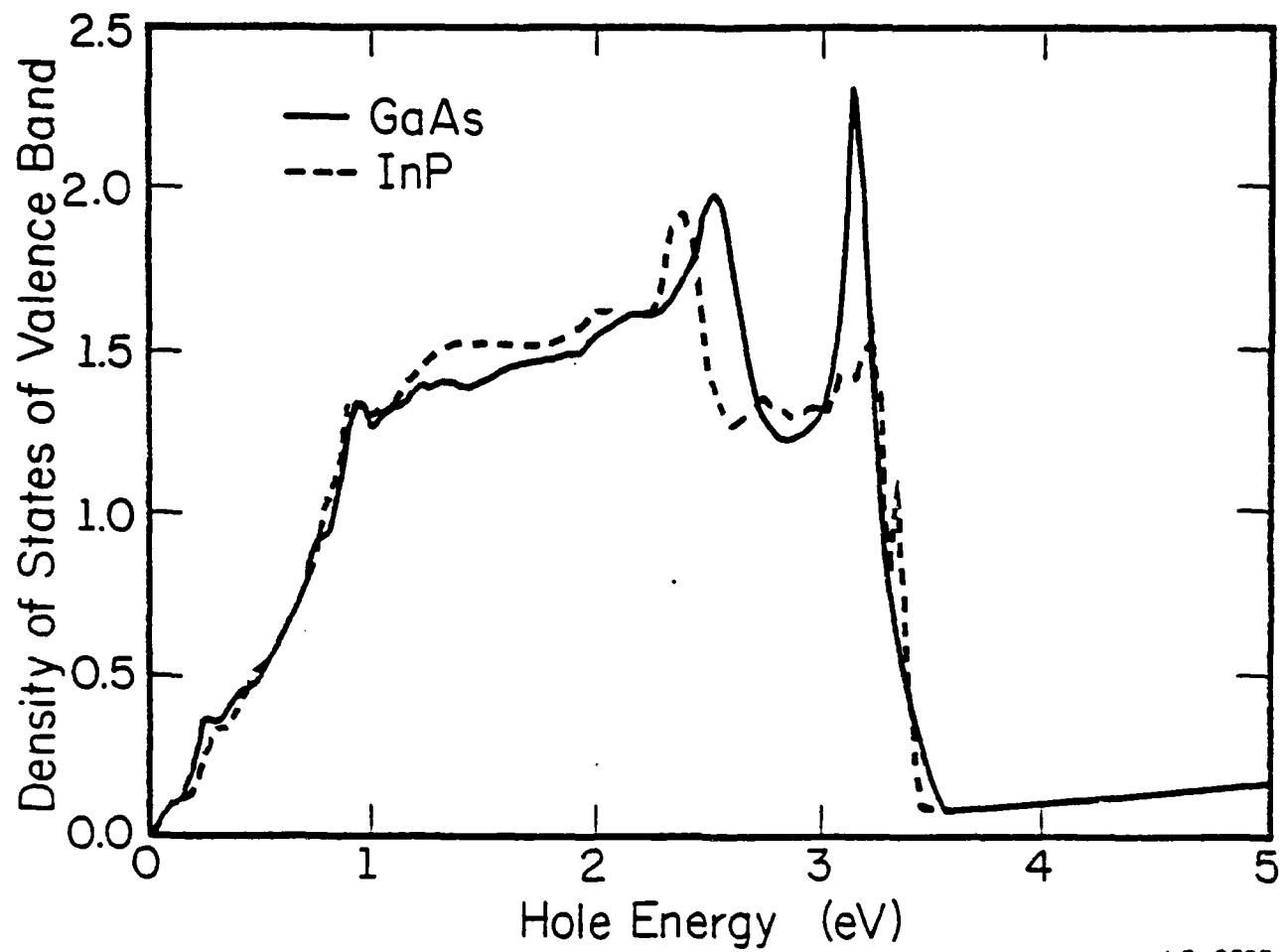
LP-2438

Fig. 4.16: Calculated hole impact ionization rate in InP as a function of inverse field in three crystallographic directions. The shaded region indicates the range of available experimental data [12].

impact ionization, treated as a scattering mechanism, is greater in InP than in GaAs, yet the overall ionization rate is much lower in InP. This apparent paradox can be explained by comparing the scattering rates and density of states between the two materials. The total phonon scattering rate in InP is significantly larger than the total phonon scattering rate in GaAs as seen from a comparison of Figures 4.9 and 4.10. Competing phonon scattering processes reduce the probability of impact ionization. Consequently, since the phonon scattering rate is much higher in InP than in GaAs, the probability of impact ionization in InP is greatly reduced.

The difference in the scattering rates between GaAs and InP is due to the different density of states in each material, Figure 4.17. The density of states is significantly higher in InP at energies above 1.0 eV. When the density of states increases it becomes more difficult for a hole to drift to states at and above threshold. Hence fewer holes in InP will reach high enough energies for impact ionization to occur.

Recent experimental measurements of the hole impact ionization rate in AlGaSb alloys suggest that the impact ionization is strongly influenced by holes in the split-off band [84,85]. Hildebrand et al. [84,85] have suggested that a 'resonance' occurs in the impact ionization rate when the split-off energy is equal to the energy band gap. Even though no 'resonance', as defined by Hildebrand [84], can occur in either GaAs or InP, since the energy gap is much larger than the split-off energy, based on these results it appears likely that the split-off band can be the dominant factor in hole impact ionization contrary to the previously presented results. We have found an additional set of parameters for GaAs such that the split-off holes are the dominant impact ionizing carriers. In this case



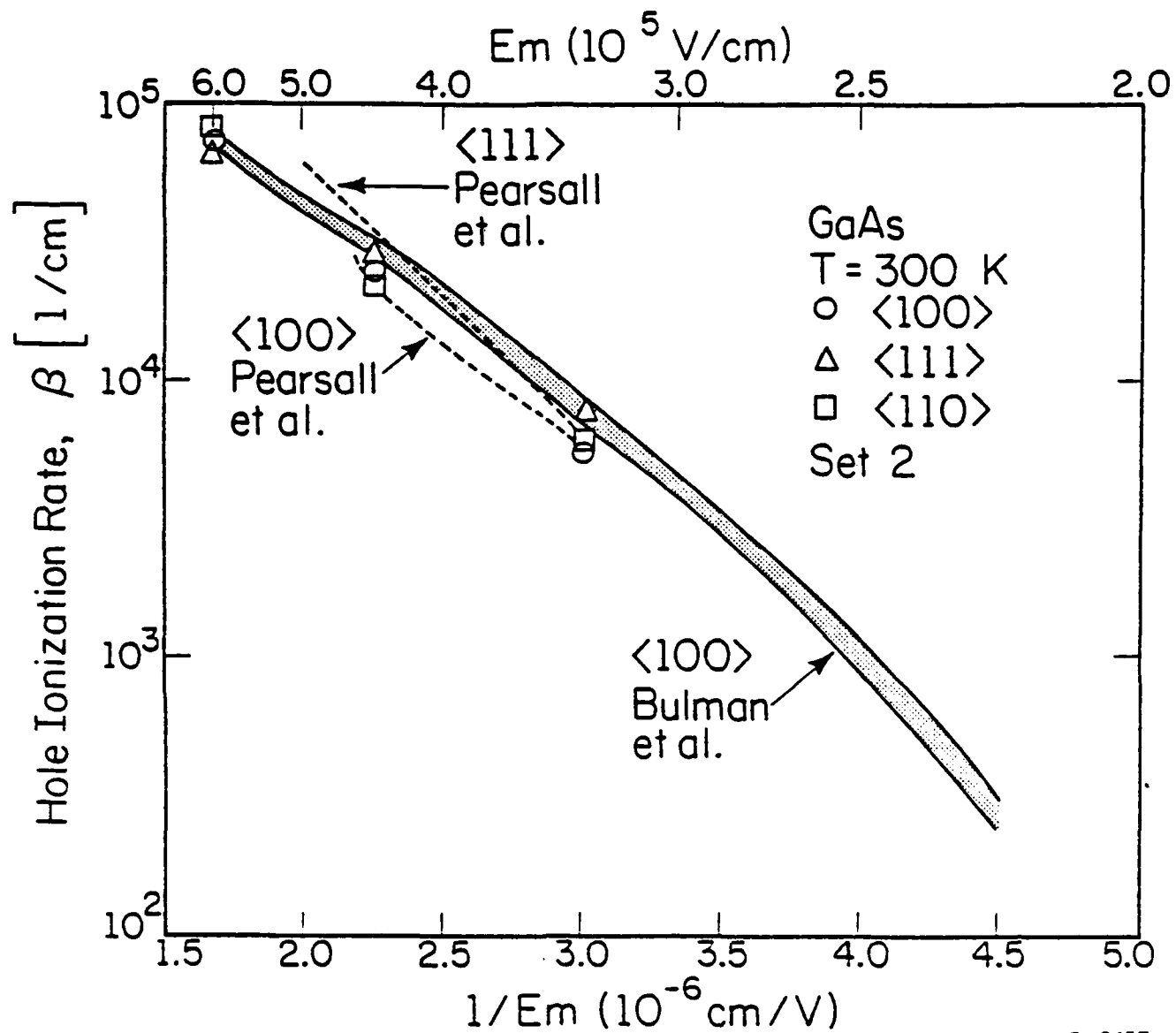
LP-2393

Fig. 4.17: Total density of states of the heavy hole, light hole, and split-off bands of GaAs and InP as a function of hole energy.

the threshold for impact ionization in the split-off band is equal to the band gap energy, while the ionization threshold is significantly higher in both the heavy and light hole bands. The  $p$  value remains the same as before in GaAs,  $p=0.25$ , for all three bands.  $E_{th}$  for the heavy and light holes is 1.80 eV. The hole impact ionization rate using these parameters is presented for GaAs in Figure 4.18. Again the calculations fit the experimental data well through a wide range of applied electric fields. There is also no orientation dependence in the impact ionization rate.

The difference between the hole impact ionization rates in GaAs and InP in this case is easily explained. The split-off energy is much larger in InP than in GaAs. The density of states in the split-off band then is much smaller in InP than in GaAs at or near the ionization threshold energy. Consequently, transfer of holes to the split-off band in InP is more unlikely than in GaAs at an energy near the impact ionization threshold energy. Results from the Monte Carlo simulation indicate that the experimental data in InP cannot be fit by assuming that the impact ionization is due largely to the split-off holes. From this result, it appears that the split-off band does not affect the impact ionization rate significantly unless the split-off energy is small with respect to the band gap energy or the split-off energy is exactly equal to the band gap energy such that a 'resonance' in the impact ionization rate can occur.

Based upon the above Monte Carlo calculations it cannot be uniquely determined which physical picture is correct in GaAs; the hole impact ionization rate is dominated by the split-off band or the heavy hole band. In Chapter 5 the nature of the 'resonance' effect in GaAlSb will be discussed and how the split-off band further influences hole impact



LP-2437

Fig. 4.18: Calculated hole impact ionization rate in GaAs as a function of inverse field in three crystallographic directions. The shaded region indicates the range of available experimental data [11]. All of the calculations are made with Set 2 parameters as discussed in the text.

ionization.

In Chapter 3, we determined the electron impact ionization rate in both GaAs and InP. The results of these calculations were presented along with the experimental measurements [11,12] in Figures 3.14 and 3.15. Comparison of these curves with Figures 4.15 and 4.16 indicates that  $\alpha$  is greater than  $\beta$  in GaAs while  $\beta$  is greater than  $\alpha$  in InP.

The results from Chapter 3 reveal that the electron ionization threshold energy in GaAs is 1.70 eV and the p factor is given as 0.5. In InP the ionization threshold energy is 1.55 eV while the p factor for electron impact ionization is 0.5. Comparing the results of the electron and hole impact ionization rates reveals that the ionization threshold energy is the same for both electrons and holes in GaAs, 1.70 eV, while the p factors differ by a factor of two. The ionization threshold energy for hole impact ionization, 1.55 eV, is much smaller than the threshold for electron ionization, 2.10 eV, in InP.

The density of states in the valence band is much flatter than the density of states in the conduction band in either GaAs or InP as seen from a comparison of Figures 4.17 and 3.16. Therefore it is easier for an electron to drift to higher energies than a hole even though the phonon scattering rates are comparable. Consequently, one expects the electron impact ionization rate to be greater than the hole ionization rate if the threshold energies are the same. This is the case in GaAs and the electron impact ionization rate is much stronger than the hole ionization rate. However in InP the hole threshold is much smaller than the electron threshold. The difference in the thresholds is sufficiently large enough that it is easier for the holes to impact ionize. Consequently,  $\beta$  is greater

than  $\alpha$  in InP.

#### 4.6. Conclusions

We have calculated, via a Monte Carlo approach, the impact ionization rate and steady state drift velocities of holes in GaAs and InP. Two models of hole impact ionization have been presented. The first model assumes a universal threshold energy for the heavy hole, light hole, and split-off bands. This model predicts that the heavy holes are the dominant ionizing agents. The second model assumes a much smaller threshold in the split-off band which results in the split-off holes dominating the impact ionization process. Either model is equally acceptable since both fit the experimental data well through a wide range of applied electric fields. A small anisotropy in the impact ionization rate is observed at low fields, while no anisotropy occurs using either model at high fields.

Previously calculated results of the electron impact ionization rate in GaAs and InP are compared with the hole ionization rate presented here. The comparison shows that the electron impact ionization rate is greater than the hole impact ionization rate in GaAs while in InP the hole ionization rate is larger than the electron ionization rate in accordance with recent experimental measurements. The reversal in the ratio of  $\alpha$  and  $\beta$  may be due to the tremendous difference between the density of states of the conduction band and that of the valence band, as well as the different electron and hole ionization threshold energies.

## 5. STEADY STATE HOLE TRANSPORT IN GaSb AND $\text{Al}_x\text{Ga}_{1-x}\text{Sb}$

### 5.1 Introduction

As discussed in Chapter 4, it cannot be determined, based upon the calculations made in GaAs, which valence band dominates the hole impact ionization rate. The existing experimental data can be fit in a variety of ways using the Monte Carlo method. For one choice of parameters, holes in the heavy hole band dominate the impact ionization process, while for another choice holes in the split-off band are dominant. Recent experimental measurements [84,85] seem to indicate that the split-off band plays a significant role in hole impact ionization. A possible 'resonance' in the hole impact ionization rate may occur in materials in which the split-off energy,  $\Delta$ , is equal to the energy gap,  $E_g$ . In this chapter the nature of this 'resonance' and the effect of the split-off band in hole impact ionization will be further explored.

### 5.2 Review of Experimental Results

The measurements of the hole impact ionization rate in GaSb and  $\text{Al}_x\text{Ga}_{1-x}\text{Sb}$  made by Hildebrand et al. [84,85] were carried out at different composition and temperature in order to vary the ratio of the spin-orbit splitting to the band gap energy. They present a range of experimental data which show a 'resonance' in the impact ionization rate. Their results are presented in Figure 5.1 where the ratio of hole to electron ionization coefficients,  $\beta/\alpha$ , is plotted as a function of  $\Delta/E_g$ , the ratio of the split-off energy to the band gap energy. As can be seen from Figure 5.1, the

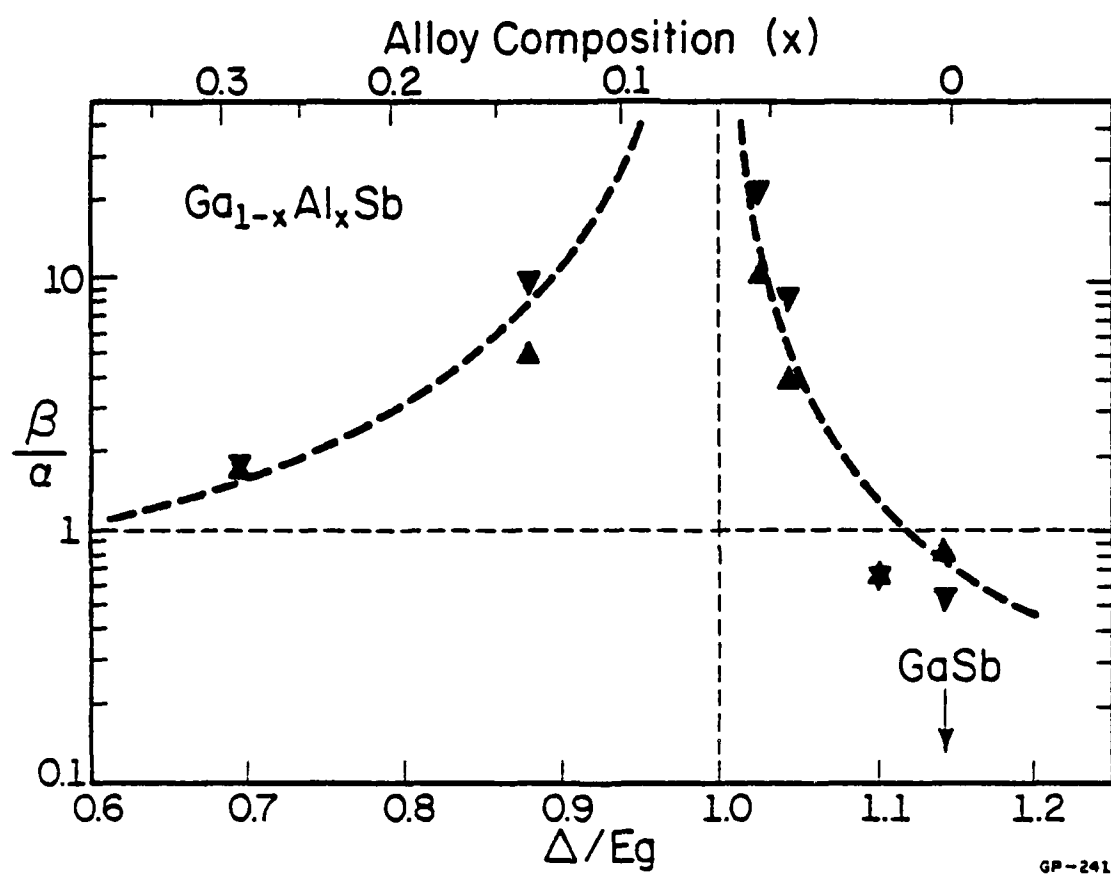
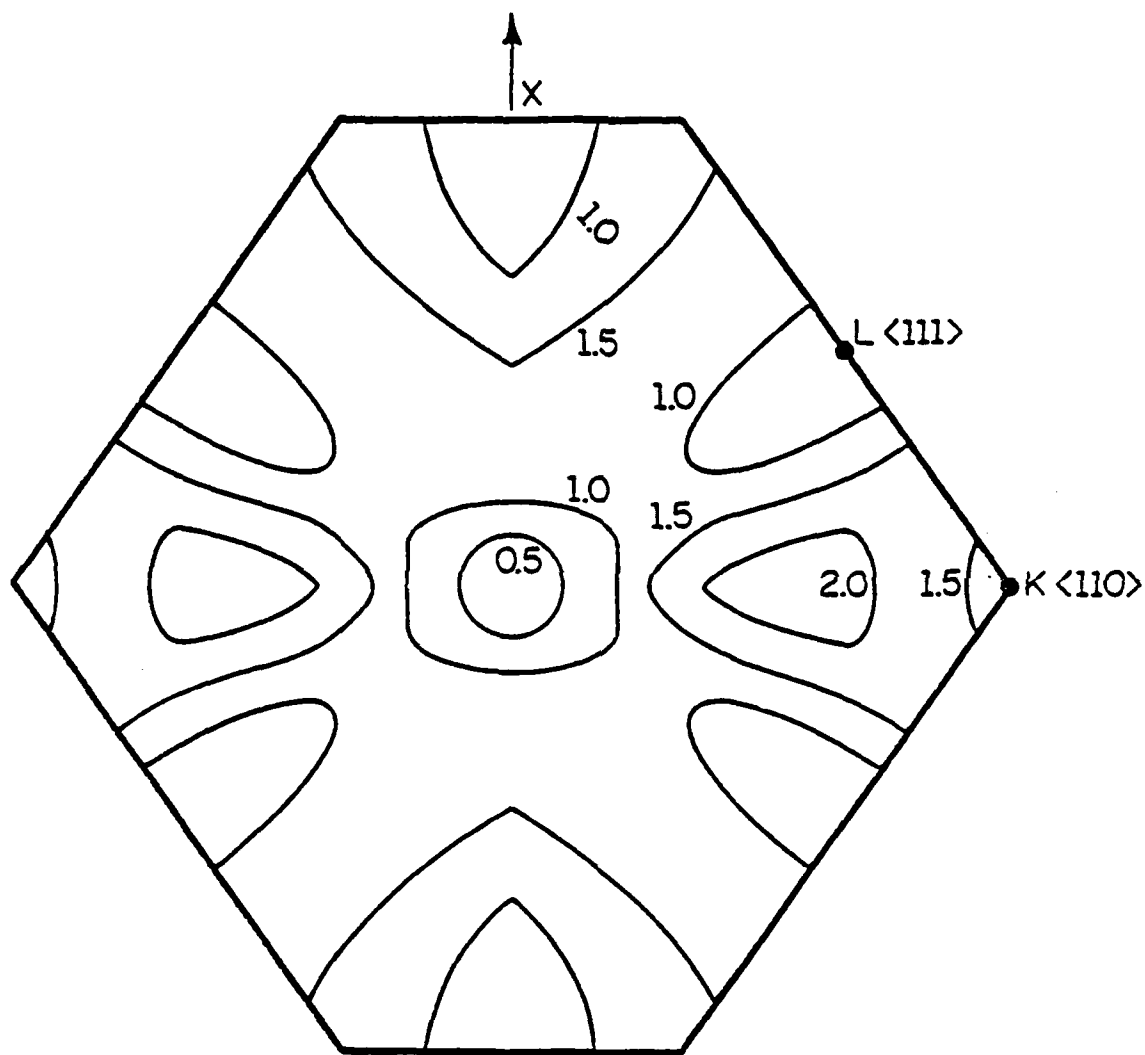


Fig. 5.1: Experimental variation of the ratio of hole to electron impact ionization rates in  $\text{Ga}_{1-x}\text{Al}_x\text{Sb}$  with alloy composition,  $x$ , and ratio of the spin-orbit splitting energy,  $\Delta$ , to the band gap energy  $E_g$  [84,85].

InP  
First Conduction Band



LP-2392

Fig. 3.6: Isoenergy lines of the first conduction band in InP in the cross section shown in Figure 3.5. The numbers represent the energies measured from the gamma minimum in eV.



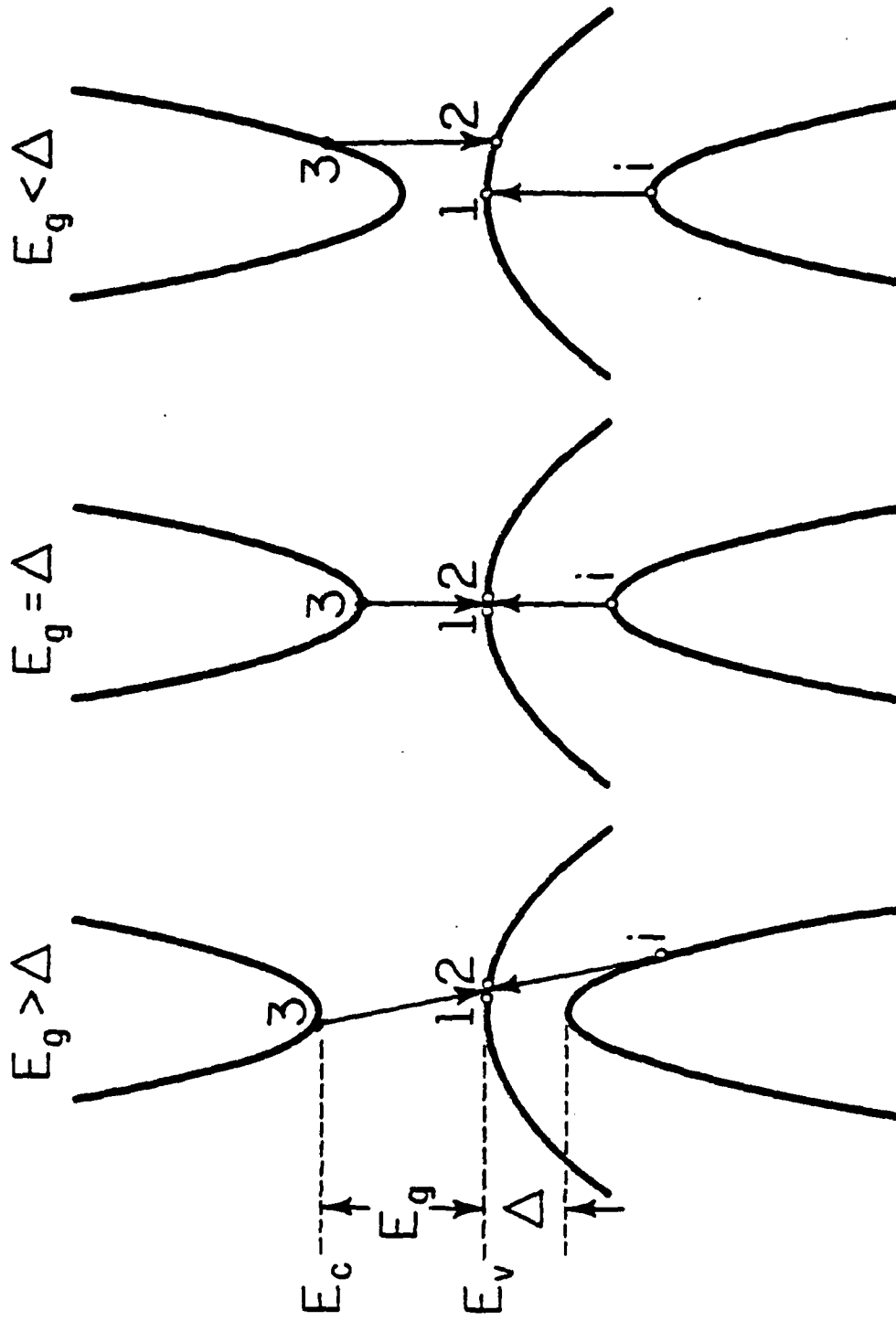
ratio of  $\beta/a$  increases drastically as the ratio of  $\Delta/E_g$  approaches one from either direction. To explain this behavior, Hildebrand et al. [84,85] propose that when  $\Delta/E_g$  is equal to one a 'resonance' occurs in the impact ionization.

Hildebrand et al. [84,85] claim that when the experimental data are fit using the Shockley-Baraff theory [51,52] that the mean free path,  $\lambda$ , has a very strong dependence upon the alloy concentration,  $x$ , as  $x$  goes from 0.0 to 0.052. This appears to be unlikely since  $\lambda$  depends essentially on the phonon scattering rate which should not change drastically for small percentage alloys [86,87]. Therefore in order to account for the very different impact ionization rates between GaSb and  $\text{Al}_x\text{Ga}_{1-x}\text{Sb}$  a different distribution function is necessary. They propose a rate governed by the following equation

$$\beta = C \exp - \left( \frac{E_i - E_g}{q \lambda F} \right) \quad (5.1)$$

This equation shows a 'resonance' as  $\Delta$  approaches  $E_g$ . A physical depiction of this 'resonant' behavior is illustrated in Figure 5.2.

Figure 5.2 schematically illustrates the hole initiated impact ionization events from the split-off band for various ratios of  $\Delta/E_g$ . Both energy and momentum are simultaneously conserved in hole initiated ionization when  $\Delta = E_g$ . Consequently, the hole ionization threshold energy is a minimum when  $\Delta/E_g = 1.0$  [85] if parabolic energy bands are assumed. Since the ionization coefficients depend greatly on the threshold energy [50,53], the hole ionization coefficient should exhibit a maximum value at the minimum threshold energy of  $\Delta = E_g$ , while the electron coefficient should remain unchanged.



GP-242

Fig. 5.2: Schematic representation of the impact ionization process in GaAs for hole initiated impact ionization from the split-off valence band (indicated by 1) for  $E_g > \Delta$ ,  $E_g = \Delta$ , and  $E_g < \Delta$ . The uppermost band represents the conduction band,  $E_g$  and the middle band is the heavy hole band.

An alternative explanation of the data presented by Hildebrand et al. [84,85] is proposed by Kasemset [88]. Kasemset claims that it is unnecessary to introduce a new impact ionization mechanism in order to explain the experimental data. Hildebrand et al. [84,85] assume that, for  $\Delta > E_g$ , the ionization threshold energy is given by  $\Delta$ . However this choice violates the Anderson-Crowell criteria [71]. Kasemset has also shown that the behavior of the mean free path,  $\lambda$ , is equally as dependent on  $x$  for the distribution given by Equation 5.1 as for the Shockley-Baraff distribution. Hence he concludes that the empirical function of Equation 5.1 is invalid.

As an alternative explanation for the experimental data, Kasemset [88] proposes that the threshold energy,  $E_i$ , does not equal  $\Delta$  for  $\Delta > E_g$ . In this case, he proposes that the heavy holes are the predominant ionizing agents. In conclusion, Kasemset claims that there is no "resonance" effect associated with the change in the ratio of  $\Delta/E_g$ . The experimental data are then explained as due to a band structure effect. When  $\Delta > E_g$ , heavy holes have the lowest threshold energy, and when  $\Delta < E_g$ , the split-off holes contribute the most.

High field experimental data of the impact ionization rate in AlGaSb and GaSb are reported by Zhingarev et al. [89,90] and Pearsall et al. [91]. Their results show no significant difference in the impact ionization rate between the two materials. The measurements of Hildebrand et al. also show that the 'resonance' disappears as the field increases to 50.0 kV/cm and above. This is not surprising, since at high electric fields, the holes are heated to high energies where they can easily impact ionize independent of any 'resonance' effects.

It is interesting to note that it does not appear that both the high and low field experimental data for GaSb can be fit using a simple exponential law. The rates between the two sets of experimental data, Hildebrand et al. [84,85] and Zhingarev et al. [89,90], are quite different even when the 'resonance' data are not considered. In the calculations, we have tried to fit as best as possible both sets of experimental data simultaneously. As we shall see, once the low field data are fit well, the high field data are not.

### 5.3 Band Structure and Phonon Scattering Rate

In the calculations of interest here, the presence of the split-off band is of importance to the transport quantities and must be included correctly. The valence band structures of both GaSb and the AlGaSb alloys considered here are calculated using the  $K * P$  method of Kane [74] which includes the spin-orbit interaction. According to our  $K * P$  calculation, the band gap energy is equal to the split-off energy in GaAlSb when the concentration of Al is 3.3%. We calculate the impact ionization rate for three cases,  $\Delta > E_g$  (GaSb),  $\Delta = E_g$  ( $\text{Al}_{0.033}\text{Ga}_{0.967}\text{Sb}$ ), and  $\Delta < E_g$  ( $\text{Al}_{0.12}\text{Ga}_{0.88}\text{Sb}$ ). From our  $K * P$  calculation at a 12% Al concentration, the split-off energy is roughly 0.1 eV less than the band gap energy.

The valence band structure of GaSb is presented in Figure 5.3. The energy band gap and the split-off energy are almost the same as can be seen from this figure. The band structure is strongly anisotropic, and nonspherical at high energy. Therefore it is essential that the full details of the band structure be included in a calculation of the hole impact ionization rate.

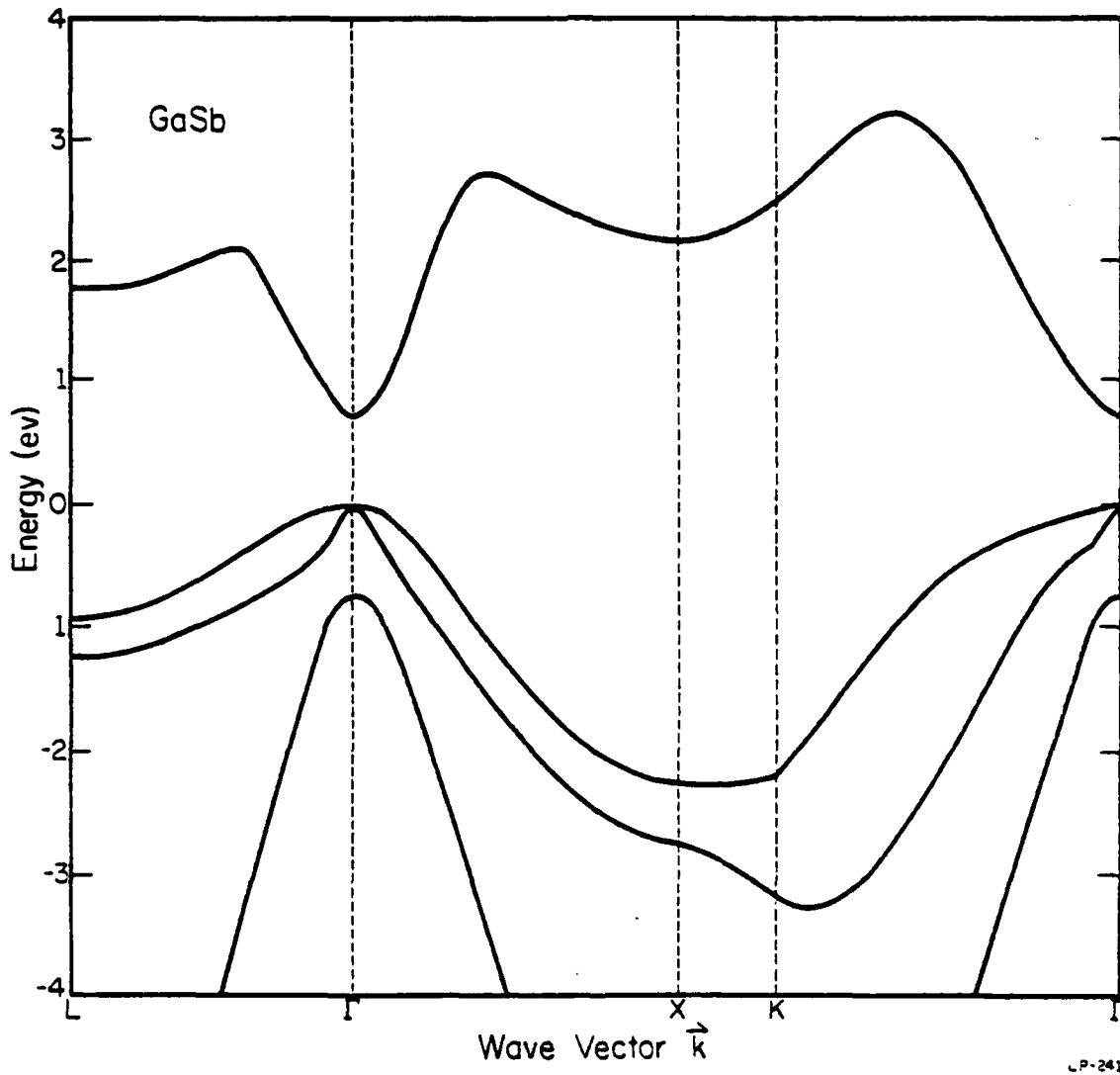


Fig. 5.3:  $E(k)$  relation for GaSb. The first conduction band is sketched based upon the results of a pseudopotential calculation while the valence bands are calculated using the K \* P method.

Again we present cross sectional cuts in the Brillouin zone which show the isoenergy lines in GaSb at high energy. Figures 5.4-5.7 illustrate the isoenergy lines in the different cross sectional cuts presented in Chapter 3. It is interesting to note that the energy band structure is very anisotropic and irregular at energies above the gamma minimum.

The principal scattering agents are the same as those in GaAs and InP, acoustic phonons, nonpolar and polar optical phonons. The scattering rate is calculated the same way as discussed in Chapter 4. The effects of the initial state collision broadening are less important in GaSb since the impact ionization threshold is smaller than in either GaAs or InP. Consequently, impact ionization can occur in GaSb at lower energy than in either GaAs or InP. In the ternary compounds alloy scattering is omitted. This is a reasonable approximation since the percentage of Al is very small. The impact ionization rate is again calculated using the Kelydsh formula [53] and the parameters,  $p$  and  $E_{th}$ , are determined from fitting the calculated results to the high field experimental data [89-91].

In the Monte Carlo calculation for the ternary compounds, material parameters, such as the density, the effective masses of the holes in each band, and the energy band gap are determined from linear interpolation [87,92]. The small change in the concentration of Ga in the compound upon the addition of Al only changes these parameters by a slight amount. Their only real effect is to slightly modify the hole-phonon scattering rate in the calculation. This is because the scattering rate, depends to a larger extent upon the change in the final density of states. Figure 5.8 shows the density of states of GaSb and  $Al_{0.033}Ga_{0.967}Sb$  as a function of hole energy. As is clearly seen from this figure, the density of states is roughly the

GaSb  
Heavy Hole Band

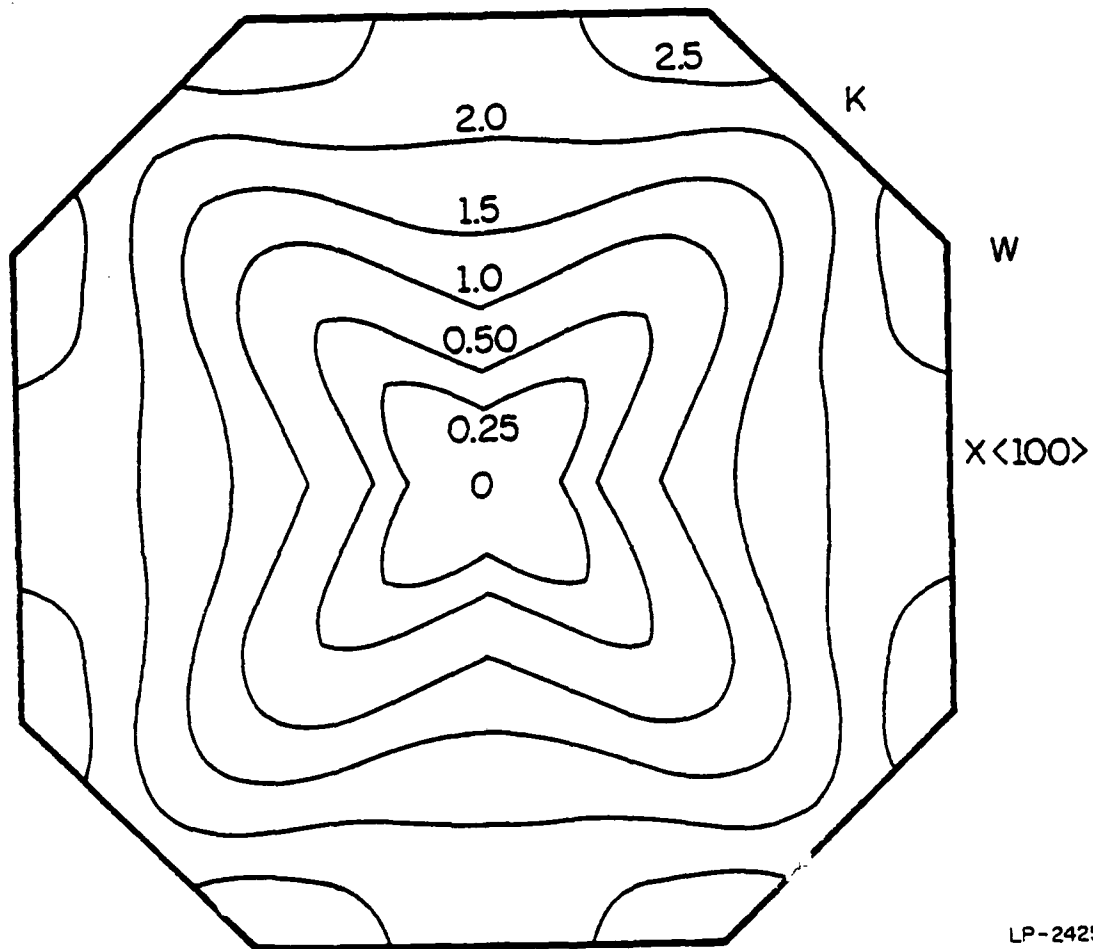
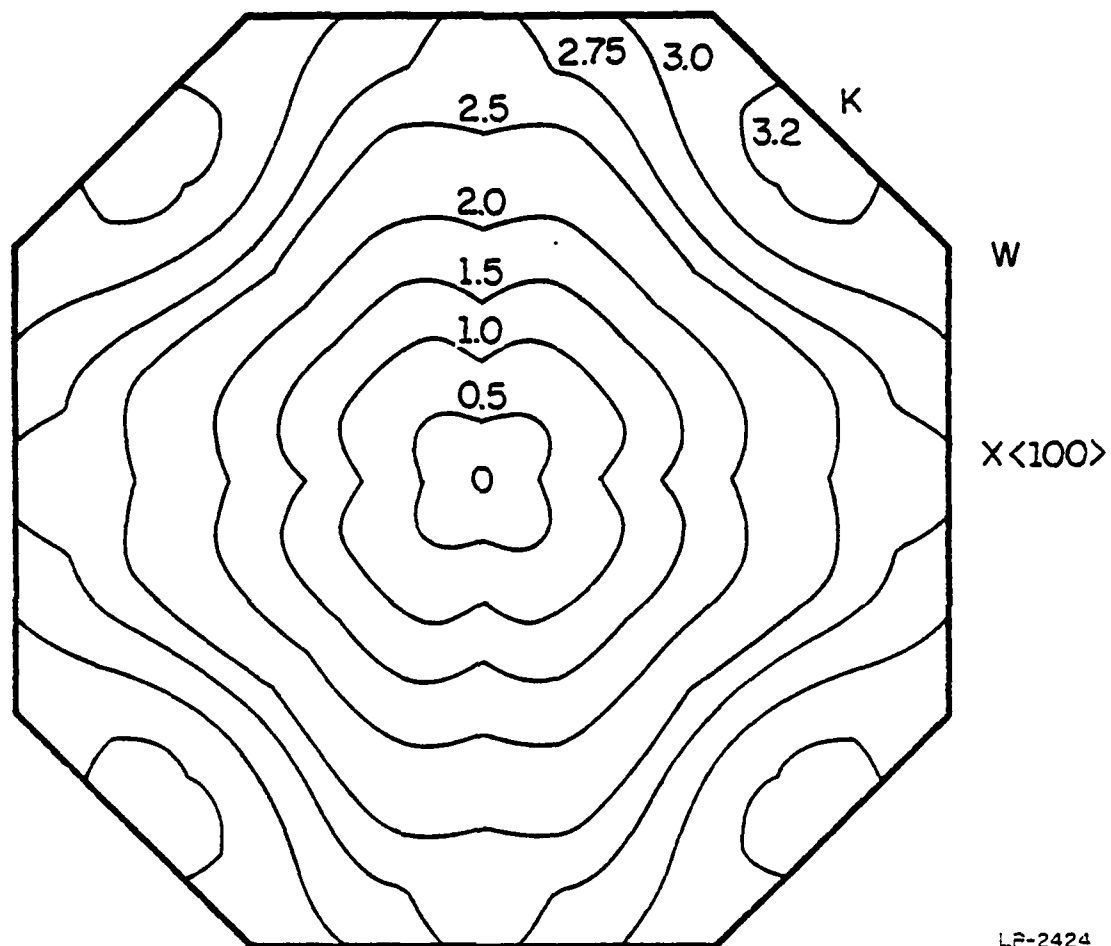


Fig. 5.4: Isoenergy lines of the heavy hole band of GaSb in the cross section of Figure 3.3. The numbers represent the energies measured from the gamma minimum in eV.

GaSb  
Light Hole Band



LP-2424

Fig. 5.5: Isoenergy lines of the light hole band of GaSb in the cross section of Figure 3.3. The numbers represent the energies measured from the gamma minimum in eV.

GaSb  
Heavy Hole Band

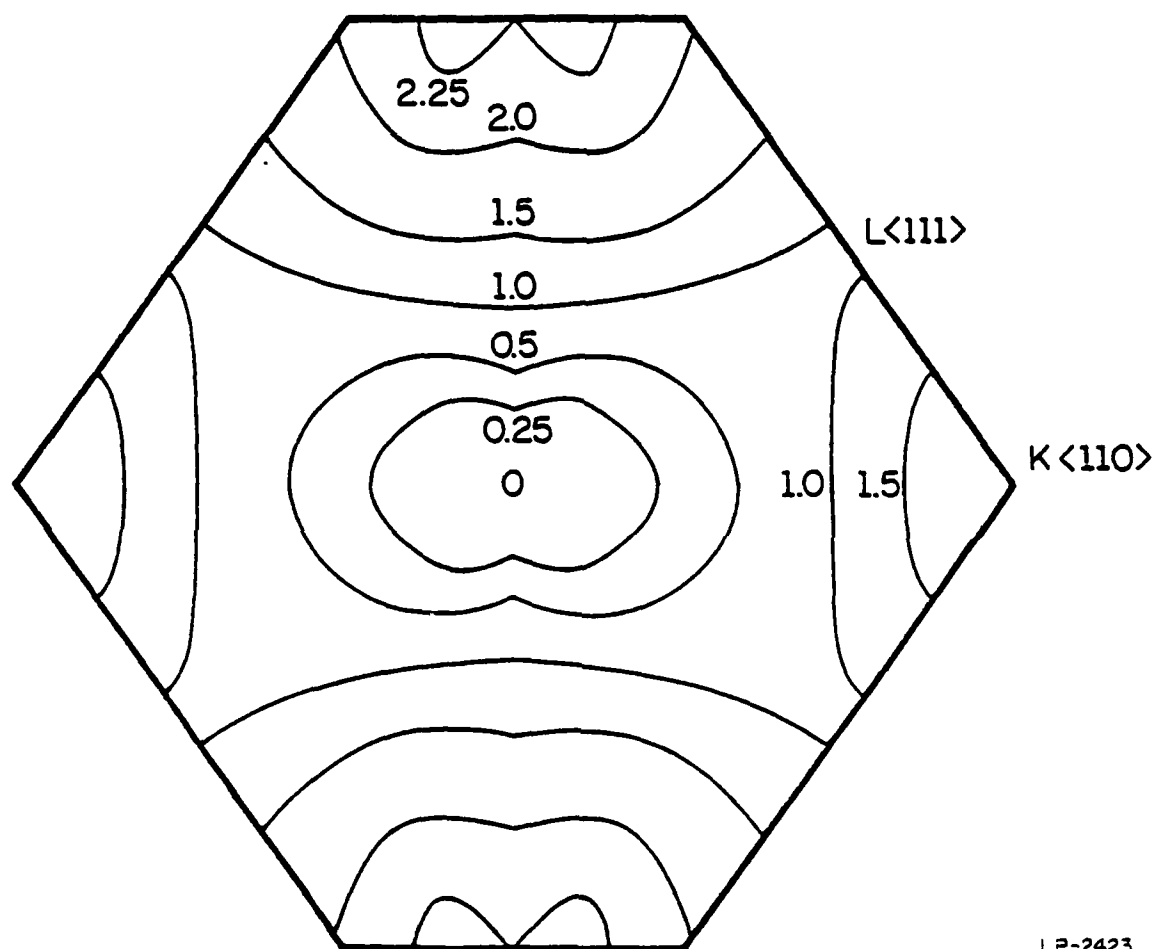


Fig. 5.6: Isoenergy lines of the heavy hole band of GaSb in the cross section of Figure 3.5. The numbers represent the energies measured from the gamma minimum in eV.

AD-A161 279

THEORETICAL STUDIES OF HIGH ENERGY TRANSPORT OF  
ELECTRONS AND HOLES IN GA. (U) ILLINOIS UNIV AT URBANA  
COORDINATED SCIENCE LAB K F BRENNAN JUN 84 R-1011

2/2

UNCLASSIFIED

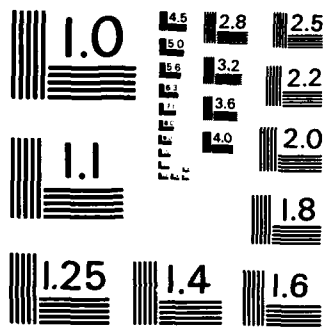
F/G 28/12

NL

END

FILMED

BTB



MICROCOPY RESOLUTION TEST CHART  
NATIONAL BUREAU OF STANDARDS-1963-A

GaSb  
Light Hole Band

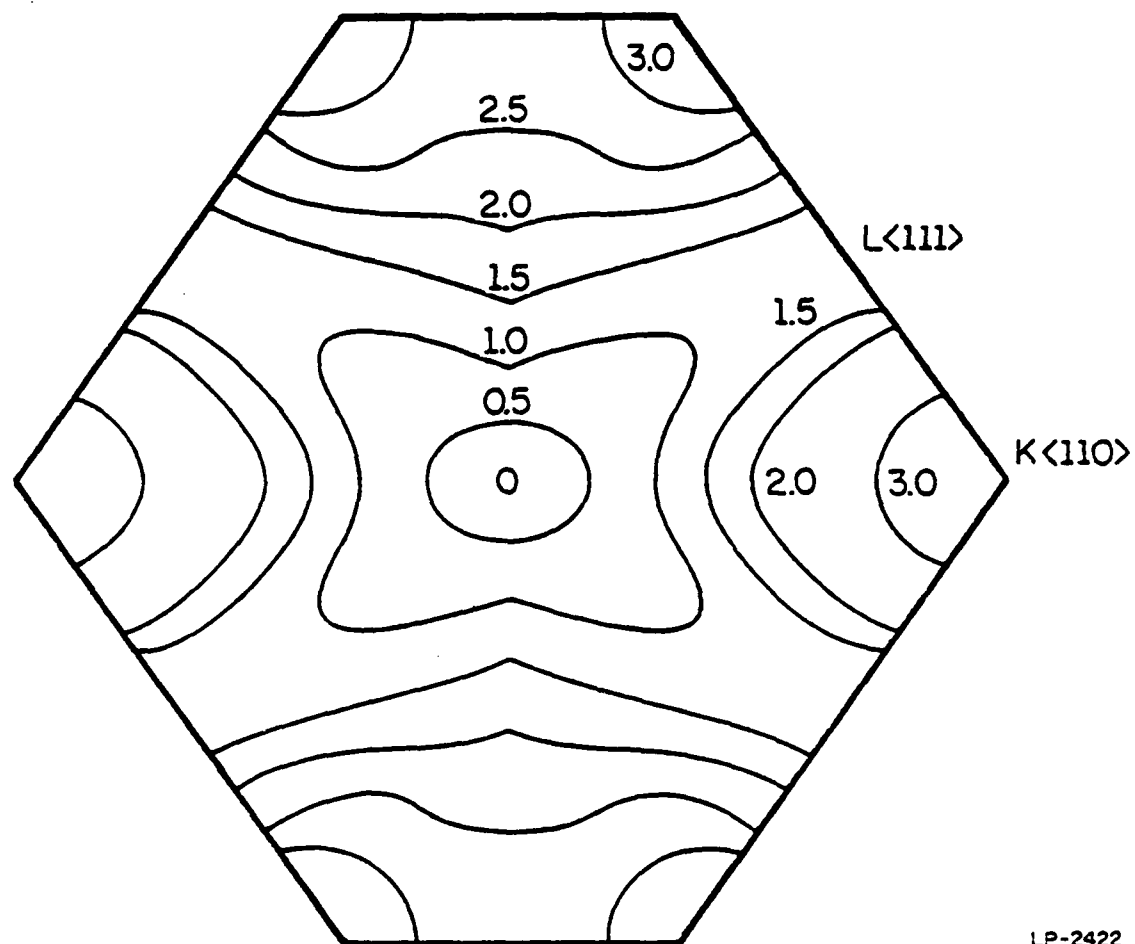


Fig. 5.7: Isoenergy lines of the light hole band of GaSb in the cross section of Figure 3.5. The numbers represent the energies measured from the gamma minimum in eV.

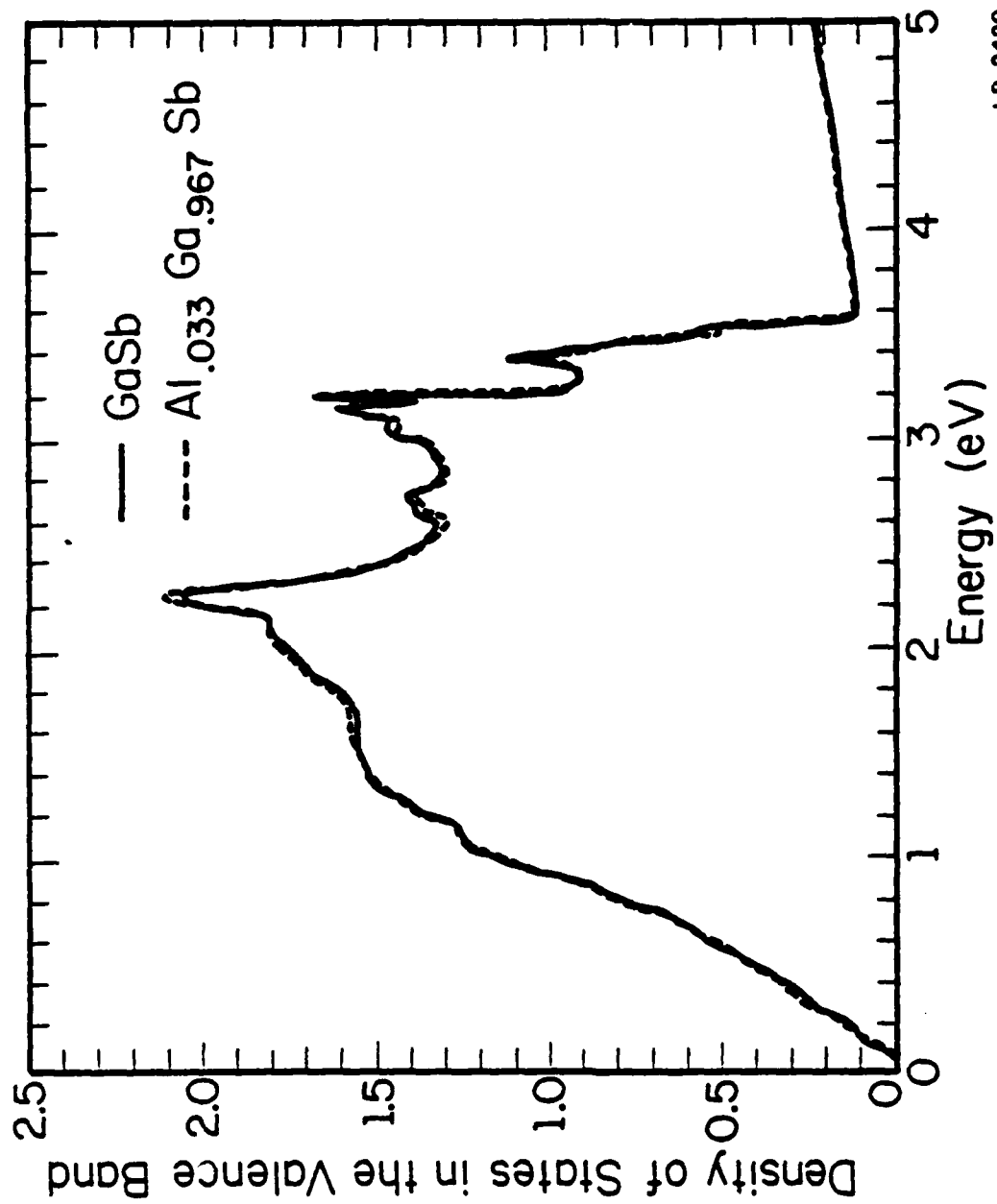


Fig. 5.8: Total density of states of the heavy hole, light hole, and split-off hole bands of GaSb and Al<sub>0.033</sub>Ga<sub>0.967</sub>Sb as a function of carrier energy.

same between the two materials. Therefore the phonon scattering rate is about the same. Any difference in the impact ionization coefficients between these two materials must then be due to the different impact ionization mechanisms.

#### 5.4 Computational Method

The 'resonance' only appears at low applied fields. The impact ionization rate at these fields is roughly  $2.0 \times 10^3$  1/cm in the alloy while it is about  $1.0 \times 10^2$  in GaSb. Because the impact ionization rates are very small it is difficult to obtain reliable statistics using the Monte Carlo method previously described. The occurrence of an impact ionization event is sufficiently improbable at these low fields that the program can run for many cpu hours without one event occurring. Consequently, it is not efficient to simply run the program without further changes.

An alternative approach has been developed. First, the hole energy distribution function is calculated using the Monte Carlo program. The hole is launched at zero launching energy and its' history is accumulated over many scatterings. The distribution function can be easily determined from the time the hole spends in a particular energy range and from the density of states at that range. Then holes are launched according to the high energy tail of the distribution function. The band from which the hole initiates from at high energy is chosen in accordance with the density of states of each band at that energy. A particular minimum energy is chosen and when a hole scatters to energies below this value another hole is relaunched in its place. Clearly, if a high launching energy range is chosen many impact ionization events can occur. The net impact ionization rate is determined from a product of the calculated impact ionization rate for the

holes in the high energy tail and the probability that a hole is in the high energy tail. Consequently, fairly good statistics are accumulated for the hole impact ionization rate at low fields.

If the suggestion of Hildebrand et al. is correct, that the impact ionization rate in GaAlSb does have a resonance, then as shown below the impact ionization mechanism itself must be much stronger in the split-off band close to  $k=0$  than in either the heavy or light hole bands. The ionization rate in the split-off band of the alloy must be very much larger than in GaSb as well. Since the details of the impact ionization process itself are not known for this material system, the impact ionization mechanism is again modeled as before using the Kelydsh formula [53] with adjustable parameters. Since the energy band gap is less than or equal to the split-off energy for either GaSb or  $\text{Al}_{0.033}\text{Ga}_{0.967}\text{Sb}$  the threshold energy for impact ionization in the split-off band is taken to be the split-off energy,  $\Delta$ . Therefore, all the states in the split-off band are at or above the threshold energy including those near  $k=0$ . For the case  $\Delta < E_g$ , ( $\text{Ga}_{0.88}\text{Al}_{0.12}\text{Sb}$ ) holes near  $k=0$  cannot impact ionize since these states lie below the impact ionization threshold energy. The resonance can be modeled by assuming that the impact ionization probability for holes within the split-off band near  $k=0.0$  is essentially infinite for  $\Delta \geq E_g$ . This can be accomplished by assuming that the  $p$  factor is very large at that point. We have chosen a  $p$  factor of  $1.0 \times 10^5$  for the resonance condition. Ordinarily, high in the band and far away from the gamma point, a much smaller value of  $p$  is appropriate [24]. To fit the experimental data, however, a very high  $p$  value is needed near the bottom of the split-off band. This suggests that at gamma the impact ionization is greatly enhanced

for holes above the threshold energy.

Since a first principle theory is not available for the impact ionization rate in the split-off band, a mechanism is chosen which exhibits a sharp increase over a small energy range close to gamma. In this model we choose a large  $p$  factor, hence a large impact ionization probability, for a limited energy range. Above this energy range we use a smaller  $p$  value, 0.20.

### 5.5 Results of the Impact Ionization Calculation

In the absence of steady state hole drift velocity data, it is difficult to determine the overall hole-phonon scattering rate with precision. For low energies, we calculate the rate in the Born approximation using the results of Costato and Reggiani [76,77] and the parameters in Tables A2.6 and A2.7 of Appendix 2. The nonpolar optical phonon deformation potential constant is not known to any great precision. An empirical relation has been given by Wiley [8] relating the optical and the acoustic deformation potential constants. This relation has been used for the initial calculations ( Set 1 ).

The high energy rate is calculated using the self-energy method and is adjusted to fit the low energy scattering rate at an energy of .5 eV. The scattering rate obtained in this way is displayed in Figure 5.9 and is labeled Set 1. The results for the impact ionization calculation are shown in Figure 5.10. Notice that, at high fields, the calculated impact ionization rate data match the experimental data quite well. However, at low applied electric fields the calculated data are much less than the experimental data. For this calculation we choose an impact ionization

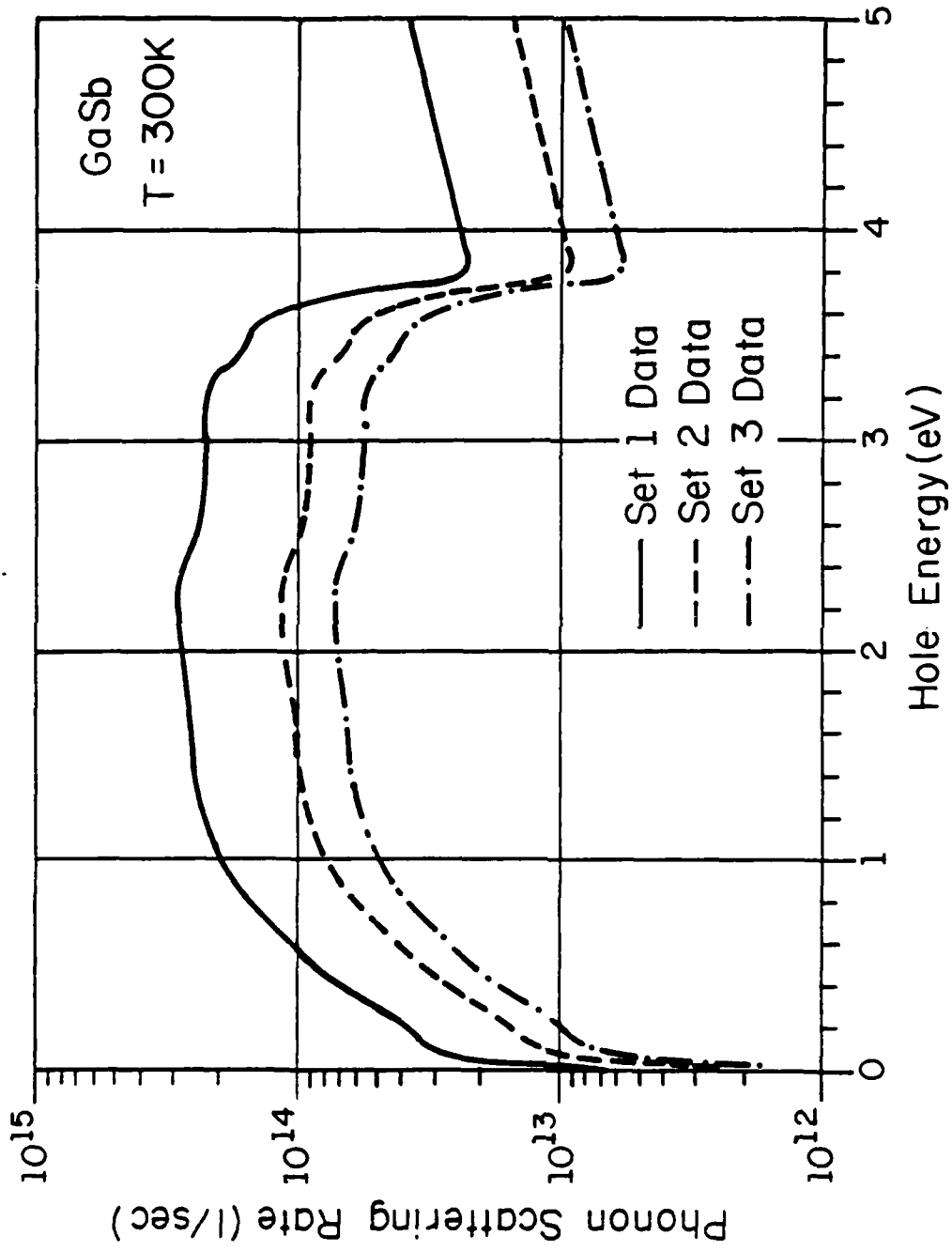


Fig. 5.9: Hole-phonon scattering rate in GaSb as a function of hole energy as described in the text.

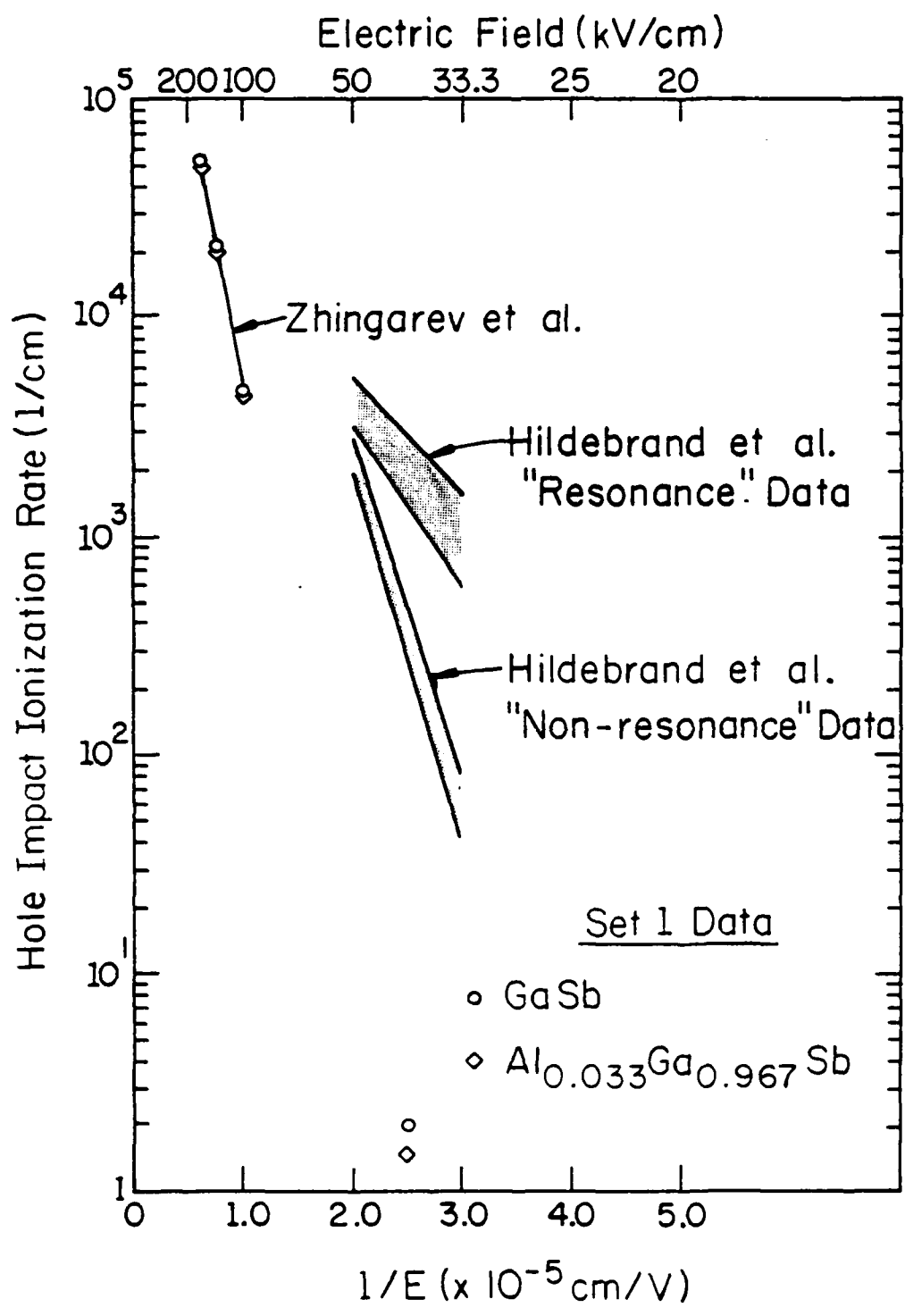


Fig. 5.10: Hole impact ionization rate in GaSb and in AlGaSb as a function of inverse applied electric field. The experimental data are from Hildebrand et al. [84,85] and Zhingarev et al. [89,90]. The calculations are made with the Set 1 parameters and scattering rate as described in the text.

threshold energy for both the heavy and light hole bands to be the same,  $\sim 0.80$  eV. The  $p$  factor used in the impact ionization rate mechanism is 100.0. The same parameters are used in the GaSb calculation as in the GaAlSb calculation. This appears to be physically reasonable since one does not expect from the virtual crystal approximation for there to be much of a difference in the deformation potentials of the heavy and light hole bands between the binary and the dilute alloy. The impact ionization rate is found to be completely dominated by holes within the heavy hole band. For this set of parameters, no impact ionization events occur due to holes in the split-off band.

For the case of the Set 1 calculations, the scattering rate is so large that the holes cannot reach the ionization threshold energy at low applied electric fields in any of the three bands. In order to fit the low field experimental data then, it is necessary to reduce the scattering rate such that the holes can drift to high enough energy in order to impact ionize. We choose to simply reduce the scattering rate by changing the deformation potential constant.

Figure 5.11 illustrates the results of the impact ionization calculation using a reduced scattering rate,  $\sim 40.0\%$  of the original rate, which is labeled as Set 2 in Figure 5.9. In order to fit the experimental data, the threshold energy and  $p$  factors must be adjusted for each band. The threshold energy for impact ionization in the heavy and light hole bands is 1.05 eV while the  $p$  factor, for the best fit, is 0.20 in the heavy hole band and 1.0 in the light hole band. Again the same parameters are used for the binary and the alloy. The  $p$  factor in the split-off band near the gamma point is  $1.0 \times 10^5$  while it is 1.0 away from the gamma point. The low field

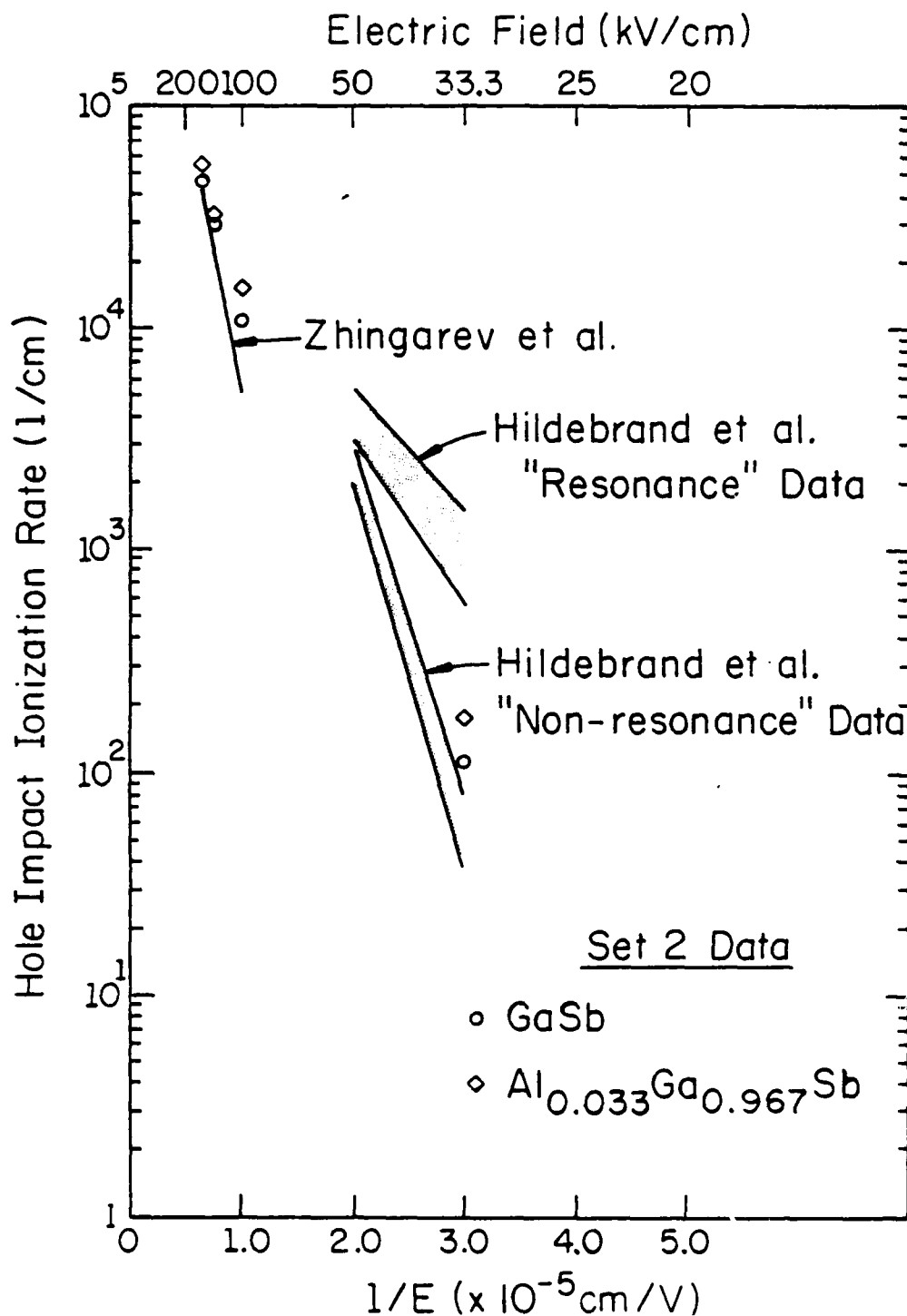


Fig. 5.11: Hole impact ionization rate in GaSb and in AlGaSb as a function of inverse applied electric field. The experimental data are from Hildebrand et al. [84,85] and Zhingarev et al. [89,90]. The calculations are made with the Set 2 parameters and scattering rate as described in the text.

data in GaSb are fit rather well but no resonance is evident in the calculation for the alloy. This appears to be due to the large number of heavy and light holes impact ionizing in both materials. Roughly 50% of the holes impact ionize from the heavy and light hole bands in this case.

The reason why the heavy and light hole bands contribute so much to the impact ionization rate is because the density of states is larger in each of these bands than in the split-off band. Therefore, the holes are easily scattered into either band, particularly the heavy hole band, and tend to stay within them. In order for the resonance to occur, it is necessary for the vast majority of the holes to impact ionize from the split-off band. This can only be accomplished if enough holes are scattered into the split-off band from which they can impact ionize before they ionize from either the heavy or light hole bands. It is necessary for the holes to drift to an energy sufficiently high that the density of states within the split-off band is appreciable before the holes can be scattered into it. Therefore, in order for the resonance to be possible, the impact ionization threshold energy must be high within the heavy and light hole bands.

Extensive numerical calculations for various sets of parameters as described above showed that the resonance data can be fit using a scattering rate  $\sim 18\%$  of the original rate from Costato and Reggiani [76,77], which is labeled as Set 3 in Figure 5.9. The results are depicted in Figure 5.12. The ionization threshold energy for the heavy and light hole bands is 1.40 eV, while the  $p$  factor is 0.10 in the heavy hole band and 1.00 in the light hole band. The impact ionization mechanism is multivalued within the split-off band;  $p$  is given as  $1.0 \times 10^5$  for states near the gamma point, and 0.20 for states at higher energies away from the gamma point.

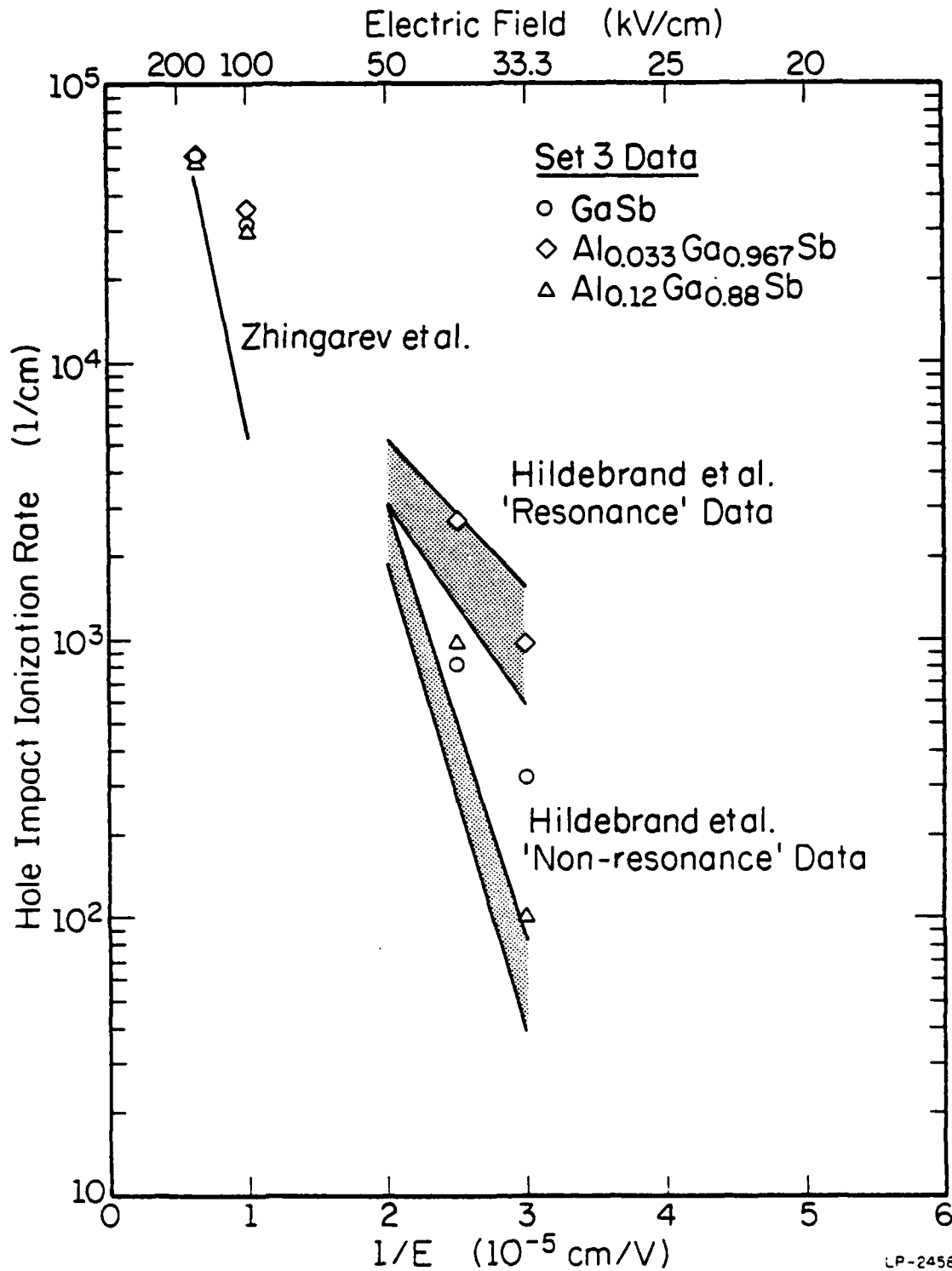


Fig. 5.12: Hole impact ionization rate in GaSb and in GaAlSb as a function of inverse applied electric field. The experimental data are from Hildebrand et al. [84,85] and Zhingarev et al. [89,90]. The calculations are made with the Set 3 parameters and scattering rate as described in the text. The impact ionization formula is multivalued with a large  $p$  factor near the top of the split-off band.

## 5.6 Conclusions

It appears that the resonance in the impact ionization rate can be explained if the hole-phonon scattering rate is very weak, much lower than that determined for GaAs and InP, and if the heavy and light hole impact ionization threshold energies are very high, 1.40 eV, twice the value of the band gap energy. In order to fit the experimental data of Hildebrand et al. [84,85], the impact ionization process must be dominated by holes in the split-off band. It is found that impact ionization of heavy holes cannot contribute by more than a few percent. Consequently, the suggestion of Kasemset [88] that the resonance is a band structure effect does not seem to be consistent with our simulation since he proposes that the heavy holes are the dominant ionizing agents when the resonance is not present (as in GaSb). We must conclude, therefore, that the only way in which the experimental data of Hildebrand et al. [84,85] can be fit is if the vast majority of holes impact ionize from the split-off band and if the impact ionization mechanism itself shows resonance behavior.

It is possible that there is yet another explanation of the data presented by Hildebrand et al. [84,85]. Instead of a k-space resonance, the enhanced impact ionization rate in the alloy can be due to a real space effect. Clustering in the alloy can lead to local high fields which can accelerate the hole to high energies and cause impact ionization. Further experimental measurements are necessary in order to determine beyond any doubt which model is correct.

## 6. TRANSIENT ELECTRONIC TRANSPORT THEORY

### 6.1. Introduction

Much attention has been given lately to devices based upon collision-free or near-collision-free transport [93-98]. High energy injection has been shown to increase substantially the achievable electron velocities [15] and new device geometries have been proposed for its realization [99-100]. The recent work by Tang and Hess [15] investigated in detail the average drift velocities and scattering events following high energy injection in GaAs using a Monte Carlo simulation method. They have concluded that a small "collision-free window" (CFW) exists in GaAs with respect to parameters such as electric field, injection energy, external voltage, and device dimensions. Certain regions of devices, particularly the emitter-base or source region, can be operated within the CFW and will exhibit very high average drift velocities. Regions which exhibit a high voltage drop (collector or drain in common FET's) are outside the CFW and will form a bottleneck in high speed operation. In the case of GaAs, this means that all voltages typically have to stay below 0.3 V if collision-free transport is expected in all device regions.

Recently, InP has also been suggested as a likely (and maybe even more promising) candidate for novel device applications. In spite of great difficulties in the fabrication and tailoring of this material, there are theoretical indications that InP will outperform other compounds, specifically GaAs, due to the large energy separation between the central and satellite valleys and due to the different surface properties.

The research performed by Tang and Hess [15] investigated the transient behavior of electrons injected into GaAs at high energies and accelerated by constant electric fields via a Monte Carlo approach. They have shown that high transient velocities for electrons injected at high energies persist in GaAs over a typical length of  $1000 \text{ \AA}$ , provided that the external fields do not accelerate the electrons to energies far above the satellite valley minima. One of their principal conclusions is that the high electron velocities are due to those electrons that escape intervalley scattering processes.

In this Chapter, the same physical model will be applied to electronic transport in InP, InAs, and heterostructures. Again, we use a complete band structure based on the pseudopotential calculation as discussed in Chapter 3. The electron is injected into the various materials of interest, where it is then accelerated (decelerated) by a constant electric field. In Chapter 7, transient hole transport will be discussed using the same physical model as presented here.

## 6.2 Basic Computational Method

The most essential difference between the computational method discussed in Chapters 3, 4 and 5 and the method that is discussed here is that in a steady state analysis the results are time independent. The initial condition of the carrier is arbitrary; the results should not depend upon the specified initial conditions in a steady state calculation. Conversely, in a transient analysis the results depend immensely upon the initial and other boundary conditions. The transient method is better adapted to modeling transport in the submicron regime because of its sensitivity to time dependent phenomena.

The Monte Carlo program used in the calculations is very similar to the program used in the steady state calculations. The electron-phonon scattering rates used are exactly the same as those presented earlier in Chapter 3, and the transport parameters are the same as those presented in Appendix 2. The primary difference in the mechanics of the calculation is that the trajectory of the electron must be traced in real space as well as in  $k$ -space. In all of the calculations we accumulate one dimensional transport quantities in real space. The initial conditions of the electron, particularly its energy and momentum, are specified at the beginning of the simulation. The assumption of ergodicity, crucial in a steady state simulation, no longer applies in a transient simulation. Instead, an ensemble of electrons must be studied. The particular scheme used here involves launching one electron, tracing its history as it moves through the device, and then returning to relaunch another electron. The simulation continues until a sufficient number of carriers are studied and the relevant transport quantities are determined. In the calculations presented here, roughly 1500 to 2000 electrons are launched. According to Glisson et al. [101], this should yield an accuracy of  $\sim 10\%$  for each measured quantity.

It is desired to evaluate the progress of the electron as it moves through the device. Quantities such as the drift velocity, average number of scatterings, average energy, etc. must be determined as a function of either time of flight or of distance traveled in real space. In all of the work reported here, the carrier's progress is monitored as a function of real space distance. In most of the calculations, the methodology for determining the velocity as a function of  $x$  is based on an examination of the electron behavior at different planes along the  $x$ -axis. We subdivide the length of

the device into a series of planes and examine the electrons as they cross each plane. This corresponds physically to taking a "snapshot" of the motion of the electrons at a certain point in real space. As an electron crosses a plane at a given device length, we treat it as if it had been swept out. Thus, we are modeling a progressively growing device and the drift velocity calculated at each plane is that corresponding to a device of the length up to that point. Another study, including backscattering at the end of the device, has also been performed. The full details of each of these methods is presented in Appendix 1.

### 6.3 Transport in GaAs, InP, and InAs

High applied fields can produce velocity overshoot over small distances by driving the electrons to velocities above the corresponding steady state velocity. Figure 6.1 shows the transient electron velocity in GaAs as a function of distance for various applied fields at zero launching energy. At low applied fields, 1 kV/cm, the velocity does not overshoot the steady state value by a large amount. Not much is gained in the average speed of the carriers over that for the steady state at low fields and low injection energy. As the field is increased, the velocity overshoots the steady state significantly. This can be seen for GaAs at fields of 10 and 30 kV/cm. The electron transit time at these fields will be substantially reduced by the overshoot from that for electrons at the steady state velocity. However as the applied field is increased more, the overshoot dramatically decreases due to the transferred electron effect. Owing to the large density of states within the satellite valleys, upon transferring, the electron drift velocity decreases sharply. Clearly there is only a limited range of applied fields that will lead to substantial velocity overshoot through a

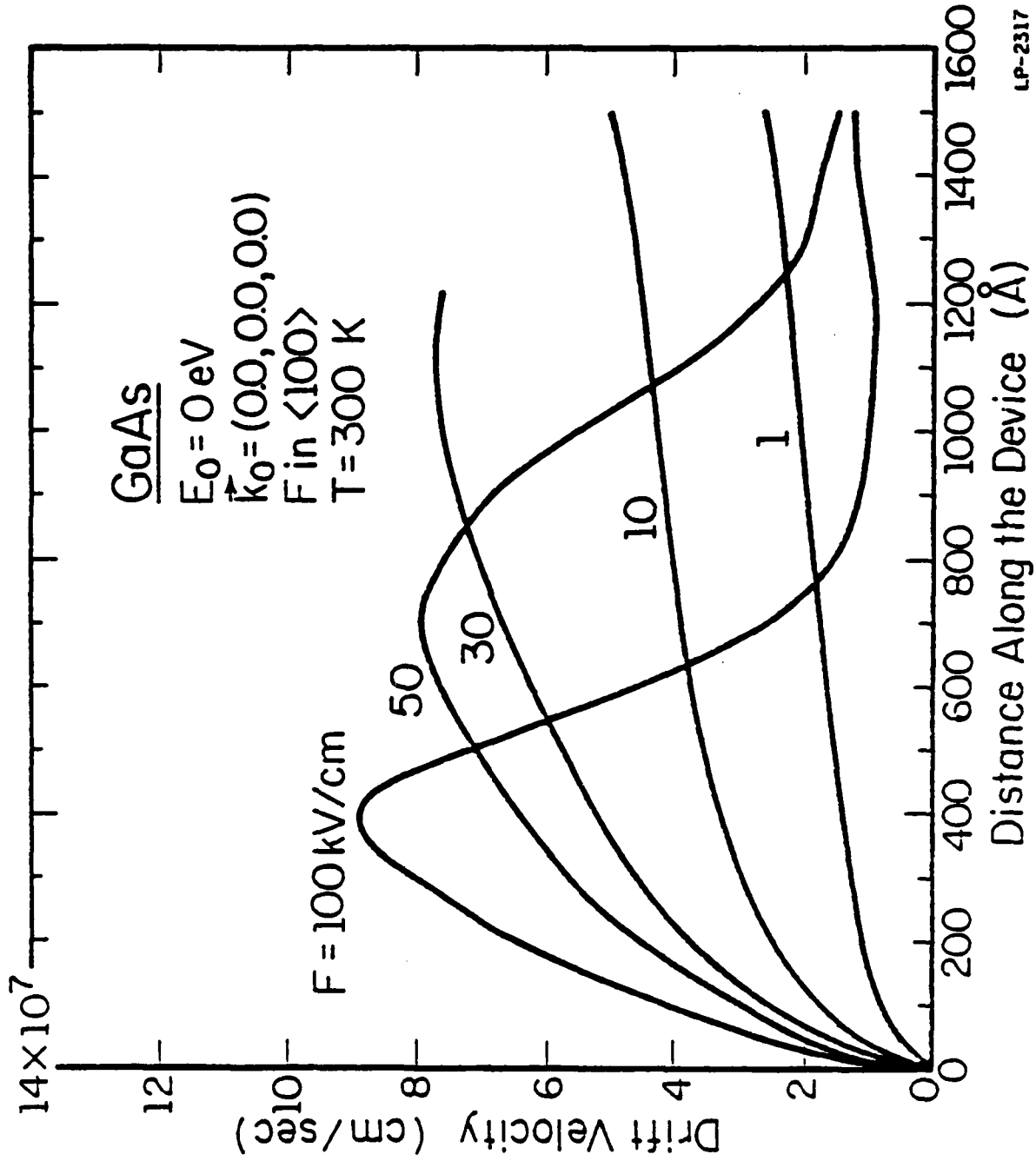


Fig. 6.1: Average electron drift velocity versus device length for various fields in GaAs at zero launching energy and 300 K.

range of 1000-1500 Å in GaAs.

Since the valley separation energy is greater in InP, it is expected that velocity overshoot can be attained at higher applied fields than in GaAs. Figure 6.2 illustrates the electron drift velocity as a function of distance in InP for various fields at zero launching energy. As is readily seen from the figure, high drift velocities are maintained over long distances at higher applied fields in InP. Devices made of InP can be operated then at greater applied voltages and still show velocity overshoot.

Velocity overshoot can be accomplished in a different way by launching the electrons at energies above the gamma point. High energy injection at various energies is possible using heterobarriers with different band edge discontinuities. In this way, the electrons start with velocities much larger than the steady state drift velocity. Figure 6.3 shows the electron velocity as a function of distance for various launching energies in GaAs at an applied field of 10 kV/cm. At zero and low launching energies the overshoot is very small and little is gained from the steady state. If the electrons are launched at energies above or near the intervalley threshold, the electrons can be easily accelerated to energies where they will transfer to the satellite valleys. This results in a sharp drop in the velocity and there is no gain from the overshoot. In GaAs the window of launching energies that gives rise to high drift velocities over distances of 1000-1500 Å is from 0.1-0.3 eV.

In InP the range of launching energies which result in a high drift velocity throughout device lengths of 1000-1500 Å is greater than in GaAs as seen in Figure 6.4. Again, at low energy injection the overshoot of the drift velocity is minimal. The overshoot is appreciable at launching

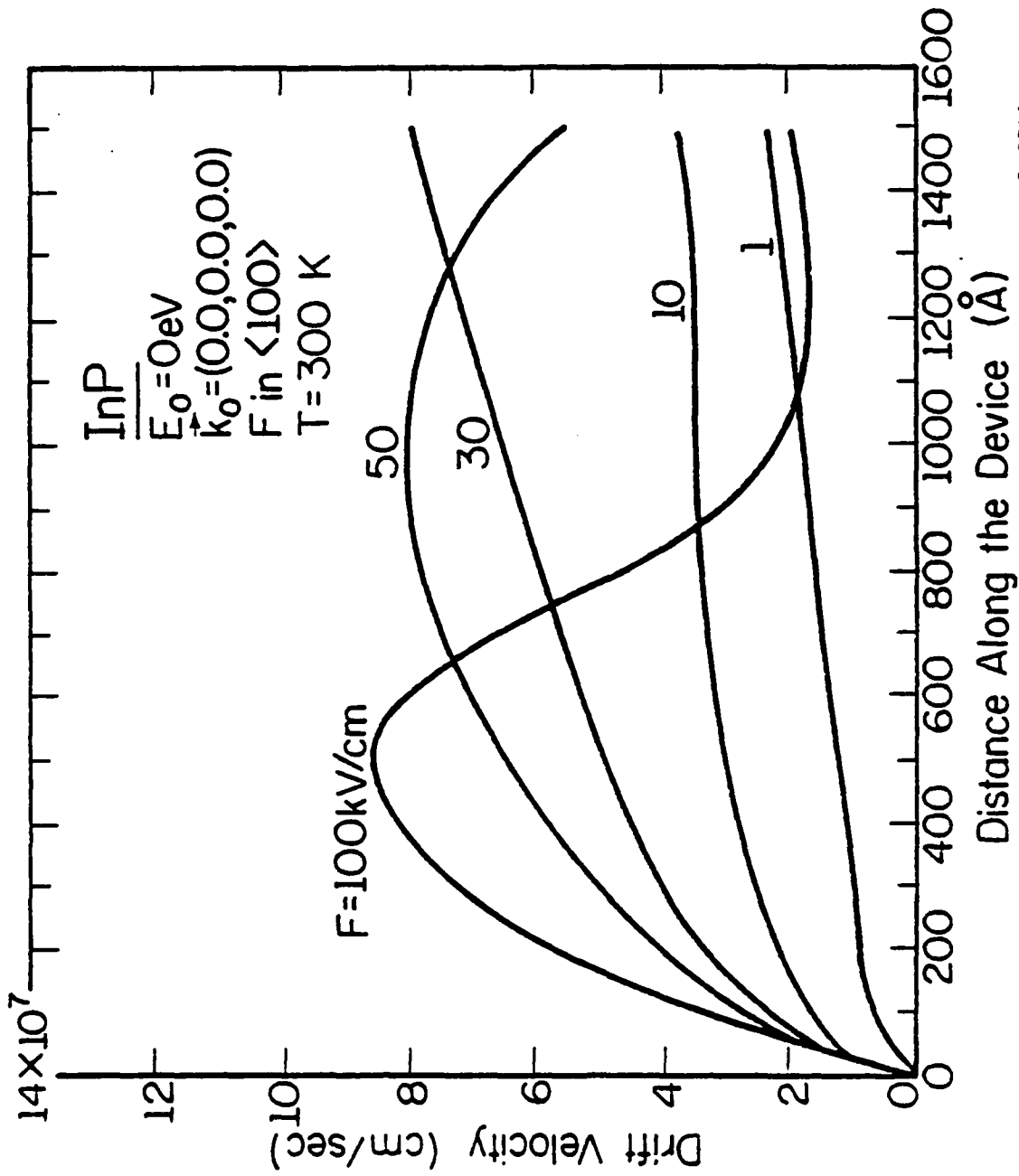
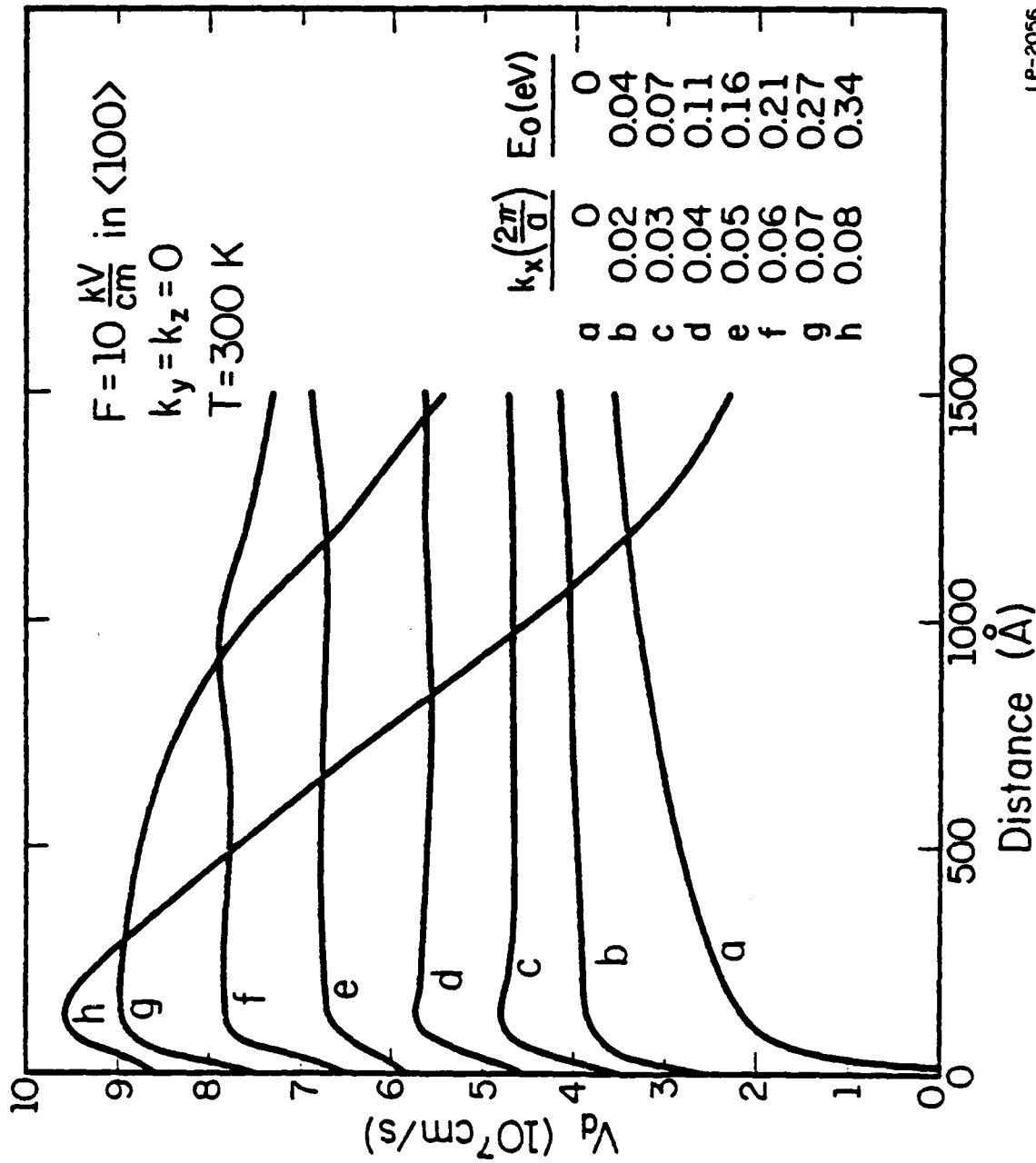


Fig. 6.2: Average electron drift velocity versus device length for various fields in InP at zero launching energy and 300 K.



LP-2056

Fig. 6.3: Average electron drift velocity versus device length with the launching energy as a parameter in GaAs for an applied field of 10 kV/cm and 300 K.

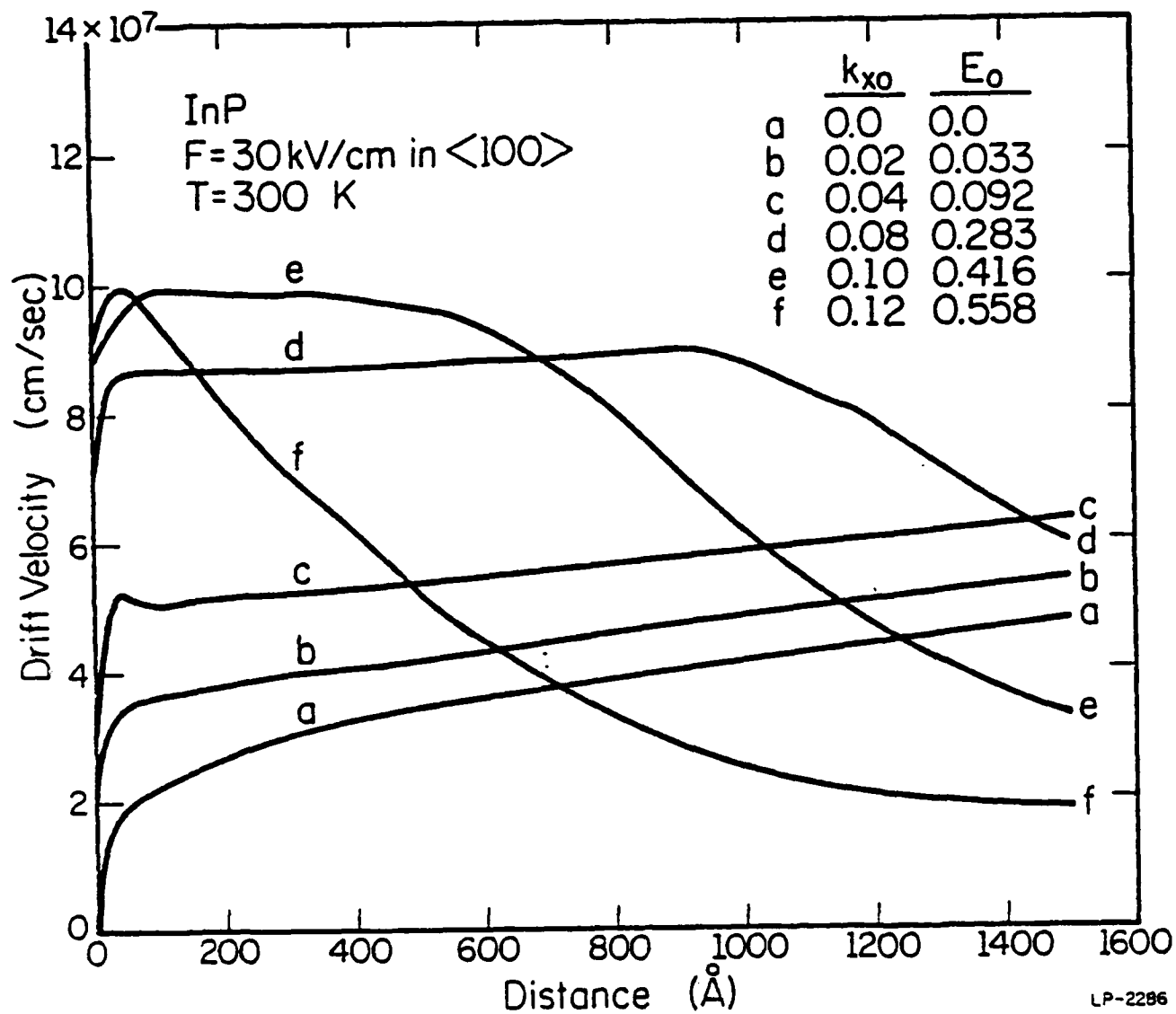


Fig. 6.4: Average electron drift velocity versus device length with the launching energy as a parameter in InP for an applied field of 30 kV/cm and 300 K.

energies from 0.1-0.5 eV in InP. At launching energies above 0.5 eV the electrons are easily transferred to the satellite valleys and the drift velocity greatly diminishes. From the previous results we conclude that InP is better suited than GaAs for devices based on velocity overshoot.

The physical explanation for this velocity versus distance behavior exhibited in Figures 6.1-6.4 is simple. The electrons initially assume the small effective mass of the central, gamma valley, whereupon they are accelerated by the electric field in the forward direction. For modest injection energies and electric fields, electrons suffer little intervalley scattering; most electrons move up in energy with little or modest polar optical scattering in the central valley, thereby raising the ensemble average of the electron drift velocity. However, for injection energies approaching the L and X minima and strong electric fields, the electrons are promoted to the high effective-mass satellite X and L valleys. Strong intervalley scattering occurs which reduces the drift velocity of carriers after a relatively short transit distance.

Figure 6.5 shows the percentage of unscattered electrons as a function of electron transit distance in InP. Initially, more electrons are scattered at low fields; this situation reverses as the electrons move through the device. The electrons experiencing high fields encounter greater scattering than those in low fields due to the introduction of intervalley scattering at high energies. As seen from Figure 6.6, high field electrons in InP are scattered more frequently since intervalley scattering is much more probable than polar optical scattering.

The drift velocity in InAs is strongly affected by the presence of impact ionization as discussed in Chapter 3. When impact ionization occurs,

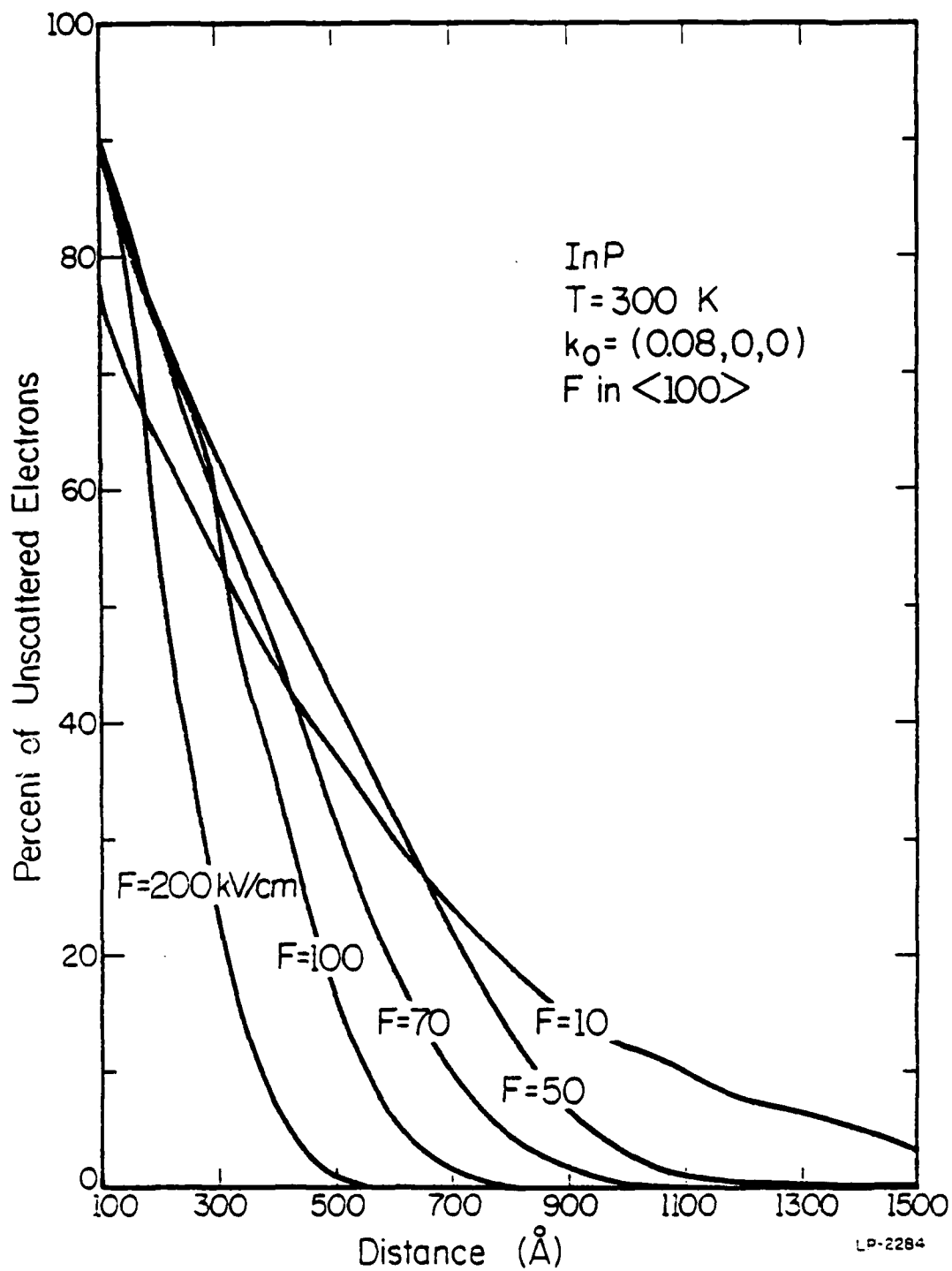


Fig. 6.5: The percentage of unscattered electrons as a function of device length with the electric field as a parameter.

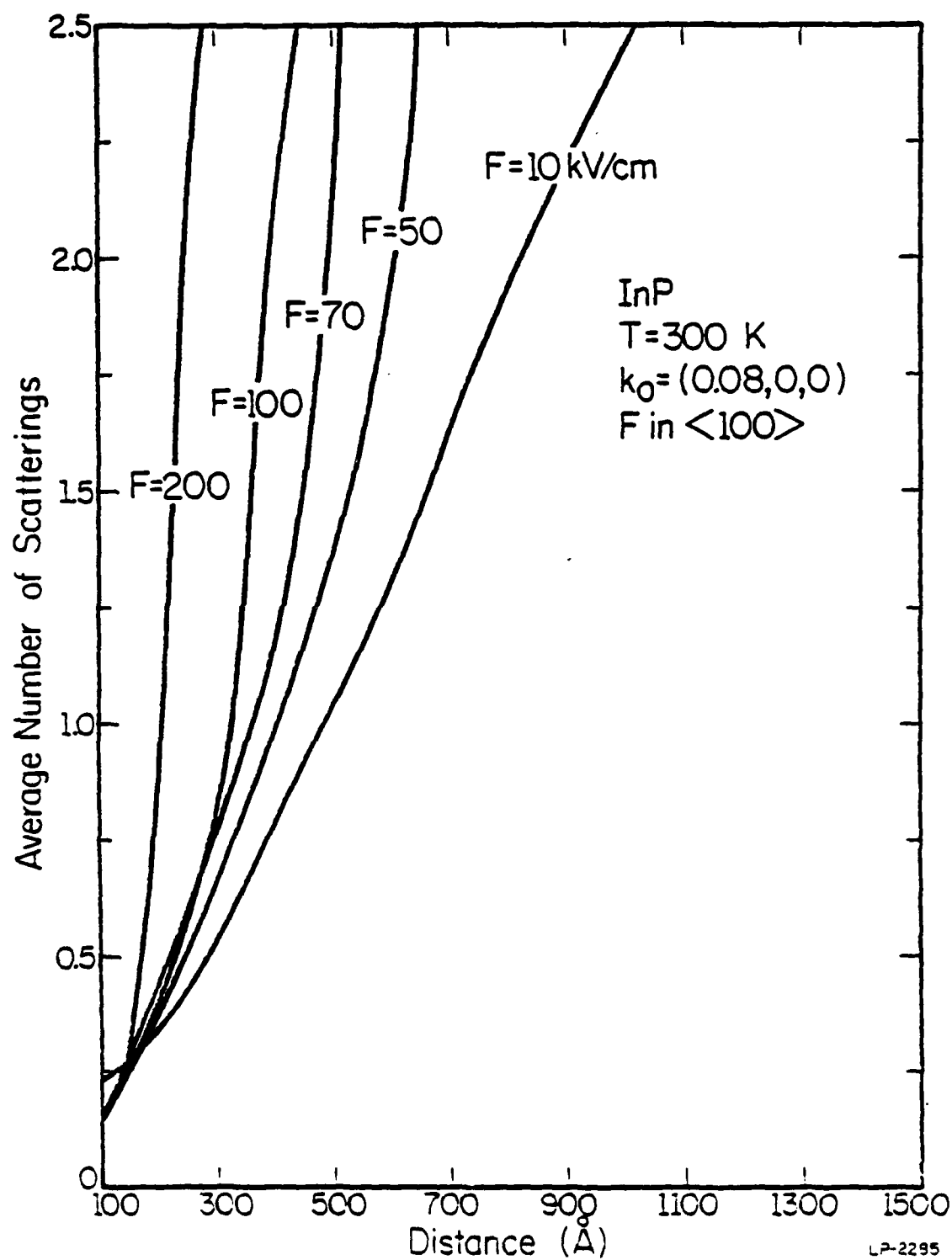
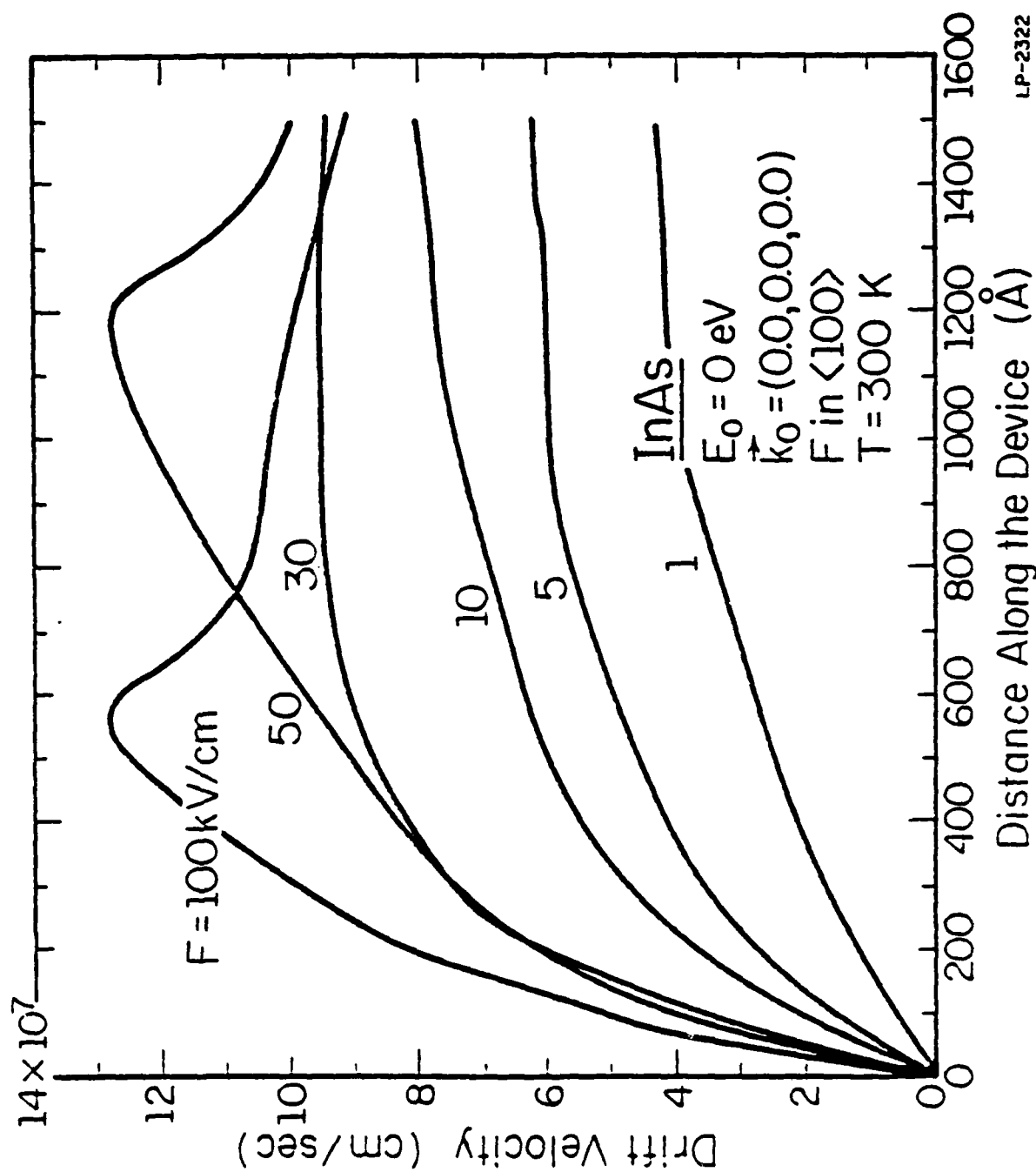


Fig. 6.6: The average number of scattering events as a function of device length with the electric field as a parameter.

very high steady state drift velocities are possible as we have seen. Figure 6.7 shows the transient electron drift velocity in InAs as a function of distance for various electric fields at zero launching energy and in the presence of impact ionization. Extremely high drift velocities are attained, greater than  $1.0 \times 10^8$  cm/sec, for most applied fields. Figures 6.8 and 6.9 show the effect of launching the electron at high energies. Notice that high velocities are attained throughout the entire structure for all the applied fields up until transfer becomes significant. Only at very high fields does transfer occur and the drift velocity is not lowered as drastically as it is in InP and GaAs. When impact ionization does not occur the behavior of the drift velocity is very different. Figure 6.10 shows the effect of neglecting impact ionization on the drift velocity following high energy injection. Transfer occurs readily for high applied fields and there is little significant overshoot in the drift velocity. InAs does not appear to be a promising material for high speed devices based upon velocity overshoot, since impact ionization is necessary in order to attain high drift velocities. This should be avoided in real device applications.

The previous results can be summarized by considering the carrier transit time through the entire structure for each of the three materials. The transit time as a function of applied field for electrons injected at zero energy is plotted in Figure 6.11. The transit time based on the steady state drift velocity of the electrons in InP is also plotted for comparison. As can be readily seen from Figure 6.11, there exists a range of applied fields in each of the three materials in which high speed transport is possible. The range of field values is very small in GaAs but is larger in InP. The electron transit time is extremely small in InAs over a very large



LP-2322

Fig. 6.7: Average electron drift velocity versus the device length for various applied fields in InAs at zero launching energy and 300 K. Impact ionization events occur.

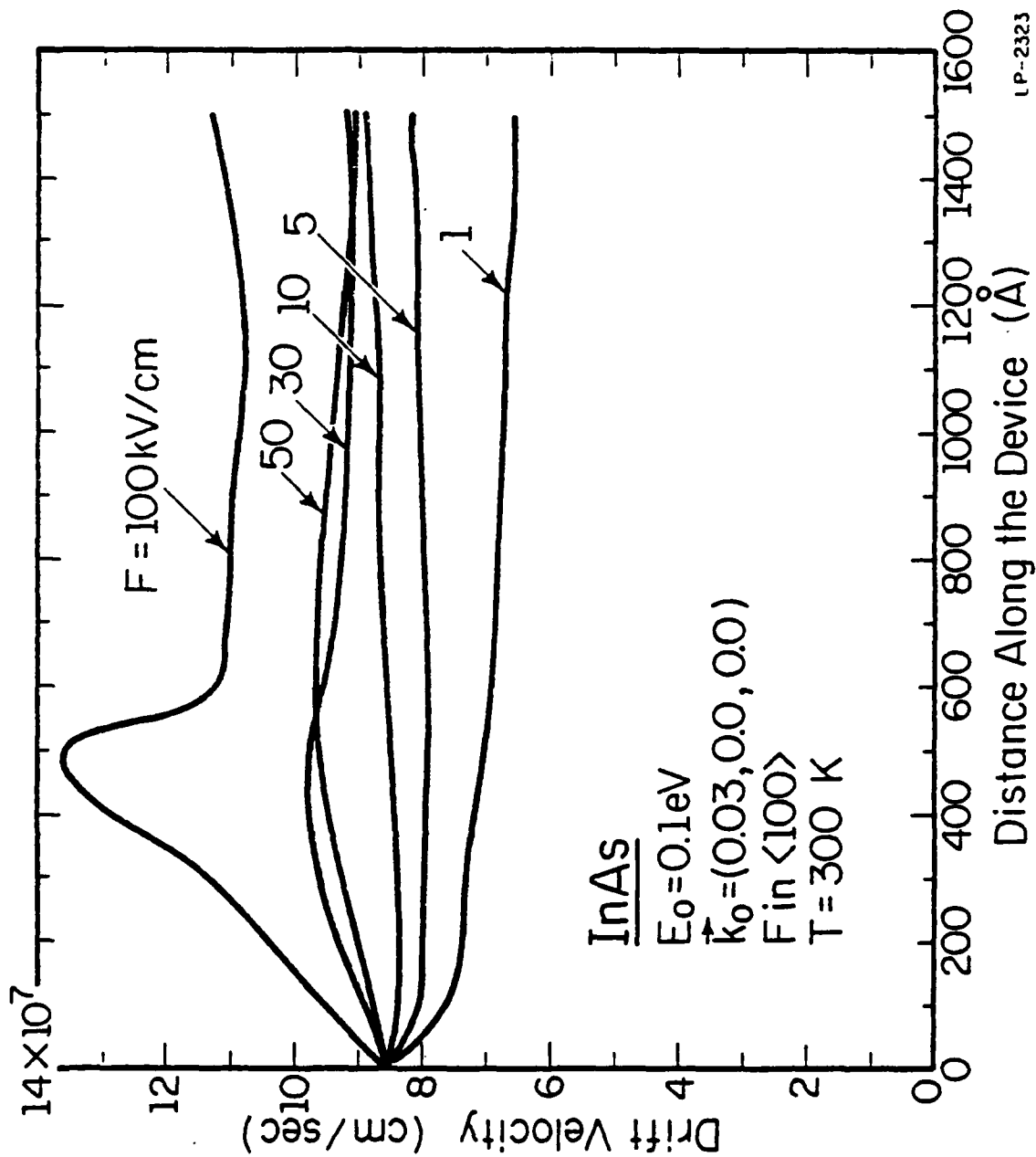
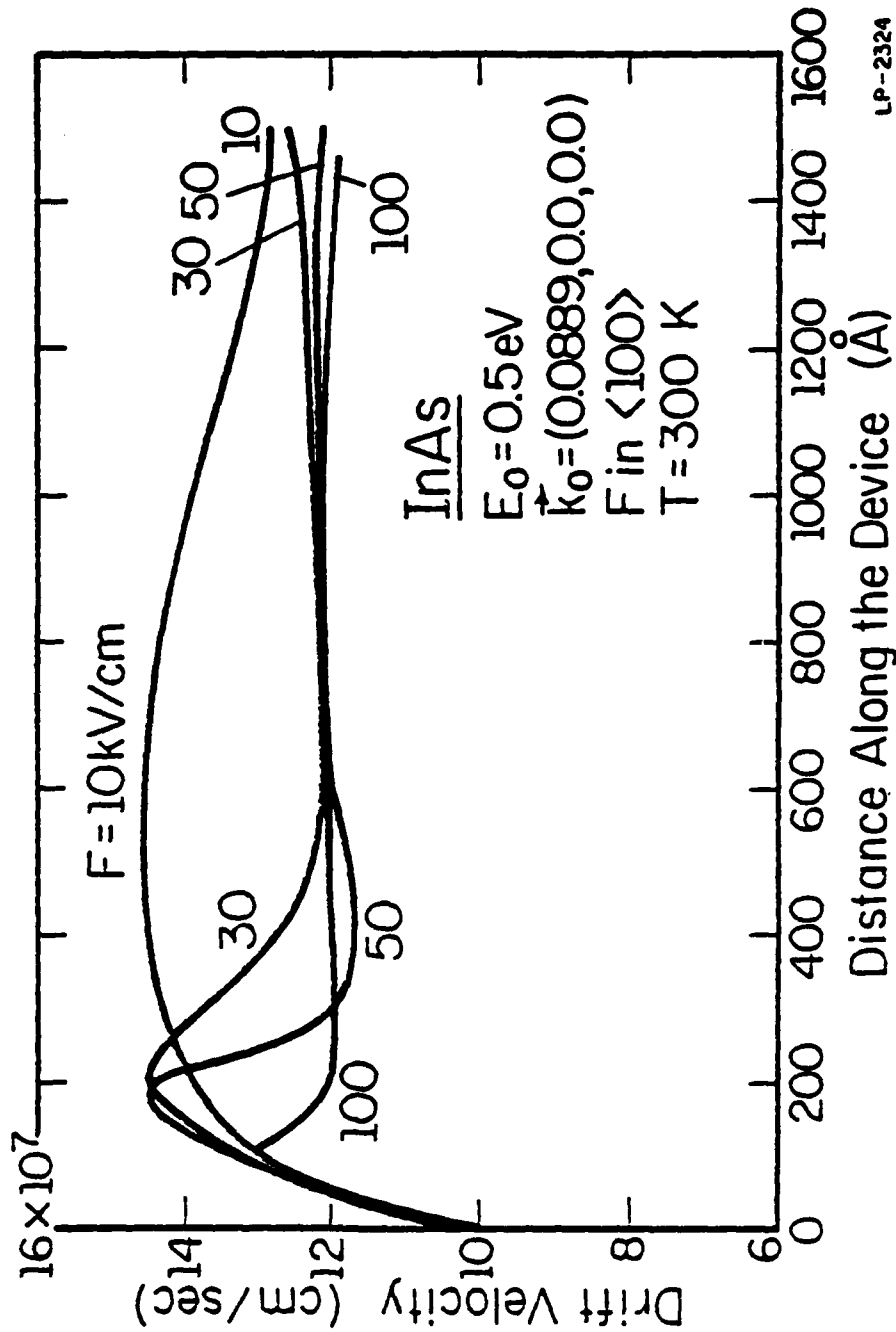
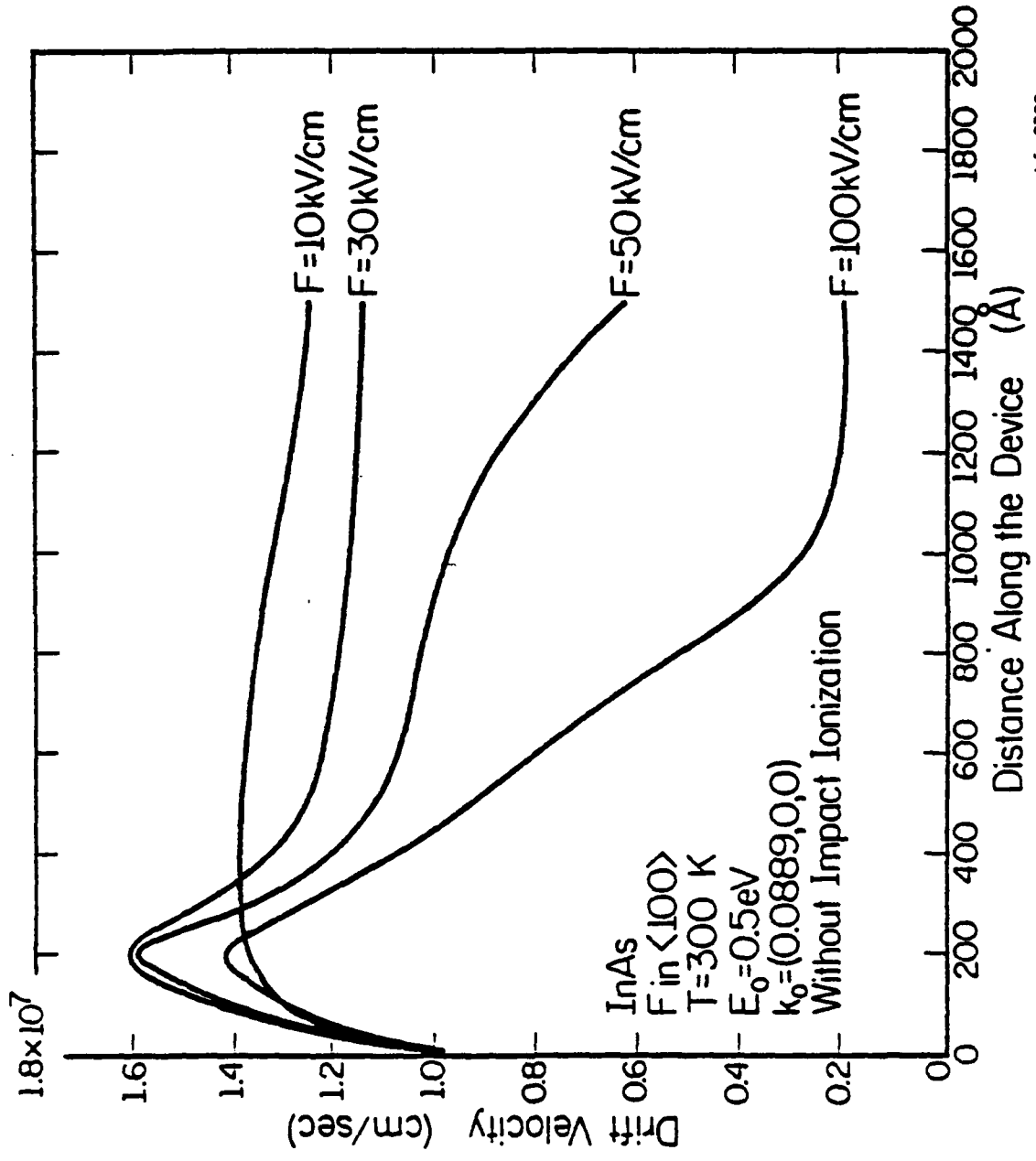


Fig. 6.8: Average electron drift velocity versus the device length for various applied fields in InAs at a launching energy of 0.1 eV and 300 K. Impact ionization events occur.



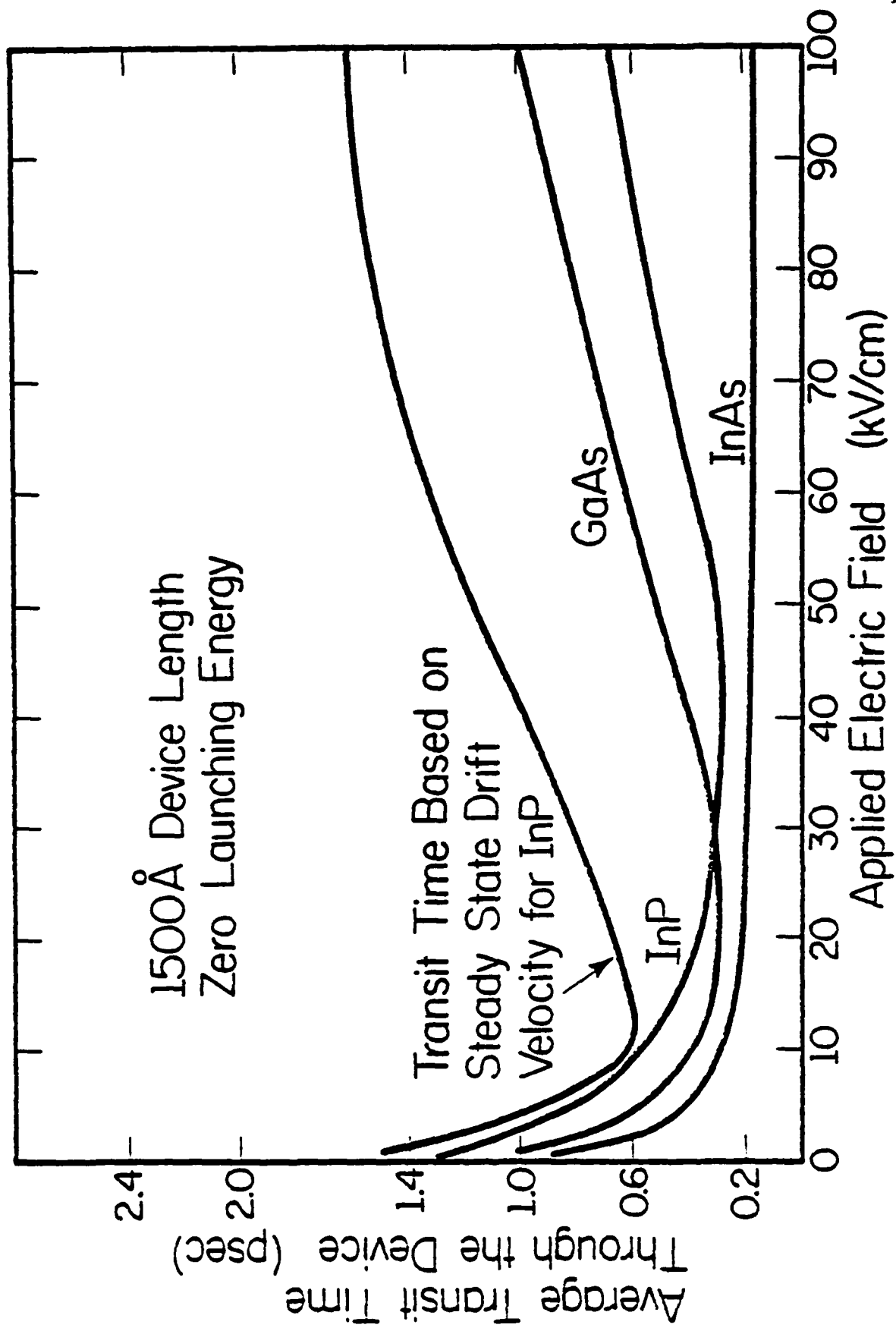
LP-2324

Fig. 6.9: Average electron drift velocity versus the device length for various applied fields in InAs at a launching energy of 0.5 eV and 300 K. Impact ionization events occur.



LI-2329

Fig. 6.10: Average electron drift velocity versus the device length for various applied fields in InAs at a launching energy of 0.5 eV and 300 K. Impact ionization events do not occur.



LP-2325

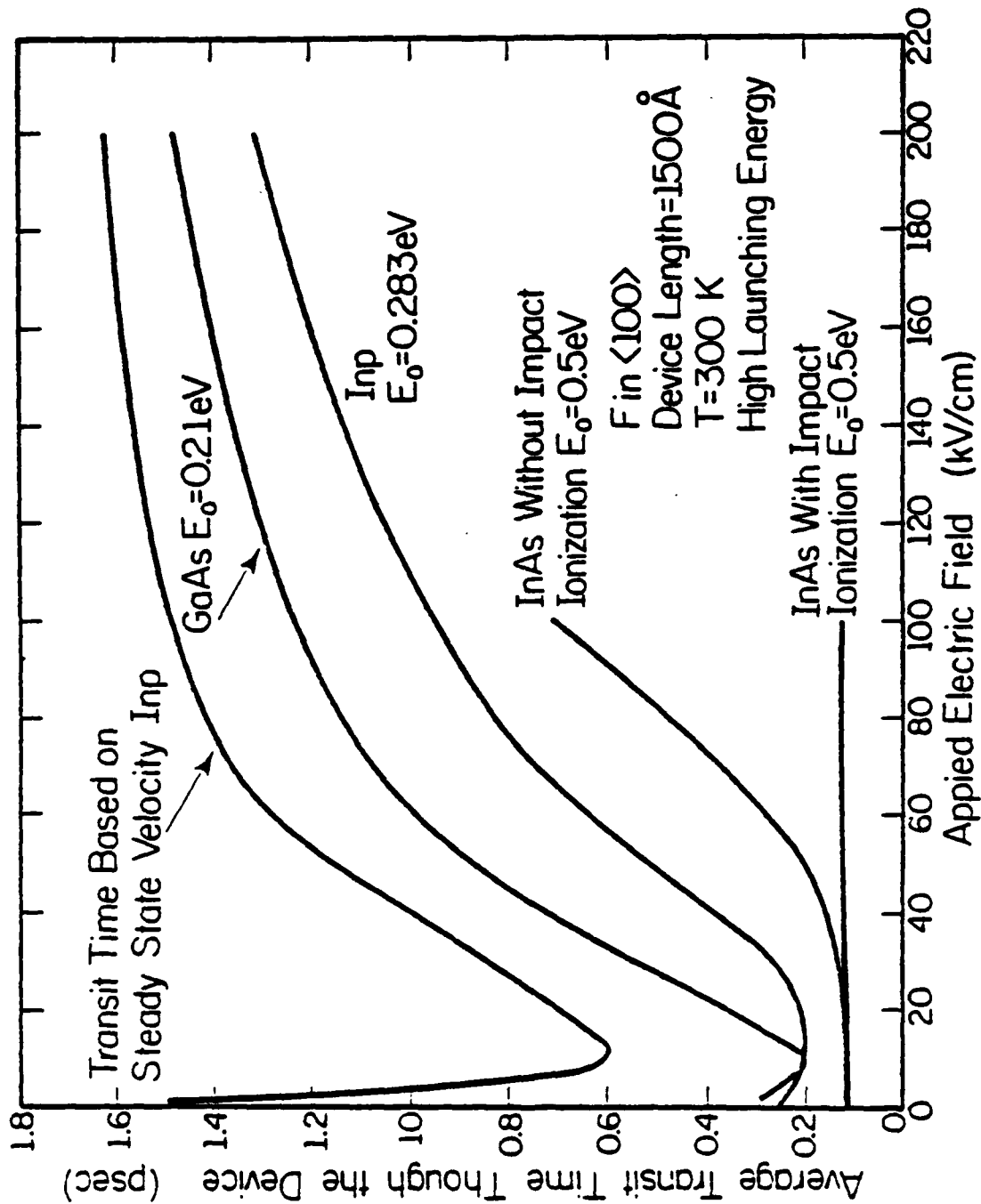
Fig. 6.11: Average electron transit time in psec through a device of 1500 Å as a function of applied electric field for GaAs, InP, and InAs at ze. launching energy and 300 K.

range of applied fields. However, this is true only when impact ionization occurs. Notice that there is very little improvement in the transit time over the steady state result for very low applied fields at zero launching energy. Even at higher fields the overshoot does not drastically improve the transit time of the electrons when they are launched at zero energy. Figure 6.12 shows the transit time as a function of applied field at high launching energy. Again the transit time for the steady state velocity is plotted for InP. The overshoot is more substantial at high launching energy and there is a fair improvement over the steady state transit time at low applied fields. However the gain is much less than an order of magnitude. The transit time in InAs is calculated with and without impact ionization. When impact ionization does not occur, the transit time increases substantially at high fields and the overshoot is minimal.

In device applications, in order for velocity overshoot to meaningfully influence operation speed, the entire structure will need to be on the order of  $1000 \text{ \AA}$ . The collecting region as well as the collecting contact can greatly influence the high speed behavior. The next section discusses the effect of the collecting contact upon the overall high speed behavior of the device. It is expected that the results presented above are an optimistic estimate of the effect of velocity overshoot.

#### 6.4 Effect of Collecting Contact

In the above calculations the effects of the collecting contact were eliminated by extending the device beyond the range of interest or by assuming an ideal sweep-out of the electrons. In a real device there exists a somewhat abrupt change at the semiconductor-contact interface. While the precise nature of this interface is not known, its behavior can be



LP-2328

Fig. 6.12: Average electron transit time in psec through a device of  $15000 \text{ \AA}$  as a function of applied electric field for GaAs, InP and InAs at high launching energy and  $300 \text{ K}$ .

approximated by a variable reflection coefficient (backscattering by the high density of ionized donors). We assume that any electron that is transmitted across the semiconductor-contact interface is swept out and cannot return to the device. Only as it crosses the interface can the electron be scattered back into the semiconductor. This can be considered ideal contact behavior.

In these calculations it is essential that a model that includes full backscattering at the end of the device is used. The full details are presented in Appendix 1. Using the bin model the net average drift velocity is the average over the entire ensemble of electrons. The velocity and time spent in each bin for a given electron are continuously recorded until the electron successfully passes through the device into the contact and is collected. In this way, we take into account the effects of backscattered electrons. Those electrons that are scattered all the way back to the initial starting point are reflected and recontinue their flight in the forward direction.

At the collecting contact, however, the electron may be transmitted or reflected. We select a random number between zero and one and compare this to a selected reflection coefficient. If the random number is greater than the reflection coefficient, the electron is transmitted into the contact and is collected. Otherwise, it is reflected back into the semiconductor.

Figure 6.13 shows the drift velocity versus distance through the device as a function of the reflection coefficient at an applied field of 10 kV/cm. The reflection coefficient varies from 0.0 to 0.70. A reflection coefficient of 0.0 implies that all of the electrons are swept out of the device at the contact interface. The electron drift velocity at the contact

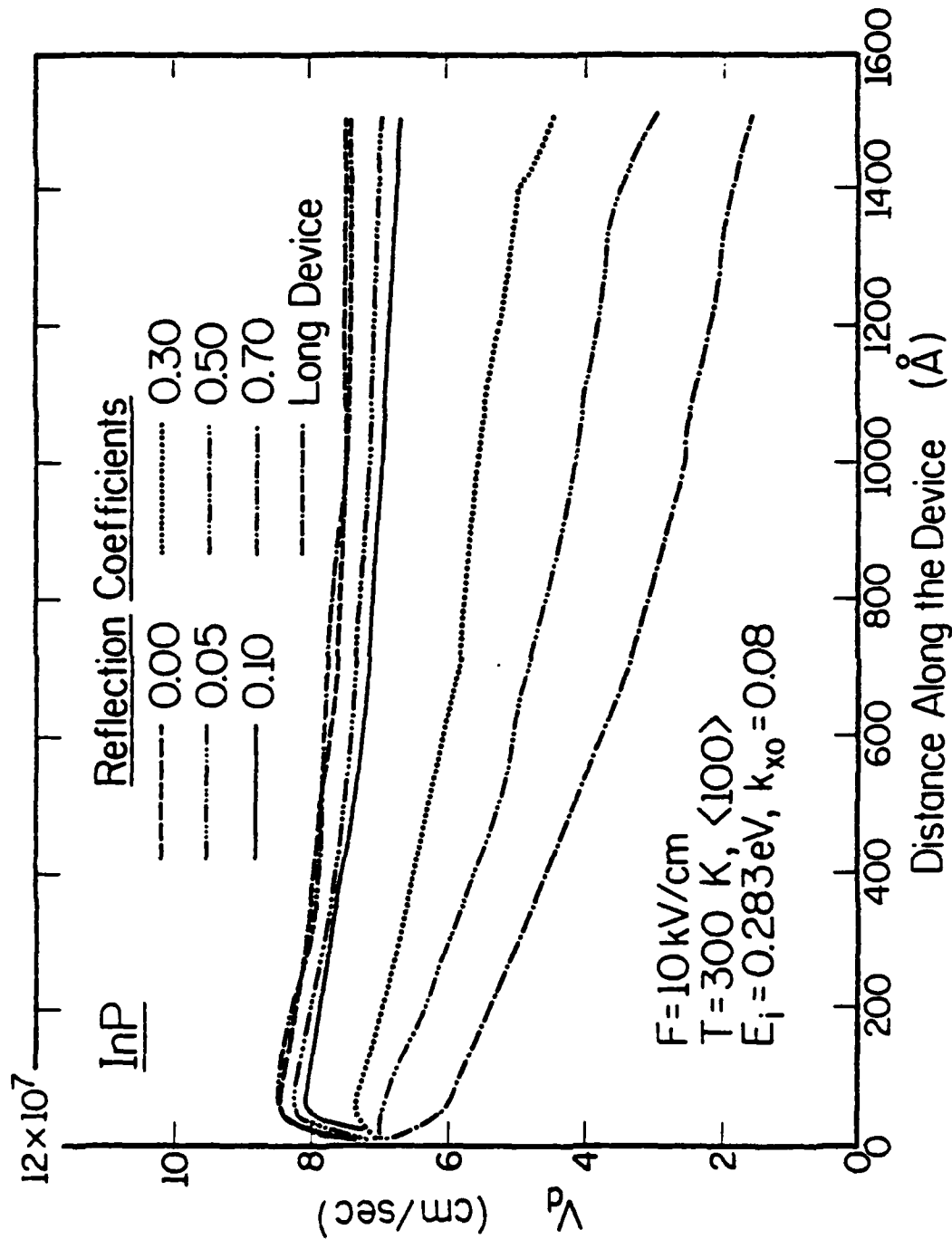


Fig. 6.13: Electron drift velocity as a function of distance along the device with the reflection coefficient as a parameter. The applied electric field is 10 kV/cm and the launching energy is 0.283 eV. The bottom-most curve corresponds to a reflection coefficient of 0.7. The result for the long device is very similar to that of  $R = 0.0$ , as can be seen from the top two curves. The long device is one that is extended beyond 1500 Å.

cannot be any faster than that of this case since there are no backscatterings present at the contact. As the reflection coefficient increases, the drift velocity throughout the entire device is seen to decrease substantially. At reflection coefficients of 0.30 and higher the drift velocity is reduced so much that the initial overshoot vanishes. This counteracts the otherwise possible high speed performance of the device. Curve g corresponds to the case of a long device, where the semiconductor structure is continued for an additional  $200 \text{ \AA}$  beyond the contact plane, which is identical to the completely swept-out case.

Figure 6.14 is similar to that of Figure 6.13 except that the applied field is  $30 \text{ kV/cm}$ . Again, we see that the drift velocity throughout the device is substantially lowered by increasing the reflection coefficient. Finally, Figure 6.15 shows these results at an applied field of  $70 \text{ kV/cm}$ . As can be seen the effect of the reflection at the contact is less drastic at higher applied fields. This can easily be understood in terms of the transfer mechanism in InP. At low fields the electrons remain in the central valley where the density of states is low, so the electron drift velocities are much higher. Therefore, upon reflection at the second contact the electrons will travel at a high velocity in the reverse direction. The only scattering agents they encounter within the central valley are polar optical phonons. Due to the focusing effect of polar optical scattering [17] the electrons are not scattered much from the field direction. Hence, they are decelerated by the applied field until they begin to drift again in the field direction. The overall speed of the ensemble is thus sharply reduced. At higher fields the electrons populate the satellite valleys where the density of states is much higher and their

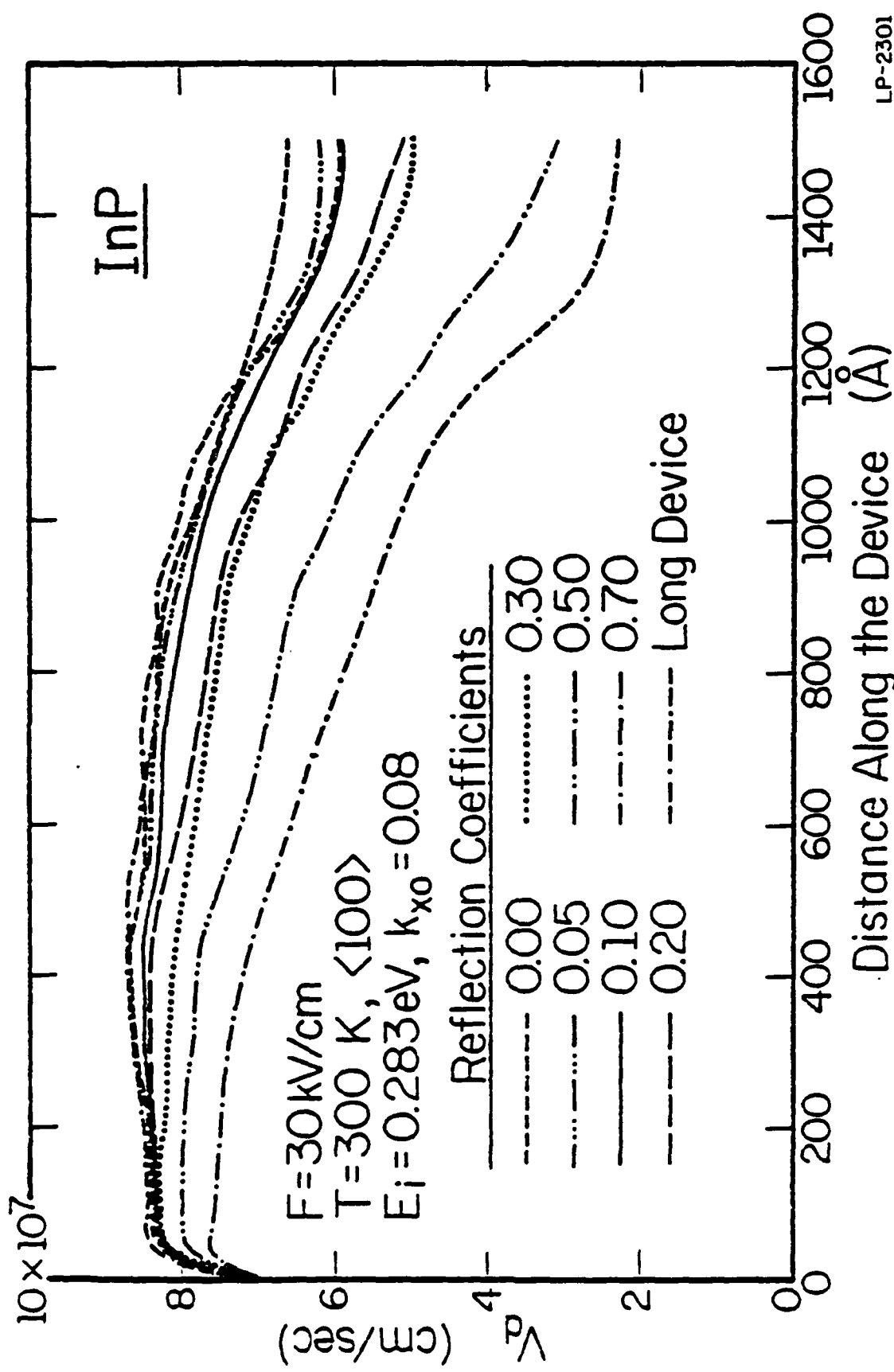


Fig. 6.14: Electron drift velocity as a function of distance along the device with the reflection coefficient as a parameter. The applied electric field is 30 kV/cm and the launching energy is 0.283 eV.



drift velocities are much lower. Upon reflection the electrons then travel at a lower velocity in the reverse direction. Within the satellite valleys the electrons encounter a rather high scattering rate due to intervalley scattering. Since intervalley scattering randomizes the electron  $k$  vector, the electron can be easily scattered back in the forward field direction. Therefore, the electrons will not travel as far back in the device before they resume their forward motion. Hence, the effect of the backscattering at the contact at high fields only influences the drift velocity near the end of the device. This can be seen from a comparison of Figures 6.13 and 6.15. At a high reflection coefficient the drift velocity over the entire range of the device is severely lowered at 10 kV/cm while at 70 kV/cm the only change in the drift velocity is near the very end of the device. The average velocity in this case, however, is always rather low.

Figure 6.16 shows the average transit time through the device as a function of electric field with the reflection coefficient as a parameter. For the case of no reflection at the contact (curve b) there is a marked minimum in the transit time at a field of 10 kV/cm. This minimum corresponds to the collision-free window discussed previously. As the reflection coefficient increases, the transit time increases drastically in this range until the curve partially flattens, smearing out the collision-free window.

We have shown that the behavior of the collecting contact greatly affects the average drift velocity of the electrons in a small device. The ensemble drift velocity is drastically reduced throughout the entire device at fields of 10-30 kV/cm in InP. Depending upon how large the reflection coefficient is at the collecting contact, the collision-free window can be

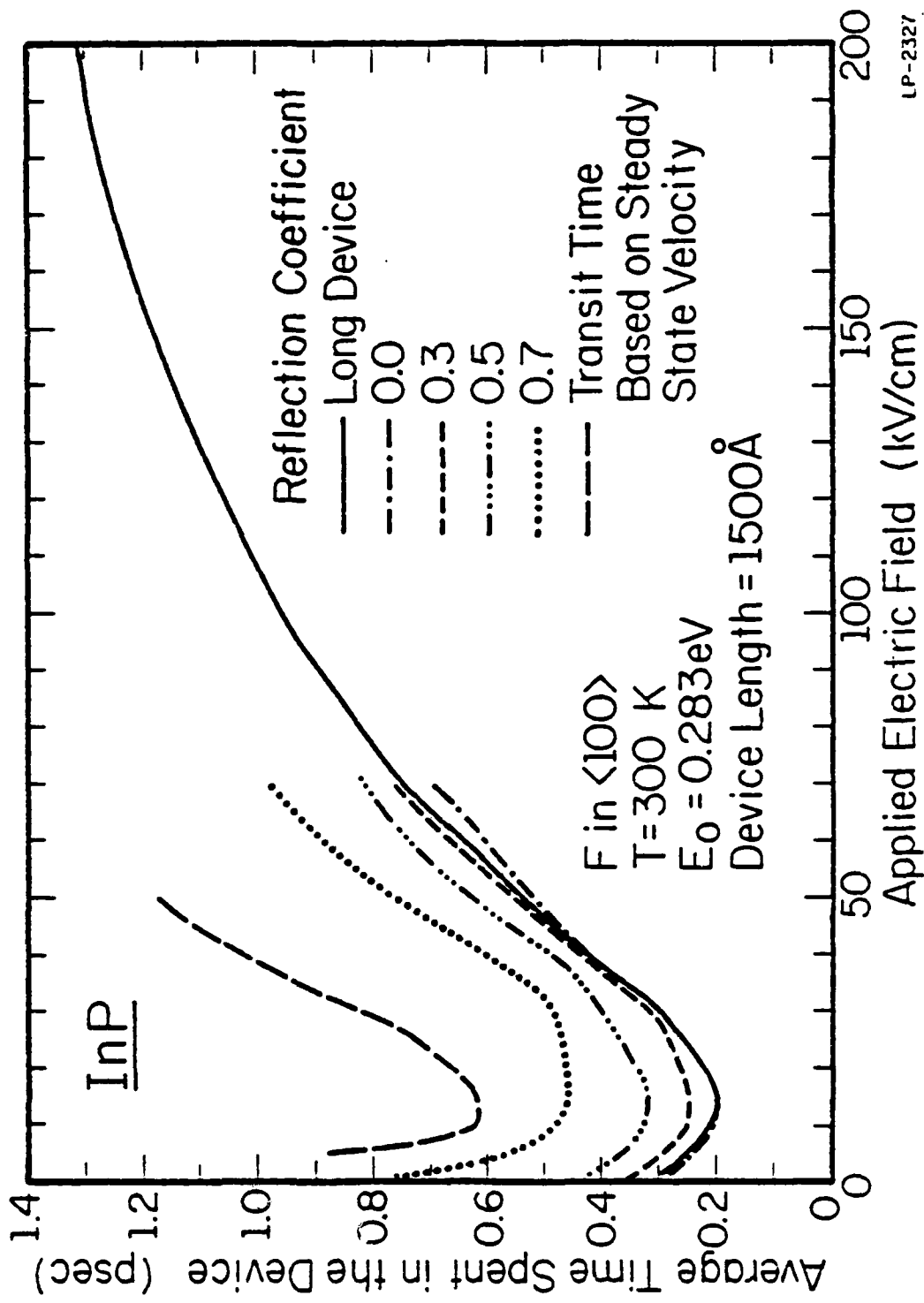


Fig. 6.16: Average electron transit time in psec through the device as a function of electric field with the reflection coefficient as a parameter.

smearred out. As the applied field increases, the effect of the contact is less important. However, the maximum drift velocities obtainable are much lower than at low fields. This suggests that the presence of a real collecting contact will drastically limit the performance of devices based on "near collision-free" (ballistic) transport.

### 6.5 Electronic Transport in Staircase Heterostructures

As discussed in Section 6.3, velocity overshoot is only substantial over fairly short distances, roughly  $1500 \text{ \AA}$ . As seen from the above calculations, the extent of the velocity overshoot is severely limited by both the initial conditions and the applied electric field. To be useful in a real device application, it is desirable that the carrier initially has a very large velocity and retains it all the way through a realistically long,  $\sim 0.5 \text{ \mu m}$  or more in length, device. Recently, Cooper et al. [102] have proposed a repeated step-like structure which enhances the velocity through repeated overshoot. In this chapter, we will discuss an alternative approach using staircase heterostructures which can produce extended velocity overshoot over distances of  $0.5 \text{ \mu m}$  or more.

In Section 6.3, we showed that impact ionization in InAs limits the electron's kinetic energy such that it stays within the gamma valley throughout a length of  $1500 \text{ \AA}$  or more. Since the energy gap is very small,  $\sim 0.40 \text{ eV}$ , and the satellite valley separation energies are much larger,  $> 1.0 \text{ eV}$ , impact ionization occurs more readily than intervalley transfer. The electrons gain energy from the field until they reach the threshold for impact ionization whereupon they ionize and lose most of their kinetic energy. In this way, the electrons are prevented from transferring to the satellite valleys in InAs and the resulting average velocity is very high.

However, this is of little practical value since it is undesirable to have carrier multiplication in most device applications.

A similar effect can be achieved, however, if we let the electrons "climb" a step-like potential structure (introduced, e.g., by the band edge discontinuity of  $\text{Al}_x\text{Ga}_{1-x}\text{As}$ -GaAs layers) under the influence of an overlaid applied field [Fig.6.17]. After being launched from a high energy barrier the electrons are accelerated by an external electric field. They gain kinetic energy until they reach the first step. If the electrons have sufficient energy to climb the step, they cross over into the higher potential region where their kinetic energy is lowered by an amount equal to the potential of the step. They continue drifting in the applied field until they reach the next step where their kinetic energy is lowered again. The steps remove the excess kinetic energy obtained from the applied field such that the electrons remain within the gamma valley. This paradoxical effect appears to be similar in nature to the impact ionization effect and also to carrier cooling via the electron-hole interaction as proposed by Shah et al. [103].

We have calculated, using the Monte Carlo method described above, the velocity as a function of position and the average electron transit time through a structure of  $0.5 \mu\text{m}$  [Fig.6.17]. We selected an applied field of  $10.0 \text{ kV/cm}$  and a launching energy of  $0.20 \text{ eV}$  from a heterobarrier for all of the calculations since these parameters have been found to produce the fastest velocities in GaAs. The average electron transit time for electrons that climb the steps in a  $0.5 \mu\text{m}$  structure is  $0.93 \text{ psec}$ . This is equivalent to a velocity of  $5.4 \times 10^7 \text{ cm/sec}$ . We can compare this to the average transit time of electrons injected at the same energy and applied field but not

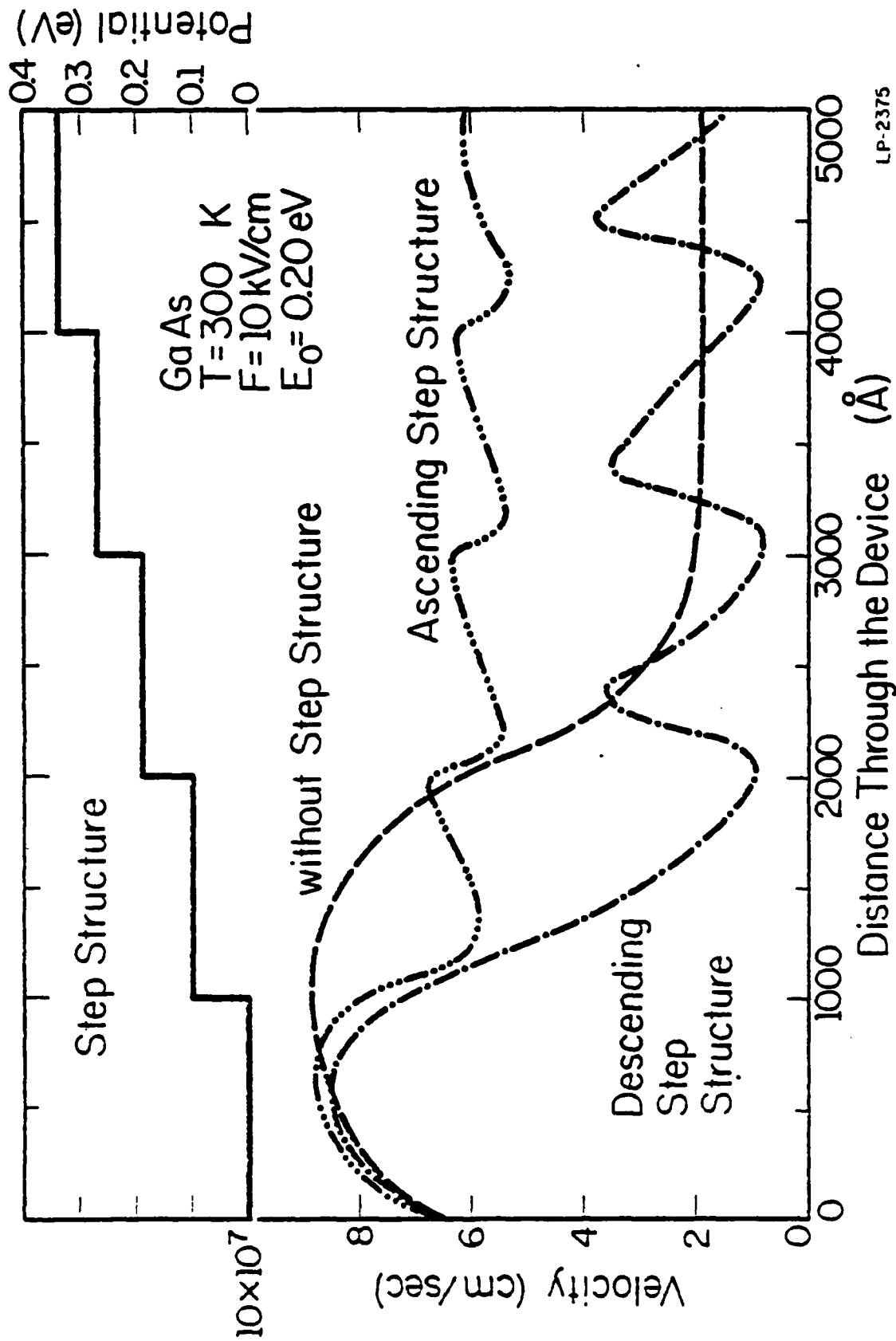
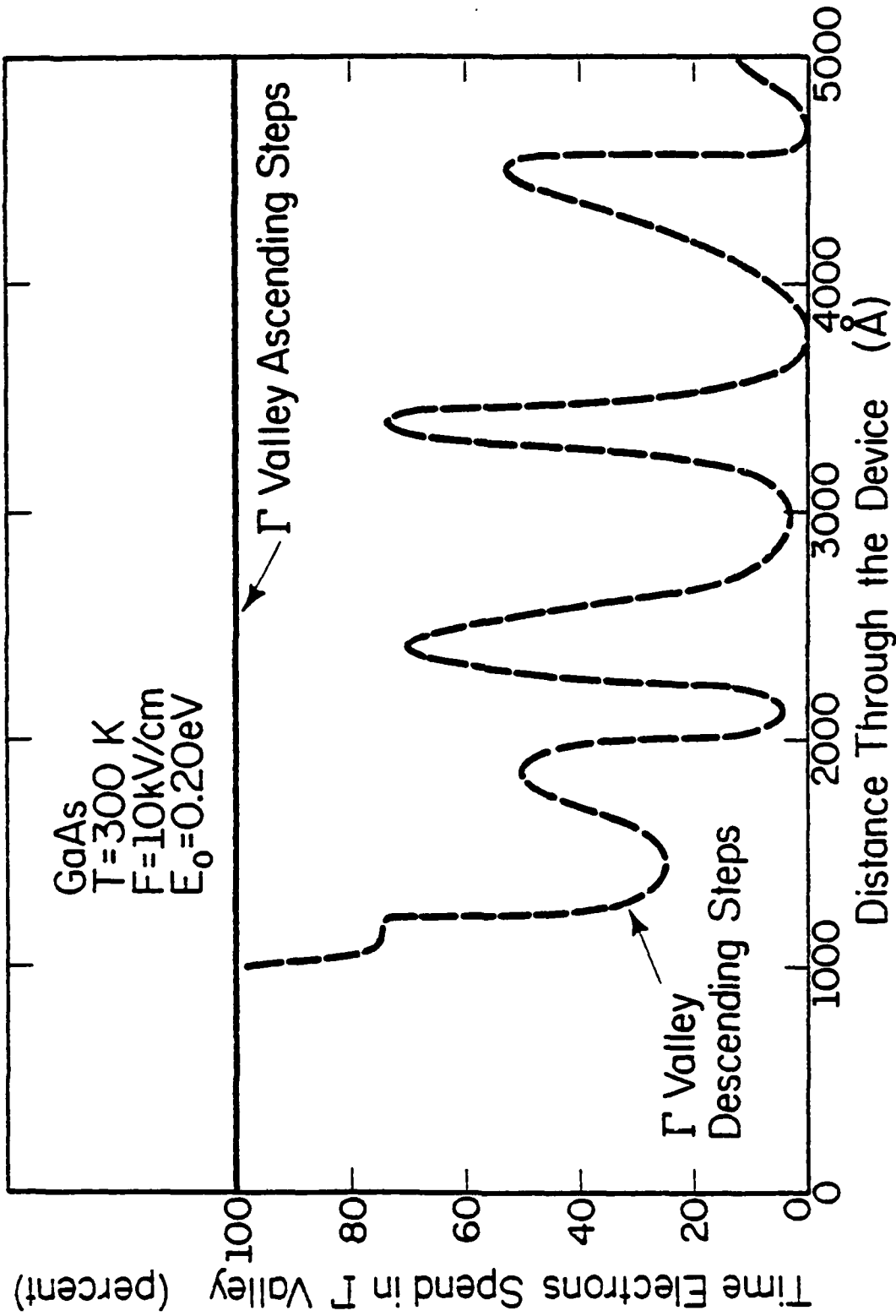


Fig. 6.17: Average electron drift velocity as a function of distance through the device for the three cases, "climbing" up the stairs, down the stairs, and no stairs present. The top part of the figure illustrates the step-like potential structure to scale.

subjected to the step-like potential. The transit time for these electrons is found to be 2.09 psec, giving an average velocity of  $2.4 \times 10^7$  cm/sec. Notice that the step-like structure results in a velocity enhancement by a factor greater than two. One can also launch the electrons such that they propagate "down" the stairs, similar to the suggestion of Cooper et al. [102]. For the given configuration and applied electric field this results in a much lower speed than if they are launched in the other direction. The reason for this is that the electrons gain kinetic energy as they traverse the steps but their velocity decreases due to the transferred electron effect. This can be clearly seen from Figure 6.18, where we show the relative population of the central valley as a function of distance through the structure for the two cases. Notice that the electrons always reside in the central valley when "climbing" the stairs (Case I) while when they propagate "downstairs" (Case II) most transfer to the L and X minima.

As can be seen from Fig. 6.17 the velocity of the electrons oscillates for Case II. If one compares these oscillations to those in Fig. 6.18 it is apparent that the velocity fluctuates because the electrons are transferred to the satellite minima and then relax back to the gamma valley. Some relax because an applied field of only 10.0 kV/cm is not high enough to heat the carriers such that they all transfer to the satellite minima and remain there.

As the length of the structure increases from 0.5  $\mu\text{m}$  to 1.0  $\mu\text{m}$ , the number of electrons which can successfully pass through the device (without reflections at the steps) decreases, since the electrons lose too much energy by phonon emission. It is desirable to transmit most of the electrons through the structure in order to achieve high current densities.



LP-2374

Fig. 6.18: Percent time the electrons spend in the gamma valley as a function of distance for the two cases, "climbing" up the stairs, and down the stairs.

For a 0.5  $\mu\text{m}$  length structure  $\sim 90\%$  of the electrons are transmitted at high speeds. For a length of 1.0  $\mu\text{m}$ , however,  $\sim 50\%$  of the electrons are reflected. Clearly one cannot build a very long structure of ascending steps without severely limiting the current. The average electron transit time in a 1.0  $\mu\text{m}$  structure is found to be 2.41 psec which gives an average velocity of  $4.15 \times 10^7$  cm/sec. This is roughly a factor of two greater than for a structure without steps, where the transit time is 4.72 psec and the velocity is  $2.1 \times 10^7$  cm/sec.

## 7. TRANSIENT HOLE TRANSPORT THEORY

As discussed in Chapter 6, under certain limited conditions of applied electric field and initial launching energy, velocity overshoot can be significant in compound semiconductors over distances of roughly  $1500 \text{ \AA}$ . The range over which velocity overshoot can be attained may be artificially lengthened by the method discussed in Chapter 6, Section 6.5. In this chapter, the effect of velocity overshoot on holes will be examined.

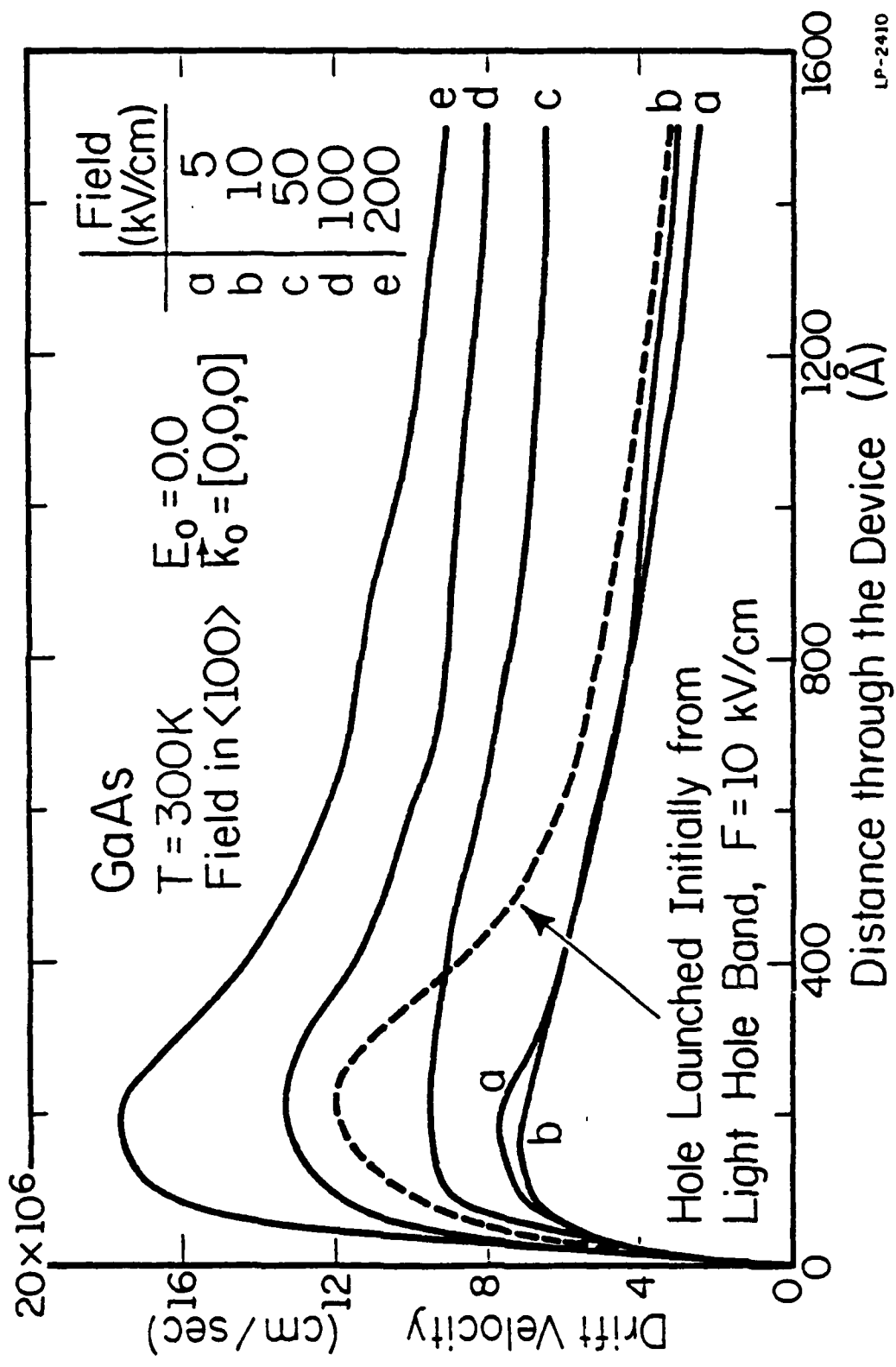
Ruch found that the electron velocity overshoots its saturation value in both silicon and gallium-arsenide [14]. However the velocity overshoot persists an order of magnitude longer in GaAs than in Si due in part to the much faster energy relaxation in Si at low energies. The electron drift velocity also is substantially higher in GaAs than in Si at low applied fields [44,104] because of the different effective masses of the electrons in each material. In GaAs, polar optical scattering is the dominant energy relaxation mechanism which on average is weaker than the deformation potential scattering present in Si. Therefore, it takes longer for the electron overshoot to relax in GaAs than in Si leading to much higher electron drift velocities over longer distances.

The presence of heavy holes and deformation potential scattering in the valence band of GaAs at low energy greatly reduces the hole velocities. Consequently, one would expect that velocity overshoot of holes would be limited by the strong energy relaxation much as it is in silicon. However, our calculations show that velocity overshoot of holes in GaAs is significant under certain conditions of field and launching energy. Velocity

overshoot of holes in GaAs is not as pronounced as that of electrons in GaAs but it is larger than for electrons in silicon as calculated by Ruch [44].

The calculations are made here using a Monte Carlo scheme similar to the program described in Chapter 4. Instead of a steady state simulation we use a transient model to analyze velocity overshoot of holes in the valence band. The velocity estimator is based on the plane model as discussed in Appendix 1. The hole-phonon scattering rates are calculated exactly the same as described in Chapter 4. The holes are launched at either zero launching energy, from the gamma point, or at 0.10 eV with a k vector of [0.09,0.0,0.0]. High energy injection may be achieved through use of heterostructures as described earlier in Chapter 6. In all of the calculations the field is along the  $\langle 100 \rangle$  direction.

Figure 7.1 shows the hole drift velocity as a function of device length for zero launching energy for various applied fields. At low applied fields, 5.0 and 10.0 kV/cm (curves a and b), the hole velocity at 1500 Å is substantially higher than the steady state drift velocity which is shown in Figure 4.13 of Chapter 4. Notice that, at zero launching energy, at an applied field of 10.0 kV/cm, the hole drift velocity is two times the steady state value. At smaller applied fields, 5.0 kV/cm, the transient drift velocity after 1500 Å is much higher than the steady state velocity, roughly three times as large. As the applied field increases in magnitude the peak drift velocity increases dramatically. At an applied field of 200.0 kV/cm the peak drift velocity is roughly  $1.8 \times 10^7$  cm/sec, more than twice the steady state velocity. However, the velocity decays much more rapidly towards the steady state value at higher fields. The overshoot is significant over a much smaller range and consequently is less advantageous



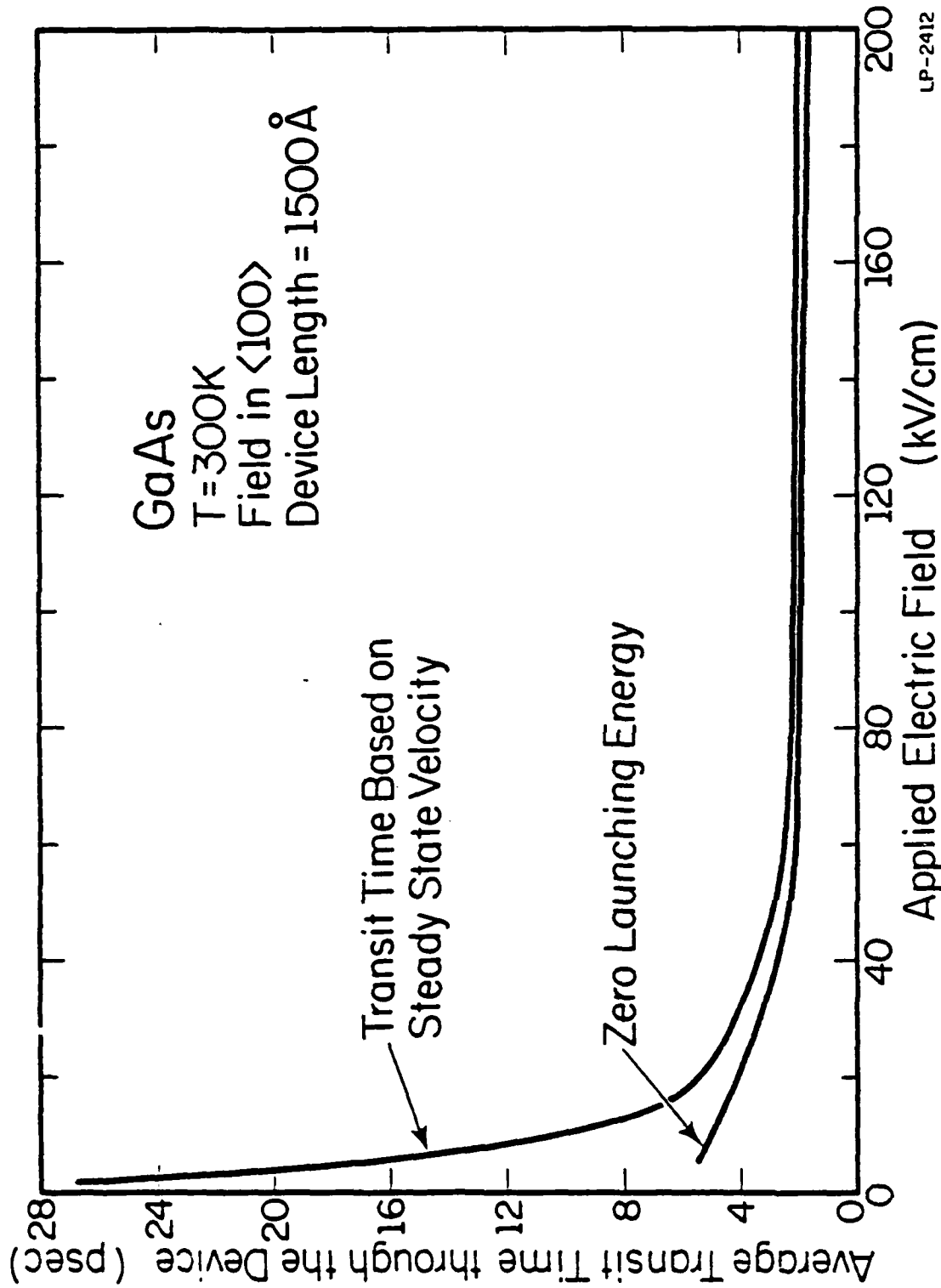
LP-2410

Fig. 7.1: Transient drift velocity of holes in the valence band of GaAs as a function of distance through the device with the applied field as a parameter. All of the holes are launched at zero energy from the gamma point in both the heavy and light hole bands.

for device applications. As seen from a comparison of Figures 7.1 and 4.13, after 1500 Å the hole velocity is only 20% greater than the steady state value. Figure 7.2 shows that the transit time is not significantly different at high applied fields from that due to carriers in steady state. However, the transit time is greatly reduced by the overshoot at lower electric fields of 10.0 and 5.0 kV/cm.

The effect of launching the hole from the light hole band initially is also depicted in Figure 7.1. As is readily seen, the extent of the velocity overshoot is greater when the holes originate in the light hole band than in the heavy hole band. This is expected since the effective mass of the light holes is much less than the effective mass of the heavy holes. The drift velocity approaches, after approximately 1000 Å, the result for the heavy holes. The strong deformation potential scattering tends to scatter the holes out of the light hole band and into the heavy hole band. Consequently, after a short time the vast majority of the holes reside within the heavy hole band.

The effect of launching the holes at a higher energy is shown in Figure 7.3. Holes are injected at an energy of 0.1 eV with an initial velocity of  $2.8 \times 10^7$  cm/sec. The initial velocity is so much greater than the steady state velocity that the holes immediately start to relax to the steady state value. Again the velocity overshoot persists over a longer distance at lower applied fields. From a comparison of Figures 7.1 and 7.3 it is clear that there is no significant gain in hole drift velocity from launching the holes at a higher energy. The results of the calculations show that at distances of 1000 Å the hole transit times are essentially independent of launching energy for the energy range considered.



LP-2412

Fig. 7.2: Average hole transit time in psec through a 1500 Å long device as a function of applied field for carriers launched at zero energy and compared to transit times based on the carrier steady state velocity.

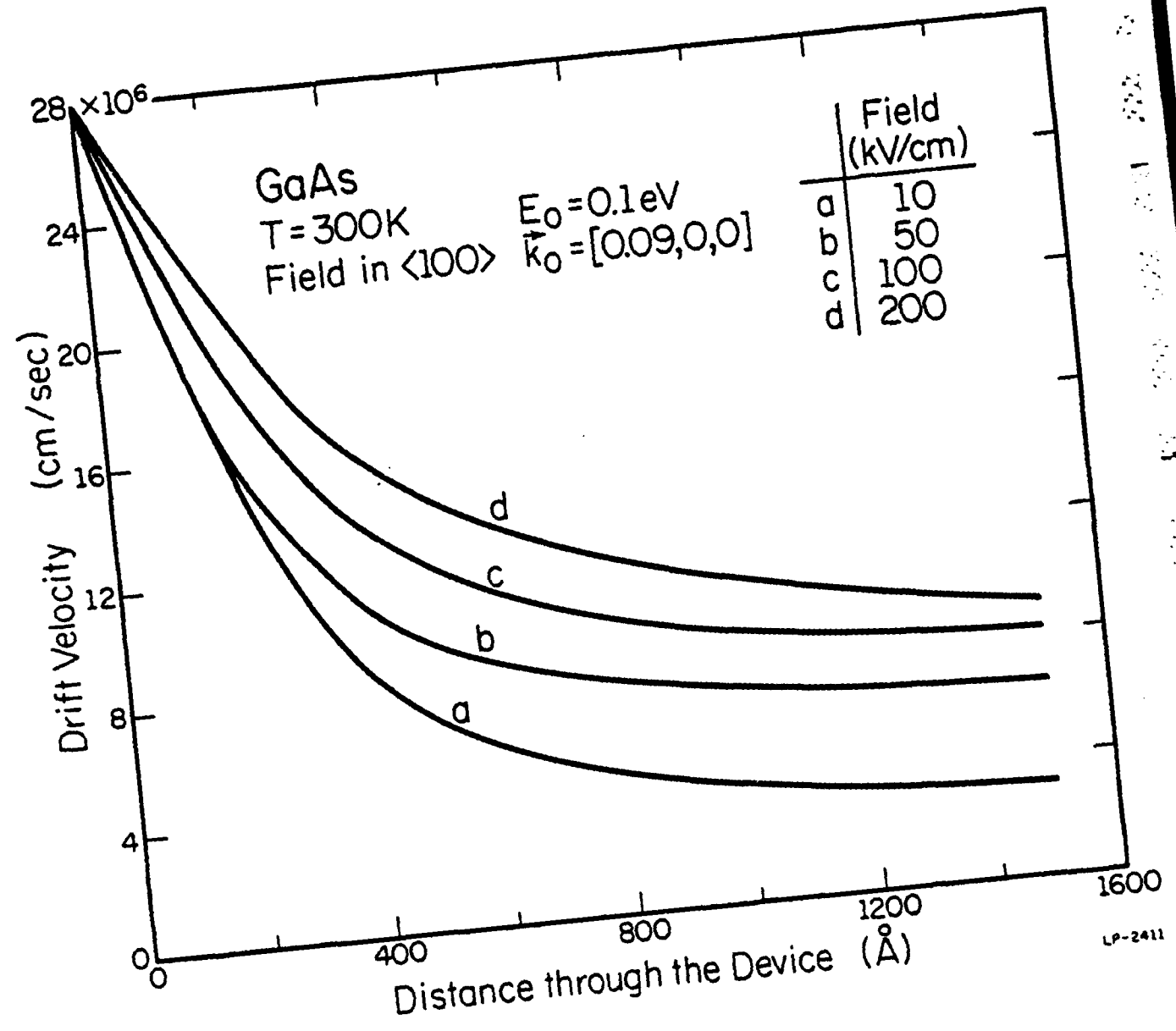


Fig. 7.3: Transient drift velocity of holes in the valence band of GaAs as a function of distance through the device with the applied field as a parameter. The holes are all launched at an energy of 0.1 eV.

We also extend the calculation to device sizes of  $2500 \text{ \AA}$  and the results are depicted in Figure 7.4. After  $2500 \text{ \AA}$  the hole velocity is essentially at saturation, roughly  $7.0 \times 10^6 \text{ cm/sec}$ , at an applied field of  $100.0 \text{ kV/cm}$ . From curves a and b it is clear that the effect of the initial launching energy is completely lost after  $2500 \text{ \AA}$ . Curves c and d show that some of the overshoot is still effective after  $2500 \text{ \AA}$  for holes accelerated by a field of  $10.0 \text{ kV/cm}$ . It takes much longer for the holes to reach the saturation velocity at smaller applied fields. However, the actual magnitude of the velocity at these fields is not large. Holes were also launched such that they move down a series of potential steps similar to the procedure proposed in Chapter 6. There is no significant difference in the drift velocity between the cases with or without the steps.

We have shown that velocity overshoot occurs for holes in GaAs and can lead to a substantial reduction in transit time from the steady state at low fields. At high applied fields, the hole drift velocity can be quite large, approximately  $1.8 \times 10^7 \text{ cm/sec}$ . However, in less than  $1500 \text{ \AA}$ , the velocity rapidly decays to the saturation velocity. Consequently, the transient velocities observed for holes in GaAs do not rival in magnitude those measured for the electrons. Nevertheless, there is a real reduction in transit time for holes under conditions of low field. This may have some significance in device applications.

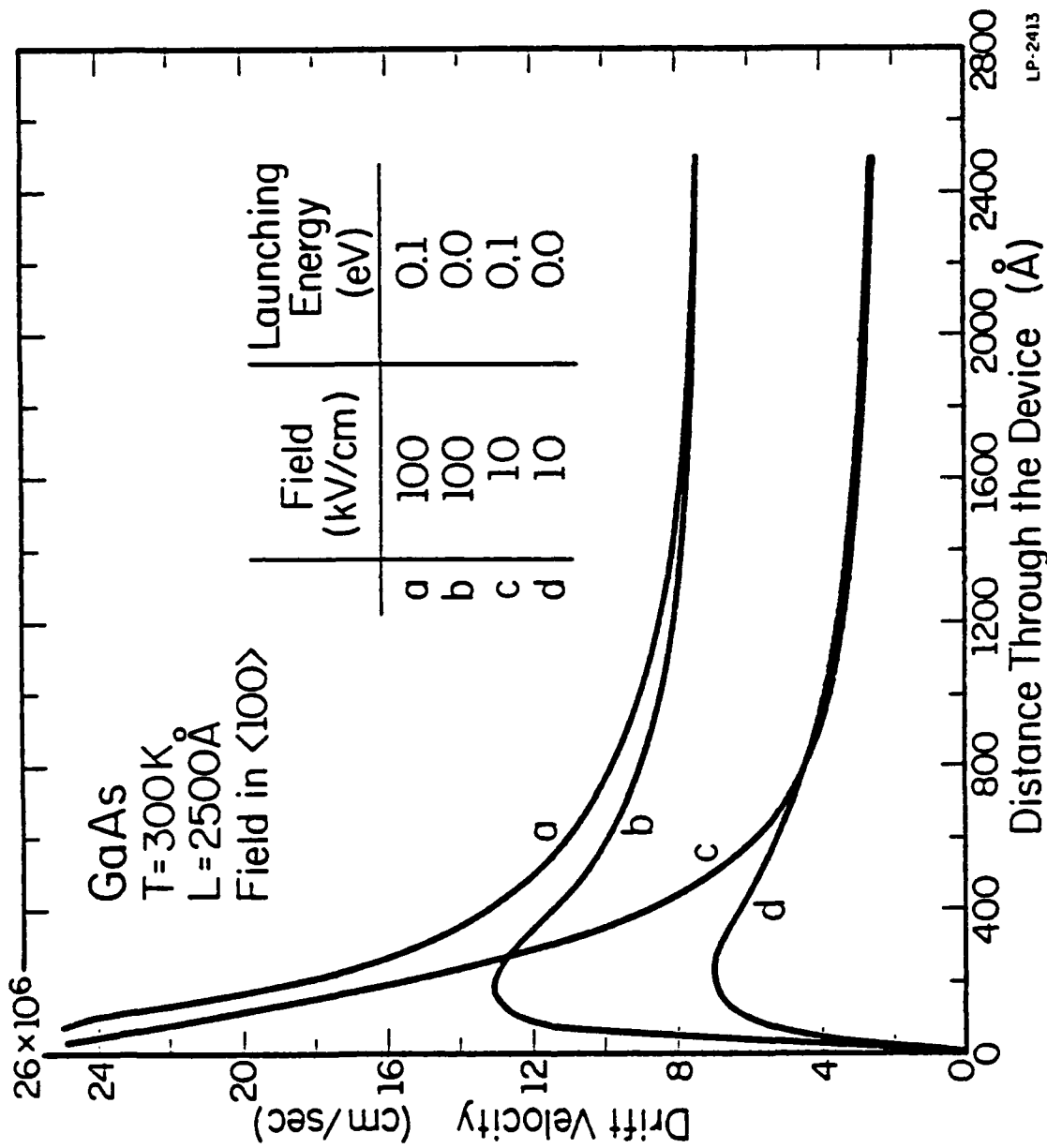


Fig. 7.4: Transient drift velocity of holes in the valence band of GaAs as a function of distance through a 2500 Å device with the applied field and launching energy as parameters.

## APPENDIX 1

### DETAILS OF THE TRANSIENT CALCULATION

In the transient transport program it is desirable to accumulate values of physical observables such as the average energy, drift velocity, and the average number of scatterings as a function of distance through the device. In the transport program used here, where electrons are launched one at a time, the method of averaging is important. There are two general techniques used to sample the value of the observables along the device, the plane and bin models. In most of the calculations presented in this thesis the plane model is used. However, the results obtained for the reflecting contact are all calculated using the bin model. It is the purpose of this appendix to more clearly define and distinguish between these two methods.

As previously mentioned in Chapter 6, in the plane model the velocity as a function of distance is determined by examining the carriers as they cross different planes along the device. This corresponds to taking a "snapshot" of the motion of the carriers at a certain point in real space. As a carrier crosses a plane at a given device length, we treat it as if it had been swept out. Once the carrier crosses a plane its history (time taken to reach that plane, energy at that plane, etc.) is accumulated. Therefore, the time is accumulated from launch and only after an electron crosses a plane is the time noted. Hence the velocity of the carrier then is simply the distance of the observing plane from the launching point times  $1/t$ , where  $t$  represents the total time of flight to that point. The distance

between the planes is constant and is denoted by  $\Delta X$ .

The average velocity of one carrier at the first plane is given by

$$v = \Delta X \frac{1}{t} \quad , \quad (A1.1)$$

where  $t$  is the time of flight to the first plane. For many,  $N$ , electrons the average velocity at the first plane is then

$$\langle v \rangle = \sum_{i=1}^N \frac{\Delta X}{(\text{total time in the device till this plane})_i} / N \quad (A1.2)$$

But we have a constant value of  $\Delta x$  which can be taken outside the sum, giving

$$\langle v \rangle = \Delta X \left( \sum_{i=1}^N \frac{1}{t_i} / N \right) \quad (A1.3)$$

The total transit time is then defined by

$$T = L / \bar{v} \quad , \quad (A1.4)$$

where  $L$  is the total length of the device and  $\bar{v}$  is the average velocity of the carriers at the end of the device. If we use the technique of Equation A1.2, then the total transit time is calculated as

$$T = \frac{N}{\sum_{i=1}^N \frac{1}{T_i}} \quad , \quad (A1.5)$$

where  $N$  is the total number of electrons launched and  $T_i$  is the total time each electron spends in the device. Notice that we accumulate the sum of  $1/t$  rather than  $t$  above. This is because we are most interested in the current and this estimator best represents how an ensemble of electrons contributes to the current.

Physically, the velocity at a particular point along the device, using the plane model, represents the average velocity of the carriers in a device

of that length. So the velocity at say  $1000 \text{ \AA}$  means the average velocity of the carriers in a device  $1000 \text{ \AA}$  long. However, it is often desirable to know what the velocity of the carriers is averaged over a small region of the device rather than over the entire length up to that point. The bin method is used to determine the velocity within small regions, bins, of roughly  $50 \text{ \AA}$  long. The observables are averaged over each bin separately and reflect the value of the velocity within that region only.

The basic idea of the bin method is that the total time the carrier spends in each bin is accumulated. Therefore, the velocity at say  $1000 \text{ \AA}$  is based solely on the time each carrier spends in the bin around  $1000 \text{ \AA}$ . This method takes into account backscattering since the time spent in the bin is accumulated independent of how many times each carrier drifts in and out of the bin. The actual way in which the time and velocity are calculated is done as follows.

The velocity is found from the product of the bin length and the sum over the number of carriers of  $1/t_i$ , where  $t_i$  is the total time each carrier spends in each bin. The total drift time in the device is found from the sum of  $1/T_i$  as before. Here  $T_i$  is again the total time each carrier spends in the device. Therefore, the average total velocity should be the same in either method but the velocity calculated along the device will be different. In the plane model, as mentioned, the velocity is the overall velocity up to that point. In the bin model, the velocity is the average velocity of the carriers in that particular bin only. Figure A1.1 illustrates the results of using the bin model. This can be compared to Figure 6.4 in which the same data are calculated using the plane model. As one can clearly see, the plane model tends to overestimate the effects of

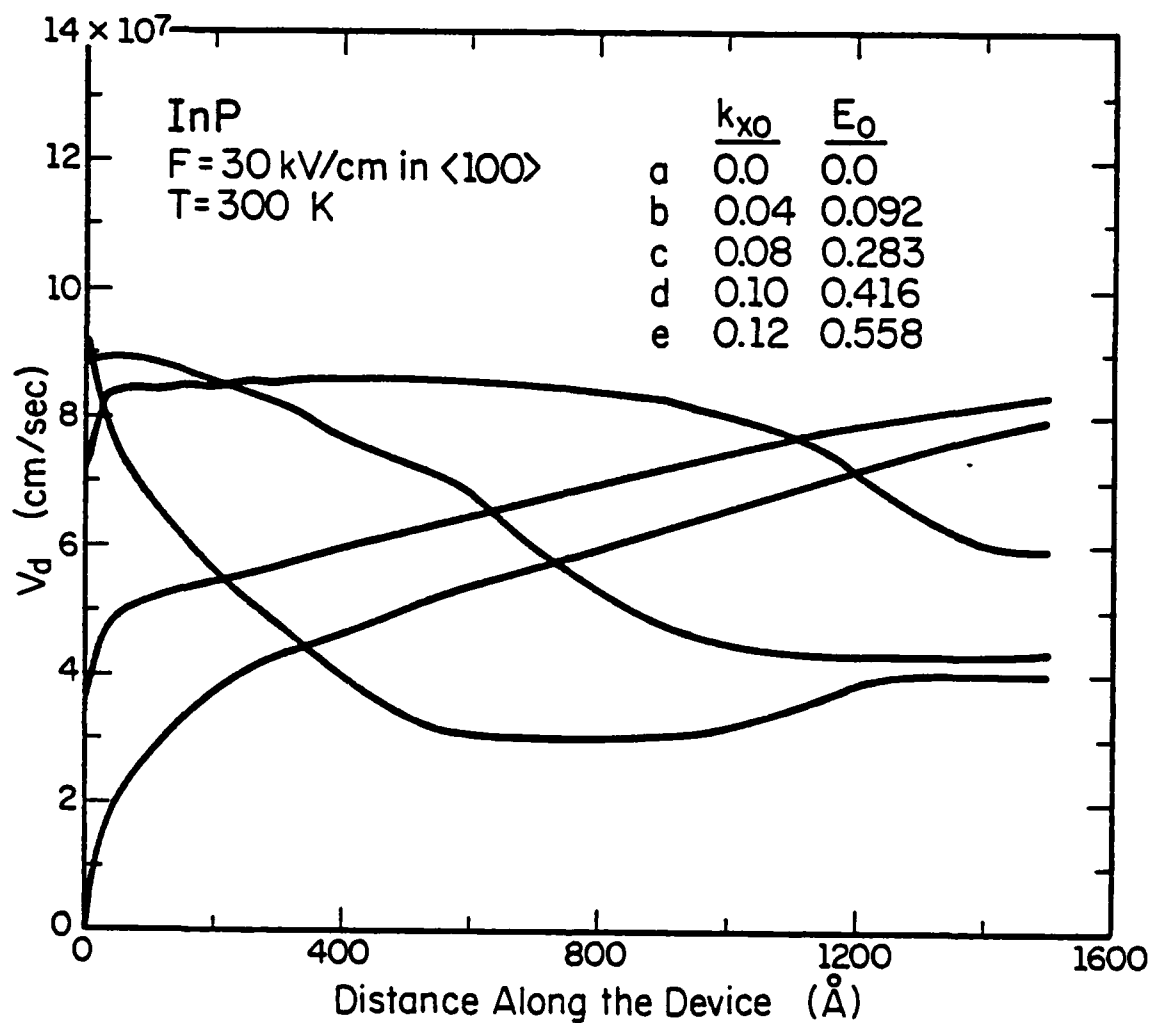


Fig. A1.1: Average electron drift velocity versus device length in InP at an applied field of 30.0 kV/cm for various launching energies. The calculation is made using the bin model as discussed in the text.

the velocity overshoot. The bin model, though shows that the velocity near the end of the device is less than the average total velocity. Either model is acceptable for use as long as it is clear what that model represents.

When a carrier crosses from one bin to another during a drift it is necessary to calculate correctly how much time is spent in each bin. A quadratic interpolation scheme is used which assumes during each drift that the acceleration is constant. This is reasonable since a constant field is assumed in each of the bins. The initial velocity, initial and final real space positions, and total drift time are all known. From these it is easy for one dimensional motion to calculate the acceleration. The time spent in each bin is easily determined from the the real space distance traveled in each bin, (starting point to end of the first bin, etc.) the initial velocity and the acceleration.

Table A2.1

Parameters for GaAs Program [105]: Electrons

Parameter	Value	$\Gamma$ valley	L valley	X valley
Density	5.36 g/cm <sup>3</sup>			
$\epsilon_{\infty}$	10.92			
$\epsilon_0$	12.90			
Number of valleys		1	4	3
Effective mass $m^*/m_0$		0.063	0.23	0.43
Non-parabolicity (eV <sup>-1</sup> )		0.690	0.65	0.36
Valley separation (eV)			0.33	0.52
Temperature	300°K			

Intervalley Coupling Contacts and Phonon Energies

$\Gamma$ -L	$1.0 \times 10^9$ eV/cm	0.026 eV
$\Gamma$ -X	$1.0 \times 10^9$ eV/cm	0.026 eV
L-L	$1.0 \times 10^9$ eV/cm	0.026 eV
L-X	$0.9 \times 10^9$ eV/cm	0.026 eV
X-X	$0.9 \times 10^9$ eV/cm	0.026 eV

Polar Optical Phonon Energies

$\Gamma$	0.035 eV
L	0.0343 eV
X	0.0343 eV

Acoustic Scattering Parameters

Deformation Potential	5.0 eV
Sound Velocity	$5.24 \times 10^5$ cm/sec

Table A2.2

Parameters for InP Program [106]: Electrons

Parameter	Value	$\Gamma$ valley	L valley	X valley
Density	4.79 g/cm <sup>3</sup>			
$\epsilon_{\infty}$	9.52			
$\epsilon$	12.35			
Number of valleys		1	4	3
Effective mass $m^*/m_0$		0.078	0.26	0.325
Non-parabolicity (eV <sup>-1</sup> )		0.83	0.23	0.380
Valley separation (eV)			0.54	0.775
Temperature	300°K			

Intervalley Coupling Constants and Phonon Energies

$\Gamma$ -L	$1.0 \times 10^9$ eV/cm	0.0278 eV
$\Gamma$ -X	$1.0 \times 10^9$ eV/cm	0.0299 eV
L-L	$1.0 \times 10^9$ eV/cm	0.0290 eV
L-X	$0.9 \times 10^9$ eV/cm	0.0293 eV
X-X	$0.9 \times 10^9$ eV/cm	0.0299 eV

Polar Optical Phonon Energies

$\Gamma$	0.043 eV
L	0.0423 eV
X	0.0416 eV

Acoustic Scattering Parameters

Deformation Potential	8 eV
Sound Velocity	$5.13 \times 10^5$ cm/sec

Table A2.3  
Parameters for InAs Program [107]: Electrons

Parameter	Value	$\Gamma$ valley	L valley	X valley
Density	5.67 g/cm <sup>3</sup>			
$\epsilon_{\infty}$	11.8			
$\epsilon_0$	14.55			
Number of valleys		1	4	3
Effective mass $m^*/m_0$		0.032	0.286	0.640
Optical phonon energies (eV)		0.0302	0.024	0.020
Non-parabolicity (eV <sup>-1</sup> )		1.390	0.536	0.900
Valley separation (eV)			1.032	1.620
Temperature	300°K			
Energy gap (eV)	0.36			

Intervalley Coupling Constants and Phonon Energies

$\Gamma$ -L	$1.0 \times 10^9$ eV/cm	0.0273 eV
$\Gamma$ -X	$1.0 \times 10^9$ eV/cm	0.0299 eV
L-L	$1.0 \times 10^9$ eV/cm	0.0290 eV
L-X	$0.9 \times 10^9$ eV/cm	0.0293 eV
X-X	$0.9 \times 10^9$ eV/cm	0.0299 eV

Acoustic Scattering Parameters

Deformation Potential	3.0 eV
Sound Velocity	$4.05 \times 10^5$ cm/sec

Table A2.4

## Parameters for GaAs Transport Program: Holes

Bulk Material Parameters [105]

Lattice Constant	5.65	Å
Density	5.36	g/cm <sup>3</sup>
Energy Band Gap (T = 300 K)	1.424	eV
Dielectric Constants		
$\epsilon_{\infty}$	10.92	
$\epsilon_0$	12.9	
Crystal Elastic Constants		
C <sub>11</sub>	11.88 x 10 <sup>11</sup>	dynes/cm <sup>2</sup>
C <sub>12</sub>	5.38 x 10 <sup>11</sup>	dynes/cm <sup>2</sup>
C <sub>44</sub>	5.49 x 10 <sup>11</sup>	dynes/cm <sup>2</sup>
[100] Longitudinal Sound velocity, S <sub>l</sub>	4.73 x 10 <sup>5</sup>	cm/sec
[100] Transverse Sound velocity, S <sub>t</sub>	3.34 x 10 <sup>5</sup>	cm/sec

Scattering Rate parameters [80,105]

Effective masses		
Heavy Hole Band, m <sub>HH</sub>	0.45	m <sub>0</sub>
Light Hole Band, m <sub>LH</sub>	0.082	m <sub>0</sub>
Split-off Band, m <sub>SO</sub>	0.154	m <sub>0</sub>
Optical Phonon Energy	0.035	eV
Deformation Potential Constants		
a	3.1	eV
b	1.7	eV
d	4.4	eV

Impact Ionization Rate Parameters

Set 1 (Identical for all 3 bands)		
Threshold Energy, E <sub>Th</sub>	1.70	eV
Multiplicative Factor, p	0.25	
Set 2		
Bands 1 & 2		
E <sub>Th</sub>	1.80	eV
p	0.25	
Band 3		
E <sub>Th</sub>	1.424	eV
p	0.25	

Table A2.5  
Parameters for InP Hole Transport Program

Bulk Material Parameters [106]

Lattice Constant	5.868	Å
Density	4.787	g/cm <sup>3</sup>
Energy Band Gap (T = 300 K)	1.35	eV
Dielectric Constants		
$\epsilon_{\infty}$	9.52	
$\epsilon_0$	12.35	
Crystal Elastic Constants		
C <sub>11</sub>	10.22 x 10 <sup>11</sup>	dynes/cm <sup>2</sup>
C <sub>11</sub>	5.76 x 10 <sup>11</sup>	dynes/cm <sup>2</sup>
C <sub>44</sub>	4.60 x 10 <sup>11</sup>	dynes/cm <sup>2</sup>
[100] Longitudinal Sound Velocity, S <sub>l</sub>	5.13 x 10 <sup>5</sup>	cm/sec
[100] Transverse Sound Velocity, S <sub>t</sub>	3.10 x 10 <sup>5</sup>	cm/sec

Scattering Rate Parameters [80,106]

Effective Masses		
Heavy Hole Band, m <sub>HH</sub>	0.45	m <sub>0</sub>
Light Hole Band, m <sub>LH</sub>	0.12	m <sub>0</sub>
Split-off Band, m <sub>SO</sub>	0.21	m <sub>0</sub>
Optical Phonon Energy	0.043	eV
Deformation Potential Constants		
a	2.8	eV
b	1.55	eV
d	4.4	eV

Impact Ionization Rate Parameters

(Identical for all 3 bands)		
Threshold Energy, E <sub>Th</sub>	1.55	eV
Multiplicative Factor, p	20.0	

Table A2.6  
Parameters For GASb Hole Transport Program

Bulk Material Parameters [108]

Lattice Constant	6.095	Å
Density	5.613	g/cm <sup>3</sup>
Energy Band Gap (T = 300K)	0.726	eV
Dielectric Constants		
$\epsilon^\infty$	14.44	
$\epsilon_0$	15.69	
Crystal Elastic Constants		
C <sub>11</sub>	8.839 x 10 <sup>11</sup>	dynes/cm <sup>2</sup>
C <sub>12</sub>	4.033 x 10 <sup>11</sup>	dynes/cm <sup>2</sup>
C <sub>44</sub>	4.316 x 10 <sup>11</sup>	dynes/cm <sup>2</sup>
[100] Longitudinal Sound Velocity, S <sub>l</sub>	3.97 x 10 <sup>5</sup>	cm/sec
[100] Transverse Sound Velocity, S <sub>t</sub>	2.77 x 10 <sup>5</sup>	cm/sec

Scattering Rate Parameters [80,92,109]

Effective Masses		
Heavy Hole Band, m <sub>HH</sub>	0.490	m <sub>0</sub>
Light Hole Band, m <sub>LH</sub>	0.046	m <sub>0</sub>
Split-off Band, m <sub>SO</sub>	0.20	m <sub>0</sub>
Optical Phonon Energy	0.0298	eV
Deformation Potential Constants		
a	2.2	eV
b	2.0	eV
d	4.6	eV

Impact Ionization Rate Parameters

Threshold Energy, E <sub>th</sub>	0.80	eV
Multiplicative Factor, p	100.0	

Table A2.7

## Parameters for AlSb Transport Program: Holes

Bulk Material Parameters [110]

Lattice Constant	6.1355	Å
Density	4.26	g/cm <sup>3</sup>
Energy Band Gap (T = 300K) (direct)	2.218	eV
Dielectric Constants		
$\epsilon_{\infty}$	10.24	
$\epsilon_0$	12.04	
Crystal Elastic Constants		
C <sub>11</sub>	8.939 x 10 <sup>11</sup>	dynes/cm <sup>2</sup>
C <sub>12</sub>	4.425 x 10 <sup>11</sup>	dynes/cm <sup>2</sup>
C <sub>44</sub>	4.155 x 10 <sup>11</sup>	dynes/cm <sup>2</sup>
[100] Longitudinal Sound Velocity, S <sub>l</sub>	4.528 x 10 <sup>5</sup>	cm/sec
[100] Transverse Sound Velocity, S <sub>t</sub>	3.087 x 10 <sup>5</sup>	cm/sec

Scattering Rate Parameters [80,92,109]

Effective Masses		
Heavy Hole Band, $m_{HH}$	0.94	$m_0$
Light Hole Band, $m_{LH}$	0.14	$m_0$
Split-off Band, $m_{SO}$	0.29	$m_0$
Optical Phonon Energy	0.042	eV
Deformation Potential Constants		
a	2.7	eV
b	1.35	eV
d	4.30	eV

Impact Ionization Rate Parameters

Threshold Energy, E <sub>ch</sub>	0.80	eV
Multiplicative Factor, p	100.0	

## APPENDIX 3

## SUMMARY OF THE SCATTERING MECHANISMS IN THE VALENCE BAND

In this appendix, the different scattering mechanisms that have been included in the Monte Carlo calculations of hole transport are summarized. The low energy scattering rates are calculated by the conventional method: the Golden rule, the Born approximation, and the effective mass density of states.

In general the transition rate from wave vector  $k$  to  $k'$  is given by the Golden rule as

$$S(\vec{k}, \vec{k}') = \frac{2\pi}{\hbar} |H_{fi}|^2 \delta(E_f - E_i) \quad , \quad (A3.1)$$

where  $H_{fi}$  is the matrix element of the perturbing potential  $H$  between the initial and final states. In calculations involving interband transitions it is more convenient to separate the overlap integral explicitly from the matrix element. Equation A3.1 then becomes

$$P_i^f = \frac{2\pi}{\hbar} |S(\vec{k}-\vec{k}')|^2 G(\vec{k}, \vec{k}') \delta(E_f - E_i) \quad , \quad (A3.2)$$

where  $G(\vec{k}, \vec{k}')$  is the overlap integral expressed as

$$G(\vec{k}, \vec{k}') = \frac{1}{2} \sum_{s_1 s_2} \left| \int u_{s_1, k'}^*(r) u_{s_2, k}(r) dr \right|^2 \quad . \quad (A3.3)$$

$G(\vec{k}, \vec{k}')$  accounts for the overlap between the periodic parts,  $u_{s, k}(r)$ , of the wave functions in the mixing of initial and final Bloch states. The overlap integral depends upon the symmetry properties of the initial and final state

## APPENDIX 3

## SUMMARY OF THE SCATTERING MECHANISMS IN THE VALENCE BAND

In this appendix, the different scattering mechanisms that have been included in the Monte Carlo calculations of hole transport are summarized. The low energy scattering rates are calculated by the conventional method: the Golden rule, the Born approximation, and the effective mass density of states.

In general the transition rate from wave vector  $k$  to  $k'$  is given by the Golden rule as

$$S(\vec{k}, \vec{k}') = \frac{2\pi}{\hbar} |H_{fi}|^2 \delta(E_f - E_i) \quad (A3.1)$$

where  $H_{fi}$  is the matrix element of the perturbing potential  $H$  between the initial and final states. In calculations involving interband transitions it is more convenient to separate the overlap integral explicitly from the matrix element. Equation A3.1 then becomes

$$P_i^{f} = \frac{2\pi}{\hbar} |B(\vec{k}-\vec{k}')|^2 G(\vec{k}, \vec{k}') \delta(E_f - E_i) \quad (A3.2)$$

where  $G(\vec{k}, \vec{k}')$  is the overlap integral expressed as

$$G(\vec{k}, \vec{k}') = \frac{1}{2} \sum_{s_1 s_2} \left| \int u_{s_1, k'}^*(\vec{r}) u_{s_2, k}(\vec{r}) d\vec{r} \right|^2 \quad (A3.3)$$

$G(\vec{k}, \vec{k}')$  accounts for the overlap between the periodic parts,  $u_{s, k}(\vec{r})$ , of the wave functions in the mixing of initial and final Bloch states. The overlap integral depends upon the symmetry properties of the initial and final state

wave functions. The valence band wavefunctions for the materials of interest here exhibit a non-spherical symmetry, mostly p-like at the top of the band [76,77].

Wiley [75] has shown that the k-dependence of  $G_{ij}$ , for  $i,j=1,2$ , is not very pronounced. An approximation of  $G_{ij}$  may be rendered which is better the wider the energy band gap of the material is.  $G_{ij}$  is approximated by  $G(\theta)$ , which depends only on the scattering angle,  $\theta$ , and is independent of k.

### A3.1 Nonpolar Optical Scattering [76]

The transition rate for nonpolar optical scattering is given by

$$P_i^f = \frac{2\pi}{\hbar} | \langle \mathbf{g}(\vec{k}-\vec{k}') \rangle |^2 G(\theta) \begin{cases} N_0 & \delta[E(k')-E(k) - \hbar\omega] \text{ (abs.)} \\ (N_0 + 1) & \delta[E(k')-E(k) + \hbar\omega] \text{ (em.)} \end{cases}, \quad (\text{A3.4})$$

where we have approximated  $G(k,k')$  by  $G(\theta)$ . The matrix element is independent of k and is given by

$$\begin{aligned} | \langle \mathbf{g}(\vec{k}-\vec{k}') \rangle |^2 &= B_0 \\ &= \frac{\hbar^2 (DK)^2}{2\rho V \hbar \omega_0} \end{aligned} \quad (\text{A3.5})$$

where  $(DK)^2$  is the deformation potential and  $\hbar\omega_0$  is the phonon energy. The total scattering rate is calculated from summing over all the final states

$$\text{as } 1/\tau = \frac{V}{(2\pi)^3} \int d\vec{k}' \frac{2\pi}{\hbar} B_0 G(\theta) \begin{cases} N_0 & \delta[E(k') - E(k) - \hbar\omega] \text{ (abs.)} \\ (N_0 + 1) & \delta[E(k') - E(k) + \hbar\omega] \text{ (em.)} \end{cases}. \quad (\text{A3.6})$$

Using the effective mass approximation, the energy can be expressed as,

$$E(k) = \frac{\hbar^2 k^2}{2M^*}, \quad E(k') = \frac{\hbar^2 k'^2}{2M^*}, \quad (\text{A3.7})$$

where

$$\frac{\hbar^2 k'^2}{2M^*} = \frac{\hbar^2 k^2}{2M^*} \pm \hbar\omega_0 .$$

The integral becomes after evaluating the integrals over  $\phi$  and  $k'$  for the case of intraband scattering

$$1/\tau_{ii} = \frac{B_0 V M_i^*}{\pi \hbar^3} k_0 \left\{ \begin{array}{l} N_0 \quad (\text{abs.}) \\ (N_0 + 1) \quad (\text{em.}) \end{array} \right\} \int_0^\pi G_{ii}(\theta) \sin \theta d\theta , \quad (\text{A3.8})$$

where

$$k_0 = \sqrt{k^2 \pm \frac{2M_i^* \omega_0}{\hbar}} , \quad B_0 = \frac{\hbar^2 [(DK)_{ii}]^2}{2\rho V \hbar \omega_0} .$$

The integral over  $\theta$  can be evaluated using Wiley's [75] approximation,

$$G_{11} = G_{22} \sim 1/4 (1 + 3 \cos^2 \theta) , \quad G_{12} = G_{21} \sim 3/4 \sin^2 \theta . \quad (\text{A3.9})$$

The integral over  $\theta$  for intraband scattering is simply

$$\int_0^\pi G_{ii}(\theta) \sin \theta d\theta = \int_0^\pi 1/4 (1 + 3 \cos^2 \theta) \sin \theta d\theta = 1 . \quad (\text{A3.10})$$

For the case of interband scattering,  $1/\tau_{ij}$  becomes

$$1/\tau_{ij} = \frac{B_0 V M_j^*}{\pi \hbar^3} k_0 \left\{ \begin{array}{l} N_0 \\ N_0 + 1 \end{array} \right\} \int_0^\pi G_{ij}(\theta) \sin \theta d\theta . \quad (\text{A3.11})$$

The integral over  $\theta$  for interband scattering is

$$\int_0^\pi G_{ij}(\theta) \sin \theta d\theta = \int_0^\pi 3/4 \sin^3 \theta d\theta , \quad (\text{A3.12})$$

which is simply equal to 1.0.

The hole-nonpolar optical phonon scattering rate for holes initially in the heavy hole band is presented in Figure A3.1. As can be seen from this Figure, the heavy hole-heavy hole scattering rate is greatest since the final density of states is largest in the heavy hole band. The calculations presented in Figure A3.1 are all made using the effective mass approximation. The scattering rate from the heavy hole band to the split-off hole band is stronger than the rate from the heavy hole band to the light hole band. This is because the effective mass of the split-off holes is larger than that of the light holes. At high energy the light hole band bends strongly such that it follows the heavy hole band. Then the effective mass approximation breaks down completely in the description of the light hole band. Consequently, the scattering rate calculated using the effective mass approximation is no longer valid at high hole energies. In order to take this into account in the calculation, the relative scattering rates between bands are calculated using the actual density of states in each band. Therefore, the actual scattering rate between the heavy and split-off bands is less than is shown here.

### A3.2 Acoustic Phonon Scattering [76,78]

As discussed in [76], the transition rate for intraband acoustic phonon scattering is given by

$$P_1^F = \frac{A_a}{E^{1/2}} \left\{ \frac{N_q(x)}{N_q(x) + 1} \right\} x^2 dx = f(x) dx, \quad (\text{A3.13})$$

where

$$A_a = \left( \frac{E_1 M_i^*}{4 \hbar^2} \right)^2 \left( \frac{1}{\tau \omega V_s} \right) \left( \frac{kT}{E_o^*} \right)^{1/2}$$

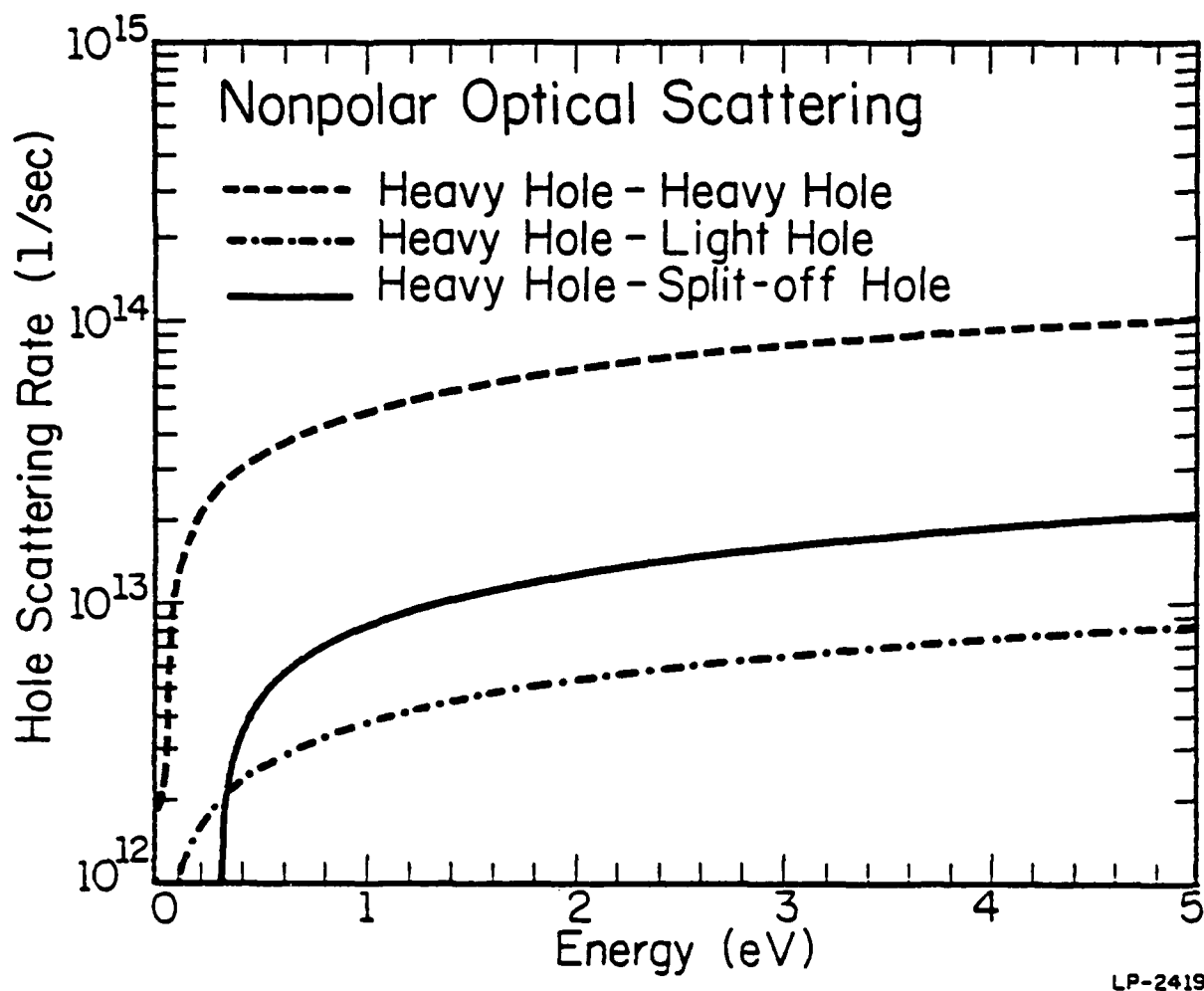


Fig. A3.1: Nonpolar optical phonon scattering of holes in GaAs at 300 K as a function of carrier energy. The relative scattering rates involving transitions from the heavy hole band to each of the other bands, heavy hole (intraband scattering), light hole, and split-off hole bands is depicted.

and

$$x = \hbar q v_s / kT$$

$E_1$  is the deformation potential constant,  $v_s$  the sound velocity,  $\rho$  the material density, and  $E_s^* = 1/2 m^* v_s^2$ .  $N_q(x)$  is the phonon distribution function which can be expressed by a truncated Laurent expansion [78]:

$$N_q(x) = \frac{1}{e^x - 1} \sim \begin{cases} 1/x - 1/2 + 1/12x - 1/720x^3 & , x < 3.5 \\ 0 & , x > 3.5 \end{cases} \quad (\text{A3.14})$$

The total scattering rate can then be calculated by integrating Equation A3.13,

$$1/\tau_{ac} = \int_{x_1}^{x_2} f(x) dx \quad (\text{A3.15})$$

where  $x_1$  and  $x_2$  are listed in Table A3.1. The resulting scattering rates are given in Table A3.2. The overlap integral is treated as in the case for nonpolar optical scattering. Therefore  $G_{ii}(\theta)$  is given by Equation A3.10 and the result of the integral over  $\theta$  is again 1.0.

The transition rate for interband scattering is given by Equation A3.13 with  $A_a$  given by

$$A_a = \left( \frac{E_1 M_i^*}{4 \hbar^2} \right)^2 \frac{1}{\pi^0 v_s} \left( \frac{kT}{E_o^* 1/2} \right)^3 \quad (\text{A3.16})$$

In this case,  $G_{ij}(\theta) = 3/4 \sin^2(\theta)$  and the result from integrating  $G_{ij}(\theta)$  with respect to  $\theta$  is given by Equation A3.12 as 1.0. The phonon energy is determined from an average given by [24]

$$\langle X \rangle = \frac{\int_{x_1}^{x_2} x f(x) dx}{\int_{x_1}^{x_2} f(x) dx} \quad (\text{A3.17})$$

Table A3.1

Integration limits for equation A3.15

with  $x = \hbar q V_s / kT$ .

$E < E_s^*$	Absorption	$\left\{ \begin{aligned} x_1 &= \frac{4E_s^{*1/2}}{kT} (E_s^{*1/2} - E^{1/2}) \\ x_2 &= \frac{4E_s^{*1/2}}{kT} (E_s^{*1/2} + E^{1/2}) \end{aligned} \right.$
	No emission	
$E > E_s^*$	Absorption	$\left\{ \begin{aligned} x_1 &= 0 \\ x_2 &= \frac{4E_s^{*1/2}}{kT} (E^{1/2} + E_s^{*1/2}) \end{aligned} \right.$
	Emission	$\left\{ \begin{aligned} x_1 &= 0 \\ x_2 &= \frac{4E_s^{*1/2}}{kT} (E^{1/2} - E_s^{*1/2}) \end{aligned} \right.$

Table A3.2

Acoustic scattering rates.

$\bar{x}$  is taken as 3.5 according to equation A3.17

$E \leq E_s^*$	Absorption	$\frac{1}{\tau_{ac}} = \frac{A_a}{E} \frac{1}{2} \left( \frac{1}{2} x_2^2 - \frac{1}{6} x_1^3 + \frac{1}{48} x_2^4 - \frac{1}{4320} x_1^6 \right), \quad x_2 < \bar{x}$
	No emission	
$E > E_s^*$	Absorption	$\frac{1}{\tau_{ac}} = \frac{A_a}{E} \frac{1}{2} \left( \frac{1}{2} x_2^2 - \frac{1}{6} x_1^3 + \frac{1}{48} x_2^4 - \frac{1}{4320} x_1^6 \right), \quad x_2 > \bar{x}$
		$\frac{1}{\tau_{ac}} = \frac{A_a}{E} \frac{1}{2} \left( \frac{1}{2} x_2^2 - \frac{1}{6} x_1^3 + \frac{1}{48} x_2^4 - \frac{1}{4320} x_1^6 \right), \quad x_2 > \bar{x}$
	Emission	$\frac{1}{\tau_{ac}} = \frac{A_a}{E} \frac{1}{2} \left( \frac{1}{2} x_2^2 + \frac{1}{6} x_1^3 + \frac{1}{48} x_2^4 - \frac{1}{4320} x_1^6 \right), \quad x_2 < \bar{x}$
		$\frac{1}{\tau_{ac}} = \frac{A_a}{E} \frac{1}{2} \left( \frac{1}{2} x_2^2 - \frac{1}{6} x_1^3 + \frac{1}{48} x_2^4 - \frac{1}{4320} x_1^6 + \frac{1}{3} x_2^3 \right), \quad x_2 > \bar{x}$

or

$$\langle \hbar\omega_q \rangle = kT \langle x \rangle \quad (\text{A3.18})$$

The hole-acoustic phonon scattering rate is displayed in Figure A3.2. Again the calculations are made using the effective mass approximation through the entire energy range.

### A3.3 Polar Optical Scattering [77]

The matrix element for polar optical scattering is given by [77]

$$\beta^2 |\vec{k}-\vec{k}'|^2 = \frac{2\pi e^2 \hbar\omega_0}{V} \left[ \frac{1}{\epsilon_\infty} - \frac{1}{\epsilon_0} \right] \frac{1}{|\vec{k}-\vec{k}'|^2} \quad (\text{A3.19})$$

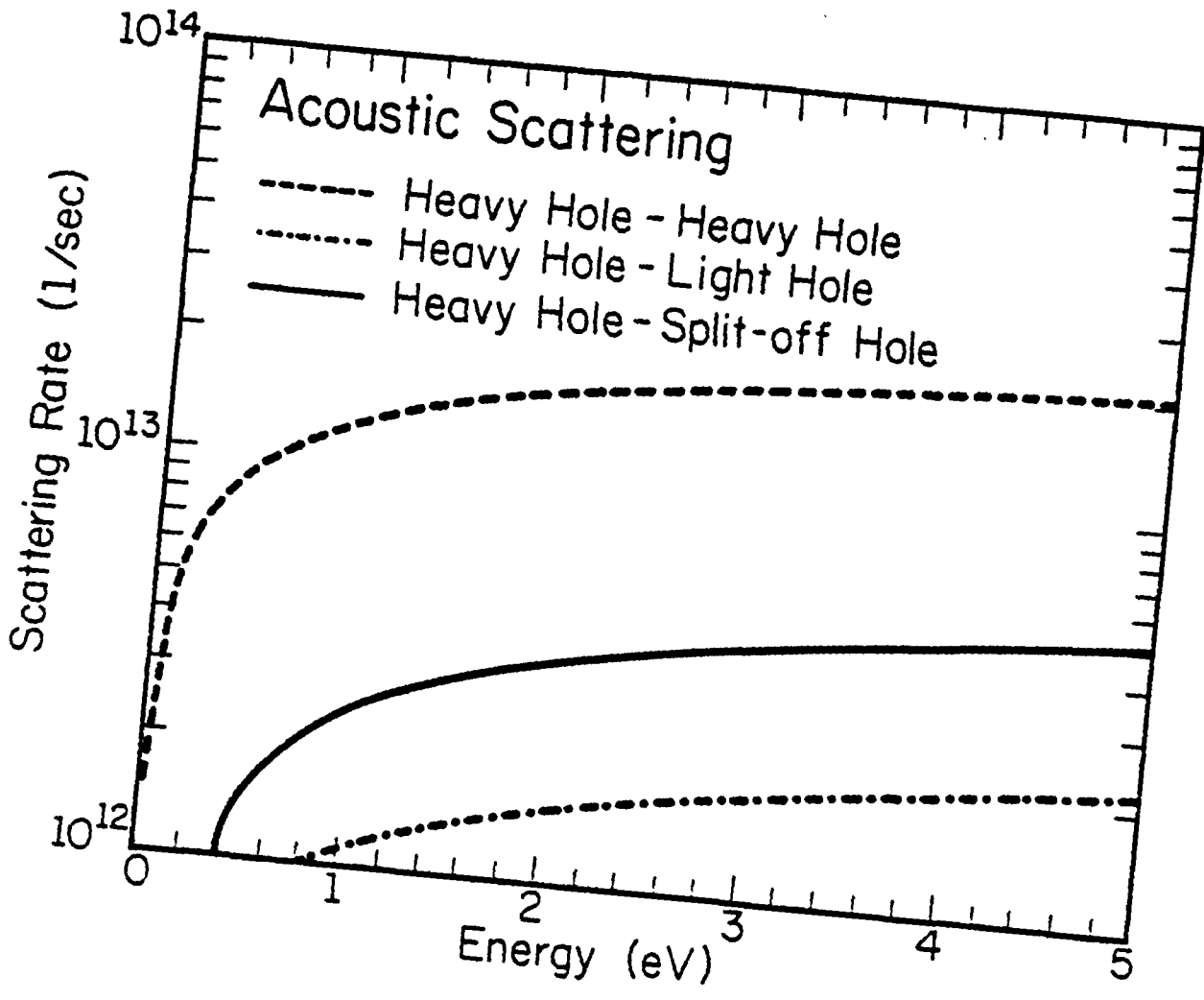
where  $\epsilon_\infty$  and  $\epsilon_0$  are the optical and static dielectric constants respectively. The total scattering rate is derived by summing over all the final states as

$$1/\tau = \frac{2\pi}{\hbar} \frac{2V}{(2\pi)^3} \int \frac{2\pi e^2 \hbar\omega_0}{V} \left[ \frac{1}{\epsilon_\infty} - \frac{1}{\epsilon_0} \right] \frac{G(\vec{k}, \vec{k}')}{|\vec{k}-\vec{k}'|^2} \delta(E_f - E_i) d\vec{k}' \quad (\text{A3.20})$$

where  $G(\vec{k}, \vec{k}')$  is given by Equation A3.3. Evaluating the integral over  $\vec{k}'$  we obtain for intraband scattering

$$\frac{1}{\tau_{ii}} = \frac{2\pi e^2 \hbar\omega_0}{V} \left[ \frac{1}{\epsilon_\infty} - \frac{1}{\epsilon_0} \right] \frac{2V}{2\pi\hbar} \int_0^\pi \sin\theta G(\theta) d\theta \cdot \int_0^k dk' k'^2 \delta \left[ \frac{\hbar^2 k'^2}{2M^*} - \frac{\hbar^2 k^2}{2M^*} = \hbar\omega_0 \right] \quad (\text{A3.21})$$

$$\frac{1}{\tau_{ii}} = \frac{2\pi e^2 \hbar\omega_0}{V} \left[ \frac{1}{\epsilon_\infty} - \frac{1}{\epsilon_0} \right] \frac{2V}{2\pi\hbar} \int_0^\pi \sin\theta G(\theta) d\theta \cdot \int_0^k dk' k'^2 \delta \left[ \frac{\hbar^2 k'^2}{2M^*} - \frac{\hbar^2 k^2}{2M^*} = \hbar\omega_0 \right] \quad (\text{A3.21})$$



LP-2418

Fig. A3.2: Acoustic phonon scattering of holes in GaAs at 300 K as a function of carrier energy. The relative scattering rates involving transitions from the heavy hole band to each of the other bands, heavy hole (intraband scattering), light hole, and split-off hole bands is depicted.

Upon evaluating the integral over  $k'$

$$\frac{1}{\tau_{ii}} = \frac{2\pi e^2 \hbar \omega_0}{V} \left[ \frac{1}{\epsilon_\infty} - \frac{1}{\epsilon_0} \right] \frac{2V}{2\pi \hbar} \frac{M_i k_0}{\hbar^2} \int_0^\pi \frac{G(\theta) \sin(\theta) d\theta}{(k_0^2 + k^2 - 2k k_0 \cos \theta)} \quad (\text{A3.22})$$

For intraband scattering,  $G(\theta)$  is given by Equation A3.9 as

$$G_{11} = G_{22} = 1/4 (1 + 3 \cos^2 \theta).$$

Integration of  $G_{ii}(\theta)$  in Equation A3.22 finally gives,

$$\frac{1}{\tau_{ii}} = \frac{2V \beta_{po}}{2\pi \hbar^3} \psi \frac{M_i}{k} \frac{1}{4} \left[ 1 + 3 \Phi (\Phi - 1/\psi) \right] \left\{ \begin{matrix} N_0 \\ N_0 + 1 \end{matrix} \right\}, \quad (\text{A3.23})$$

where

$$\beta_{po} = \frac{2\pi e^2 \hbar \omega_0}{V} \left[ \frac{1}{\epsilon_\infty} - \frac{1}{\epsilon_0} \right],$$

$$\psi = \log \left| \frac{k + \sqrt{k^2 + 2M_i \omega_0 / \hbar}}{k - \sqrt{k^2 + 2M_i \omega_0 / \hbar}} \right|,$$

$$\Phi = \frac{k^2 + M_i \omega_0 / \hbar}{k \sqrt{k^2 + 2M_i \omega_0 / \hbar}}.$$

The case for interband scattering is similar to the above except that  $G(\theta)$  becomes  $G_{ij}(\theta) = 3/4 \sin^2(\theta)$  in Equation A3.20. The expression for the interband scattering rate is given as

$$\frac{1}{\tau_{ij}} = \frac{2\pi e^2 \hbar \omega_0}{V} \left( \frac{1}{\epsilon_\infty} - \frac{1}{\epsilon_0} \right) \frac{2V}{(2\pi)^3} \frac{2\pi}{\hbar} \cdot \frac{M_i}{\hbar^2} k_0 \int_0^\pi \frac{3/4 \sin^2 \theta \sin \theta d\theta}{(k^2 + k_0^2 - 2k k_0 \cos \theta)}. \quad (\text{A3.24})$$

Performing the integral over  $\theta$  yields

$$\frac{1}{\tau_{ij}} = \frac{3}{2} \frac{e^2 \hbar \omega_o M_j}{\hbar^3 k} \left( \frac{1}{\epsilon_\infty} - \frac{1}{\epsilon_o} \right) \psi_{ij} \left[ 1 - \Phi_{ij} (\Phi_{ij} - \psi_{ij}^{-1}) \right] \left\{ \frac{N_o}{N_o + 1} \right\}, \quad (\text{A3.25})$$

where

$$\psi_{ij} = \log \left| \frac{k + \sqrt{M_j/M_i k^2 \pm 2M_j \omega_o / \hbar}}{k - \sqrt{M_j/M_i k^2 \pm 2M_j \omega_o / \hbar}} \right|,$$

$$\Phi_{ij} = \frac{k^2 \left[ 1 + M_j/M_i \right] \pm 2M_j \omega_o / \hbar}{2k \sqrt{M_j/M_i} \sqrt{k^2 \pm 2M_j \omega_o / \hbar}}.$$

The hole-polar optical phonon scattering rate is calculated and displayed in Figure A3.3. The effective mass approximation is used throughout the entire energy range of the calculation.

#### A3.4 Treatment of the Split-Off Band

The split-off band lies at an energy,  $\Delta$ , above the heavy and light hole bands at the gamma point. Due to this nondegeneracy at the gamma point, the scattering rate formulas must be slightly modified for holes scattered to the split-off band from either the heavy or light hole bands. The situation is analogous to that of the satellite valleys in the conduction band.

In all three scattering mechanisms, polar optical, nonpolar, and acoustic scattering for interband processes initiating in either the heavy or light hole bands the final energy of the hole is given as

$$E_F = E_i \pm \hbar \omega - \Delta \quad (\text{A3.26})$$

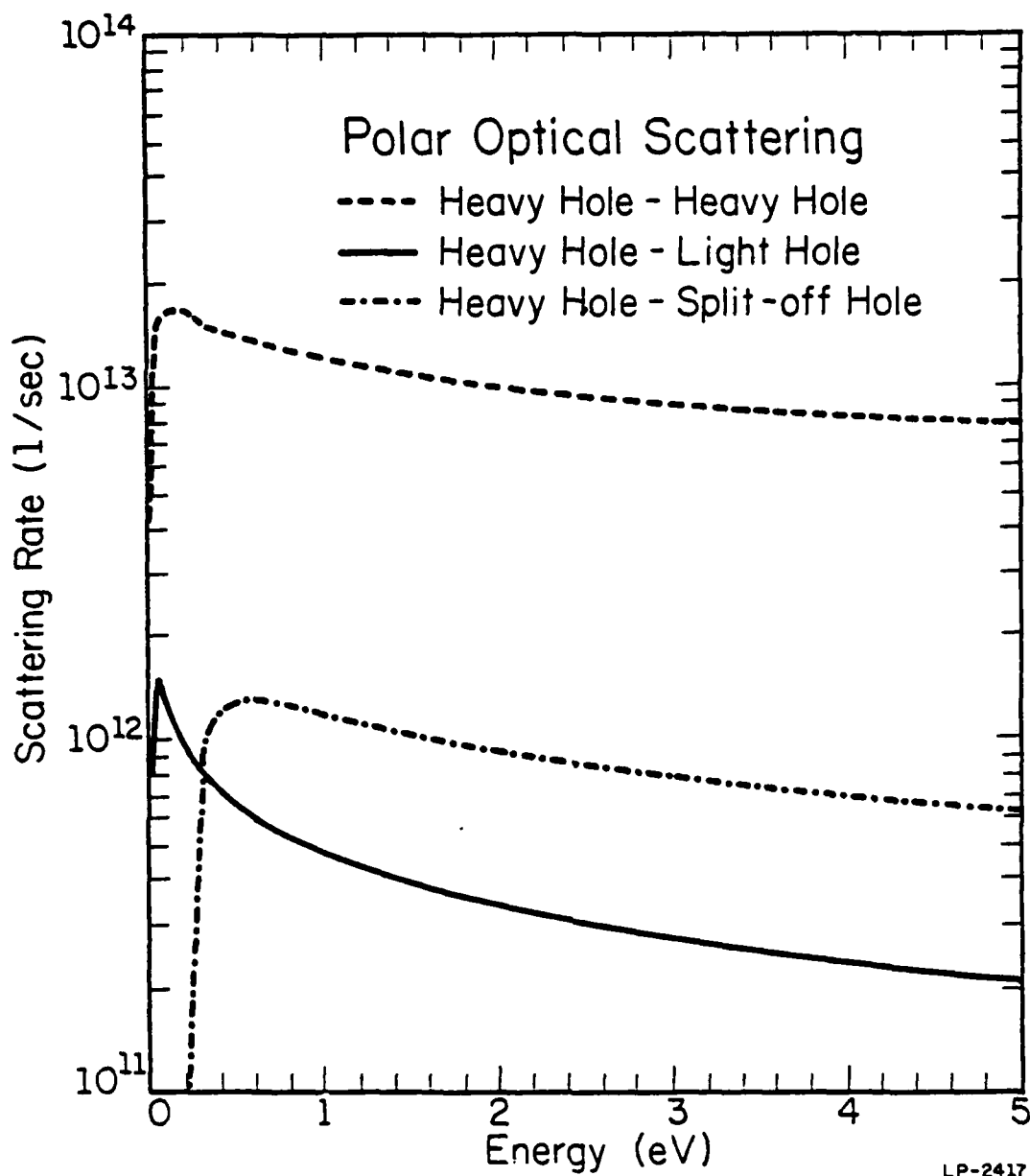


Fig. A3.3: Polar optical phonon scattering of holes in GaAs at 300 K as a function of carrier energy. The relative scattering rates involving transitions from the heavy hole band to each of the other bands, heavy hole (intraband scattering), light hole, and split-off hole bands is depicted.

where  $E_i$  is the initial hole energy in either band 1 or band 2,  $\hbar\omega$  is the phonon energy, and  $\Delta$  is the split-off energy. If  $E_i + \hbar\omega$  or  $E_i - \hbar\omega < \Delta$ , no interband scattering process involving the split-off band can occur.

## REFERENCES

- [1] S. M. Sze, Physics of Semiconductor Devices, 2<sup>nd</sup> Edition, John Wiley and Sons, New York, 1981.
- [2] P. Chatterjee, "Physics and modeling of active and passive devices associated with current VLSI structures," Proceedings of the 3<sup>rd</sup> workshop on the physics of submicron structures, edited by D. K. Ferry, H. Grubin, K. Hess, and G. J. Iafrate, Plenum Press, 1982.
- [3] D. K. Ferry, J. R. Barker, and C. Jacoboni (Editors), Physics of Nonlinear Transport in Semiconductors, Plenum Press, New York and London, 1980.
- [4] H. L. Grubin, D. K. Ferry, G. J. Iafrate, and J. R. Barker, VLSI Electronics: Microstructure Science, N. G. Einspruch (Editor), Academic Press, New York, 1981.
- [5] G. E. Stillman and C. M. Wolfe, "Avalanche photodiodes," Semiconductors and Semimetals, Academic Press, New York, pp. 291-393, 1977.
- [6] R. J. McIntyre, "Multiplication noise in uniform avalanche diodes," IEEE Trans. Electron. Dev., vol. ED-13, pp. 164-167, 1966.
- [7] G. E. Bulman, "The experimental determination of impact ionization coefficients in Gallium Arsenide and Indium Phosphide," Thesis, Univ. of Ill., Urbana, Ill., 1983.
- [8] R. Chin, N. Holonyak, Jr., G. E. Stillman, J. Y. Tang, and K. Hess, "Impact ionization in multilayered heterojunction structures," Electron. Lett., vol. 16, pp. 467-469, 1980.
- [9] F. Capasso, "The channeling avalanche photodiode: A novel ultra-low-noise interdigitated p-n junction detector," IEEE Trans. Electron. Dev., vol. ED-29, pp. 1388-1395, 1982.
- [10] F. Capasso, W. T. Tsang, A. L. Hutchinson, and G. F. Williams, "Enhancement of electron impact ionization in a superlattice: A new avalanche photodiode with a large ionization rate ratio," Appl. Phys. Lett., vol. 40, pp. 38-40, 1982.

- [11] G. E. Bulman, V. M. Robbins, K. F. Brennan, K. Hess, and G. E. Stillman, "Experimental determination of impact ionization coefficients in (100) GaAs," *IEEE Electron Dev. Lett.*, vol. EDL-4, pp. 181-185, 1983.
- [12] L. W. Cook, G. E. Bulman, and G. E. Stillman, "Electron and hole impact ionization coefficients in InP determined by photomultiplication measurements," *Appl. Phys. Lett.*, vol. 40, pp. 589-591, 1982.
- [13] N. Tabatabaie, V. M. Robbins, K. F. Brennan, K. Hess, and G. E. Stillman, "Lack of orientation dependence of impact ionization coefficients in InP," Presented at the 41<sup>st</sup> Annual Device Research Conference, Burlington, Vt., 1983.
- [14] J. Ruch, "Electron dynamics in short channel field-effect transistors," *IEEE Trans. Electron Dev.*, vol. ED-19, pp. 652-654, 1971.
- [15] J. Y. Tang and K. Hess, "Investigation of transient and electronic transport in GaAs following high energy injection," *IEEE Trans. Electron Dev.*, vol. ED-29, pp. 1906-1910, 1982.
- [16] K. Brennan, K. Hess, J. Y. Tang, and G. J. Iafrate, "Transient electronic transport in InP following high energy injection," *IEEE Trans. Electron Dev.*, vol. ED-30, pp. 1750-1754, 1983.
- [17] E. M. Conwell, High Field Transport in Semiconductors, Solid State Physics, F. Seitz, D. Turnbull, and H. Ehrenreich, (Editors), Suppl. 9, Academic Press, New York, 1967.
- [18] K. Brennan and K. Hess, "High field transport in GaAs, InP, and InAs," to be published in *Solid-State Electron.*
- [19] J. A. Cooper, F. Capasso, and K. K. Thornber, "Semiconductor structures for repeated velocity overshoot," *IEEE Electron Dev. Lett.*, vol. EDL-3, pp. 407-408, 1982.
- [20] K. Brennan and K. Hess, "Transient electronic transport in staircase heterostructures," *IEEE Electron Dev. Lett.*, vol. EDL-4, pp. 419-421, 1983.
- [21] C. Jacoboni and L. Reggiani, "The Monte Carlo method for the solution of charge transport in semiconductors with applications to covalent materials," *Rev. of Mod. Phys.*, vol. 55, pp. 645-705, 1983.

- [22] T. Kurosawa, "The application of the Monte Carlo method in semiconductor transport," Proc. Internat. Conf. Phys. Semicond., Kyoto, Japan, Phys. Soc. Japan., Suppl. 21, p. 424, 1966.
- [23] W. Fawcett, A. D. Boardman, and S. Swain, "Monte Carlo determination of electron transport properties in GaAs," J. Phys. Chem. Solids, vol. 31, pp. 1963-1990, 1970.
- [24] J. Y. Tang, "Theoretical studies of high field, high energy transport in gallium arsenide, silicon, and heterostructures," Thesis, Univ. of Ill., Urbana, Ill., 1983.
- [25] P. A. Lebowitz and P. J. Price, "Hybrid method for hot electron calculations," Solid State Commun., vol. 9, pp. 1221-1224, 1971.
- [26] P. J. Price, "Monte Carlo calculation of electron transport in solids," Semiconductors and Semimetals, R. K. Willardson and A. C. Beers, (Editors), vol. 14, Academic Press, New York, pp. 249-309, 1979.
- [27] A. D. Boardman, "Computer simulations of hot electron behavior in semiconductors using the Monte Carlo method," Physics Programs, John Wiley and Sons, Ltd., New York, pp.355-410, 1980.
- [28] J. R. Barker, "Quantum Transport Theory," Physics of Nonlinear Transport in Semiconductors, D. K. Ferry, J. R. Barker, and C. Jacoboni, (Editors), Plenum Press, New York and London, 1980.
- [29] M. Dresden, "Recent developments in the quantum theory of transport and galvanomagnetic phenomena," Rev. of Mod. Phys., vol. 33, pp. 265-342, 1961.
- [30] R. Peierls, "Some simple remarks on the basis of transport theory," Lecture Notes in Physics, No. 31, Transport Phenomena, Springer-Verlag, New York, 1974.
- [31] C. Kittel, Elementary Statistical Physics, John Wiley and Sons, New York, 1958.
- [32] R. P. Feynman, Statistical Mechanics, A Set of Lectures, W. A. Benjamin, Reading Ma., 1972.
- [33] G. J. Iafrate, "Quantum transport and the Wigner function," Presented at the NATO Advanced Study Institute on Submicron Devices, San Miniato, Italy, 1983.

- [34] W. Kohn and J. M. Luttinger, "Quantum theory of electrical transport phenomena," *Phys. Rev.*, vol. 108, pp. 590-611, 1957.
- [35] J. M. Luttinger and W. Kohn, "Quantum theory of electrical transport phenomena, II," *Phys. Rev.*, vol. 109, pp. 1892-1909, 1958.
- [36] E. Wigner, "On the quantum correction for thermodynamic equilibrium," *Phys. Rev.*, vol. 40, pp. 749-759, 1932.
- [37] C. H. Scott and E. J. Moore, "Quasiparticles for the quantum electron-impurity transport problem," *Physica*, vol. 62, pp. 312-320, 1972.
- [38] D. Pines, Elementary Excitations in Solids, W. A. Benjamin, New York, 1977.
- [39] Y. C. Chang, D. Z.-Y. Ting, J. Y. Tang, and K. Hess, "Monte Carlo simulation of impact ionization in GaAs including quantum effects," *Appl. Phys. Lett.*, vol. 42, pp. 26-28, 1983.
- [40] R. C. Eden, A. R. Livingston, and B. M. Welch, "Integrated circuits: the case for gallium arsenide," *IEEE Spectrum*, pp. 30-37, Dec. 1983.
- [41] E. Constant, "Modeling of submicron devices," Presented at the NATO Advanced Study Institute on Submicron Devices, San Miniato, Italy, 1983.
- [42] R. P. Mandal, "III-V semiconductor integrated circuits, a perspective," *Solid State Tech.*, pp. 94-103, Jan., 1982.
- [43] C. V. Shank and D. H. Auston, "Ultrafast phenomena in semiconductor devices," *Science*, vol. 215, pp. 797-801, 12 Feb., 1982.
- [44] J. G. Ruch and G. S. Kino, "Transport properties of GaAs," *Phys. Rev.*, vol. 174, pp. 921-931, 1968.
- [45] T. J. Maloney and J. Frey, "Transient and steady-state electron transport properties of GaAs and InP," *J. Appl. Phys.*, vol. 48, p. 781, 1977.
- [46] J. R. Hauser, T. H. Glisson, and M. A. Littlejohn, "Negative resistance and peak velocity in the central (100) valley of III-V semiconductors," *Solid-State Electron.*, vol. 22, pp. 487-493, 1979.
- [47] B. K. Ridley, "Anatomy of the transferred electron effect in III-V semiconductors," *J. Appl. Phys.*, vol. 48, pp. 754-764, 1977.

- [48] H. L. Grubin and T. M. McHugh, "Hot electron transport effects in field effect transistors," *Solid-State Electron.*, vol. 21, pp. 69-73, 1978.
- [49] M. L. Cohen and T. K. Bergstresser, "Band structures and pseudopotential form factors for fourteen semiconductors of the diamond and zinc-blende structures," *Phys. Rev.*, vol. 141, pp. 789-796, 1966.
- [50] P. A. Wolff, "Theory of electron multiplication in silicon and germanium," *Phys. Rev.*, vol. 95, pp. 1415-1420, 1954.
- [51] W. Shockley, "Problems related to p-n junctions in silicon," *Solid-State Electron.*, vol. 2, pp. 35-67, 1961.
- [52] G. A. Baraff, "Distribution functions and ionization rates for hot electrons in semiconductors," *Phys. Rev.*, vol. 128, pp. 2507-2517, 1962.
- [53] L. V. Keldysh, "Concerning the theory of impact ionization in semiconductors," *Sov. Phys. JETP*, vol. 21, pp. 1135-1144, 1965.
- [54] W. P. Dumke, "Theory of avalanche breakdown in InSb and InAs," *Phys. Rev.*, vol. 167, pp. 783-789, 1968.
- [55] R. Chwang, C. W. Kao, and C. R. Crowell, "Normalized theory of impact ionization and velocity saturation in nonpolar semiconductors via a Markov chain approach," *Solid-State Electron.*, vol. 22, pp. 599-620, 1979.
- [56] H. Shichijo and K. Hess, "Band-structure-dependent transport and impact ionization in GaAs," *Phys. Rev. B*, vol. 23, pp. 4197-4207, 1981.
- [57] M. A. Littlejohn, J. R. Hauser, and T. H. Glisson, "Velocity-field characteristics of GaAs with  $c_{-L}^c - x^c$  conduction-band ordering," *J. Appl. Phys.*, vol. 48, pp. 4587-4590, 1977.
- [58] P. A. Houston and A. G. R. Evans, "Electron drift velocity in n-GaAs at high electric fields," *Solid-State Electron.*, vol. 20, pp. 197-204, 1977.
- [59] T. H. Windhorn, T. J. Roth, L. M. Zinkiewicz, O. L. Gaddy, and G. E. Stillman, "High field temperature dependent electron drift velocities in GaAs," *Appl. Phys. Lett.*, vol. 40, pp. 513-515, 1982.

- [60] T. H. Windhorn, L. W. Cook, M. A. Haase, and G. E. Stillman, "Electron transport in InP at high electric fields," to be published in Appl. Phys. Lett.
- [61] K. Hess and J. D. Dow, "Deformation potentials of bulk semiconductors," Solid State Commun., vol. 40, pp. 371-373, 1981.
- [62] K. K. Mon, K. Hess, and J. D. Dow, "Deformation potentials of superlattices and interfaces," J. Vac. Sci. Technol., vol. 19, pp. 564-566, 1981.
- [63] A. B. Migdal, "Interaction between electrons and lattice vibrations in a normal metal," Sov. Phys. JETP, vol. 34, pp. 996-1001, 1958.
- [64] W. Jones and N. A. March, Theoretical Solid-State Physics, John Wiley and Sons, New York, 1973.
- [65] A. Messiah, Quantum Mechanics, John Wiley and Sons, New York, 1958.
- [66] H. W. Wyld, Mathematical Methods for Physics, Benjamin Cummings, New York, 1976.
- [67] F. Capasso, J. P. Pearsall, K. K. Thornber, R. E. Nahory, M. A. Pollack, G. B. Bachelet, and J. R. Chelikowsky, "Comment on 'Simulation of high-field transport in GaAs using a Monte Carlo method and pseudopotential band structures,' and on 'Band-structure dependent transport and impact ionization in GaAs,'" J. Appl. Phys., vol. 53, pp. 3324-3326, 1982.
- [68] K. Hess, J. Y. Tang, K. Brennan, H. Shichijo, and G. E. Stillman, "Reply to 'Comment on 'Simulation of high-field transport in GaAs using a Monte Carlo method and pseudopotential band structures,' and on 'Band-structure dependent transport and impact ionization in GaAs''", J. Appl. Phys., vol. 53, pp. 3327-3329, 1982.
- [69] T. P. Pearsall, F. Capasso, R. E. Nahory, M. A. Pollack, and J. R. Chelikowsky, "The band structure dependence of impact ionization by hot carriers in semiconductors: GaAs," Solid-State Electron., vol. 21, pp. 294-302, 1978.
- [70] T. P. Pearsall, R. E. Nahory, and J. R. Chelikowsky, "Threshold energies for impact ionization by electrons and holes in the GaAs-GaSb system," Inst. Phys. Conf. Ser. No. 33b, Chapter 6, pp. 331-338, 1977.
- [71] C. L. Anderson and C. R. Crowell, "Threshold energies for electron-hole pair production by impact ionization in semiconductors," Phys. Rev. B, vol. 5, pp. 2267-2272, 1972.

- [72] B. K. Ridley, "A model for impact ionization in wide-gap semiconductors," *J. Phys. C : Solid State Phys.*, vol. 16, pp. 4733-4751, 1983.
- [73] B. K. Ridley, "Lucky-drift mechanism for impact ionization in semiconductors," *J. Phys. C : Solid State Phys.*, vol. 16, pp. 3373-3388, 1983.
- [74] E. O. Kane, "Band structure of Indium Antimonide," *J. Phys. Chem. Solids*, Pergamon Press, vol. 1, pp. 633-636, 1980.
- [75] J. D. Wiley, "Mobility of holes in III-V compounds," *Semiconductors and Semimetals*, R. K. Willardson and A. C. Beer (Editors), Academic Press, pp. 91-174, 1975.
- [76] M. Costato and L. Reggiani, "Scattering probabilities for holes, I. Deformation potential and ionized impurity scattering mechanisms," *Phys. Stat. Sol. (b)*, vol. 58, pp. 471-482, 1973.
- [77] M. Costato and L. Reggiani, "Scattering probabilities for holes, II. Polar optical scattering mechanism," *Phys. Stat. Sol. (b)*, vol. 58, pp. 47-54, 1973.
- [78] C. Canali, C. Jacoboni, F. Nava, G. Ottaviani, and A. Albeirgi-Quaranta, "Electron drift velocity in silicon," *Phys. Rev. B*, vol. 12, pp. 2265-2284, 1975.
- [79] G. L. Bir and G. E. Pikus, "Theory of the deformation potential for semiconductors with a complex band structure," *Sov. Phys.-Solid State*, vol. 2, pp. 2039-2051, 1961.
- [80] J. D. Wiley, "Valence-band deformation potentials for the III-V compounds," *Solid State Commun.*, vol. 8, pp. 1865-1868, 1970.
- [81] J. Y. Tang and K. Hess, "Impact ionization of electrons in silicon (steady state)," *J. Appl. Phys.*, vol. 54, pp. 5139-5144, 1983.
- [82] L. H. Holway, S. R. Steele, and M. G. Alderstein, "Measurement of electron and hole properties in p-type GaAs," *Proceedings of the Seventh Biennial Cornell Electrical Engineering Conference*, pp. 199-208, 1979.
- [83] E. O. Kane, "Electron scattering by pair production in silicon," *Phys. Rev.*, vol. 159, pp. 624-631, 1967.
- [84] O. Hildebrand, W. Kuebart, K. W. Benz, and M. H. Pilkuhn, " $\text{Ga}_{1-x}\text{Al}_x\text{Sb}$  avalanche photodiodes: resonant impact ionization with very high ratio

- of ionization coefficients," IEEE J. Quantum Electron., vol. QE-17, pp. 284-288, 1981.
- [85] O. Hildebrand, W. Kuebart, and M. H. Pilkuhn, "Resonant enhancement of impact ionization in  $\text{Ga}_{1-x}\text{Al}_x\text{Sb}$ ," Appl. Phys. Lett., vol. 37, pp. 801-803, 1980.
- [86] M. A. Littlejohn, J. R. Hauser, T. H. Glisson, D. K. Ferry, and J. W. Harrison, "Alloy scattering and high field transport in ternary and quaternary III-V semiconductors," Solid-State Electron., vol. 21, pp. 107-114, 1978.
- [87] J. W. Harrison and J. R. Hauser, "Theoretical calculations of electron mobility in ternary III-V compounds," J. Appl. Phys., vol. 47, pp. 292-300, 1976.
- [88] D. Kasemset, "Impact ionization in  $\text{Ga}_{1-x}\text{Al}_x\text{Sb}$ : an alternative interpretation," (unpublished).
- [89] M. Z. Zhingarev, V. I. Korolkov, M. P. Mikhailova, V. V. Sazonov, and D. N. Tretyakov, "Avalanche multiplication and coefficients of impact ionization in p-n homojunctions and heterojunctions made of GaSb and its solid solutions," Sov. Phys. Semicond., vol. 14, pp. 801-806, 1980.
- [90] M. Z. Zhingarev, V. I. Korolkov, M. P. Mikhailova, and I. N. Yassievich, "Impact ionization in GaSb and its solid solutions," Sov. Tech. Phys. Lett., vol. 5, pp. 355-357, 1979.
- [91] T. P. Pearsall, R. E. Nahory, and M. A. Pollack, "Impact ionization rates for electrons and holes in  $\text{GaAs}_{1-x}\text{Sb}_x$  alloys," Appl. Phys. Lett., vol. 28, pp. 403-405, 1976.
- [92] H. C. Casey, Jr. and M. B. Panish, Heterostructure Lasers, Academic Press, New York, 1978.
- [93] M. S. Shur and L. F. Eastman, "Near ballistic electron transport in GaAs devices at 77 K," Solid-State Electron., vol. 24, pp. 11-18, 1981.
- [94] J. Frey, "Ballistic transport in semiconductor devices," IEDM Tech. Dig., pp. 613-617, 1980.
- [95] K. Hess, "Ballistic electron transport in semiconductors," IEEE Trans. Electron Dev., vol. ED-28, pp. 937-940, 1981.

- [96] T. J. Maloney and J. Frey, "Transient and steady-state electron transport properties of GaAs and InP," *J. Appl. Phys.*, vol. 48, p.781, 1977.
- [97] T. J. Maloney, "Polar mode scattering in ballistic transport GaAs devices," *IEEE Electron Dev. Lett.*, vol. EDL-1, p. 54, 1980.
- [98] C. K. Williams, M. A. Littlejohn, T. H. Glisson, and J. R. Hauser, "Ballistic transport in GaAs," *IEEE Electron Dev. Lett.*, vol. EDL-4, pp. 161-163, 1983.
- [99] R. J. Malik, K. Board, L. F. Eastman, C. E. C. Wood, T. R. Avion, and R. L. Ross, "Rectifying variable planar-doped barrier structures in GaAs," Gallium Arsenide and Related Compounds, 1980, Inst. Phys. Conf. Ser. No. 56, Ch. 9, pp. 697-710.
- [100] A. Ghis, E. Constant, and B. Boittiaux, "Ballistic and overshoot electron transport in bulk semiconductors and in submicronic devices," *J. Appl. Phys.*, vol. 54, pp. 214-221, 1983.
- [101] T. H. Glisson, C. K. Williams, J. R. Hauser, and M. A. Littlejohn, "Transient response of electron transport in GaAs using the Monte Carlo method," VLSI Electronics: Microstructure Science, Vol. 4, N. G. Einspruch (Editor), Academic Press, New York, pp. 99-145, 1982.
- [102] J. A. Cooper, F. Capasso, and K. K. Thornber, "Semiconductor structures for repeated velocity overshoot," *IEEE Electron Dev. Lett.*, vol EDL-3, pp. 407-408, 1982.
- [103] J. Shah, R. E. Nahory, R. F. Leheny, J. Degani, and A. E. Digiovanni, "Hot-carrier relaxation in p-In<sub>0.53</sub>Ga<sub>0.47</sub>As," *Appl. Phys. Lett.*, vol. 40, pp. 505-507, 1982.
- [104] C. Jacoboni, C. Canali, G. Ottaviani, and A. Alberiga-Quaranta, "A review of some charge transport properties of silicon," *Solid-State Electron.*, vol. 20, pp. 77-89, 1977.
- [105] M. Neuberger, Handbook of Electronic Materials, Vol. 2, Plenum Press, New York, pp. 45-56, 1971.
- [106] Reference 105, pp. 108-112.
- [107] Reference 105, pp. 93-103.
- [108] Reference 105, pp. 35-40.

[109] P. Lawaetz, "Valence-band parameters in cubic semiconductors," Phys. Rev. B, vol. 4, pp. 3460-3467, 1971.

[110] Reference 105, pp. 7-12.

**VITA**

Kevin Francis Brennan was born on October 18, 1956 in Elizabeth, N.J. He attended the Massachusetts Institute of Technology in Cambridge, Massachusetts. He graduated with a Bachelor of Science degree in Physics in May, 1978. He has been attending the University of Illinois at Urbana-Champaign since September, 1978. He received a Master of Science degree in Physics in January, 1980. In July, 1983, he was awarded a scholarship to the NATO Advanced Study Institute, San Miniato, Italy for the school on the physics of submicron devices. He is a member of the American Physical Society and the Institute of Electrical and Electronics Engineers. He has been elected to Sigma Xi, the National Research Society. He is presently a candidate for the degree of Doctor of Philosophy in Electrical Engineering from the University of Illinois.

**END**

**FILMED**

---

*1-86*

**DTIC**